Computational design of molecules for dye sensitized solar cells and nano electronics

Ørnsø, Kristian Baruël

Publication date:
2015

Document Version
Publisher's PDF, also known as Version of record

Computational design of molecules for dye sensitized solar cells and nano electronics

Kristian Baruël Ørnsø

Ph.D. thesis

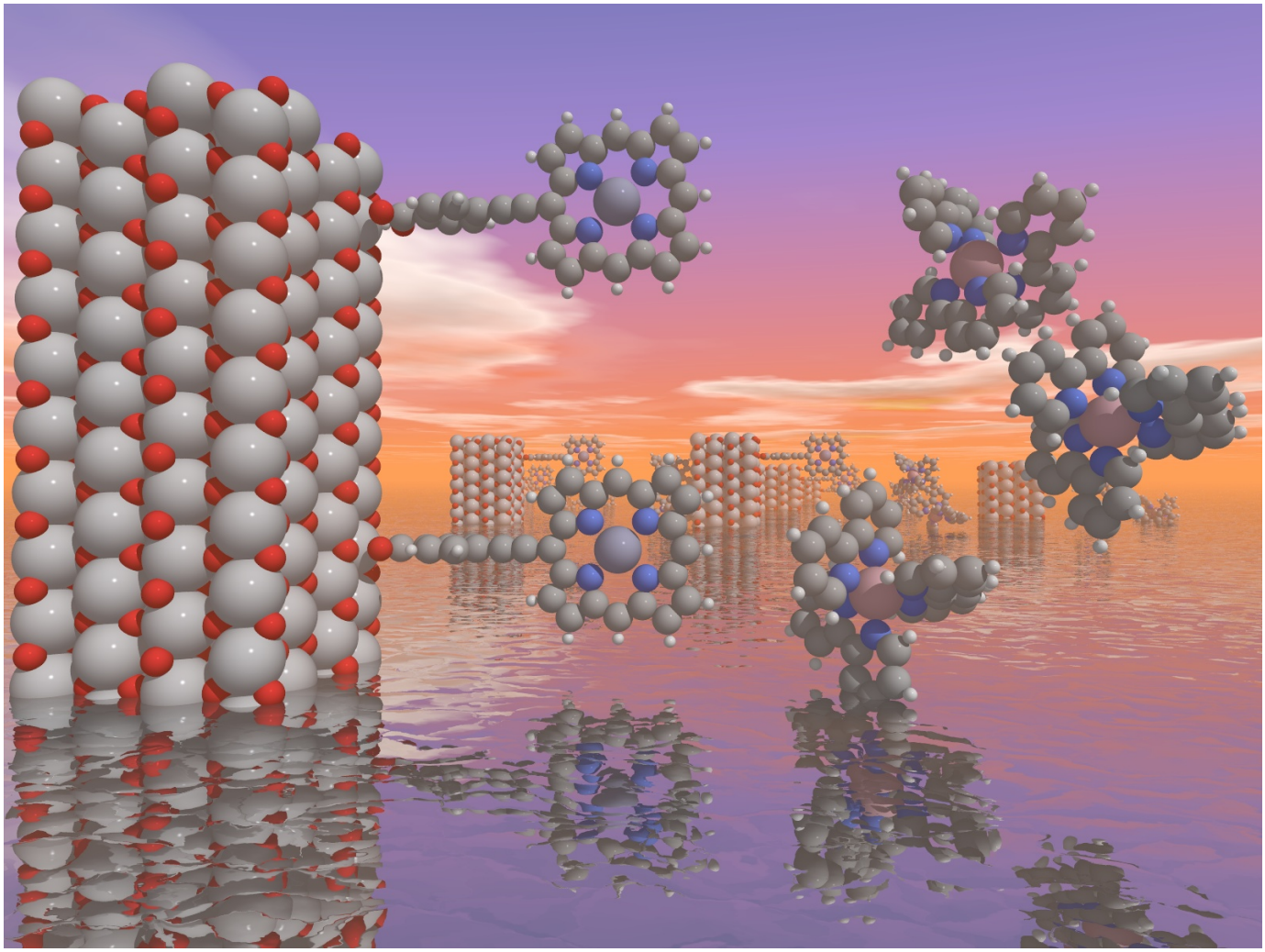

DTU Physics
Department of Physics

Kristian Baruël Ørnsø

Computational design of molecules for dye sensitized solar cells and nano electronics

Ph.D. thesis

Center for Atomic-scale Materials Design
Department of Physics
Technical University of Denmark

DTU Physics
Department of Physics

Preface

Kgs. Lyngby d. 31/07-2015

This thesis is submitted in candidacy for the title of *Philosophiae Doctor* in Physics. The work presented herein represents three years of full time studies from August, 1st 2012 to July, 31st 2015. The project has been carried out at the Center for Atomic-scale Materials Design, Department of Physics, Technical University of Denmark under the supervision of Prof. Kristian S. Thygesen with a two month external stay in the group of Prof. Angel Rubio at the University of the Basque Country, San Sebastian, Spain.

Kristian Baruël Ørnsø
M.Sc.

Acknowledgements

For me as a chemist, joining the Department of Physics was a huge step, but never something I have regretted. Three years of being exposed to the physicists' approaches to electronic structure problems have taught me very much and opened my eyes to the multitude of angles from which you can approach the same problem. Furthermore, I have been so fortunate as to work on a very interesting project where I have been challenged with new theories and the handling of large amounts of data. However, the most important factor in overcoming great challenges, is the help of many dedicated people to whom I would like to extend my sincere gratitude.

First and foremost, I would like to thank my supervisor Kristian S. Thygesen for his patience with a stubborn chemist and his molecules. I have really enjoyed our discussions, teaching me everything from electron transport theory to the writing of scientific papers. I would also like to thank my co-supervisor Karsten W. Jacobsen for his help and support, especially in connection with our discussions of Marcus Theory. In connection with this, I would furthermore like to thank my former office mate Elvar Ö. Jónsson for all his help with scripts, theory notes and countless discussions and e-mails. I would also like to thank Mohnish Pandey, Niels B. Halck, Manuel Šarić, Korina Kuhar, Christopher Patrick, Kirsten Andersen, Martin H. Hansen, Morten N. Gjerding, Simone Latini, Filip A. Rasmussen, Per S. Schmidt, Ulrik G. Vej-Hansen and the rest of the students and employees in CAMd for creating a great atmosphere.

For great collaboration and sharing of their results, I would like to extend my gratitude to Juan Maria Garcia-Lastra, Christian S. Pedersen, Chengjun Jin, Troels Markussen, Franz Himpsel, Gema De La Torre and Wenjing Hong. I would especially like to thank Angel Rubio for his great hospitality and supervision during my stay in San Sebastian and his enthusiasm regarding our molecular tandem project.

If the practical setup is missing, every project will fail. Hence, I would very much like to thank Marianne Ærsøe for her help with every administrative problem I have faced and Cecilia Benguria for all her help with practical issues in San Sebastian. Furthermore, I would like to express my great admiration of Marcin Dulak, Jens Jørgen Mortensen and Ole H. Nielsen for their ability to simultaneously administer a huge computer infrastructure, a complex electronic structure code and a group of demanding scientists.

In the past three years, I have been so privileged as to help supervise a few B.Sc. and M.Sc. projects. In connection with this, I would very much like to thank Anders Jensen, André Anda, Christian S. Pedersen and Rasmus Just for all our interesting discussions, which helped me realize that you do not really know a subject until you have taught it to someone else.

I would furthermore like to thank Sten Rettrup, Elvar Ö. Jónsson, Chengjun Jin, Bjørn B. Petersen, Birgitte Ørnsø, Marie B. Overballe and Henrik Overballe for taking the time to read parts of my thesis and offer very helpful suggestions. I am furthermore very grateful for the financial support provided by DFF-Sapere Aude and the Idella foundation.

Finally, I would like to thank all my friends and my family for their support during three years with successes and difficulties. A very special thank goes to my wife Marie B. Overballe for her endless love and care. I could not have done this without her.

Abstract

The huge increase in computational power has enabled the use of high-throughput computational screening methods for many purposes. In combination with more detailed computational studies, this provides a powerful tool in the search for new materials and molecules useful for *e.g.* photovoltaics. This is illustrated in this thesis, where a high-throughput Density Functional Theory study of a total of 5145 porphyrin based dye molecules is presented. Initially, the structures of the dyes are optimized and the frontier energy orbital energies calculated. Following this, the dyes are scored for use in a dye sensitized solar cell (DSSC) in terms of a loss-less level alignment quality. This scoring only takes into account a simplified absorption spectrum of the dye in combination with the alignment between the molecular levels, the semi-conductor conduction band edge and the redox mediator. To improve on this, the effect of the free energy barrier associated with the dye regeneration reaction is included through extensive molecular dynamics simulations for a simple model dye, followed by an extrapolation of the result to the 5145 porphyrins. This model succeeds in rediscovering high efficiency dyes and suggests that the next generation of high efficiency porphyrin dyes may utilize a titanium metal center. Furthermore, the large internal reorganization energies calculated for the octahedral cobalt complexes, used as redox mediators, lead to the requirement of a large driving force for the regeneration reaction. Hence, using redox mediators with a lower internal reorganization energy would allow for a less constrained choice of dye, possibly boosting the efficiency.

The obtained data is furthermore used to search for suitable pairs of porphyrins for a novel type of DSSC schemes, using two dyes in a molecular two-photon tandem approach. Here, a high current is sacrificed for a larger voltage. As a smaller current is however often associated with a better fill-factor, the proposed scheme may lead to an increase in the efficiency. Specific candidates for the different schemes are identified and the resulting setups have theoretically obtainable open-circuit voltages exceeding 1.5 V.

Creating a metal-molecule-metal junction allows tuning the conductance through the junction by manipulating the molecular energy levels. In this thesis a computational approach to model the conductance as a function of the applied bias voltage, shifting the molecular levels, for a redox active molecule is presented and compared to experimental results. Here, it is shown that shifting the molecular energy levels in and out of resonance with the Fermi level of the electrodes, allows for a standard tuning of the conductance. In addition to this, reversibly changing the redox state, allows for switching quantum interference on and off, shifting the conductance by an order of magnitude. The simple computational model used is furthermore qualitatively found to be in very good agreement with experiments.

A different way of tuning the conductance through a molecular junction, is by controlling the junction geometry. This is achieved by designing a molecule with two sets of anchor groups, which bind to gold with significantly different strengths. Hence, it is proposed that the geometry can be controlled by chemical passivisation of one type of anchor group. Using a simple computational model, this experimental hypothesis is verified and the change in conductance upon changing junction geometry is reproduced.

Resumé

Den drastiske stigning i tilgængelig computerkraft har medført, at beregninger i stor skala i mange sammenhænge er blevet realiserbare. Især kombinationen af stor-skala beregninger med mere detaljerede beregningsmetoder, er et effektivt værktøj til at finde nye materialer og molekyler til f.eks. solceller. Dette illustreres i denne afhandling, hvor et Density Functional Theory studie af 5145 porphyrin baserede farvestoffer præsenteres. Det første trin i projektet er at optimere strukturen af alle farvestofferne, hvorefter energien af de vigtigste molekylære orbitaler beregnes. Efterfølgende ranglistes farvestofferne efter deres anvendelighed i en dye sensitized solar cell (DSSC) ved hjælp af en såkaldt level alignment quality, der negligerer alle tabsmekanismer. Denne metode tager således kun et simplificeret absorptionspektrum, samt overenstemmelsen mellem de molekylære orbitaler, konduktionsbåndskanten af halvlederen og den redoxaktive elektrolyt, i betragtning. Måden hvorpå farvestofferne ranglistes, forbedres herefter ved at indrage den frie energibarriere associeret med regenerationsreaktionen. Dette gøres ved at udføre ekstensive molecular dynamics simulationer for et modelsystem, og derefter overføre resultatet til de 5145 oprindelige kandidater. Ved hjælp af denne metode genfindes velkendte højtydende farvestoffer, samt en række titanbaserede porphyriner, der bør undersøges nærmere med henblik på anvendelse i DSSCs. Derudover identificerer metoden den høje interne reorganiseringsenergi af de oktaedriske cobaltkomplekser, der udgør den redoxaktive elektrolyt, som et problem der påtvinger farvestofferne et krav om en høj drivkraft for regenerationsreaktionen. Muligheden for at bruge andre redoxaktive elektrolytter med en mindre intern reorganiseringsenergi, bør derfor undersøges, da dette vil give et mere frit valg af farvestof og dermed muligheden for en højere solcelleeffektivitet.

Den store mængde beregnet data er yderligere blevet brugt til at identificere porphyrinpar, som vil være velegnede i en ny type DSSC opsætning, hvori der indgår to farvestofsmolekyler, der sammenlagt absorberer to fotoner i en molekylær udgave af en tandemsolcelle. I denne type opsætning ofres strømstyrken på bekostning af en høj spænding, men en lav strømstyrke er ofte forbundet med en højere fill-factor og dette kan således sammenlagt lede til en forøgelse af solcelleeffektiviteten. I denne afhandling identificeres specifikke porphyrinpar til brug i de forskellige opsætninger, og den maksimalt teoretisk opnåelige spænding beregnes til at overstige 1,5 V.

Ved at konstruere en metal-molekyle-metal kontakt, er det muligt at bruge de molekylære energiniveauer til at manipulere konduktansen igennem kontakten. I denne afhandling præsenteres en beregningsmodel, der anvendes til at modellere konduktansen som funktion af bias spændingen, der flytter de molekylære energiniveauer op og ned, for en kontakt med et redoxaktivt molekyle. Resultaterne sammenlignes herefter med eksperimentielle data. Det vises, at der sker en normal ændring af konduktansen, når de molekylære energiniveauer flyttes ind eller ud af resonans med metalelektrodernes Ferminiveau. Yderligere kan konduktansen ændres med en størrelsesorden, ved reversibelt at skifte redoxtilstand af molekylet, hvorved dennes kvanteinterferens tændes og slukkes. Derudover vises det, at den anvendte simple beregningsmodel er kvalitativt i overenstemmelse med eksperiementielle data.

En anden måde hvorpå konduktansen af en molekylær kontakt kan modificeres, er ved at kontrollere kontaktens geometri. Dette kan opnås ved at designe et molekyle med to sæt ankergrupper, der binder til guld med meget forskellig styrke. Det postuleres dermed, at kontaktgeometrien kan kontolleres ved kemisk at passivere den ene type ankergruppe. Dette postulat eftervises ved brug af en simpel beregningsmodel, der yderligere reproducerer det konduktansskifte, der følger af at ændre kontaktgeometrien.

Included publications

Paper I

Computational screening of functionalized zinc porphyrins for dye sensitized solar cells
K. B. Ørnsø, J. M. Garcia-Lastra and K. S. Thygesen
Phys. Chem. Chem. Phys., **2013**, *15*, 19478-19486

Paper II

Optimizing porphyrins for dye sensitized solar cells using large-scale *ab initio* calculations
K. B. Ørnsø, C. S. Pedersen, J. M. Garcia-Lastra and K. S. Thygesen
Phys. Chem. Chem. Phys., **2014**, *16*, 16246-16254

Paper III

Importance of the reorganization energy barrier in computational design of porphyrin-based solar cells with cobalt-based redox mediators
K. B. Ørnsø, E. Ö. Jónsson, K. W. Jacobsen and K. S. Thygesen
J. Phys. Chem. C, **2015**, *119*, 12792-12800

Paper IV

Design of two-photon molecular tandem architectures for solar cells by *ab initio* theory
K. B. Ørnsø, J. M. Garcia-Lastra, G. De La Torre, F. J. Himpsel, A. Rubio and K. S. Thygesen
Chem. Sci., **2015**, *6*, 3018-3025

Paper V

Electrochemical control of single-molecule conductance by Fermi-level tuning and conjugation switching
M. Baghernejad, X. Zhao, K. B. Ørnsø, M. Füeg, P. Moreno-Garcia, A. V. Rudnev, V. Kaliginedi, S. Vesztergom, C. Huang, W. Hong, P. Broekmann, T. Wandlowski, K. S. Thygesen and M. R. Bryce
J. Am. Chem. Soc., **2014**, *136*, 17922-17925

Paper VI

Controlling electrical conductance through a π-conjugated cruciform molecule via selective anchoring to gold electrodes
C. Huang, S. Chen, K. B. Ørnsø, D. Reber, M. Baghernejad, Y. Fu, T. Wandlowski, S. Decurtins, W. Hong, K. S. Thygesen and S.-X. Liu
2015, *submitted*

Contents

Chapter 1

Introduction

"The clear and present danger of climate change means we cannot burn our way to prosperity. We already rely too heavily on fossil fuels. We need to find a new, sustainable path to the future we want. We need a clean industrial revolution."

Ban Ki-moon
UN Secretary-General
"Clean Industrial Revolution"
Durban, South Africa
December 2011

In December 2011, UN Secretary-General Ban Ki-moon called for a clean industrial revolution to replace fossil fuels with sustainable energy,[1] but so far this proposed revolution has not been overwhelmingly successful. The absence of revolutionary steps should however not be mistaken as absence of progress and the world has witnessed several breakthroughs in sustainable technologies in the past decades. Focusing on the vast energy source presented by the sun alone, it is estimated that 600 TW solar power is practically available at the Earth surface.[2] In comparison, the global energy consumption in the beginning of this millennium was 13 TW, with a projected need of additionally 12-30 TW by 2050.[3;4] A straightforward analysis hence shows that solar cells, with around 10% efficiency, should be more than sufficient to cover the global energy need for several years. An important factor not included in the above argument, is however the economical aspect of exploiting the sunlight. According to calculations by McFarland,[5] in order to sustain the economical growth, the total cost of a solar converter with an efficiency of 15% producing energy priced at $ 15 / GJ, should be lower than $ 54 / m^2 including manufacturing, installing and energy production upstart. The same study states that in 2014, the cheapest solar conversion module was priced at $ 150 / m^2, leaving *e.g.* nuclear power as a more cost efficient alternative. However, as the price of silicon continues to drop, higher solar conversion efficiency plays an increasingly important role in making competitive solar cell designs. At present, the actual silicon solar cell accounts for less than 1/4 of the cost of a complete solar panel installation and the cost of the support structure is becoming increasingly important.[6] As higher efficiency reduces the required area, this in terms leads to a reduced cost of both the solar cells and their support structure.

1.1 Dye sensitized solar cells

Since the emergence of the first efficient system in 1991,[8] the dye sensitized solar cell (DSSC) has been considered a promising technology in terms of achieving a high efficiency at a low cost.[2;9] The primary component of a standard DSSC is porous semi-conductor nano-particles, usually TiO_2, attached to a transparent electrode and covered by dye molecules. This is together with a counter electrode, usually Pt, embedded by a solvent, often acetonitrile, containing a redox mediator. The full mechanism of a DSSC is explained in Chapter 5, but the most essential point

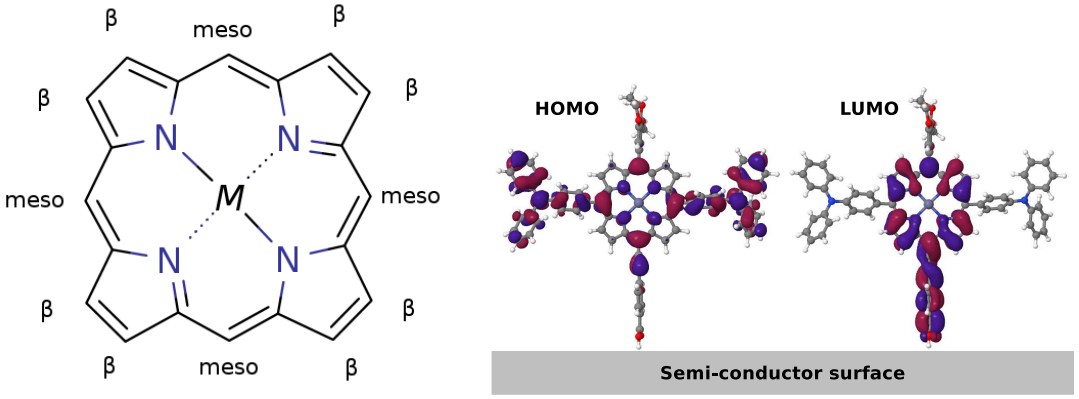

Figure 1.1: **Left:** Illustration of a porphyrin backbone indicating the meso and β sites. The central M represents a metal center or alternatively two hydrogen atoms. **Right:** Visual representation of the calculated HOMO and LUMO of the Donor-π-Acceptor M3T2P zinc porphyrin dye molecule.[7]

is that the sunlight is absorbed by the dyes, converting the photons into electrons used in the electric circuit connecting the transparent electrode with the counter electrode. Hence, a vital component is the dye molecule. Initially, ruthenium-based dyes dominated the DSSC community, but the high cost of ruthenium lead to expensive devices.[10] Thus, the focus shifted towards cheaper alternatives and here using a porphyrin based dye was a natural choice, since porphyrins were already used in various other contexts including light absorption in nature.[11;12] This proved to be an excellent choice, as porphyrins are very well suited for DSSCs due to their high absorption of visible light and high customizability,[13–30] including the possibility to construct dimers and trimers.[31;32]

As illustrated in the left part of Figure 1.1, the porphyrin backbone can be functionalized at both the meso and the β sites. Functionalizing porphyrins with electron donating side groups at three of the meso sites and an electron accepting anchor group at the remaining meso site, yields so-called donor-π-acceptor porphyrin dyes. These dyes are characterized by exhibiting excellent charge separation upon excitation, as the highest occupied molecular orbital (HOMO) is localized mostly on the side groups, while the lowest unoccupied molecular orbital (LUMO) is localized more on the anchor group.[7;33;34] This is illustrated in the right part of Figure 1.1. The success of donor-π-acceptor porphyrin dyes is underlined by the current record holding dye, with a DSSC efficiency of 13%, which belongs to this class.[35] Apart from functionalizing the porphyrin backbone, it is also possible to modify the backbone itself. The record efficiency dye employs a zinc metal center in the porphyrin backbone, but modifying the backbone by exchanging zinc as the metal center can alter the electronic structure of the dye significantly.[36;37] In addition, replacing hydrogens at the β positions with fluorine in copper-phthalocyanine, a class of dyes closely related to porphyrins, has been shown to produce a significant lowering of the frontier orbital energies.[38] Furthermore, using a Ti^{4+} metal center in the porphyrin allows for the use of axial ligands. As shown by Pickup *et al.* for titanium phthalocyanines, this can have a large impact on the frontier orbitals.[39]

A separate issue in a DSSC is to choose the right redox mediator with suitable properties such as redox potential and electron transfer kinetics.[40–42] Lately, high efficiencies have been obtained employing cobalt based octahedral complexes as redox mediators.[27;43;44] Interactions between Ru based dyes and Co based redox mediators however limit electron injection and enhance losses through electron recombination, making this combination unfavourable.[45] In general, bulky groups on either the dye or the redox mediator providing steric hindrance for keeping the redox mediator away from the TiO_2 surface are needed for all transition metal complex based redox mediators to prevent recombination.[27;46;47] In connection with this, Pazoki *et al.* reported that the main efficiency boost obtained by increasing the dye coverage of the semi-conductor is actually ascribed to the better blocking of the redox mediator.[48] On the other hand, increased dye coverage may promote the unwanted recombination from the conduction band of the semi-conductor to the oxidized dye.[49] Recently, a more advanced tandem like setup with both a cobalt based redox mediator and a purely

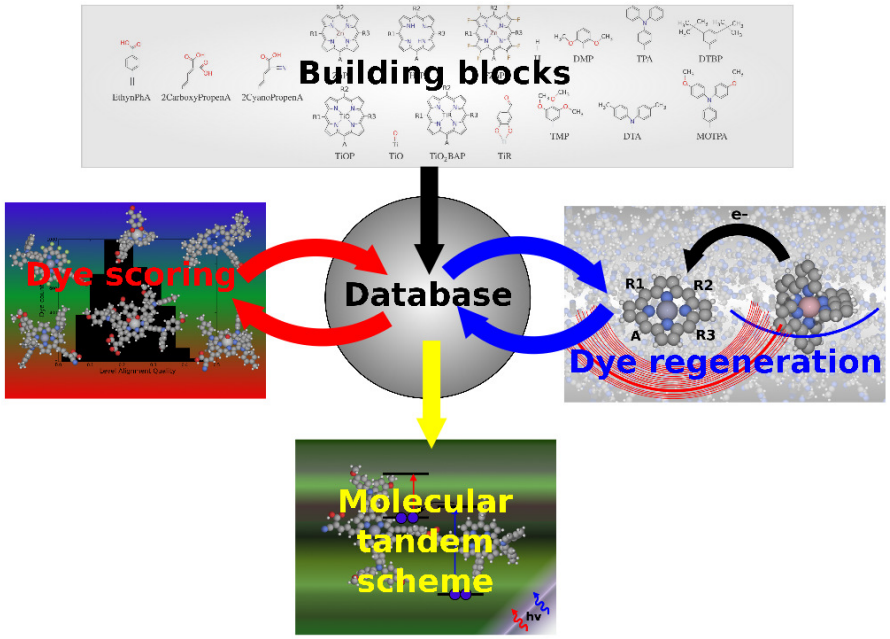

Figure 1.2: Illustration of the concepts used to construct and exploit a database of porphyrin dyes for use in a dye sensitized solar cell (DSSC). A set of building blocks are initially chosen to construct several thousand dyes which are then scored based on their calculated energetics. This scoring is saved in the database and subsequently improved by inclusion of the free energy barrier associated with the dye regeneration reaction. Finally, the energetics stored in the database are used to propose possible candidates for a novel molecular tandem scheme, designed to boost the efficiency of a DSSC.

organic redox mediator, has been proposed to improve the open-circuit voltage.[50] Here, the organic redox mediator is primarily responsible for the regeneration of the oxidized dye and is then itself swiftly regenerated by the cobalt based redox mediator, leading to a fast dye regeneration process. Purely organic redox mediators have also been introduced as a cheap and non-toxic alternative to the metal based redox mediators.[51;52] A consequence of employing these is the possibility to exchange the expensive Pt counter electrode with *e.g.* a nanoporous polymer electrode[53] or cheaper transition metal carbides,[54] retaining, or even increasing, the power conversion efficiency.

The many aspects of DSSCs make them ideal for computational studies in which detailed information, not directly observable in experiments, can be obtained.[55–64] In addition to the more detailed studies, high-throughput computational screening can assist the development of DSSC by *e.g* speeding up the discovery of new and better dyes. Thanks to the enormous growth in computer power, high-throughput methods are rapidly becoming an essential tool for accelerated materials discovery within a wide range of areas.[65–76]

The goal of the DSSC project described in this thesis is to optimize the porphyrin based dyes, maximizing the efficiency through a combination of high-throughput computational screening and more detailed studies. To this end, a set of porphyrin backbones, side groups and anchor groups are chosen to systematically construct several thousand donor-π-acceptor dyes. Through a high-throughput computational scheme, the optimized structures and various energetics for these dyes are then stored in a database as sketched in Figure 1.2. This data can then subsequently be used to score the dyes based on the alignment of the dye molecular orbitals with *e.g.* the TiO_2 conduction band edge. This scoring is then added to the data in the database, ensuring that a calculation only has to be performed once. The free energy barrier associated with the electron transfer from the redox mediator to the oxidized dye, the so-called regeneration reaction, is an important factor neglected in the initial scoring of these dyes. However, by using detailed and computationally demanding methods, it is possible to calculate the height of this barrier for a single

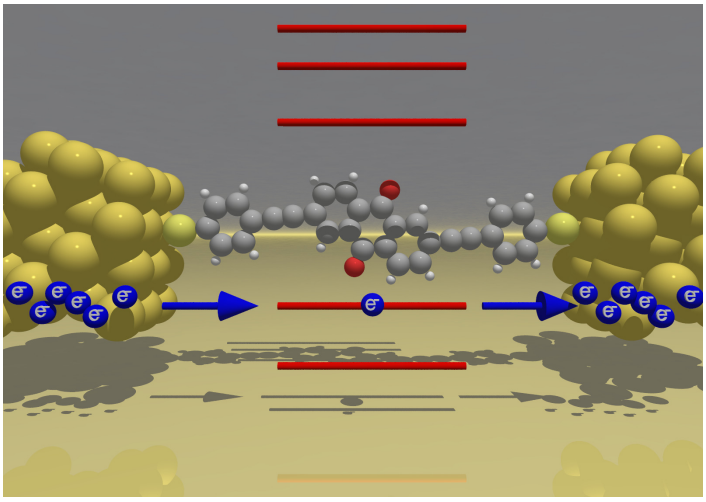

Figure 1.3: Illustration of a metal-molecule-metal junction. The blue balls illustrates the electrons which are being transported from the left electrode to the right *via* the molecular orbital energy levels indicated by red lines.

model dye. Using a classical expression, this barrier height can then be extrapolated to thousands of dyes in the database and used to correct the scoring of these. In this way, by combining detailed computational studies with a high-throughput screening, we obtain an improved model for scoring dyes to be used in DSSCs. The database containing all the data is part of the Computational Materials Repository and is available free of charge at http://cmr.fysik.dtu.dk.

In the final part of the DSSC project we illustrate how having a significant amount of data furthermore allows us to rationally combine dyes with suitable orbital alignment to *e.g.* propose novel molecular tandem structures, which may boost the efficiency beyond what is obtainable by using a single dye.

1.2 Molecular electronics

The detailed knowledge of molecular energy levels is useful even beyond the context of a DSSC. An example of this is the use of metal-molecule-metal contacts in single molecule electronics. This type of contact is illustrated in Figure 1.3. Since the first idea of molecular electronics appeared in 1974,[77] the use of this type of molecular junctions have been explored for many purposes.[78] Especially the influence of the molecular levels on the electric conductance through the junction has attracted interest due to the possibility of creating a molecular transistor. As will be discussed in Chapter 4, the conductance peaks when a molecular level is in resonance with the Fermi level of the metals (assuming no bias voltage). Hence, the conductance can be controlled by a gate electrode shifting the positions of the molecular levels relative to the Fermi level. Another way of controlling the conductance is to chemically modify the molecule trapped in the junction *e.g.* by photoinduced proton transfer.[79]

In the electron transport project included in this thesis, we investigate a system with a redox active molecule and an applied gate voltage. In this way, the gate influences the conductance both by shifting the molecular levels in and out of resonance and by changing the redox state of the molecule. Additionally, a system where the geometry of the junction is controlled by the metal-molecule binding energy of different functional groups is investigated. In both cases, the computationally obtained electron transmission is compared to experimentally obtained results and the strength of this combination is illustrated.

Part I

Methods

Chapter 2

Electronic structure theory

The use of computational approaches to predict the behaviour of molecules and solids is an ever growing field due to the potentially huge amount of time that can be saved compared to performing physical experiments. Furthermore, computational studies may be used to model conditions unobtainable in a laboratory. Since molecules and solids consist of atomic nuclei and electrons, the foundation of *ab-initio* computational studies is quantum mechanics and the corresponding language of wavefunctions, densities and operators. In the following, a brief introduction to the general electronic structure problem and the numerical solution through Density Functional Theory (DFT) is given, highlighting a few important topics. A more comprehensive overview of the electronic structure problem and its numerical solutions, can be found in several textbooks.[80–83] It should be noted that atomic units and the Dirac notation (see Appendix A) will be used in the rest of this thesis unless otherwise stated.

2.1 The electronic structure problem

The fundamental question in computational chemistry is to describe how electrons and nuclei behave. For a stationary, non-relativistic system this question can in principle be answered by solving the Schrödinger equation

$$\hat{\mathrm{H}}\Psi = \mathrm{E}\Psi \tag{2.1}$$

where the Hamiltonian in atomic units for a system of N electrons with spatial coordinates $\mathbf{r} = \{\overline{r}_1, ..., \overline{r}_i, ..., \overline{r}_N\}$, $\overline{r}_i = (x_i, y_i, z_i)$, and K nuclei with spatial coordinates $\mathbf{R} = \{\overline{R}_1, ..., \overline{R}_a, ..., \overline{R}_K\}$, $\overline{R}_a = (x_a, y_a, z_a)$, contains the following contributions

$$\hat{\mathrm{H}} = \underbrace{-\frac{1}{2}\sum_{i=1}^{N}\nabla_i^2 - \sum_{i=1}^{N}\sum_{a=1}^{K}\frac{Z_a}{|\overline{r}_i - \overline{R}_a|} + \sum_{i<j}\frac{1}{|\overline{r}_i - \overline{r}_j|} + \sum_{a<b}\frac{Z_a Z_b}{|\overline{R}_a - \overline{R}_b|}}_{\hat{\mathrm{H}}_\mathrm{e}} \underbrace{-\sum_{a=1}^{K}\frac{1}{2m_a}\nabla_a^2}_{\hat{\mathrm{T}}_\mathrm{K}} \tag{2.2}$$

where nuclei a has the charge Z_a and mass m_a. The first part of the above equation, denoted $\hat{\mathrm{H}}_\mathrm{e}$, is the electronic part of the Hamiltonian containing the electronic kinetic energy, the electron-nuclear attraction, the electron-electron repulsion and the nuclear-nuclear repulsion. The last part, denoted $\hat{\mathrm{T}}_\mathrm{K}$, is the nuclear kinetic energy which is separated out to give the Born-Oppenheimer approximation. The *ansatz* of this approximation is to write the total wavefunction as a product of an electronic wavefunction and a nuclear wavefunction

$$\Psi(\mathbf{r}, \mathbf{R}) \approx \Psi_e(\mathbf{r}; \mathbf{R})\chi(\mathbf{R}) \tag{2.3}$$

Here, the nuclear wavefunction is only dependent of the nuclear coordinates, while the electronic wavefunction is dependent of the electronic coordinates and parametric dependent of the nuclear coordinates. Furthermore, the electronic wavefunction is an eigenfunction of the electronic Hamiltonian

$$\hat{\mathrm{H}}_\mathrm{e}\Psi_e(\mathbf{r}; \mathbf{R}) = \mathrm{E}_\mathrm{e}(\mathbf{R})\Psi_e(\mathbf{r}; \mathbf{R}) \tag{2.4}$$

Since the mass of an electron is much smaller than that of a nucleus (around three orders of magnitude in difference of the mass of an electron and a proton), the electrons can be assumed to react

instantaneously to any change in the nuclear coordinates, leading to the assumption

$$\hat{\mathrm{T}}_{\mathrm{K}}\Psi_e(\mathbf{r};\mathbf{R})\chi(\mathbf{R}) \approx \Psi_e(\mathbf{r};\mathbf{R})\hat{\mathrm{T}}_{\mathrm{K}}\chi(\mathbf{R}) \tag{2.5}$$

which inserted into the Schrödinger equation gives

$$\left(\hat{\mathrm{T}}_{\mathrm{K}} + \mathrm{E_e}(\mathbf{R})\right)\chi(\mathbf{R}) = \mathrm{E}\chi(\mathbf{R}) \tag{2.6}$$

Hence, the nuclei move in a potential defined by the electronic energy. This *e.g.* has the consequence that the optimal geometry of a molecule can be determined by finding the nuclear configuration that corresponds to the lowest electronic energy. Unless otherwise stated, the Born-Oppenheimer approximation will be used in the remainder of this thesis and $\hat{\mathrm{H}}$ and E will refer to the electronic Hamiltonian and the electronic energy.

2.2 Density Functional Theory

Solutions to the electronic Schrödinger equation can be approximated by constructing wavefunctions as *e.g.* Slater determinants of one-electron wavefunctions, which is the foundation of the so-called wavefunction methods such as Hartree-Fock, Configuration Interaction and Coupled Cluster. Especially the latter is a very accurate but computational expensive method. A comprehensive overview of wavefunction methods is provided in the textbook by Helgaker, Jørgensen and Olsen.[83] As the true electronic wavefunction is a function of $3N$ variables, it is an inherently memory heavy problem to solve. Thus, it would be highly advantageous to instead describe the system using the electronic density, $n(\overline{r})$, which is a function of only 3 variables. Theoretically, this is possible by using Density Functional Theory (DFT) due to the Hohenberg-Kohn theorem, which states that:[84]

- The external potential is uniquely determined by the ground state density to within an additive constant.
- For any trial density, $n'(\overline{r})$, it holds $E_0 \leq E[n'(\overline{r})]$, where E_0 is the ground state energy of the system.

The first part of the theorem ensures that for a given nuclear configuration, magnetic field *etc.* the density is unique and that this density fully describes the system. Mathematically, this can be expressed as

$$\mathrm{E}[n] = \langle\Psi[n]|\hat{\mathrm{H}}|\Psi[n]\rangle = \langle\Psi[n]|\hat{\mathrm{T}}_{\mathrm{e}} + \hat{\mathrm{U}}_{\mathrm{ee}} + \hat{\mathrm{V}}_{\mathrm{ext}}|\Psi[n]\rangle = F[n] + \int v_{\mathrm{ion}}(\overline{r})n(\overline{r})\mathrm{d}\overline{r} \tag{2.7}$$

where we have split the electronic Hamiltonian into a kinetic part, $\hat{\mathrm{T}}_{\mathrm{e}}$, an electron-electron interaction part, $\hat{\mathrm{U}}_{\mathrm{ee}}$, and a part due to the external potential, $\hat{\mathrm{V}}_{\mathrm{ext}}$, which through $v_{\mathrm{ion}}(\overline{r})$, as mentioned, contains the electron-nuclear attraction as well as any magnetic field *etc.* The second part of the theorem ensures that, given $F[n]$, the ground state density can be found by minimizing the energy. However, there is no information on the shape of the universal $F[n]$, which in practice has proven very hard to approximate accurately.

2.3 Kohn-Sham theory

To simplify the task of finding the universal functional, Kohn and Sham suggested to introduce a system with non-interacting electrons, but with the same electronic density as the real system.[85] Due to the non-interacting electrons, this reference system can be described using one-electron so-called Kohn-Sham (KS) orbitals

$$\hat{\mathrm{H}}_{\mathrm{R}}\psi_i(\overline{r}) = \varepsilon_i\psi_i(\overline{r}) \tag{2.8}$$

where the non-interacting Hamiltonian is given as

$$\hat{\mathrm{H}}_{\mathrm{R}} = -\frac{1}{2}\nabla^2 + v_{\mathrm{R}}(\overline{r}) \tag{2.9}$$

In the above, the reference potential, $v_{\mathrm{R}}(\overline{r})$, ensures that the system has the same density as the real system, such that

$$n(\overline{r}) = \sum_{i=1}^{N} |\psi_i(\overline{r})|^2 \tag{2.10}$$

Due to the introduction of orbitals, the kinetic energy of the electrons in the reference system is well-defined and the energy of the reference system can be written as

$$\mathrm{E_R}[n] = \underbrace{-\frac{1}{2}\sum_{i=1}^{N}\langle\psi_i|\nabla^2|\psi_i\rangle}_{\mathrm{T_s}[n]} + \int v_{\mathrm{R}}(\overline{r})n(\overline{r})\mathrm{d}\overline{r} \tag{2.11}$$

We can now use the kinetic energy of the reference system as a first approximation of the kinetic energy of the real system and if we at the same time approximate the electron-electron interaction with the simple Coulombic repulsion (or Hartree term), we get the following expression for the energy of the real system

$$\mathrm{E}[n] = \mathrm{T_s}[n] + \frac{1}{2}\int\int \frac{n(\overline{r})n(\overline{r}')}{|\overline{r}-\overline{r}'|}\mathrm{d}\overline{r}\mathrm{d}\overline{r}' + \int v_{\mathrm{ion}}(\overline{r})n(\overline{r})\mathrm{d}\overline{r} + \mathrm{E_{xc}}[n] \tag{2.12}$$

where the exchange-correlation functional, $\mathrm{E_{xc}}[n]$, is defined as the error in approximating the energy with the reference kinetic energy and Hartree term

$$\mathrm{E_{xc}}[n] = \mathrm{T_e}[n] - \mathrm{T_s}[n] + \mathrm{U_{ee}}[n] - \frac{1}{2}\int\int \frac{n(\overline{r})n(\overline{r}')}{|\overline{r}-\overline{r}'|}\mathrm{d}\overline{r}\mathrm{d}\overline{r}' \tag{2.13}$$

Finally, from the expressions of the energy of the reference and real systems, it can be shown that the reference potential defining the reference system is given by

$$v_{\mathrm{R}}(\overline{r}) = \underbrace{\int \frac{n(\overline{r}')}{|\overline{r}-\overline{r}'|}\mathrm{d}\overline{r}'}_{v_{\mathrm{H}}(\overline{r})} + v_{\mathrm{ion}}(\overline{r}) + \underbrace{\frac{\partial \mathrm{E_{xc}}[n]}{\partial n}}_{v_{\mathrm{xc}}(\overline{r})} \tag{2.14}$$

Hence, the reference potential is seen to be dependent on the density and the Kohn-Sham equations must therefore be solved in a self-consistent way from an initial guess of $n(\overline{r})$.

2.4 Exchange-correlation functionals

By introducing the Kohn-Sham reference system, the problem of finding a universal functional has been reduced from estimating the full energy, *via* $F[n]$, to only estimating a correction to the energy in the exchange-correlation functional. Furthermore, this correction can be split into two parts known from wavefunction theory, namely *exchange* and *correlation*. In the electron-electron interaction part of the expression for the DFT energy of the true system (Equation 2.12), we have only included the Hartree term which is a simple Coulombic repulsion between different parts of the electronic density. However, since electrons are fermions, electrons with the same spin can not occupy the same physical space. Hence, the contribution to the Coulombic repulsion attributed to overlapping density contributions from electrons with the same spin should be subtracted from the Hartree term through the *exchange* part of the correction. The Hartree term furthermore treats the electron-electron repulsion as a local property, in which an electron feels the mean field created by the remaining electrons. The true electron-electron interaction is however highly non-local, depending on all electronic coordinates and the correction for this is the *correlation* part of the exchange-correlation functional.

The simplest approach to model the exchange-correlation functional is to assume a uniform electron gas and derive the correct behaviour of the exchange-correlation functional for this system.[85] This gives rise to the so-called Local Density Approximation (LDA), which is defined by

$$\mathrm{E}_{xc}^{\mathrm{LDA}}[n] = \int n(\overline{r})\varepsilon_{xc}^{\mathrm{unif}}[n]\mathrm{d}\overline{r} \tag{2.15}$$

where $\varepsilon_{xc}^{\text{unif}}[n]$ is the single-electron exchange-correlation energy for a uniform electron gas, which has been thoroughly parametrised. Since LDA is based on the uniform electron gas, the functional is good at describing systems in which the electronic density varies very slowly. However, for molecules, where the density varies significantly, it has proven necessary to correct for these variations by including the density gradient, $\nabla n(\overline{r})$, defining the Generalized Gradient Approximation (GGA) type of exchange-correlation functionals. A specific GGA functional is the popular Perdew-Burke-Ernzerhof (PBE) functional.[86] The exchange and correlation part of the PBE functional is defined as gradient dependent corrections to the LDA functional

$$\mathrm{E}_x^{\text{PBE}}[n, \nabla n] = \int n(\overline{r}) \varepsilon_x^{\text{unif}}[n] F_X[\nabla n] \mathrm{d}\overline{r} \tag{2.16}$$

$$\mathrm{E}_c^{\text{PBE}}[n, \zeta, \nabla n] = \int n(\overline{r}) \left(\varepsilon_c^{\text{unif}}[n, \zeta] + H[n, \zeta, \nabla n] \right) \mathrm{d}\overline{r} \tag{2.17}$$

$$\mathrm{E}_{xc}^{\text{PBE}}[n, \zeta, \nabla n] = \mathrm{E}_x^{\text{PBE}}[n, \nabla n] + \mathrm{E}_c^{\text{PBE}}[n, \zeta, \nabla n] = \int n(\overline{r}) \varepsilon_x^{\text{unif}}[n] F_{XC}[n, \zeta, \nabla n] \mathrm{d}\overline{r} \tag{2.18}$$

where $\zeta(r) = \frac{n_\uparrow(\overline{r}) - n_\downarrow(\overline{r})}{n(\overline{r})}$ is the relative spin polarization and F_{XC} is the parametrised enhancement function. For PBE the parameters are chosen to fulfil certain theoretical requirements, but other functionals use empirically determined parameters.

2.5 GPAW

The practical implementation of the Kohn-Sham scheme leads to several choices on how to numerically calculate and represent the different functions and variables. The GPAW code[87;88] used in this study is a real-space implementation of the projector augmented-wave method. In brief, this means that the wavefunctions, potentials *etc.* are evaluated and stored on a real-space grid, but with the addition that the part of the real-space inside spheres of radius r_a^c around each atom is treated differently. Here, the "correct" wavefunctions, ψ_i, are replaced with smoother functions $\tilde{\psi}_i$ *via* a linear transformation

$$\psi_i = \hat{T} \tilde{\psi}_i \tag{2.19}$$

Outside the atomic spheres $\psi_i = \tilde{\psi}_i$, leading to the expression

$$\psi_i = \tilde{\psi}_i + \sum_{a=1}^{K} \left(\psi_i^a - \tilde{\psi}_i^a \right) \tag{2.20}$$

where the functions with the superscript a denotes the part of the function inside the atomic sphere. As the "correct" wavefunctions oscillate significantly close to the atomic nuclei, requiring a very fine grid to represent all fluctuations, the use of smoother wavefunctions allows for using a more crude grid. On the other hand, this method relies significantly on the accuracy of the wavefunction transformation which for GPAW is governed through a set of element specific setups. In GPAW, only the valence electrons are treated explicitly, while the core electrons are fixed to a reference state from the isolated atoms. As mentioned, the wavefunctions are in GPAW evaluated on a real-space grid and the standard approach to obtain derivatives is by using the *finite difference* approach, which takes the values of the nearest neighbouring grid points into account. In this way the complete basis set limit can be systematically approached by decreasing the grid spacing. This method is however generally computational expensive. An alternative method is to generate the wavefunctions from a *linear combination of atomic orbitals* (LCAO), where the wavefunctions are given by[89]

$$\tilde{\psi}_i = \sum_\mu c_{\mu i} \Phi_\mu \tag{2.21}$$

where the basis function, Φ_{nlm}^a, for atom a with the quantum numbers nlm is given as a product of a radial function, R_{nl}^a, and a spherical harmonic, Y_{lm}

$$\Phi_{nlm}^a(\overline{r}) = \mathrm{R}_{nl}^a \left(\left| \overline{r} - \overline{R}_a \right| \right) \mathrm{Y}_{lm} \left(\theta_a, \phi_a \right) \tag{2.22}$$

where θ_a and ϕ_a are spherical angles with origin in $\overline{R}_a$. In LCAO mode, the wavefunction is still evaluated on a grid, but the derivatives and overlap matrix elements can be calculated analytically, significantly lowering the computational cost. The quality of the basis set can be improved by adding more basis functions, including functions with higher l quantum number as polarization functions, but the strictly systematic convergence towards the complete basis set limit is lost.

2.6 Energy levels

In many applications it is useful to investigate the individual electronic levels (or orbitals) of a molecule. Especially the orbitals around the highest occupied molecular orbital (HOMO) and the lowest unoccupied molecular orbital (LUMO) are interesting from a chemical point of view as these are usually involved in chemical binding, optical absorption *etc.* The construction of the Kohn-Sham orbitals however has the consequence that the eigenvalue gap between HOMO and LUMO, $\varepsilon^{\mathrm{KS}}_{\mathrm{LUMO}} - \varepsilon^{\mathrm{KS}}_{\mathrm{HOMO}}$, does not correspond to the energy difference between the cost of removing an electron from the system (the ionization potential, I_P) and the energy gained by adding an electron (the electron affinity, E_A), which is denoted the fundamental gap. In fact, Baerends *et al.*[90] argue that the Kohn-Sham eigenvalue gap should rather represent the optical gap, which is the energy cost of exciting an electron from the HOMO to the LUMO. As the excited electron in the LUMO interacts with the positive hole left in the HOMO, the optical gap is generally much smaller than the fundamental gap. To circumvent the issue of Kohn-Sham eigenvalues, the fundamental gap can be obtained from total energy calculations through

$$\begin{aligned} E_{\mathrm{gap}} &= E_{\mathrm{LUMO}} - E_{\mathrm{HOMO}} \\ &= (E[-1] - E[0]) - (E[0] - E[+1]) \\ &= I_P - E_A \end{aligned} \tag{2.23}$$

where $E[0]$ is the ground state total energy and, $E[-1]$ and $E[+1]$ are the total energy of the negatively and positively charged ions of the molecule, respectively.

Chapter 3

Marcus theory

Electron transfer reactions constitute one of the most important classes of reactions and are essential for life on Earth through *e.g.* photosynthesis and the human respiratory process. Furthermore, electron transfer reactions are a key constituent in any device harvesting or storing energy. An example of this is the reduction of the photo-excited and oxidized dye by the redox mediator in a dye sensitized solar cell (DSSC). Here, both the dye and the redox mediator are embedded in a solvent and the electron transfer induces changes in both reactants as well as the solvent, creating a free energy barrier that must be energetically overcome. In the following, the Marcus theory governing this free energy barrier and the rate of electron transfer reactions is introduced, followed by a brief description on how to obtain the free energy barrier in practice using Molecular Dynamics (MD) simulations in combination with the weighted histogram analysis method (WHAM). The discussion in this chapter is focused on the electron transfer between two molecules in a solvent. A more general introduction to the theory can be found in the textbook by Kuznetsov and Ulstrup.[91]

3.1 Electron transfer reactions

To introduce the concept of Marcus theory it is illustrative to start from the well-known Arrhenius equation governing the reaction rate of a general chemical reaction

$$k = A \exp\left(\frac{-E_a}{k_B T}\right) \tag{3.1}$$

where A is a constant related to the frequency of incidents that increase the energy, or activates, the reactants *e.g.* vibrations or collisions and E_a is the activation energy that must be overcome for a reaction to occur. The constant A and the activation energy, E_a, can be determined experimentally by measuring the reaction rate as a function of the temperature and computationally using *e.g.* transition state theory (for a comprehensive overview see the textbook by Henriksen and Hansen[92]). Consider now a general electron transfer reaction between a donor, D, and an acceptor, A, in a solvent

$$\underbrace{\mathrm{D}^- + \mathrm{A}}_{i} \rightarrow \underbrace{\mathrm{D} + \mathrm{A}^-}_{f} \tag{3.2}$$

where we denote the *initial* state as i and the *final* state as f. For this type of reaction, Marcus suggested that the constant A in the Arrhenius equation is related to the electronic coupling, κ, between the donor and the acceptor, while the activation energy is due to the energy cost of reorganizing the reactants and the solvent, expressed by the free energy electron transfer barrier $\Delta F^\ddagger$. Reformulating Equation 3.1 we thus get the Marcus rate[93–97]

$$k^{\mathrm{Marcus}} = \kappa \exp\left(\frac{-\Delta F^\ddagger}{k_B T}\right) \tag{3.3}$$

For outer-sphere, diabatic electron transfers, in which the electronic coupling is weak, the change in κ for similar donor-acceptor pairs can be assumed to be negligible. In this case, the difference in rate will thus be dominated by the free energy electron transfer barrier. To obtain an expression for $\Delta F^\ddagger$,

we start out by defining the energy of the *initial* state at a given nuclear configuration $\mathbf{R}$ including the nuclei of both reactants and the solvent

$$E_i(\mathbf{R}) = U_i + V_i(\mathbf{R}) + \varepsilon_i(\mathbf{R}) \tag{3.4}$$

where U_i is the gas-phase energy of the reactants in the *initial* electronic state, $\varepsilon_i(\mathbf{R})$ is the interaction between the solvent and the electron to be transferred in Equation 3.2 and $V_i(\mathbf{R})$ is the interaction between the reactants and the solvent, *excluding* the electron to be transferred. Assuming that the electron transfer does not involve any other chemical reaction, *e.g.* bond formation and breaking, we have that $V_i(\mathbf{R}) = V_f(\mathbf{R})$, leading to

$$\Delta E(\mathbf{R}) = E_f(\mathbf{R}) - E_i(\mathbf{R}) = \underbrace{U_f - U_i}_{\Delta U} + \underbrace{\varepsilon_f(\mathbf{R}) - \varepsilon_i(\mathbf{R})}_{\Delta\varepsilon(\mathbf{R})} \tag{3.5}$$

The transition state between the *initial* and *final* state in Equation 3.2 can now be defined as the nuclear configuration, $\mathbf{R}^\ddagger$, where the potential energy difference between the two states is zero, $\Delta E(\mathbf{R}^\ddagger) = 0$, leading to

$$\Delta\varepsilon(\mathbf{R}^\ddagger) = -\Delta U \tag{3.6}$$

giving the physical interpretation of the transition state as the configuration in which the difference in gas phase potential energy is exactly overcome by the difference in solvation energy of the transferring electron.

3.2 The free energy function

In the above we have used the nuclear coordinates, $\mathbf{R}$, as the reaction coordinate for the charge transfer reaction in Equation 3.2. However, due to the very high dimensionality of $\mathbf{R}$, it is more beneficial to use a simpler reaction coordinate, x, defined as

$$x \equiv \Delta E(\mathbf{R}) \tag{3.7}$$

Using this reaction coordinate we can write the restricted partition function for the *initial* state as[98–100]

$$F_i(x) = -\frac{1}{\beta}\ln\int \delta\left[x - \Delta E(\mathbf{R})\right]\exp\left[-\beta E_i(\mathbf{R})\right]\mathrm{d}\mathbf{R} \tag{3.8}$$

where $\beta = \frac{1}{k_B T}$ and the reaction coordinate is introduced through the δ-function. From the Boltzmann distribution we can write the probability of observing a specific x for our *initial* state as

$$P_i(x) = \frac{\int \delta\left[x - \Delta E(\mathbf{R})\right]\exp\left[-\beta E_i(\mathbf{R})\right]\mathrm{d}\mathbf{R}}{\int \exp\left[-\beta E_i(\mathbf{R})\right]\mathrm{d}\mathbf{R}} \tag{3.9}$$

which inserted into Equation 3.8 gives

$$F_i(x) = -\frac{1}{\beta}\ln\left[P_i(x)\right]\underbrace{-\frac{1}{\beta}\ln\int \exp\left[-\beta E_i(\mathbf{R})\right]\mathrm{d}\mathbf{R}}_{F_i^*} \tag{3.10}$$

where F_i^* is the free energy of the state. This constant is however usually neglected since we are more interested in the relative free energy upon varying x to *e.g.* obtain the free energy electron transfer barrier from Equation 3.3

$$\Delta F^\ddagger = F_i(x^\ddagger) - F_i(x_{\min}) \tag{3.11}$$

where $x_{\min}$ is the minimum point of the free energy curve. In the same manner as above, the free energy function for the *final* state can be found

$$\begin{aligned}
F_f(x) &= -\frac{1}{\beta}\ln\int \delta\left[x - \Delta E(\mathbf{R})\right]\exp\left[-\beta E_f(\mathbf{R})\right]\mathrm{d}\mathbf{R} \\
&= -\frac{1}{\beta}\ln\int \delta\left[x - \Delta E(\mathbf{R})\right]\exp\left[-\beta E_i(\mathbf{R})\right]\exp\left[-\beta\Delta E(\mathbf{R})\right]\mathrm{d}\mathbf{R} \\
&= -\frac{1}{\beta}\ln\int \delta\left[x - \Delta E(\mathbf{R})\right]\exp\left[-\beta E_i(\mathbf{R})\right]\mathrm{d}\mathbf{R} + x \\
&= F_i(x) + x
\end{aligned} \tag{3.12}$$

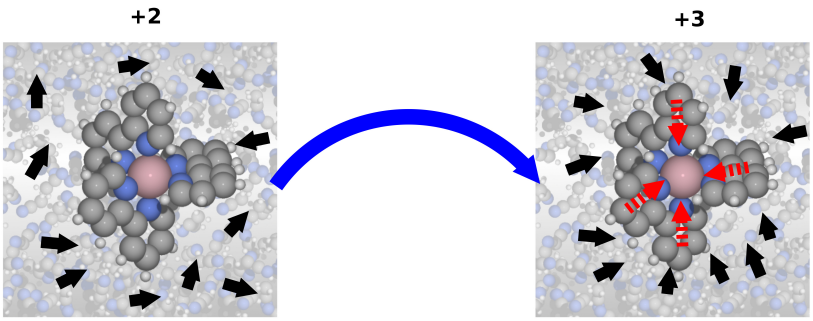

Figure 3.1: Illustration of the outer and inner reorganization energy upon charging a molecule in a solvent. The outer reorganization energy is due to the solvent reorganization (black arrows) and the inner reorganization energy is due to structural changes in the molecule (red arrows).

The final result in Equation 3.12 has the consequence that only the free energy function for either the *initial* or the *final* state has to be calculated to get the other. In the linear response regime the probability in Equation 3.9 will be a Gaussian, giving the characteristic parabolic free energy function[98–100]

$$F_i(x) = \frac{1}{4\lambda}(x - x_{\min})^2 + F_i^* \tag{3.13}$$

where the reorganization energy, λ, is defined as

$$\lambda = F_i(x_{f,\min}) - F_i(x_{i,\min}) \tag{3.14}$$

where $x_{f,\min}$ and $x_{i,\min}$ are the minimum points of the free energy curve for the *final* and *initial* state respectively. The reorganization energy is usually split into two parts

$$\lambda = \lambda^{\text{in}} + \lambda^{\text{out}} \tag{3.15}$$

where λ^{in} is the *inner* reorganization energy, which is due to structural changes in the molecule, and λ^{out} is the *outer* reorganization energy, which is due to the solvent reorganization. This separation is illustrated in Figure 3.1 where the black arrows represents the orientation of the solvent molecules and the red arrows represents the change in bond length in the molecule upon charging it. Having parabolic functions for the free energy of both the *initial* and *final* state, the free energy electron transfer barrier can be shown to be given as[93–97]

$$\Delta F^{\ddagger} = \frac{\left(\lambda + \Delta F^0\right)^2}{4\lambda} \tag{3.16}$$

where $\Delta F^0 = F_f(x_{f,\min}) - F_i(x_{i,\min})$ is the free energy difference between the *final* and *initial* state. Figure 3.2 gives an illustration of the free energy functions, the free energy barrier, $\Delta F^{\ddagger}$, the free energy difference, ΔF^0, and the reorganization energy, λ. As stated in the previous section, for a diabatic outer-sphere electron transfer reaction, the kinetics are dominated by the free energy barrier and hence the reorganization energy. From the definition in Equation 3.14, it is seen that $\lambda > 0$. Thus, the free energy barrier can be reduced by making the reaction more exergonic. However, due to the square in the numerator in Equation 3.16, the barrier height will increase if ΔF^0 becomes too negative. This counter-intuitive situation is known as the Marcus inverted region, which has been experimentally realized for different electron transfer reactions.[101–104]

3.3 Sampling and analysis

The free energy function can in practice be calculated from Equation 3.10 by computationally obtaining the probability function, $P_i(x)$. This function is a statistical average over many nuclear configurations, $\mathbf{R}$, which needs to be computationally sampled using *e.g.* Molecular Dynamics (MD). The essence of MD simulations is to fulfil Newtons second law

$$\mathrm{F}_a = m_a \frac{\mathrm{d}^2 \overline{R}_a}{\mathrm{d}t^2} \tag{3.17}$$

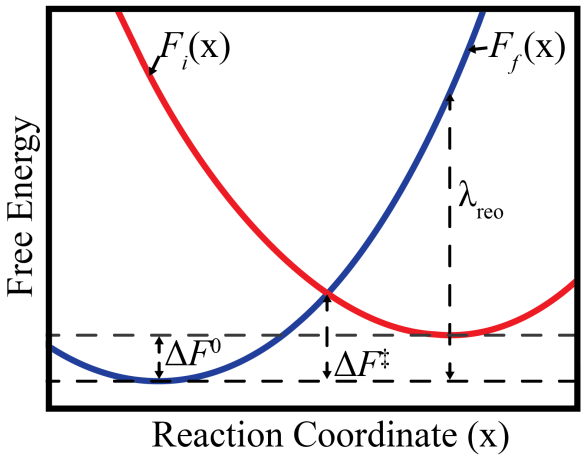

Figure 3.2: Schematic illustration of the free energy function for the *initial*, $F_i(x)$, and *final*, $F_f(x)$, electronic states, the free energy barrier, $\Delta F^{\ddagger}$, the free energy difference, ΔF^0, and the reorganization energy, λ. The parabolas presented here are an idealized case assuming linear response. Figure adapted from Ph.D. thesis by E. Ö. Jónsson.[105]

where F_a is the force on nucleus a, m_a is the mass of the nucleus and $\frac{\mathrm{d}^2\overline{R}_a}{\mathrm{d}t^2}$ is its acceleration. Thus, knowing the force enables us to calculate the acceleration and hence the time dependent positions of the nuclei in the system. For the charge transfer reactions investigated in this thesis, we will be working at a constant number of particles, constant volume and constant temperature, which is known as the NVT canonical ensemble. Here, the Langevin dynamics formalism is used to govern the MD simulations[105–107]

$$m_a \frac{\mathrm{d}^2\overline{R}_a}{\mathrm{d}t^2} = \mathrm{F}_a(\mathbf{R}) - \gamma m_a \frac{\mathrm{d}\overline{R}_a}{\mathrm{d}t} + dW(t)\sqrt{2k_B T\gamma m_a} \tag{3.18}$$

where $\mathrm{F}_a(\mathbf{R})$ are the forces obtained from an electronic structure calculation at nuclear coordinates $\mathbf{R}$, γ is a positive friction constant and $dW(t)$ is a stochastic function representing the Brownian motion. The temperature control enters through the relation between γ and $dW(t)$. Using MD simulations, it is possible to directly sample the *initial* and *final* states. However, the simulation will energetically be focused around the equilibrium configurations of the two states, while the sampling around the transition state will be sparse. Hence, it is necessary to explicitly introduce a bias, shifting the sampling region towards the non-equilibrium configurations. This can be done by defining a coupling constant, $\{\chi_\alpha : 0 \leq \chi_\alpha \leq 1\}$, bringing the system from the *initial* state to the *final* state via the intermediate state α

$$E_\alpha(\mathbf{R}) = (1-\chi_\alpha)E_i(\mathbf{R}) + \chi_\alpha E_f(\mathbf{R}) = E_i(\mathbf{R}) + \chi_\alpha \Delta E(\mathbf{R}) \tag{3.19}$$

The MD samplings of the relevant phase-spaces are then based on a simple linear combination of the forces

$$\mathbf{F}_\alpha(\mathbf{R}) = (1-\chi_\alpha)\mathbf{F}_i(\mathbf{R}) + \chi_\alpha \mathbf{F}_f(\mathbf{R}) \tag{3.20}$$

where $\mathbf{F}_i(\mathbf{R})$ and $\mathbf{F}_f(\mathbf{R})$ are the force vectors for the *initial* and *final* states, respectively. A consequence of forcing the system to sample the region around *e.g.* the transition state is artificially high probabilities for observing these configurations, so-called biased probabilities, which are obtained as normalized histograms

$$P^b_\alpha(x) = \frac{1}{n_\alpha}\sum_{l=1}^{n_\alpha} \delta[x - \Delta E(\mathbf{R}_l)] \tag{3.21}$$

where n_α is the number of sampled configurations of $\mathbf{R}$ using the coupling χ_α. To obtain the unbiased probabilities necessary to construct the free energy curves, it is possible to use the weighted histogram analysis method (WHAM), in which the unbiased probabilities are given by[108–110]

$$P^u_\alpha(x) = P^b_\alpha(x)\exp\left(\beta[\chi_\alpha \Delta E(\mathbf{R}) - f_\alpha]\right) \tag{3.22}$$

where f_α is the free energy change induced by the bias term, $\chi_\alpha \Delta E(\mathbf{R})$, from Equation 3.19 through[105]

$$\exp\left(-\beta f_\alpha\right) = \langle \exp\left(-\beta[\chi_\alpha \Delta E(\mathbf{R})]\right)\rangle = \int \exp\left(-\beta[\chi_\alpha \Delta E(\mathbf{R})]\right) P_i(x) \mathrm{d}\mathbf{R} \tag{3.23}$$

If the total number of values used for the coupling parameter χ_α is N_α, the total probability curve for the *initial* state can be written as

$$P_i(x) = C \sum_{\alpha=1}^{N_\alpha} \rho_\alpha(x) P_\alpha^u(x) \tag{3.24}$$

where C is a normalization constant and $\rho_\alpha(x)$ is the weight of the coupling α for a specific value of x. Using normalized weights, $\sum_{\alpha=1}^{N_\alpha} \rho_\alpha(x) = 1$, it can be shown that the statistical error in the sampling is minimized by using[108;109]

$$\begin{aligned} P_i(x) &= C \sum_{\alpha=1}^{N_\alpha} \frac{n_\alpha \exp\left(-\beta[\chi_\alpha \Delta E(\mathbf{R}) - f_\alpha]\right)}{\sum_{\alpha'=1}^{N_\alpha} n_{\alpha'} \exp\left(-\beta[\chi_{\alpha'} \Delta E(\mathbf{R}) - f_{\alpha'}]\right)} P_\alpha^u(x) \\ &= C \sum_{\alpha=1}^{N_\alpha} \frac{n_\alpha}{\sum_{\alpha'=1}^{N_\alpha} n_{\alpha'} \exp\left(-\beta[\chi_{\alpha'} \Delta E(\mathbf{R}) - f_{\alpha'}]\right)} P_\alpha^b(x) \end{aligned} \tag{3.25}$$

To use the above expression for obtaining the probability curve, we only need an expression for the free energy bias, f_α. Rewriting Equation 3.23 using Equation 3.25 gives the following expression

$$\exp\left(-\beta f_\alpha\right) = C \sum_{\alpha=1}^{N_\alpha} \frac{n_\alpha \exp\left(-\beta[\chi_\alpha \Delta E(\mathbf{R})]\right)}{\sum_{\alpha'=1}^{N_\alpha} n_{\alpha'} \exp\left(-\beta[\chi_{\alpha'} \Delta E(\mathbf{R}) - f_{\alpha'}]\right)} P_\alpha^b(x) \tag{3.26}$$

which has to be solved self-consistently as the free energy bias enters on both sides of the equation.

Chapter 4

Electron transport

The continuous search for smaller electronic components is rapidly pushing the scale towards a regime where single electrons and molecular energy levels dominate. In this regime, the wave like nature of electrons leads to concepts like tunnelling and quantum interference, greatly influencing the properties of single molecule junctions. In the following, the transmission of an electron through a square potential is considered to provide an illustration of the difference between the electron and a classical particle in terms of tunnelling. The scope is then expanded to consider the transmission through a single molecule junction and how to obtain this from an electronic structure calculation including how to correct for some well-known numerical issues through the DFT+Σ correction. Finally, the concept of quantum interference (QI) in which the transmission is zero due to destructive interference is introduced and a simple model to predict this phenomena is presented.

4.1 Electronic tunnelling

The concept of electronic tunnelling through a potential barrier is best illustrated by looking at the simple one-dimensional square potential, which is defined by

$$V(x) = \begin{cases} 0 & \text{for } x < 0 \quad \text{(zone I)} \\ V_0 & \text{for } 0 \leq x \leq L \quad \text{(zone II)} \\ 0 & \text{for } x > L \quad \text{(zone III)} \end{cases} \tag{4.1}$$

where L is the width of the potential and V_0 is the potential barrier height (see Figure 4.1). For a classical particle in this potential to cross from zone I to zone III, it would need sufficient energy to overcome the barrier so that the probability, expressed as the transmission function, would simply be given by

$$T_{\text{class}}(\varepsilon) = \begin{cases} 1 & \text{for } \varepsilon \geq V_0 \\ 0 & \text{for } \varepsilon < V_0 \end{cases} \tag{4.2}$$

To evaluate the transmission function for an electron travelling from zone I to III, we on the other hand need to solve the Schrödinger equation

$$\left(-\frac{1}{2}\frac{\mathrm{d}^2}{\mathrm{d}x^2} + V(x)\right)\psi(x) = \varepsilon\psi(x) \tag{4.3}$$

which can be shown to have the following solution

$$\psi(x) = \begin{cases} a_1 \exp\left(i\sqrt{2\varepsilon}x\right) + a_2 \exp\left(-i\sqrt{2\varepsilon}x\right) & \text{(zone I)} \\ b_1 \exp\left(i\sqrt{2(\varepsilon - V_0)}x\right) + b_2 \exp\left(-i\sqrt{2(\varepsilon - V_0)}x\right) & \text{(zone II)} \\ c_1 \exp\left(i\sqrt{2\varepsilon}x\right) + c_2 \exp\left(-i\sqrt{2\varepsilon}x\right) & \text{(zone III)} \end{cases} \tag{4.4}$$

Each of the above wavefunctions is seen to consist of a sum of two parts, where each part can be interpreted as either the wavefunction for particles moving in positive x-direction or the wavefunction for particles moving in negative x-direction. Assuming that all the particles are approaching the barrier in the positive x-direction, that we are only interested in the ratio between the coefficients

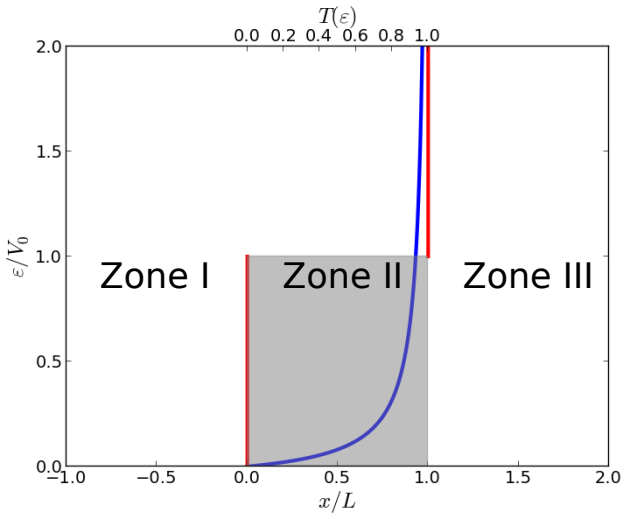

Figure 4.1: Illustration of a square potential (gray box) with the classical transmission function $T_{\text{class}}(\varepsilon)$ (red curve) and the electronic transmission function $T_{\text{elec}}(\varepsilon)$ (blue curve). The potential has the dimensions of $V_0 = 1$ eV and $L = 2\,a_0$, where a_0 is the Bohr radius.

and that the wavefunction has to be continuous and differentiable in the points $x = 0$ and $x = L$, the transmission function can be shown to be given by [111]

$$T_{\text{elec}}(\varepsilon) = \begin{cases} \frac{4\varepsilon(V_0-\varepsilon)}{V_0^2 \sinh^2\left(L\sqrt{2(V_0-\varepsilon)}\right)+4\varepsilon(V_0-\varepsilon)} & \text{for } \varepsilon < V_0 \\ \left(1+\frac{L^2 V_0}{2}\right)^{-1} & \text{for } \varepsilon = V_0 \\ \frac{4\varepsilon(\varepsilon-V_0)}{V_0^2 \sin^2\left(L\sqrt{2(\varepsilon-V_0)}\right)+4\varepsilon(\varepsilon-V_0)} & \text{for } \varepsilon > V_0 \end{cases} \tag{4.5}$$

which is visualized in Figure 4.1. From Equation 4.5 it is seen that, as opposed to the classical particle, the electron does have a finite probability of crossing a potential even when it does not posses enough energy to overcome the potential barrier height. This probability however decreases as the potential widens (increasing L).

4.2 Single molecule electron transport

A physical version of a square potential like problem is to imagine two metal leads connected through a single molecule forming a so-called single molecule junction (see illustration in Figure 4.2 left). Here, the molecular levels serve as channels for the electron to move from one metal tip to the other and V_0 can thus be thought of as the energy difference between the Fermi level of the leads (assuming no bias voltage) and the nearest molecular level (see Figure 4.2 right). For a system with a molecule with a single molecular level with the energy ε_a, it can be shown that the transmission function is given as a Lorentzian function centred on ε_a, with a width determined by the coupling, Γ, between the molecule and the metal leads [112]

$$T(\varepsilon) = \frac{\Gamma^2}{(\varepsilon-\varepsilon_a)^2+\Gamma^2} \tag{4.6}$$

Here, we have assumed that the transport through the molecule is phase-coherent, meaning that the electron does not experience any phase altering interactions such as *e.g.* interaction between the electron and the vibrational degrees of motion of the molecule, and that the junction is symmetric. A general single molecule junction can be split up into three parts as shown in Figure 4.2 left: A finite *scattering* region containing the junction itself and two infinite *leads*, denoted right or left, representing the metal contacts. Having this division, the general phase-coherent transmission function is given as [113]

$$T(\varepsilon) = \text{Tr}\left[\mathbf{G}_S^r(\varepsilon)\mathbf{\Gamma}_L(\varepsilon)\mathbf{G}_S^a(\varepsilon)\mathbf{\Gamma}_R(\varepsilon)\right] \tag{4.7}$$

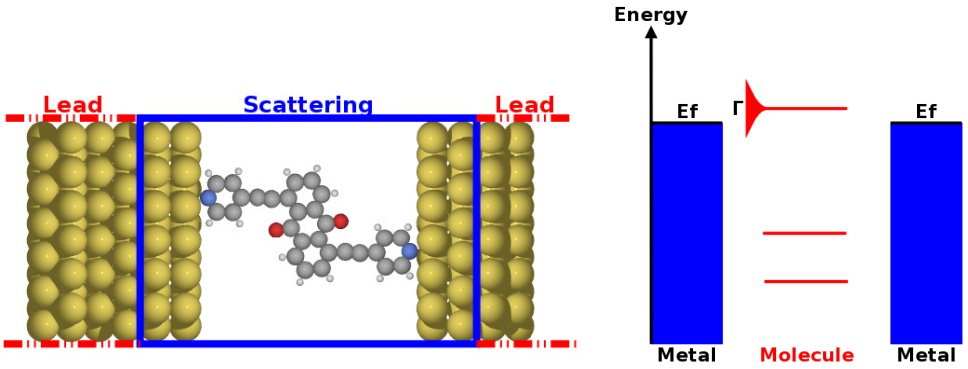

Figure 4.2: **Left:** Division of a molecular junction into lead and scattering regions. **Right:** Schematic illustration of the energetics of a molecular junction indicating the Fermi level and the broadening, $\mathbf{\Gamma}$, of the molecular level due to hybridization with the electronic levels of the metal.

where $\mathbf{G}_S^{r/a}(\varepsilon)$ is the retarded/advanced Green's function for the scattering region and $\mathbf{\Gamma}_{R/L}(\varepsilon)$ is coupling to the right/left lead defined from the self-energy

$$\mathbf{\Gamma}_{R/L}(\varepsilon) = i\left(\mathbf{\Sigma}^r_{R/L}(\varepsilon) - \mathbf{\Sigma}^a_{R/L}(\varepsilon)\right) \tag{4.8}$$

The Green's functions and self-energies are related to the electronic structure of the leads and the molecule through the following relations [112;113]

$$\begin{aligned}
\mathbf{G}^r_S(\varepsilon) &= \left[z\mathbf{S}_S - \mathbf{H}_S - \mathbf{\Sigma}^r_L(\varepsilon) - \mathbf{\Sigma}^r_R(\varepsilon)\right]^{-1} \\
\mathbf{\Sigma}^r_{R/L}(\varepsilon) &= \left(z\mathbf{S}_{SR/SL} - \mathbf{H}_{SR/SL}\right)\mathbf{g}^{0,r}_{R/L}(\varepsilon)\left(z\mathbf{S}^\dagger_{SR/SL} - \mathbf{H}^\dagger_{SR/SL}\right) \\
\mathbf{g}^{0,r}_{R/L}(\varepsilon) &= \left(z\mathbf{S}_{R/L} - \mathbf{H}_{R/L}\right)^{-1}
\end{aligned} \tag{4.9}$$

where $\mathbf{H}_{ij} = \langle\phi_i|\hat{\mathrm{H}}|\phi_j\rangle$ is the Hamiltonian matrix, $\mathbf{S}_{ij} = \langle\phi_i|\phi_j\rangle$ is the overlap and $z = \varepsilon + i\eta$, where η is a positive infinitesimal.* The overlap and Hamiltonian matrices are both split up into pure lead and scattering parts and parts coupling the leads with the scattering region

$$\mathbf{H} = \begin{pmatrix} \mathbf{H}_L & \mathbf{H}^\dagger_{SL} & 0 \\ \mathbf{H}_{SL} & \mathbf{H}_S & \mathbf{H}_{SR} \\ 0 & \mathbf{H}^\dagger_{SR} & \mathbf{H}_R \end{pmatrix}, \ \mathbf{S} = \begin{pmatrix} \mathbf{S}_L & \mathbf{S}^\dagger_{SL} & 0 \\ \mathbf{S}_{SL} & \mathbf{S}_S & \mathbf{S}_{SR} \\ 0 & \mathbf{S}^\dagger_{SR} & \mathbf{S}_R \end{pmatrix} \tag{4.10}$$

where it may be noted that we assume a sufficiently large scattering region such that the coupling between the leads can be neglected. Furthermore, only the $\mathbf{H}_S$ and $\mathbf{S}_S$ matrices are finite due to the infinite leads. However, the leads are chosen such that they consist of repeated principal layers and in this way we avoid inverting an infinite matrix in the above equation. Both $\mathbf{H}$ and $\mathbf{S}$ can be obtained using DFT within the Kohn-Sham scheme (see Chapter 2).

4.3 DFT+Σ

A consequence of obtaining the transmission function from Kohn-Sham based DFT is the use of Kohn-Sham eigenvalues for the molecular energy levels. As discussed in Chapter 2, these eigenvalues give rise to a significantly smaller gap than the fundamental gap, $E_{\mathrm{gap}} = I_P - E_A$. To correct for this, the HOMO and LUMO energy can be obtained from Equation 2.23 in which total energy calculations are used. Due to the presence of the metal electrodes, the effect of the induced image charge in the metal surfaces on the molecular levels must also be considered. Here, the classical image charge of a point charge located at a distance z above a perfect metal surface is given by [114]

$$V = \frac{-q^2}{4(z - z_0)} \tag{4.11}$$

*Substituting z with $z^\dagger = \varepsilon - i\eta$ in Equation 4.9 gives the advanced Green's function $\mathbf{G}^a_S(\varepsilon)$.

where q is the charge of the point charge and z_0 is the effective image plane lying around 0.5 - 1.0 Å above the surface.[114] Using the above expression, it follows from Equation 2.23 that the image charge effect decreases the LUMO energy and increases the HOMO energy. The corrections to the HOMO and LUMO Kohn-Sham eigenvalues can thus be summarized as

$$\delta\varepsilon_{\mathrm{HOMO}} = E[0] - E[+1] - V - \varepsilon^{\mathrm{KS}}_{\mathrm{HOMO}} \tag{4.12}$$

$$\delta\varepsilon_{\mathrm{LUMO}} = E[-1] - E[0] + V - \varepsilon^{\mathrm{KS}}_{\mathrm{LUMO}} \tag{4.13}$$

where $E[0]$ is the ground state total energy and, $E[-1]$ and $E[+1]$ are the total energy of the negatively and positively charged ions of the molecule, respectively. Applying the $\delta\varepsilon_{\mathrm{HOMO}}$ correction to the eigenvalues of all occupied orbitals and the $\delta\varepsilon_{\mathrm{LUMO}}$ to all virtual orbitals gives the so-called DFT+Σ correction to the transmission function. This is a computationally cheap correction that has shown to give reasonable results.[115–117]

4.4 Quantum interference

A special case of electron transport is when the transmission function is exactly zero even suppressing electronic tunnelling through the junction. This effect is due to destructive interference between different electronic paths through the molecule in the junction and is known as quantum interference (QI). In molecular electronics it is usually of interest to have as high an on/off ratio as possible and thus the QI phenomena has received extensive attention as a way of completely turning off the current. However, in order to predict for which molecules QI will occur it is essential to have a theoretical model describing when the transmission function is zero. In the following, the graphical model by Markussen *et al.*[118] is briefly introduced. Starting from the expression for phase-coherent transport in Equation 4.7 and assuming that only the molecular orbitals ψ_1 and ψ_N couples to the left and right lead, respectively, the transmission function reduces to[118]

$$T(\varepsilon) = \gamma(\varepsilon)^2 \left|[\mathbf{G}^r_S(\varepsilon)]_{1N}\right|^2 \tag{4.14}$$

where $\gamma(\varepsilon) = [\mathbf{\Gamma}_L(\varepsilon)]_{11} = [\mathbf{\Gamma}_R(\varepsilon)]_{NN}$ assuming similar coupling to both leads. The QI phenomena is due to the molecular states and we therefore evaluate the $1N$ matrix element of the Green's function using Cramer's rule[118]

$$[\mathbf{G}^r_S(\varepsilon)]_{1N} = \frac{\det_{1N}(\varepsilon - \mathbf{H}_S)}{\det\left[\varepsilon - \mathbf{H}_S - \mathbf{\Sigma}^r_L(\varepsilon) - \mathbf{\Sigma}^r_R(\varepsilon)\right]} \tag{4.15}$$

where we assume an orthogonal basis set[†] and define $\det_{1N}(\varepsilon - \mathbf{H}_S)$ as the determinant of the matrix obtained by removing the first row and Nth column from $\varepsilon - \mathbf{H}_S$ and multiplying with $(-1)^{1+N}$. Assuming zero Fermi energy, $\varepsilon_F = 0$, the condition for having zero transmission at the Fermi level, $T(\varepsilon_F) = T(0) = 0$, is given by

$$\det_{1N}(\mathbf{H}_S) = 0 \tag{4.16}$$

The "true" Hamiltonian is very complicated and thus the above condition will rarely be exactly fulfilled. For a conjugated molecule, in which the transport is dominantly governed by the π electrons in the p_z orbitals, we can however approximate the "true" Hamiltonian using a Hückel model. By setting the the on-site energy for all p_z orbitals to zero and only include the hopping between neighbouring orbitals, t, we can obtain the following Hückel model Hamiltonian

$$\tilde{\mathbf{H}}_S = \begin{pmatrix} 0 & t & 0 & \dots & 0 \\ t & 0 & t & \dots & 0 \\ \vdots & \ddots & \ddots & \ddots & \vdots \\ 0 & \dots & t & 0 & t \\ 0 & \dots & 0 & t & 0 \end{pmatrix} \tag{4.17}$$

which is dominated by zeros that will leave only very few non-vanishing terms in the expression for the determinant of this $(N-1)\times(N-1)$ matrix

$$\det(\tilde{\mathbf{H}}_S) = \sum_\sigma \mathrm{sgn}(\sigma) \prod_{i=1}^{N-1} [\tilde{\mathbf{H}}_S]_{i\sigma(i)} \tag{4.18}$$

[†]Assuming an orthogonal basis set and neglecting the infinitesimal η allow us to set $z\mathbf{S}_S = \varepsilon$.

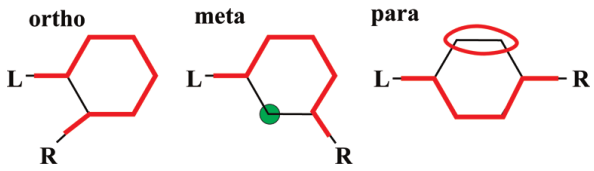

Figure 4.3: Illustration of the simple graphical model to predict quantum interference (QI). To avoid QI it is necessary to have a path for the electron through the molecule in which every site has one incoming and one outgoing path. This is the case for the *ortho* connection. Furthermore, sites not included in the electron path must be able to be connected in closed loops which is the case for the *para* connection. For the *meta* connection the path leaves out the site with the green dot and thus this connection is expected to exhibit QI. Figure adapted from Markussen *et al.*[118]

Thus, unless it is possible to find a permutation in which only nearest neighbour hopping is occurring, the system will exhibit QI. Graphically, this can be thought of as to require that a path for the electron through the molecule can be drawn in which every site has one incoming and one outgoing path. Furthermore, sites not included in the electron path must be able to be connected in closed loops. These rules are illustrated for the benzene molecule in Figure 4.3. Here, it is seen that only transport through the *ortho* and *para* positions is possible, whereas the *meta* position exhibits QI. Even though this simple graphical model is only formally correct within the Hückel model, it has proven to correctly predict QI in form of a transmission dip around the Fermi level for several conjugated molecules.[117;118]

Part II

Results and discussion

Chapter 5

Dye sensitized solar cells

As mentioned in Chapter 1, the dye sensitized solar cell (DSSC) has attracted significant interest as it constitutes a cheap and flexible alternative to the Si-based technologies. This is in part due to the apparently simple physical light harvesting mechanism of a DSSC, which is illustrated in Figure 5.1. Here, the incoming photons from the sun are absorbed by a molecular dye, which is anchored to a semi-conductor nanoparticle (typically TiO_2). The excited electrons on the dye are then transferred to the conduction band of the semiconductor in an ultrafast charge separation process and extracted to an external circuit. In the last step, the electron is transferred from the counter electrode back to the dye by an electrolyte. As illustrated in the figure, a number of criterion must be fulfilled in order to obtain a high DSSC efficiency. First, the energy of the highest occupied molecular orbital (HOMO) should be smaller than the redox potential of the electrolyte while the first excited state should lie above the conduction band edge of the semiconductor. Second, the absorption spectrum of the dye should have a large overlap with the solar spectrum. In addition to these level alignment criterion, the charge injection from the dye to the semiconductor, the regeneration of the oxidized dye by the electrolyte, losses due to charge transport and recombination *etc.* further influences the efficiency. The optimization of a DSSC is hence a complicated task with many parameters to tweak.

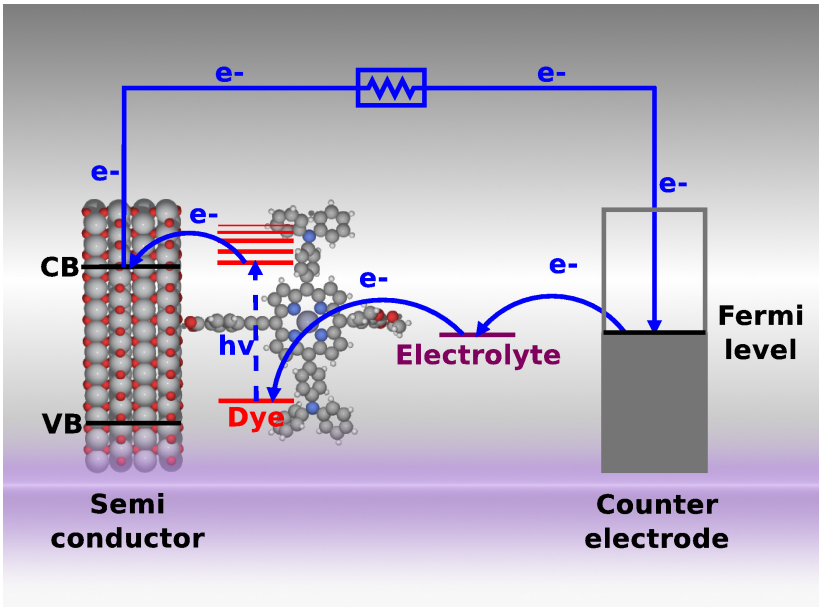

Figure 5.1: Schematic overview of the working mechanisms of a dye sensitized solar cell (DSSC). The incoming photons from the sun are absorbed by a molecular dye which is anchored to a semi-conductor nanoparticle (typically TiO_2). The excited electrons on the dye are then transferred to the conduction band of the semiconductor in an ultrafast charge separation process and extracted to an external circuit. In the last step, the electron is transferred from the counter electrode back to the dye by an electrolyte.

Synthesizing and experimentally measuring *e.g.* the energy levels of just a single dye can furthermore be a non-trivial and time consuming process which should only be performed for dyes that have significant probability of giving a high solar cell efficiency. Using electronic structure theory on the other hand offers a more simple and fast way of obtaining the relevant energy levels for up to several thousand dyes and, in this manner, the cheap computational result could work as a guide for which dyes it would beneficial to perform experimental studies.

In the following, a computational approach to optimize a few of the important parameters in a DSSC is introduced. In Section 5.1 the results from Paper I and II are presented, targeting the level alignment of the dye molecular levels with *e.g.* the conduction band of the semi-conductor. In Section 5.2 the results from Paper III are presented, correcting the level alignment results with the electron transfer barrier for the dye regeneration process. Last, in Section 5.3 the results from Paper IV are presented, proposing new ways of combining dyes to create molecular tandem solar cells.

5.1 Optimizing porphyrin based dyes using large-scale computations

To fully exploit the advantages of high-throughput computational screening methods it is important to have a data set that can be systematically extended. In this study we have chosen our data set to consist of porphyrin dyes functionalized at the *meso* positions as this class of molecules is easily customized and currently holds the efficiency record for DSSCs.[35] The systematic handling of the dyes is ensured by splitting them up into a *backbone*, an electron accepting *anchor group* and three electron donating *side groups*. The backbone of the dye is the porphyrin moiety itself, where we choose 5 different candidates as illustrated in Figure 5.2. Here, the ZnP backbone is chosen due to its popularity in high efficiency dyes and the simple H_2P backbone is chosen to investigate the effect of not having a metal center. The three last backbones are chosen since modifying the backbone by exchanging zinc as the metal center and use fluorine in the β positions, as discussed in Chapter 1, has been shown to alter the electronic structure of the dye significantly.[36–39] The five more or less electron donating side groups and the three electron accepting anchor groups used to construct the dyes in this study are shown in Figure 5.3. The TPA, MOTPA and TMP side groups as well as the EthynPhA anchor group have been investigated experimentally by Liu *et al.*,[19] the DMP, DTBP and DTA side groups are modified versions of those investigated experimentally by Yella *et al.*[27] and the 2CarboxyPropenA and 2CyanoPropenA anchor groups have been investigated theoretically by Lee *et al.*[57] Generally, the groups have been chosen to represent well-known building blocks that should be experimentally available.

The dyes are assembled by functionalizing the backbones with an anchor group and three side groups in the *meso* positions, giving 5145 dyes in total. Then, electronic structure calculations are performed for all dyes using Density Functional Theory (DFT)[85] with the PBE[86] exchange-correlation functional as implemented in the GPAW code.[88] For all standard calculations we use a basis set of numerical atomic orbitals[89] (LCAO mode) with a double-ζ polarized basis set, a grid-spacing of 0.18 Å and a unit cell with 5.0 Å vacuum added on both sides of the molecule in all directions. The structures of all dyes are optimized using the BFGS method as implemented in the Atomic Simulation Environment (ASE)[119] until all forces are below 0.05 eV/Å. After the geometry optimization, the location of the highest occupied molecular orbital (HOMO), E_{HOMO}, and lowest unoccupied molecular orbital (LUMO), E_{LUMO}, are calculated as the ionization potential, I_P, and electron affinity, E_A, of the molecule (see Equation 2.23) to overcome the challenges discussed in Section 2.6. It may be noted that the obtained E_{HOMO} values are in good agreement with results obtained from PBE calculations with the all-electron Gaussian09 programme suite[120] and accurate Coupled-Cluster results obtained using the Molpro programme suite.[121] For the E_{LUMO}, the agreement is worse with differences up to $\approx$ 0.2 eV between PBE and both the Gaussian09 DFT and Coupled-Cluster values. We furthermore stress that the effect of hybridization and image charge screening by the TiO_2 surface as well as the effect of solvent on the orbital energies have not been included in the calculations.[59;114;122;123] However, for screening several thousands of dyes these approximations are acceptable and we believe that we still obtain reliable trends.

The calculated E_{HOMO} and E_{LUMO} for all dyes created with the ZnP backbone are visualized

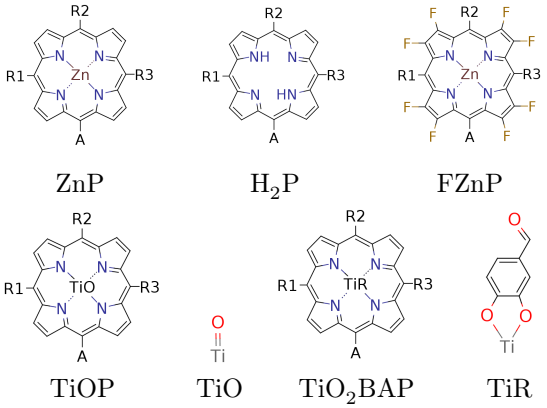

Figure 5.2: The porphyrin backbones investigated in this work. The axial ligands used for TiOP and TiO_2BAP are shown next to the backbones. To construct the dyes, the backbones are functionalized with an anchor group at the location A and three side groups at locations R1, R2 and R3 respectively.

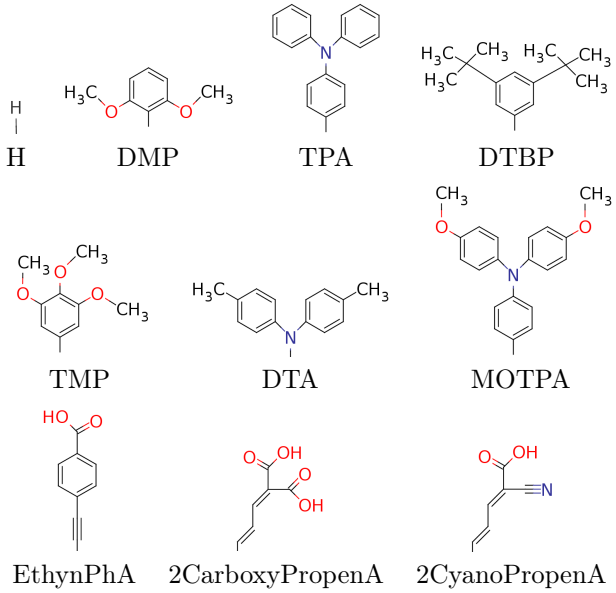

Figure 5.3: **Top rows:** The side groups investigated in this work. Note that when the fluorinated FZnP backbone is used, the H side group is replaced by the F group consisting of a fluorine atom. **Bottom row:** The anchor groups investigated in this work.

in the left part of Figure 5.4. Here, it is readily observed that E_{HOMO} can be varied significantly by modifying the side groups while E_{LUMO} is almost constant upon this modification. This is consistent with the picture shown in the right part of Figure 5.4 where we retain the backbone and anchor group but vary the side groups. Here, it is seen that the spatial shape of the HOMO changes dramatically upon this modification, while the LUMO is left unchanged. On the other hand, changing the anchor group greatly influences the LUMO while the HOMO energies are kept almost constant. Thus, we have two independent handles to switch up and down the important E_{HOMO} and E_{LUMO} of the dyes. Looking at the E_{HOMO} and E_{LUMO} values for the isolated backbones, side groups and anchor groups given in Table 5.1 and using a simple perturbation theory based interpretation, where the interaction is proportional to the inverse energy difference, we can give a simple explanation of this effect. From the table it is clearly observed that there is a match between the HOMO energy of the isolated side groups and the backbones, while the LUMO energies are far apart. Furthermore, it can be observed that the difference in E_{HOMO} between the ZnP backbone and *e.g.* the DTA side group is smaller than the difference between the backbone and *e.g.* the DMP group. Hence, we expect a larger change of the HOMO when we functionalize ZnP with DTA compared to DMP. This is consistent with the

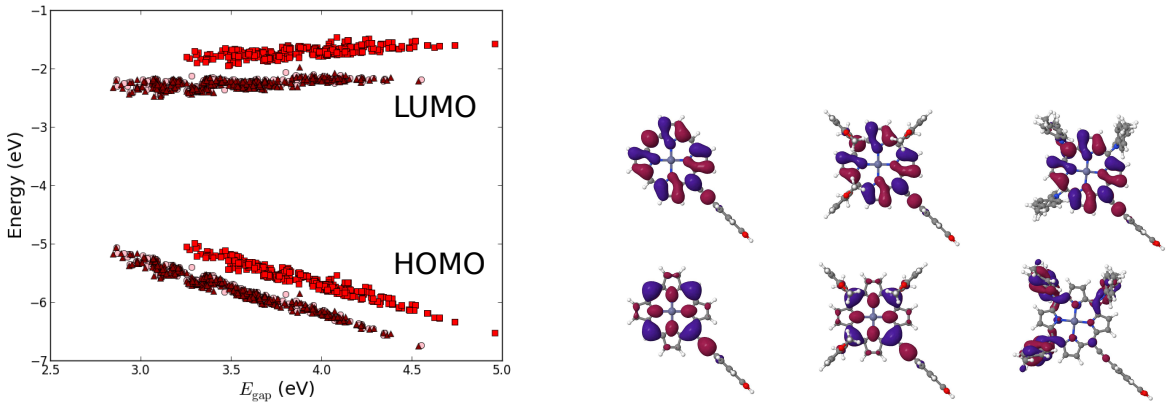

Figure 5.4: **Left:** Calculated E_{HOMO} and E_{LUMO} relative to vacuum ordered by the resulting E_{gap} of functionalized porphyrins with the ZnP backbone and the EthynPhA (red square), 2CarboxyPropenA (pink circle) and 2CyanoPropenA (darkred triangle) anchor groups. **Right:** Visualization of the HOMOs (bottom) and LUMOs (top) for zinc [H,H,H]-porphyrin (left), zinc [DMP, DMP, DMP]-porphyrin (middle) and zinc [DTA, DTA, DTA]-porphyrin (right) respectively. All with the EthynPhA group as anchor group.

Table 5.1: E_{HOMO} and E_{LUMO} for the isolated backbones, side groups and anchor groups.

Backbone	E_{HOMO} (eV)	E_{LUMO} (eV)
ZnP	-6.71	-1.10
H_2P	-6.72	-1.20
TiOP	-6.88	-1.37
TiO_2BAP	-6.56	-1.80
FZnP	-7.20	-1.85

Group	E_{HOMO} (eV)	E_{LUMO} (eV)
DMP	-7.65	2.08
TPA	-6.75	0.42
MOTPA	-6.49	0.58
TMP	-7.04	2.23
DTA	-6.70	0.99
DTBP	-8.22	1.61
EthynPhA	-8.56	-0.24
2CarboxyPropenA	-9.24	-1.04
2CyanoPropenA	-9.37	-1.03

finding that E_{HOMO} for the zinc [DTA, DTA, DTA]-porphyrin with the EthynPhA anchor group is -5.43 eV, while it for the zinc [DMP, DMP, DMP]-porphyrin with the EthynPhA anchor group is -5.97 eV, which is closer to the value of the isolated backbone of -6.71 eV. The larger interaction is also visible in the right part of Figure 5.4, where the HOMO for the DMP functionalized dye is much more similar to the HOMO of the unfunctionalized dye than the HOMO of the DTA functionalized dye, which is strongly influenced by, and localized on, the side groups. The same type of argument holds for the anchor groups and their influence on the LUMO. In the left part of Figure 5.4 it is observed that the LUMO is lowered most by the 2CarboxyPropenA and 2CyanoPropenA groups, consistent with the small difference in E_{LUMO} between these and the isolated ZnP backbone.

Having established the effect of varying the side and anchor groups, we can turn to the differences upon using different backbones. These results are visualized in Figure 5.5. Here, it is immediately observed that the effect of going from ZnP to the metal-free H_2P backbone is negligible. From a pure energetic point of view this agrees well with the very similar frontier orbital energies for both backbones (see Table 5.1). Visually, this can furthermore be explained from the fact that the HOMO and LUMO orbital weights on the central Zn are very small as seen in the right part of Figure 5.4. Thus, substituting the zinc center with hydrogens should not affect the shape of the orbitals which is indeed observed in Figure 5.6, which shows the visual representation of the frontier orbitals for dyes with the five different backbones. In the figure it is furthermore observed that using the TiOP backbone, which features an axial ligand in the form of O^{2-}, induces a small modification of the frontiers orbitals as there is some orbital weight on the axial oxygen atom. Energetically, this also causes a change in the E_{HOMO} and E_{LUMO} for the pure backbone. However, as observed in the top left part of Figure 5.5, this has only negligible effect on the HOMO and

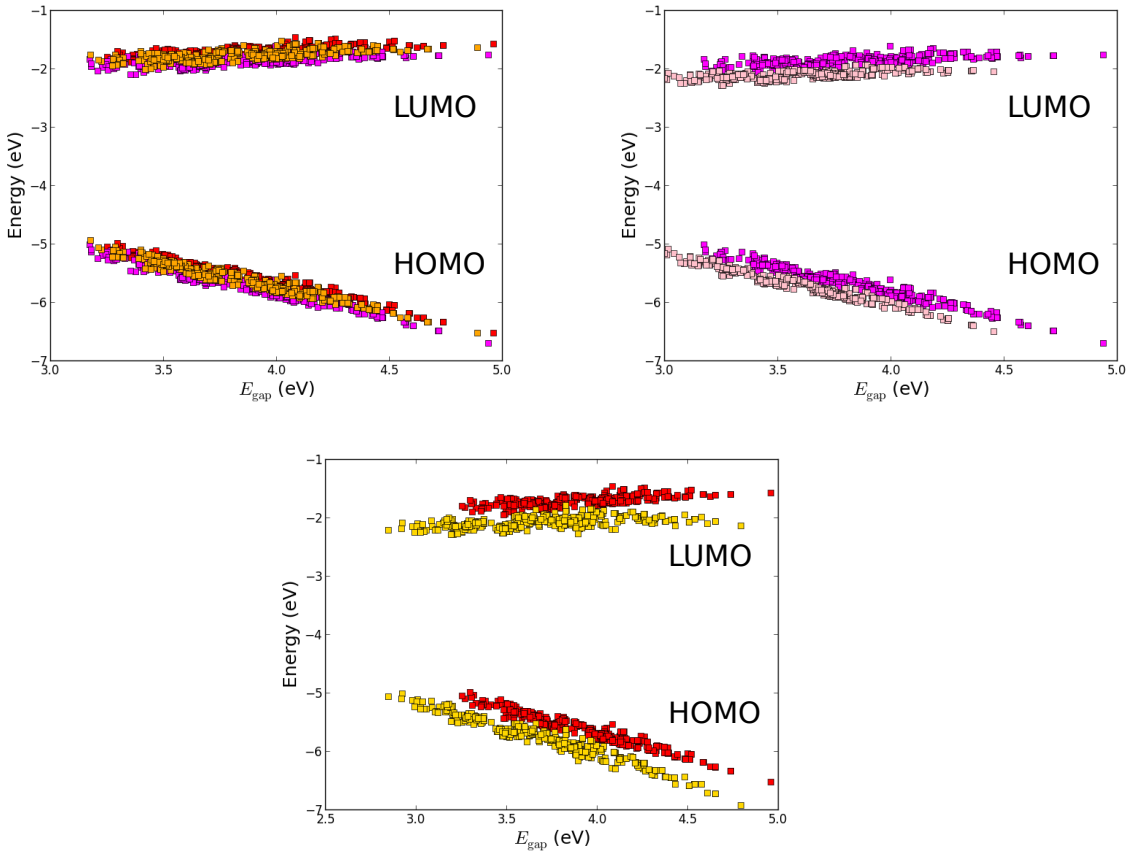

Figure 5.5: Calculated E_{HOMO} and E_{LUMO} relative to vacuum ordered by the resulting E_{gap} of functionalized porphyrins with the EthynPhA anchor group and the ZnP (red), H_2P (orange), TiOP (magenta), TiO_2BAP (pink) and FZnP (yellow) backbones. The top left figure compares ZnP, H_2P and TiOP, the top right figure compares TiOP and TiO_2BAP and the bottom figure compares ZnP and FZnP.

LUMO energies of the dyes. A larger shift in HOMO and LUMO energies are however observed when exchanging the simple axial oxygen in the TiOP backbone, with the larger $CHOC_6H_3OO^{2-}$ ligand in the TiO_2BAP backbone. Using the latter backbone is here observed to result in a constant down-shift of the LUMO energies, generally lowering the resulting fundamental gap, E_{gap}. The range of E_{gap} is furthermore lowered as the range of obtainable E_{HOMO} energies is slightly lowered. This is especially observed for dyes with the most negative E_{HOMO}, which generally have a large HOMO orbital weight on the porphyrin backbone. For these systems, the strong interaction with the axial ligand (see Figure 5.6) leads to an up-shift of the HOMO energy. On the other hand, for dyes with stronger electron donating side groups and HOMOs more localized on these, the effect of the axial ligand is vanishing and these dyes will hence not exhibit any up-shift in HOMO orbital energy. In this way, modifying the axial ligand is a third handle influencing both the HOMO and LUMO energies, which energetically can be used to shift the range of obtainable fundamental gaps.

An even more dramatic modification of the porphyrin backbone is to introduce fluorine instead of hydrogen at the β positions of the porphyrin backbone as illustrated by the FZnP backbone. The high electronegativity of the fluorine atoms leads to a transfer of charge from the porphyrin backbones towards the fluorine atoms, generating an electrostatic potential on the backbone. This induced potential leads to a lowering of all LUMO energies as well as a lowering of the HOMO energies for dyes with less donating side groups, as seen in the bottom part of Figure 5.5. The common feature of these orbitals is that they are all located mainly on the backbone, thus feeling the induced potential. As a consequence of this, the range of obtainable E_{HOMO} values increase,

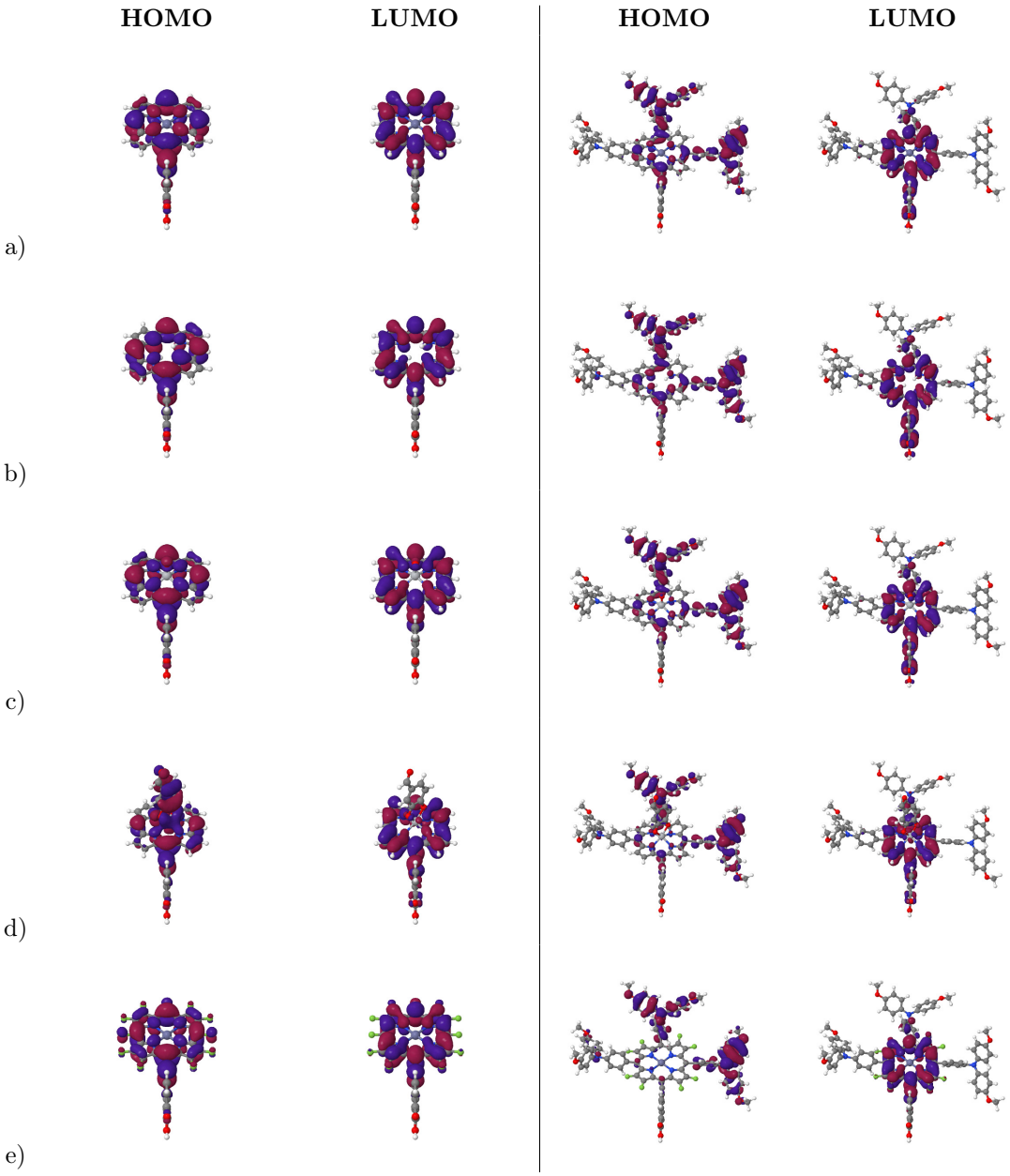

Figure 5.6: Comparison of the spatial shape of the HOMO and LUMO of dyes using only the H side group (left) or the MOTPA side group (right) and the EthynPhA anchor group together with the a) ZnP, b) H_2P, c) TiOP, d) TiO_2BAP and e) FZnP backbones.

significantly increasing the range of E_{gap}. The total range, when using all backbones, side groups and anchor groups, of E_{HOMO} is 2.3 eV, the range of E_{LUMO} is 1.3 eV and the range of E_{gap} is 2.4 eV. Thus, by using these handles it is possible to significantly tune the frontier orbital energies of porphyrins.

In addition to the fundamental gap, the optical gap, E_1, which includes the electron-hole interaction, has been calculated. The calculation of E_1 is done by forcing the molecule to the triplet ground state by fixing the magnetic moment and thus promoting one of the two electrons in the HOMO to the LUMO. We use the triplet excitation energy rather than the singlet excitation because this is technically simpler to compute. Comparing the singlet and triplet excitation energies for a few porphyrins dyes with the ZnP backbones shows that these are within 0.3 eV and that their dependence on molecular structure is very similar. Thus, we believe that the calculated triplet

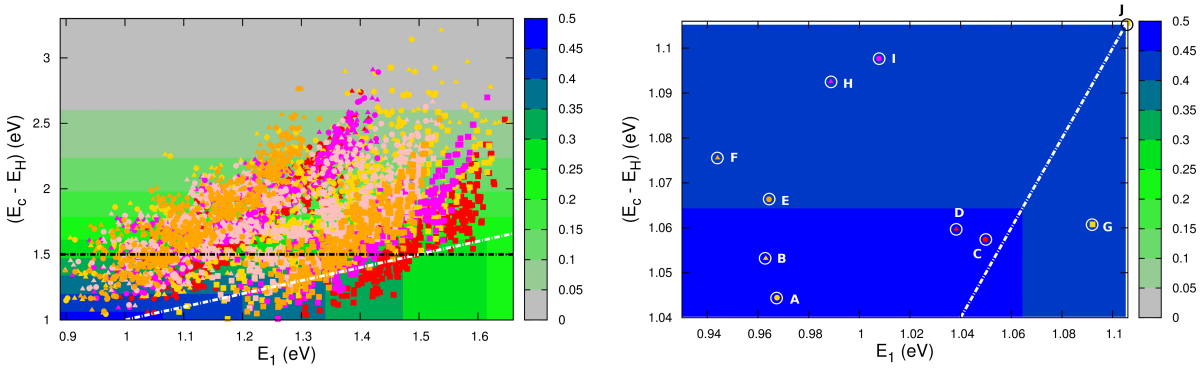

Figure 5.7: **Left:** Calculated level alignment quality as function of the optical gap, E_1, and the energy difference between the conduction band of TiO_2 and the HOMO level of the dyes, $E_c - E_H$, for candidates with the ZnP (red), H_2P (orange), TiOP (magenta), TiO_2BAP (pink) and FZnP (yellow) backbones and the EthynPhA (square), 2CarboxyPropenA (circle) and 2CyanoPropenA (triangle) anchor groups. The black dotted line indicates the lower limit of $E_c - E_H$ for dyes to be used with the I^-/I_3^- electrolyte and the white dotted line indicates where $E_c - E_H = E_1$. **Right:** Zoom of the above figure onto the region with the highest level alignment quality. The letters identifies the top ten candidates and correspond to the letters in Table 5.2.

energies provides a reasonable alternative for large-scale screening. In general, we find that the calculated E_1 values correlates well with the calculated E_{gap} values but with a significantly smaller obtainable range (0.8 eV). This is as expected since the Coulombic attraction between electron and hole depends strongly on the distance between the charges. Since the porphyrins with the largest E_{gap} have both HOMO and LUMO located on the porphyrin backbone, these porphyrins have a higher electron-hole interaction than porphyrins with smaller E_{gap}, thus decreasing the range of E_1.

The efficiency of a DSSC is given by[2]

$$\mu = \frac{V_{oc} J_{sc} \text{FF}}{P_{in}} \tag{5.1}$$

where P_{in} is the power of the incident light, the open-circuit voltage, V_{oc}, is the maximum voltage available when no current is running and the short-circuit current, J_{sc}, is the maximum available current obtainable upon short circuiting the system. The fill-factor, FF, is defined as

$$\text{FF} = \frac{P_{max}}{V_{oc} J_{sc}} \tag{5.2}$$

where P_{max} is the maximal experimentally obtainable power of a given DSSC device. Considering an ideal DSSC with a unity fill-factor and a J_{sc} solemnly dependent on the number of photons absorbed by the dye allows us to define a *level alignment quality*, η, which we use to score all 5145 investigated dyes

$$\eta = \frac{eV_{oc} \int_{E_c - E_H}^{\infty} \Theta(E - E_1) \cdot I_{\text{solar}}(E) dE}{\int_0^{\infty} E \cdot I_{\text{solar}}(E) dE} \tag{5.3}$$

where

$$\Theta(E - E_1) = \begin{cases} 1 \text{ for } E - E_1 \geq 0 \\ 0 \text{ for } E - E_1 < 0 \end{cases}$$

Here, $E_c - E_H$ is the distance from the HOMO level to the conduction band, E_1 is the optical gap of the dye, $\Theta(E - E_1)$ is a step function representing the absorption of the dye molecules, $I_{\text{solar}}(E)$ is the photon flux of the ASTM G-173-03 (AM 1.5 G) solar spectrum and eV_{oc} is the open-circuit voltage multiplied with the charge of the electron. In the following we assume that $E_c = -4.0$ eV and $V_{oc} = 1.0$ V consistent with using TiO_2 as the semi-conductor and I^-/I_3^- as the redox mediator. We note that using a single value for E_c for all dyes is an assumption, since different dyes will

Table 5.2: Top ten candidates measured by the level alignment quality under the assumption that $E_c = -4.0$ eV and $V_{oc} = 1.0$ V. The letters correspond to the letters in the right part of Figure 5.7

Dye	Backbone	A	R1	R2	R3	E_{HOMO} (eV)	E_1 (eV)	η
A	FZnP	2CarboxyPropenA	MOTPA	MOTPA	MOTPA	-5.04	0.97	0.46
B	FZnP	2CyanoPropenA	MOTPA	MOTPA	MOTPA	-5.05	0.96	0.45
C	ZnP	2CarboxyPropenA	MOTPA	MOTPA	MOTPA	-5.06	1.05	0.45
D	ZnP	2CyanoPropenA	MOTPA	MOTPA	MOTPA	-5.06	1.04	0.45
E	H_2P	2CarboxyPropenA	MOTPA	MOTPA	MOTPA	-5.07	0.96	0.45
F	H_2P	2CyanoPropenA	MOTPA	MOTPA	MOTPA	-5.08	0.94	0.45
G	FZnP	EthynPhA	DTA	MOTPA	MOTPA	-5.06	1.09	0.44
H	TiOP	2CyanoPropenA	MOTPA	MOTPA	MOTPA	-5.09	0.99	0.44
I	TiOP	2CarboxyPropenA	MOTPA	MOTPA	MOTPA	-5.10	1.01	0.44
J	FZnP	EthynPhA	MOTPA	DTA	MOTPA	-5.11	1.11	0.44

affect the conduction band via interface-dipole interactions.[124] Furthermore, using the $\Theta(E - E_1)$ step function to represent the dye absorption is based on the assumption that all solar photons with an energy higher than E_1 of the dye are absorbed by the dye molecules. We thus assume that all investigated dyes regardless their size covers the nano-structured TiO_2 to effectively form several layers of dye in the device and that vibrational modes enhance the oscillator strength of any symmetry-forbidden transitions in the dyes.[125] It should be noted that the level alignment quality only describes the alignment between the dye and semi-conductor and is thus only one component in order to obtain a high efficiency in a DSSC.

The left part of Figure 5.7 gives a visual representation of the level alignment quality as a function of E_1 and $E_c - E_H$ with the calculated values for all 5145 dyes indicated. In the figure a white dotted line indicating $E_c - E_H = E_1$ is added since excited electrons in molecules where $E_c - E_H > E_1$, due to thermal relaxation, can get trapped below the conduction band of the semi-conductor. However, since we in this study operate with a relatively high uncertainty we will not exclude any candidates from our investigation based on this criteria and the lines thus only serves as an indicator for the readers. The black dotted line furthermore indicates where $E_{\mathrm{HOMO}} = -5.50$ eV, which corresponds to the upper limit of E_{HOMO} for dyes used in a DSSC with the I^-/I_3^- redox pair. This strict limit stems from the need to have a 0.6 V potential difference between E_{HOMO} and the redox potential of the I^-/I_3^- redox pair in order to drive the charge transfer.[2;126–128] A more comprehensive discussion of the role of the redox mediator is given in the next section.

From Equation 5.3 it can be seen that the level alignment quality in general is a competition between absorbing a greater part of the sunlight (small $E_c - E_H$ and E_1) and obtaining a high open-circuit voltage defined as the potential difference between the redox potential, E_{red}, of the redox mediator and the conduction band edge, E_c. For the redox mediator to be able to regenerate the oxidized dye, it is a constraint that $E_{\mathrm{HOMO}} < E_{\mathrm{red}}$. Hence, a large open-circuit voltage requires a more negative E_{HOMO}, increasing $E_c - E_H$. However, by choosing a specific redox mediator, in this case the I^-/I_3^- redox couple and thus fixing $V_{oc} = 1.0$ V, we have reduced the importance of the open-circuit voltage to the constraint that $E_c - E_H > 1.0$ eV. Thus, the level alignment quality is dominated by the absorption, which is also observed in Figure 5.7 and Table 5.2 giving the top ten candidates measured by the level alignment quality. Here, the common feature of the top ten candidates is that they have a E_1 value around 1.0 eV and a E_{HOMO} value around -5.1 eV (corresponding to a $E_c - E_H$ around 1.1 eV). The similar values of E_1 and $E_c - E_H$ can be explained from having all the photoexcited electrons on the dye contributing to the photocurrent. The optimal value of $E_1 \approx 1.1$ eV is furthermore in agreement with the optimal value predicted for semi-conductor solar cells by Shockley and Queisser.[129]

From Figure 5.5 it is seen that in order to get $E_{\mathrm{HOMO}} \approx -5.0$ eV it is necessary to have very electron donating side groups, explaining the preference for the MOTPA group in Table 5.2. The preference for the 2CarboxyPropenA and 2CyanoPropenA anchor groups can on the other hand be explained by the requirement of lowering the optical gap as these groups are more electron accepting and thus lowers E_{LUMO} of the dyes, which is highly correlated with E_1. Here, it should be

Table 5.3: Using the YD2-o-C8[27] dye as a starting point, the level alignment quality is optimized by varying 1 or 2 structural parameters

No. of opt. par.	Backbone	A	R1	R2	R3	E_{HOMO} (eV)	E_1 (eV)	η
0 parameters	ZnP	EthynPhA	DMP	DTA	DMP	-5.77	1.48	0.20
1 parameter[a]	ZnP	EthynPhA	DMP	DTA	TPA	-5.54	1.40	0.27
1 parameter[b]	ZnP	EthynPhA	MOTPA	DTA	DMP	-5.40	1.40	0.33
2 parameters[a]	ZnP	EthynPhA	DMP	DMP	MOTPA	-5.51	1.46	0.29
2 parameters[b]	ZnP	EthynPhA	TPA	DTA	TPA	-5.36	1.34	0.34

[a] The optimization is performed under the constraint that $E_{\mathrm{HOMO}} \leq -5.50$ eV corresponding to the requirement of using the I^-/I_3^- redox pair.[2;126–128]

[b] The optimization is performed under the constraint that $E_{\mathrm{HOMO}} \leq -5.36$ eV corresponding to the requirement of using the $[Co^{II/III}(bpy-pz)_2]$ redox pair.[133]

noted that the 2CyanoPropenA group has been reported to undergo photoisomerization, significantly decreasing the stability of the dyes.[130]

The presence of four different backbones among the top ten dyes indicates that the choice of backbone is less important in order to obtain a high level alignment quality. This can be explained from the presence of highly electron donating side groups and highly electron accepting anchor groups in the top ten dyes, which thus will have HOMOs and LUMOs that are more localized on the side- and anchor groups, minimizing the the influence of the backbone structure. The relative free choice of backbone introduces a high flexibility in designing dyes by *e.g.* allowing for more bulky axial ligands to provide steric hindrance between the dyes limiting dye aggregation.[15;16;22;131;132]

The level alignment quality is, as mentioned, only one of the components that should be optimized for obtaining a high efficiency. However, having an already well-performing dye, finding a closely related dye with increased level alignment quality could lead to increased efficiency. Table 5.3 gives an example of how to use the constructed database for this purpose. Here, the well-performing dye YD2-o-C8 dye[27] is investigated varying 1 or 2 structural parameters under the constraint that $E_{\mathrm{HOMO}} \leq -5.50$ eV, corresponding to the requirement imposed by the I^-/I_3^- redox pair, and the constraint $E_{\mathrm{HOMO}} \leq -5.36$ eV, corresponding to the requirement imposed by the $[Co^{II/III}(bpy-pz)_2]$ redox pair,[133] respectively. From the table it is seen that changing the side groups has the largest impact on the level alignment quality for this particular dye. In fact, by substituting a single side group, the level alignment quality is expected to increase significantly. Since the structural change is negligible this could lead to a higher efficiency of an actual DSSC.

5.2 The role of the redox mediator

Until this point we have only included the redox mediator as a constant redox potential in the calculation of the level alignment quality. The role of the redox mediator is however more complex as exemplified by *e.g.* the black line in Figure 5.7, which indicates the high overpotential needed when using the I^-/I_3^- redox couple as redox mediator. This is proposed to be due to the complicated mechanism of the redox process which is believed to involve the $I_2^{-\cdot}$ radical anion.[134–136] Recently, the focus has shifted towards cobalt based redox mediators as these are considered more promising in terms of achieving higher DSSC efficiencies[27;43] while the electron transfer is believed to be a simple outer-sphere process. Using a cobalt based redox mediator, the DSSC dye regeneration process is defined as the electron transfer from the cobalt complex to the oxidized dye

$$D^+ + [Co(red)]^{2+} \rightarrow D + [Co(red)]^{3+} \tag{5.4}$$

where D/D^+ is the neutral/oxidized dye and $[Co(red)]^{2+}/[Co(red)]^{3+}$ is the reduced/oxidized cobalt based redox mediator. As discussed in Chapter 3, this type of electron transfer reaction is associated with a barrier due to the reorganization of the solvent and the molecules. A schematic overview of these energetics is given in the left part of Figure 5.8, where the driving force for the regeneration reaction, ΔF^0, and the free energy barrier associated with the electron transfer, $\Delta F^\ddagger$, are both defined in Figure 3.2 and explained in more details in Chapter 3. In this study we

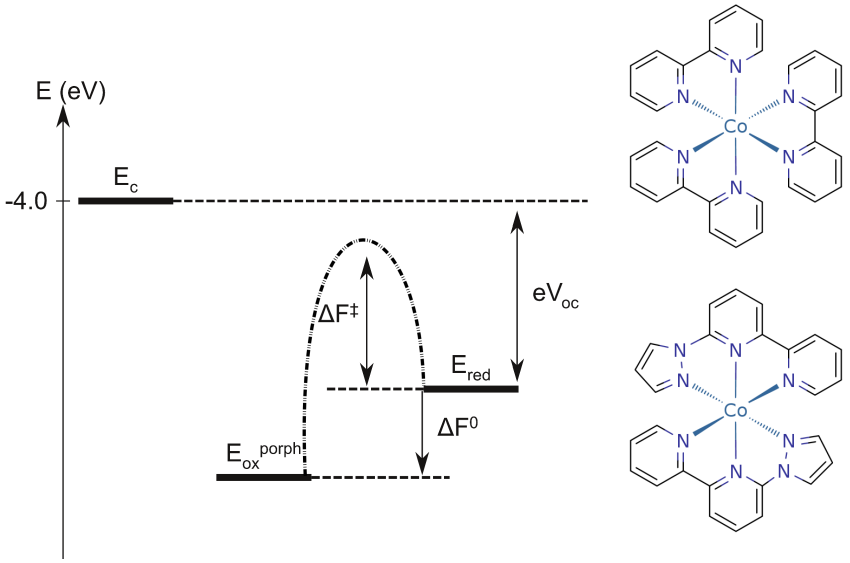

Figure 5.8: **Left:** Scheme of the energetics associated with the regeneration reaction. Here, E_c is the conduction band edge of TiO_2, $E_{\text{ox}}^{\text{porph}}$ is the oxidation potential of the porphyrin based dyes, E_{red} is the redox potential of the cobalt based redox mediator, ΔF^0 is the driving force for the regeneration reaction, $\Delta F^{\ddagger}$ is the barrier associated with the electron transfer and eV_{oc} is the open-circuit voltage multiplied with the electronic charge. **Right:** The redox mediators investigated in this work: The $[\text{Co}^{\text{II/III}}(\text{bpy})_3]$ redox mediator (top) and the $[\text{Co}^{\text{II/III}}(\text{bpy}-\text{pz})_2]$ redox mediator (bottom).

will focus on the two commonly used redox mediators: $[\text{Co}^{\text{II/III}}(\text{bpy})_3]$ and $[\text{Co}^{\text{II/III}}(\text{bpy}-\text{pz})_2]$ (bpy-pz=6-(1H-pyrazol-1-yl)-2,2'-bipyridine).[43;133] The structure of the two redox mediators are shown in the right part of Figure 5.8.

To include the effect of the electron transfer reorganization barrier, we, inspired by the Arrhenius expression, define a weighted level alignment quality as

$$\eta_{\text{reg}}(\Delta F^0, \lambda; T) = C(\Delta F^0, \lambda; T) \cdot \eta \tag{5.5}$$

where the open-circuit voltages used to compute η correspond to using the redox potentials of the two redox mediators and the correction factor is defined by

$$C(\Delta F^0, \lambda; T) = \begin{cases} \exp\left(\frac{-\Delta F^{\ddagger}(\Delta F^0, \lambda)}{k_B T}\right) & \text{for } \Delta F^0 \leq 0 \\ 0 & \text{for } \Delta F^0 > 0 \end{cases} \tag{5.6}$$

Here, the correction factor is seen to depend on the free energy barrier, $\Delta F^{\ddagger}$, which in turn depends on the reorganization energy, λ, and the driving force, ΔF^0, as given in Equation 3.16. Hence, in order to calculate the weighted level alignment quality, we need the reorganization energy and ΔF^0 for the regeneration of all 5145 dyes by the two redox mediators. Due to limited computational resources it is however necessary to only explicitly calculate the reorganization energy for the simplest zinc porphyrin with hydrogen acting as both side groups and anchor group (denoted ZnP) and then extrapolate this value to the functionalized porphyrins.

The explicit calculation of the reorganization energy follows the sampling procedure described in Section 3.3 in which all quantum mechanical calculations again are performed using DFT with the PBE[86] exchange-correlation functional as implemented in the GPAW code.[88] For all standard calculations we have used a basis set of numerical atomic orbitals[89] (LCAO mode) with a double-ζ polarized basis set, a grid-spacing of 0.18 Å and a 20 Å x 20 Å x 15 Å unit cell with periodic boundary conditions in all directions. To prepare for the Molecular Dynamics (MD) simulations, the cell was initially filled with acetonitrile to obtain a density of $\rho = 786\,\text{mg}\,\text{mL}^{-1}$ which was thermalized to 300K with 2.0 fs time steps. This is accomplished with an in-house Langevin

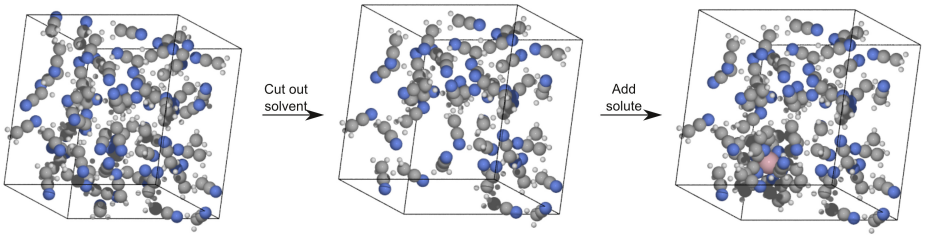

Figure 5.9: Illustration of the procedure to create the simulation cell for $[Co^{II/III}(bpy)_3]$. A 20 Å x 20 Å x 15 Å unit cell with periodic boundary conditions is filled with acetonitrile and thermalized. After this a hole is cut and in the last step the desired molecule is inserted.

integrator employing the RATTLE[137] constraint scheme (algorithm based on the formulation by Eijnden *et al.*[138]). The constraints introduced consist in the pacification of all C-H bonds which allows us to take larger time steps and thus decrease the computational time required. Since the role of the C-H bonds in the simulations are very limited, we believe that the pacification is justified. After the thermalization, a block of solvent molecules were cut out of the unit cell to make room for the dye or redox mediator molecule (see Figure 5.9 for an illustration of the procedure). Effectively, this gives a concentration of 0.28 M. Since all boxes are similar in size and only contain one solute molecule, the concentration ratio between all species is unity. The solutes are however electrostatically decoupled from the neighbouring cell, resulting from the periodic boundary conditions, through a background potential used in the Ewald method for handling periodic systems. Thus, we are focusing on a single species, corresponding to the infinite dilution limit. The box containing the solvated molecule was thermalized in the same manner as the initial solvent box. To obtain data for the WHAM method, we created five copies of the thermalized box with the solvated molecule and thermalized them using a linear combination of *initial*- and *final* state forces with $\chi_\alpha = 0.0$, 0.25, 0.50, 0.75 and 1.00 for each box respectively (see Equation 3.20). After 1.0 ps of thermalization, we ran the simulation for additionally 5.0 ps production time resulting in 2500 data points for every configuration. Combining the data points for the WHAM procedure lead to in total 6.25 million data points for every linear force combination.

To extrapolate the explicitly calculated reorganization energy of the simplest porphyrin to the 5145 other dyes, we exploit that in terms of a continuum model representing the solvent surrounding two solute species A and D, represented as charged spheres of radius r_A and r_D, respectively, the outer reorganization energy in atomic units can be expressed as[93]

$$\lambda^{\text{out}} = (\Delta q^2)\left(\frac{1}{\epsilon^\infty} - \frac{1}{\epsilon^{\text{st}}}\right)\left(\frac{1}{2r_A} + \frac{1}{2r_D} - \frac{1}{R_{AD}}\right) \tag{5.7}$$

where ϵ^∞ and ϵ^{st} are the high frequency and static dielectric constants of the solvent and Δq is the total charge transferred. The last term on the right hand side is the screened Coulomb interaction between the donor and acceptor where R_{AD} is the distance between the two solute species. Assuming that the charge transfer occurs when the two spheres come in contact, R_{AD} is simply given by the sum of the two solute species radii.

In connection with this we note that upon functionalizing porphyrins there is a significant change in the size of the dye. To account for this change, we have used the *Jmol* programme suite[139] to obtain a volume of all 5145 porphyrin dyes using the predefined Van der Waals surfaces of the atoms. This volume is then transformed into a radius of a sphere using

$$r = \left(\frac{3V}{4\pi}\right)^{\frac{1}{3}} \tag{5.8}$$

We note that converting the volumes of porphyrins into spheres is a major simplification as porphyrins usually have a flat structure. The way the dye is connected to the surface has furthermore been neglected, despite the influence this has on the actual radius and accessible surface area of

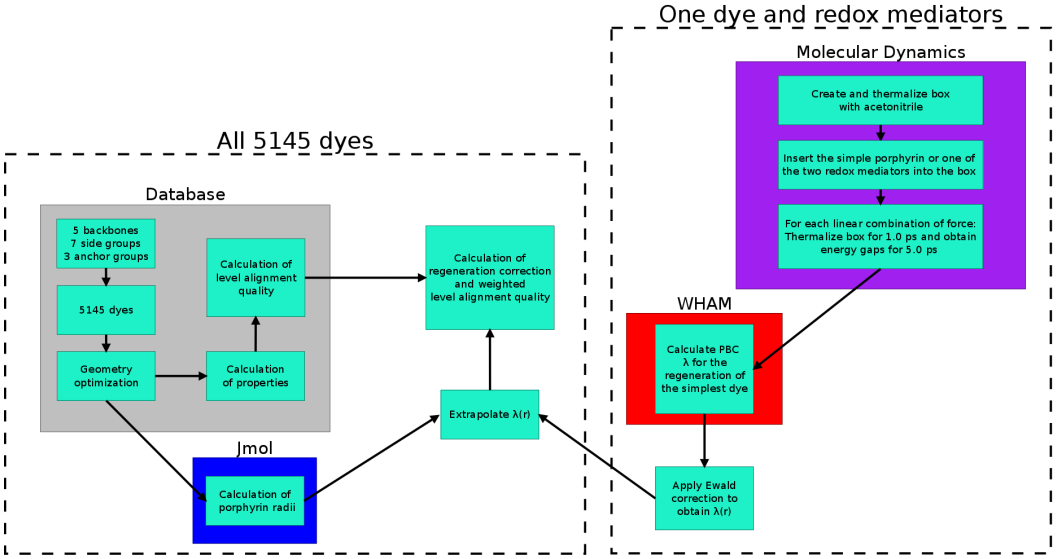

Figure 5.10: Flowchart for the calculations of the weighted level alignment quality. The dashed boxes indicate whether all dyes or only a single dye (and the redox mediators) are investigated in that particular part of the calculation scheme. The coloured boxes indicate specific methods or programmes.

the dye as well as the distance to the redox complex.[140] However, since the radii only enter the correction to an explicitly computed reorganization energy, we believe that we will obtain the correct trends in the size dependency using these.

Having defined the radius of a porphyrin dye, we can use a modified version of Equation 5.7 in which we include a correction for using a finite cell with periodic boundary conditions to obtain the correlation between our chosen convention for r and the explicitly calculated reorganization energy for the simplest zinc porphyrin[141–143]

$$\lambda_{\mathrm{PBC}}^{\mathrm{out}} = (\Delta q)^2 c \left(\frac{1}{2r} + \frac{1}{2L_c} \left[\xi_{\mathrm{Ew}} + \frac{4\pi}{3} \left(\frac{r}{L_c} \right)^2 - \frac{16\pi^2}{45} \left(\frac{r}{L_c} \right)^5 \right] \right) \tag{5.9}$$

Here, $\lambda_{\mathrm{PBC}}^{\mathrm{out}}$ is the uncorrected reorganization energy obtained from our MD simulation, L_c is the linearised cell length, $L_c = V^{1/3}$, where V is the volume of the cell and ξ_{Ew} is the Madelung constant, defined as $\xi_{\mathrm{Ew}} = \frac{V^{\mathrm{bg}}}{L_c}$. In the definition of the Madelung constant, V^{bg} is the background potential applied to counter the charge in our periodic cell. For the cell used in this study, the Madelung constant is $\xi_{\mathrm{Ew}} = -2.757$. From the above equation we can estimate $c = \left(\frac{1}{\epsilon^{\infty}} - \frac{1}{\epsilon^{\mathrm{st}}}\right)$. This fitting was tested for both the 'flat' zinc porphyrin species, as well as the octahedral $Co(bpy)_3$ species, giving $c = 0.502$ and 0.520, respectively. These values are in good agreement with the inverse of the experimental dielectric constant of acetonitrile, $c \approx 0.53$, and in the following $c = 0.502$ is used for the extrapolation scheme of the zinc porphyrin based dyes.

Having corrected for the finite size of the cell with periodic boundary conditions, we can define the r dependent outer reorganization energy for the functionalized porphyrins as

$$\lambda_{\mathrm{porph}}^{\mathrm{out}}(r) = (\Delta q)^2 c \frac{1}{2r} \tag{5.10}$$

To further account for the screened coulomb interaction between the acceptor and donor, we apply a correction based on the $\frac{1}{R_{\mathrm{AD}}}$ part of Equation 5.7. Assuming that the electron transfer occurs when the acceptor and donor are right next to each other corresponds to setting $R_{\mathrm{AD}} = r + r_{\mathrm{red}}$, where r is still the dye radius and r_{red} is the radius of the redox mediator. Using this convention, we obtain a correction to the outer reorganization given by

$$\lambda_{\mathrm{R}}^{\mathrm{out}}(r) = -(\Delta q)^2 c \frac{1}{r + r_{\mathrm{red}}} \tag{5.11}$$

Hence, we now have the size-dependent part of the reorganization energy and the corrections, and we can thus obtain the total reorganization energy for the regeneration reaction as

$$\lambda(r) = \lambda^{\text{out}}_{\text{porph}}(r) + \lambda^{\text{in+out}}_{\text{redox}} + \lambda^{\text{in}}_{\text{porph}} + \lambda^{\text{out}}_{\text{R}}(r) \tag{5.12}$$

where we assume that $\lambda^{\text{in}}_{\text{porph}}$ is r independent due to the similarity in chemical structure of all the porphyrin dyes. The r independent parts of the above equation are found explicitly from a MD simulation of the diabatic regeneration reaction (Equation 5.4) with the smallest porphyrin in which $\lambda^{\text{in+out}}_{\text{redox}}$ have been corrected for the effect of using a finite cell with periodic boundary conditions.

To obtain the electron transfer barrier we, in addition to the reorganization energy, also need the driving force, ΔF^0, for the regeneration reaction. This quantity is defined as

$$\Delta F^0 = E^{\text{porph}}_{\text{ox}} - E_{\text{red}} \tag{5.13}$$

where $E^{\text{porph}}_{\text{ox}}$ is the oxidation potential of the porphyrin dye and E_{red} is the redox potential of the redox mediator. To obtain $E^{\text{porph}}_{\text{ox}}$ from our calculations, we assume that the oxidation potential scales linearly with the vacuum ionization potential, E_{HOMO}, of the dyes with a constant shift due to solvation energies, image charge effects *etc.* Fitting our calculations to the experimental oxidation potentials of five porphyrin dyes on TiO_2 measured by Liu *et al.*[19] gives the relation

$$E^{\text{porph}}_{\text{ox}} = E_{\text{HOMO}} - 0.11\,\text{eV} \tag{5.14}$$

Hence, we have now obtained both λ and ΔF^0 for all 5145 dyes with both redox mediators, enabling us to calculate the free energy barrier (Equation 3.16) and ultimately the correction factor, $C(\Delta F^0, \lambda; T)$, and the weighted level alignment quality (Equations 5.5 and 5.6) for all dyes. A flowchart summarizing the steps described above is given in Figure 5.10.

To test the validity of our method, we have compared the obtained results with experimental data. Here, the reorganization energy of $\lambda = 0.84$ eV reported by Osuka *et al.*[144] for the electron transfer in porphyrin dyads in dimethylformamide compares very well with our calculated reorganization energy of $\lambda = 0.89$ eV for the symmetric electron transfer between two porphyrins ($\text{ZnP} + \text{ZnP}^+ \rightarrow \text{ZnP}^+ + \text{ZnP}$), including Ewald and screened coulomb interaction corrections. When using cobalt based redox mediators it should be noted that it is important to consider both the high-spin (HS) and low-spin (LS) states of cobalt(II). However, since the energy difference between these spin states is small,[145] it may be hard to identify the correct spin ground state using DFT. Therefore, we have investigated both HS and LS for the two redox mediators in question and in line with previously reported results[146] we find that the reorganization energy involving the HS is around 1.0 eV higher than for the LS case. Furthermore, since our calculated and corrected reorganization energies for the regeneration reactions with the LS species resemble the experimental values obtained for the regeneration of an organic dye using different cobalt based redox mediators reported by Feldt *et al.*[104;147] we believe that using the LS state for cobalt(II) provides the best representation. Hence, we assume in the following that all cobalt species are LS. Additionally, we note that our obtained reorganization energies are higher than those recently reported for the cobalt redox mediators using continuum models for the solvent.[146;148] This is however expected since, by explicitly including the solvent, we also capture the solvent reorientation. Last, we note that we do not include the lowering of the reorganization caused by the immobilization of the dyes introduced by the bonding to the semi-conductor.

The calculated free energy barriers for the regeneration reaction of all 5145 dyes with the two redox mediators are shown in Figure 5.11. The striking feature of the two plots is the quadratic dependence of the free energy barrier on the driving force, which stems from Equation 3.16. Here, the free energy barrier is defined as a parabola with a minimum point in $\Delta F^0 = -\lambda$. Hence, as the deviation from a single parabola in both plots is negligible, this indicates that the shift in reorganization energy upon changing the backbone, side groups and anchor group of the dyes is small compared to the total reorganization energy. This is in agreement with the relatively large reorganization energies observed in the plots, where the minimum points of the two parabolas are located at $\Delta F^0 = -1.2$ eV for $[\text{Co}^{\text{II/III}}(\text{bpy})_3]$ and $\Delta F^0 = -1.3$ eV for $[\text{Co}^{\text{II/III}}(\text{bpy}-\text{pz})_2]$. The

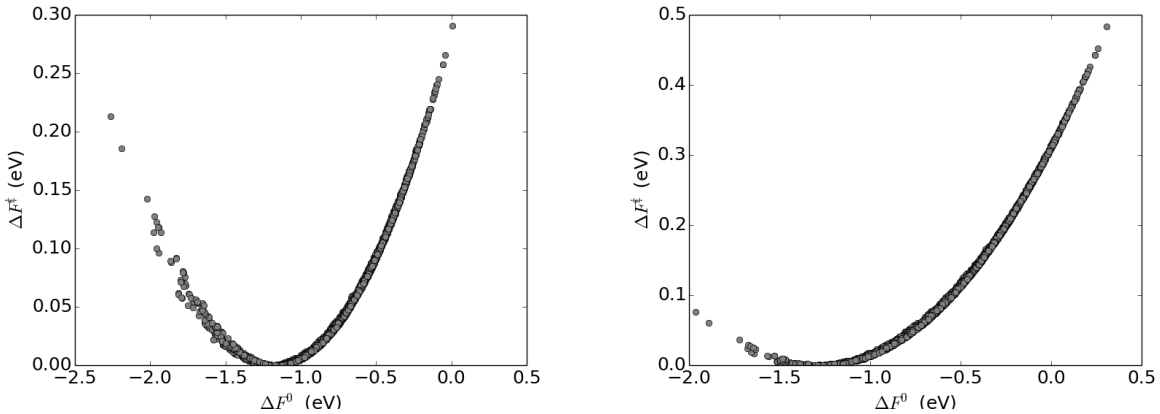

Figure 5.11: Barrier *vs.* driving force for $[Co^{II/III}(bpy)_3]$ (left) and $[Co^{II/III}(bpy-pz)_2]$ (right).

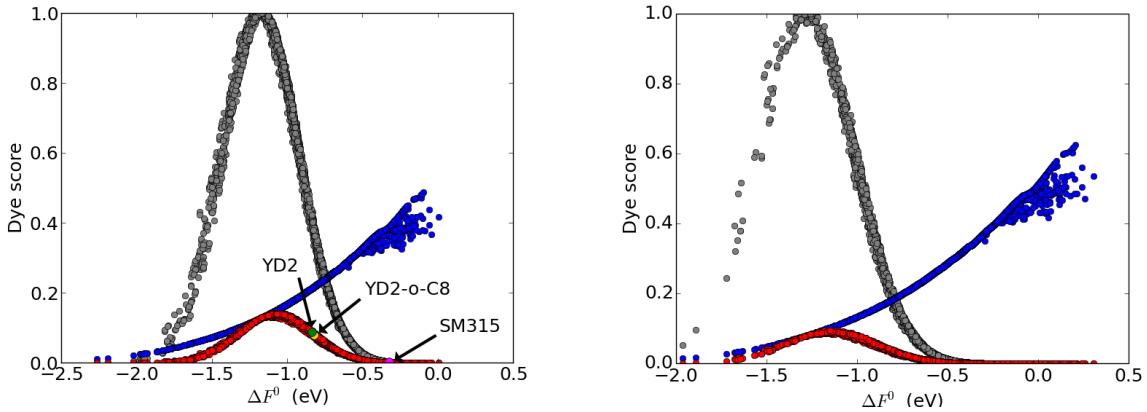

Figure 5.12: Level alignment quality, η, (blue), regeneration correction, $C(\Delta F^0, \lambda)$, (gray) and weighted level alignment quality, $\eta_{\text{reg}} = C(\Delta F^0, \lambda; T) \cdot \eta$, (red) for $[Co^{II/III}(bpy)_3]$ (left) and $[Co^{II/III}(bpy-pz)_2]$ (right) at 298.15 K. For $[Co^{II/III}(bpy)_3]$ the weighted level alignment qualities for the known high-efficiency dyes YD2 (green), YD2-o-C8[27] (gold) and SM315[35] (magenta) are indicated.

internal reorganization energies for $[Co^{II/III}(bpy)_3]$ and $[Co^{II/III}(bpy-pz)_2]$ are 0.4 eV and 0.5 eV, respectively, and are thus the major reason for the high λ values observed for the regeneration reactions. This large internal reorganization energy can be explained by the relatively large change in bond length upon changing oxidation state and is expected to be symptomatic for all octahedral transition metal complexes.

The redox potentials of the $[Co^{II/III}(bpy)_3]$ and $[Co^{II/III}(bpy-pz)_2]$ redox mediators are -5.06 eV[43] and -5.36 eV,[133] respectively. Hence, the driving force for the regeneration reaction using $[Co^{II/III}(bpy-pz)_2]$ is generally smaller compared to using $[Co^{II/III}(bpy)_3]$. This can be observed in Figure 5.11 as the largest barriers for $[Co^{II/III}(bpy-pz)_2]$ is obtained for dyes with only a small driving force while the source of large barriers for $[Co^{II/III}(bpy)_3]$ can be both too small and too large driving force, the latter corresponding to the Marcus inverted region ($-\Delta F^0 > \lambda$).

Using these barriers to calculate the correction factor, $C(\Delta F^0, \lambda)$ (Equation 5.6), and the weighted level alignment quality, $\eta_{\text{reg}} = C(\Delta F^0, \lambda; T) \cdot \eta$, gives the results shown in Figure 5.12. In the figure, the uncorrected level alignment, η, is also plotted and seen to increase with decreasing driving force. This is explained from, as mentioned in the previous section, the level alignment quality being a competition between open-circuit voltage and sunlight absorption. As the latter is

Table 5.4: Top ten candidates measured by the weighted level alignment quality using $[Co^{II/III}(bpy)_3]$ at 298.15K and using the alternative correction factor C'.

Backbone	A	R1	R2	R3	ΔF^0 (eV)	$\Delta F^\ddagger$ (eV)	η	$C'(\Delta F^0, \lambda; T)$	η_{reg}
TiO2R	DTBP	DTBP	MOTPA	EthynPhA	-0.67	0.05	0.26	1.00	0.26
TiO2R	TMP	TPA	TPA	EthynPhA	-0.67	0.05	0.26	1.00	0.26
TiO2R	TMP	DTA	TPA	EthynPhA	-0.67	0.05	0.26	1.00	0.26
TiO2R	TPA	TMP	TPA	2CyanoPropenA	-0.68	0.05	0.26	1.00	0.26
TiO2R	DTBP	MOTPA	TMP	2CyanoPropenA	-0.68	0.05	0.26	1.00	0.26
TiO	DTBP	MOTPA	TMP	2CyanoPropenA	-0.68	0.05	0.26	1.00	0.26
TiO2R	DTA	TMP	DTA	EthynPhA	-0.68	0.05	0.26	1.00	0.26
TiO2R	DTBP	MOTPA	TMP	2CarboxyPropenA	-0.68	0.05	0.26	1.00	0.26
TiO2R	DMP	DMP	MOTPA	2CyanoPropenA	-0.68	0.05	0.26	1.00	0.26
H2	TPA	TPA	TMP	2CarboxyPropenA	-0.68	0.05	0.26	1.00	0.26

generally increased by increasing the energy of the HOMO, a high level alignment quality is obtained when the HOMO energy, or rather the oxidation potential of the dye, is aligned with the redox potential of the redox mediator minimizing the driving force for the regeneration reaction. However, as a consequence of having a parabolic dependence of the free energy barrier on the driving force, the correction factor as a function of ΔF^0 will be a Gaussian centred around $\Delta F^0 = -\lambda$. Hence, only dyes with a driving force around 1.1 - 1.3 eV are predicted to have a high weighted level alignment quality in sharp contrast to the uncorrected level alignment quality. As the $[Co^{II/III}(bpy)_3]$ redox mediator has both a smaller λ and larger driving force of the regeneration reaction, we observe significantly higher weighted level alignment qualities using this redox mediator compared to using $[Co^{II/III}(bpy - pz)_2]$. Here, we note that the larger open-circuit voltage, obtainable using the latter redox mediator, has been taken into account in the level alignment quality and thus the V_{oc} is of less importance compared to ΔF^0 and λ. For illustrative purposes, the calculated weighted level alignment qualities of the known high efficiency dyes YD2, YD2-o-C8 [27] and SM315 [35] with the $[Co^{II/III}(bpy)_3]$ redox mediator have been indicated in the left part of Figure 5.12. The weighted level alignment quality of the first two dyes is seen to be relatively high, while the last dye, which in fact has the highest overall DSSC efficiency reported (13.0%), is predicted to have a very low η_{reg}.

One reason for the failure of our model to re-discover the record holding dye can be due to the very strict correction factor which puts a penalty on *any* electron transfer free energy barrier. In reality, the *regeneration* reaction competes with, among others, the *recombination* reaction in which the oxidized dye is reduced by an electron from the conduction band of the semi-conductor. Hence, a free energy barrier for the regeneration reaction is acceptable as long as the resulting rate for the regeneration reaction is still higher than the rate of the recombination reaction. Feldt *et al.* [147] has investigated the regeneration of the organic D35 dye with different cobalt redox mediators and found that a system with $\lambda = 0.8$ eV and $\Delta F^0 = -0.39$ eV for the regeneration reaction still had the regeneration reaction dominating over the recombination reaction. Using Equation 3.16, the free energy barrier of this system is $\Delta F^\ddagger = 0.05$ eV. Extrapolating this to our systems, we can then define a modified correction factor, C', that allows for free energy barriers of this magnitude

$$C' = \begin{cases} 1 & \text{for } \Delta F^\ddagger \leq 0.05\,\text{eV} \\ \exp\left(\frac{-\Delta F^\ddagger(\Delta F^0,\lambda)+0.05\,\text{eV}}{k_B T}\right) & \text{for } \Delta F^\ddagger > 0.05\,\text{eV} \end{cases} \tag{5.15}$$

where we still enforce that $C' = 0$ if $\Delta F^0 > 0$. Using this definition for the $[Co^{II/III}(bpy)_3]$ redox mediator gives the correction factors and weighted level alignment qualities shown in Figure 5.13. Here, the modified correction factor results in a wider driving force window for obtaining high weighted level alignment quality values and the YD2 and YD2-o-C8 dyes are now located near the very top. On the other hand, the record holding SM315 dye is still predicted to have a too low regeneration driving force. Here, it is important to note that in addition to the uncertainty in the DFT calculated driving force, the choice of allowing for free energy barriers smaller than 0.05 eV is a choice based on only one experimental example. A slight increase of this threshold would widen the preferred driving force window and could easily lead to the inclusion of the SM315 dye.

Table 5.4 gives the structure of the top ten dyes scored by the weighted level alignment with the modified correction factor. The table is dominated by dyes with free energy barriers of exactly

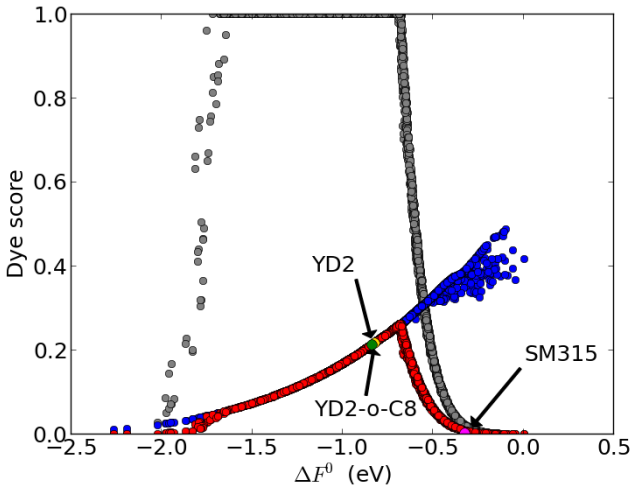

Figure 5.13: Level alignment quality, η, (blue), regeneration correction, $C'(\Delta F^0, \lambda)$, (gray) and weighted level alignment quality, $\eta_{\text{reg}} = C'(\Delta F^0, \lambda; T) \cdot \eta$, (red) for $[\text{Co}^{\text{II/III}}(\text{bpy})_3]$ at 298.15 K using the alternative correction factor C'. The weighted level alignment qualities for the known high-efficiency dyes YD2 (green), YD2-o-C8 [27] (gold) and SM315 [35] (magenta) are indicated.

0.05 eV, again illustrating the sensitivity of the presented model. However, compared to the top ten dyes scored by the uncorrected level alignment quality (Table 5.2), the present top candidates are characterized by more moderately donating side groups and the moderately accepting EthynPhA anchor group. Furthermore, almost all dyes in the top ten list are based on the TiO_2R backbone. Hence, we believe that our results should encourage exploring titanium based alternatives in the ongoing pursuit for porphyrin based dyes with high DSSC efficiencies. Furthermore, non-octahedral redox mediators should also be investigated in an attempt to avoid the large internal reorganization energy found for the cobalt complexes.

5.3 Constructing new molecular architectures

In the previous sections we have focused on optimizing the level alignment of a single dye. However, this approach is limited by how efficient a single dye can absorb the full solar spectrum without seriously limiting the open-circuit voltage. A possible solution to this problem is to incorporate a second dye into the cell to construct a so-called tandem cell. Conventional tandem solar cells (organic as well as inorganic) combine two or more types of materials that are separated by interfaces where electrons and holes are exchanged. These interfaces are highly critical and inevitably contain defects and other imperfections which act as scattering- and recombination centres for the charge carriers. The problem of controlling the atomic structure of the interface can however be circumvented by using molecular complexes where molecules are combined with atomic precision by synthetic chemistry. In this type of cells, the two dyes are chosen such that one absorbs the blue part of the solar spectrum and the second absorbs the red part. Here, it is however important to note that the higher open-circuit voltage comes at the expense of lower current, since two photons are required to generate one electron in the electric circuit. On the other hand, as lower currents are associated with smaller losses and higher fill-factors, as observed in experiments under low light intensity, [22;27] trading a high current for a high voltage could boost the efficiency of the cell.

Earlier attempts to improve the light absorption in DSSCs include the intermediate band solar cell design [149;150] and especially the molecular version of this, [151] attempts to use supramolecular porphyrin structures to enhance the efficiency, [152–154] as well as combining the conventional n-type DSSC with a p-type DSSC [155] to construct a tandem pn-DSSC. [156] However, despite high theoretical obtainable efficiencies, [157] pn-type tandem DSSCs have not been able to surpass the efficiency of single DSSCs so far. [158;159] Inspired by the above mentioned earlier attempts, we propose three

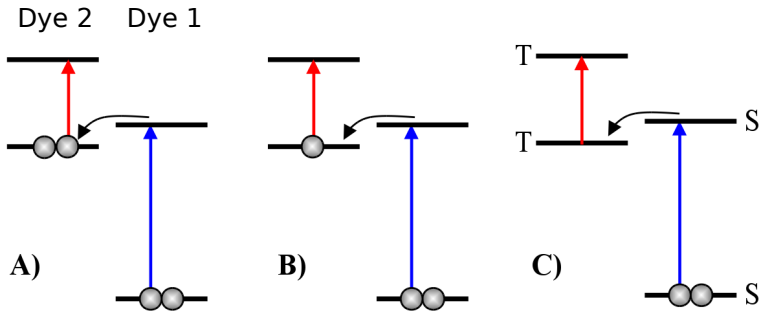

Figure 5.14: Various proposed energy level schemes for solar cells based on two dye molecules connected by a molecular linker. The occupancy is given for the ground state. **A)** Simplest concept with both HOMOs doubly occupied. Both dye molecules need to be excited at the same time to generate a hole in the upper HOMO that can take up an electron from the lower LUMO. **B)** The upper HOMO is partially occupied to allow facile charge transfer between the two dye molecules. Such a situation can be realized in metal-organic dye molecules with an odd number of electrons. This is the analogue of an intermediate band solar cell.[149–151] **C)** Using singlet (S) and triplet (T) excitations. The long lifetime of the triplet allows a significant electron population to accumulate in the lower triplet level, which can be excited into the upper triplet level. This scheme could also be realized with a single dye molecule.

Table 5.5: Calculated singlet excitation energies and level alignment of the individual dyes used in the tandem scheme

Species	E_{HOMO} (eV)	$E_{\mathrm{HOMO}}+E_1$ (eV)	E_1 (eV)
Dye 1	-5.9	-4.7	1.2
Dye 2	-5.3	-4.1	1.2

different molecular two-photon schemes shown in Figure 5.14 and in order to find possible candidates for the different schemes, we again turn to our 5145 porphyrin dyes and the calculated frontier orbital energies.

Starting with Scheme **A** in Figure 5.14, denoted the tandem scheme, we search for two dyes with the following characteristics: One dye with a low lying HOMO (dye 1) and a second dye with the LUMO aligned with the conduction band of TiO_2 (dye 2). To optimize the efficiency of a tandem cell it has been proposed to have one species with an optical gap of 1.0 eV and another with 1.9 eV.[160] However, while this is true for semi-conductors which absorb most photons above the band gap, for dyes with limited absorption it may be better to use two dyes with optical gaps of 1.1 eV in agreement with the Shockley-Quessier limit.[129] A search through our data for dyes with these characteristics is illustrated in the left part of Figure 5.15 where E_{HOMO} and $E_{\mathrm{HOMO}} + E_1$ for all 5145 porphyrins are plotted against the lowest optical excitation energy, E_1. The light blue and light red points indicate dyes where $E_{\mathrm{HOMO}} + E_1$ lies at a lower energy than the maximum value of E_{HOMO} making it a potential candidate for dye 1 in the tandem scheme and the gray shaded area indicates the region of interest around $E_1 = 1.1$ eV. Several candidates are identified, but taking into account that the molecule should be possible to synthesize, the best candidate is the molecule shown in the right part of Figure 5.15.

The calculated singlet excitation energies and level alignment of the individual dyes used in the tandem scheme are given in Table 5.5. Here, the singlet excitation energies are calculated using the all-electron Amsterdam Density Functional (ADF) code with a double-ζ Slater-type basis set with polarization functions.[161] The linker between the two dyes are chosen to minimize hybridization between the orbitals on the two dyes allowing for a mechanism for the tandem scheme as shown in Figure 5.16. Here, the working principle is described in six simple steps: **I→II:** A photon excites an electron from the HOMO of dye 2 to an excited level. **II→III:** The excited electron on dye 2 is rapidly injected into the conduction band of the semi-conductor. **III→IV:** A second photon excites

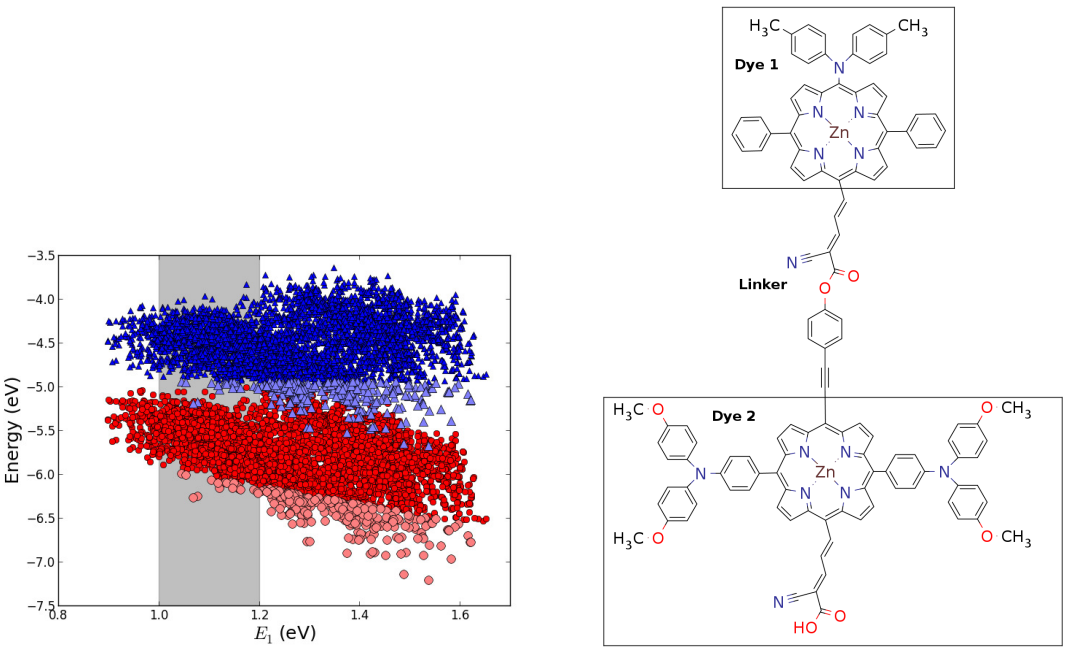

Figure 5.15: **Left:** E_{HOMO} (red circles) and $E_{\mathrm{HOMO}} + E_1$ (blue triangles) for all 5000+ porphyrins in our database[7;34] plotted against the lowest optical excitation energy, E_1. The light blue and light red points indicate dyes where $E_{\mathrm{HOMO}} + E_1$ lies at a lower energy than the maximum value of E_{HOMO} making it a potential candidate for dye 1 in the tandem scheme and the gray shaded area indicates the region of interest around $E_1 = 1.1$ eV. **Right:** Chemical structure of the dyad used in the molecular tandem schemes.

an electron from the HOMO of dye 1 to the LUMO of dye 1. **IV→V:** The excited electron on dye 1 tunnels to fill the hole on the HOMO of dye 2. **V→VI:** An electron from the redox-mediator regenerates the dye by filling the hole on the HOMO of dye 1. **VI→I:** The electron in the conduction band of the semi-conductor is used for performing electric work after which it is transferred back to the electrolyte via the counter electrode as in standard DSSCs. This proposed mechanism effectively transfers an electron from the backbone of dye 1 to the anchor group of dye 2 and hence achieves excellent charge separation with the electron overlapping with the conduction band of the semi-conductor and the hole located close to the electrolyte.

Using the values from Table 5.5, assuming that the electronic excitations are faster than the structural relaxation of the individual dyes and taking TiO_2 as the semi-conductor with the conduction band located at -4.1 eV in combination with an electrolyte with a redox potential aligned 0.3 eV above the HOMO of dye 1, we can construct the detailed energetics indicated in Figure 5.16. From these, we observe that the mechanism, apart from the two photo-excitations, is downhill with a theoretical open-circuit voltage of 1.5 V which is a significant improvement compared to current DSSC devices. In practice, we are however limited by the low lying $[\mathrm{Co}^{\mathrm{II/III}}(\mathrm{bpy}-\mathrm{pz})_2]$ redox pair which only has a redox potential of -5.36 eV *vs.* vacuum[133] resulting in a theoretical open-circuit voltage of 1.26 V (using $V_{oc} = E_c - E_{\mathrm{red}}$). Thus, it is crucial to use an electrolyte with a lower redox potential which could be achieved by modifying the ligands of the popular cobalt-based redox couple as shown by Feldt *et al.*[147] or by designing completely new redox mediators.

A limiting factor for the tandem scheme is the two absorption steps (I→II and III→IV) and especially the intramolecular electron transfer in step IV→V. However, calculations on the full tandem dyad reveals large oscillator strength for the local excitations on both parts of the dyad and a similar sized oscillator strength associated with the charge transfer from dye 2 to dye 1 in the dyad.[162] Thus, the charge transfer is possible at least in terms of energetics but the full kinetics have yet to be evaluated.[144;163]

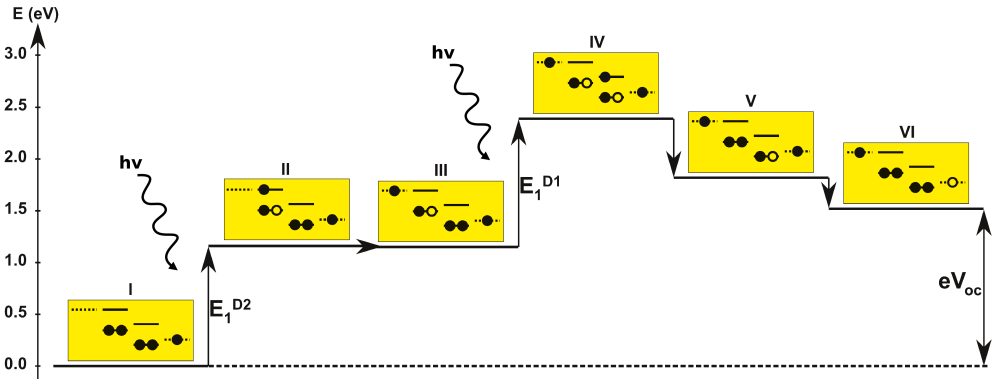

Figure 5.16: One-particle state based sketch of the steps involved in the molecular tandem device proposed here. For each state the energetics are indicated by the y-axis while the one-particle mechanism associated with the step is shown in the corresponding yellow box. Here, the filled circles represent electrons and the empty circles represent holes. From right to left in each box the dotted state is the redox mediator, the first set of solid lines represents the ground state and excited state of dye 1, the second set of solid lines represents the ground and excited state of dye 2 and the last dotted line represents the conduction band of the semi-conductor.

Table 5.6: Calculated singlet and triplet orbital energies for the dye used in the single dye intermediate triplet state scheme

State	$E_{\text{state}}^{\text{singlet}}$ (eV)	$E_{\text{state}}^{\text{triplet}}$ (eV)
HOMO	-6.2	-
LUMO	-4.9	-5.0
LUMO+2	-	-4.1

Scheme **B** in Figure 5.14 is the so-called intermediate band scheme which addresses the possible problems of step IV→V in the tandem scheme. Despite the high predicted oscillator strength for this step, the time-scale on which the excited electron on dye 1 tunnels to the hole on dye 2 is still unknown. Thus, this could constitute a bottleneck since there are very few photoexcited electrons in the LUMO of dye 1, which have to find one of the very few photo-generated holes which are in the HOMO of dye 2 at the same place and the same time. In the intermediate band scheme this is proposed to be overcome by having the HOMO of dye 2 half-filled in the ground state as this would leave the excited electron on dye 1 with a better change of finding a hole on dye 2. A possibility for realizing this scheme could be to use a porphyrin with a transition metal center with an uneven number of electrons such as Fe^{3+} (d^5-system) where the presence of an unpaired electron in an orbital similar to the HOMO of the iron(II) porphyrin has previously been found computationally. [164;165]

The last scheme (Scheme **C**) in Figure 5.14 is the intermediate triplet state scheme. This scheme can be realized using a single dye which has a low lying HOMO, a LUMO located inside the gap of the used semi-conductor and a higher excited state aligned with the semi-conductor conduction band edge. In this way, the first photon should excite an electron from the HOMO to the LUMO followed by a second photon further exciting the electron to the higher excited state. The bottleneck here is the lifetime of the first excited state, which has to exist long enough for a second photon to further excite the molecule. To overcome this, we can exploit inter-system-crossing (ISC) to prepare the first excited state in a triplet state with a long lifetime. This mechanism is depicted in Figure 5.17 where the six steps are: **I→II:** A photon excites an electron from the HOMO of the dye to the first excited singlet state. **II→III:** The excited electron undergoes ISC to the first excited triplet state. **III→IV:** A second photon excites the electron from the first excited triplet state to a higher excited triplet state. **IV→V:** The excited electron is injected into the conduction band of the semi-conductor. **V→VI:** An electron from the redox-mediator regenerates the dye by filling the hole on the HOMO of the dye. **VI→I:** The electron in the conduction band of the semi-conductor is used for performing electric work after which it is transferred back to the electrolyte via the counter electrode as in standard DSSCs.

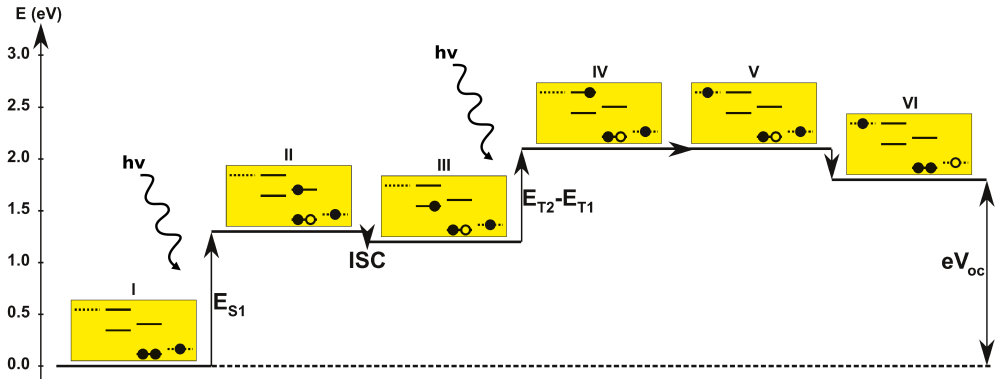

Figure 5.17: One-particle state based sketch of the steps involved in the single dye intermediate triplet state scheme. For each state the energetics are indicated by the y-axis while the one-particle mechanism associated with the step is shown in the corresponding yellow box. Here, the filled circles represent electrons, the empty circles represent holes. From right to left in each box the dotted state is the redox mediator, the first set of solid lines represents the singlet ground state and the first singlet excited state of the dye, the second set of solid lines represents the first and second triplet excited state of the dye and the last dotted line represents the conduction band of the semi-conductor. The step involving inter-system-crossing is marked by ISC.

Searching through the 5145 investigated porphyrin dyes yields a candidate with suitable energy levels as shown in Table 5.6. Here, the LUMO is located in the band gap of TiO_2 and the triplet is located at a slightly lower energy than the singlet state making it energetically favourable to perform ISC. Furthermore, the triplet LUMO+2 is well aligned with the conduction band of TiO_2 making this level perfect as the second excited state used in this scheme. Using the energy levels presented in Table 5.6 results in the energetics shown in Figure 5.17. Here, a theoretical open-circuit voltage of up to 1.8 V for this scheme is obtained even exceeding the obtainable V_{oc} for the tandem scheme. However, a crucial component for this approach to be realistic is having a dye with a high ISC. Since the fluorescence lifetime of a zinc porphyrin molecule has been reported to be greater than 1.0 ns, this indicates that there will be almost no ISC for dyes using the ZnP backbone.[166] Hence, we may need to exchange the Zn metal center with a heavier metal to obtain a higher ISC yield. Here, especially porphyrins with a Pd metal center have previously been shown to undergo efficient ISC with a quantum yield close to unity.[167]

The structure of the proposed dye and visualizations of the frontier orbitals using both a Zn and a Pd metal center are given in Figure 5.18. Here, it is observed that the orbitals are nearly identical for the two metal centres and that the orbitals are very well suited for this type of scheme as the HOMO is located mostly on the backbone and side group whereas the LUMO is located more on the anchor group. As a consequence of this, the first excitation obtains a great charge separation possibly limiting the recombination of hole and electron. Furthermore, due to the large overlap of the second excited state (LUMO+2) of both porphyrins with the LUMO, a high oscillator strength for the second transition is expected. Finally, the localization of the LUMO+2 on the anchor group should result in a very fast injection of the excited electron into the conduction band. As for the tandem scheme, the redox potentials of the commonly used redox mediators are located at too high energies for this scheme to be efficient and thus new redox mediators are needed for optimizing this scheme.

The above schemes and proposed candidates illustrates how data obtained from high-throughput screenings can be used in a creative way going beyond the original project. Still experimental verification, guided by the computational data, of any of the proposed schemes is essential, underlining the desirable symbiosis between experimental and computational chemistry.

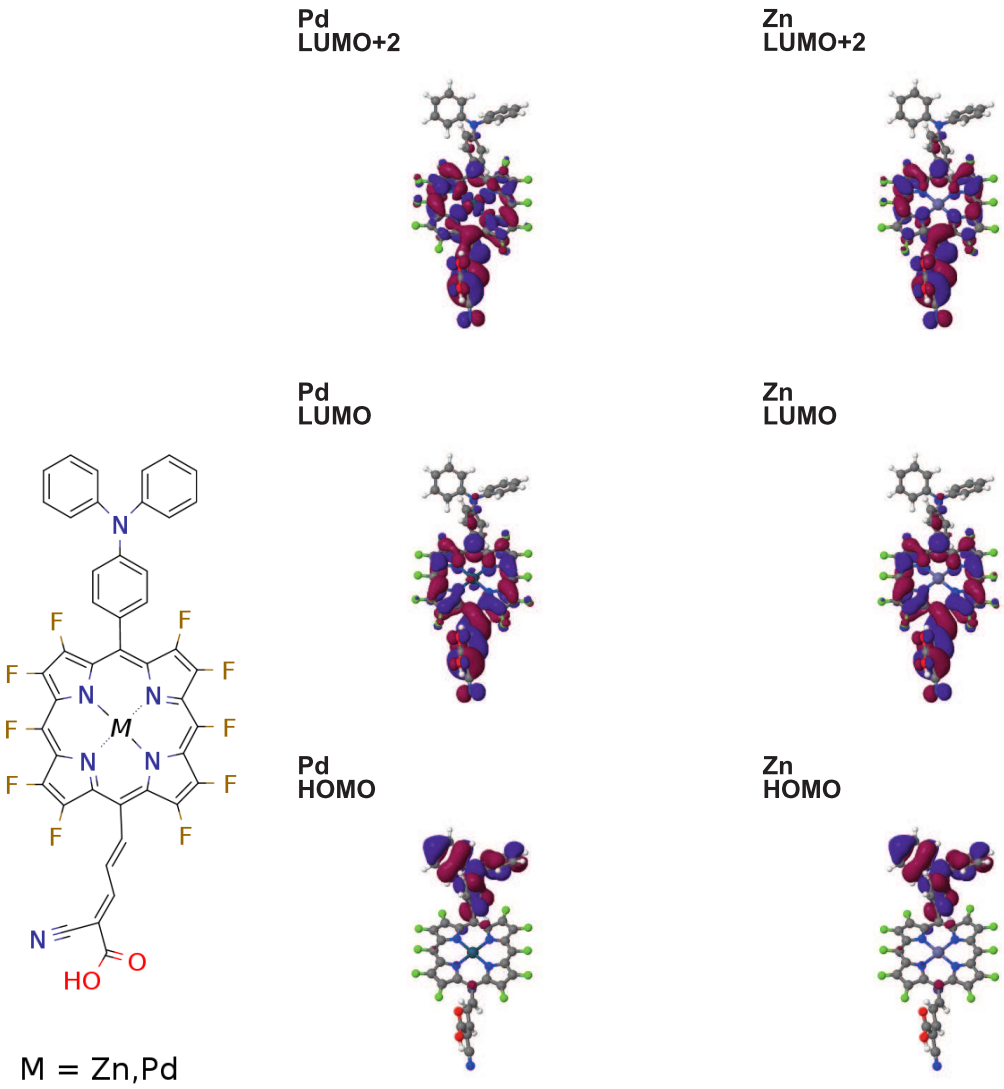

Figure 5.18: **Left:** Scheme of the proposed dye for the single dye intermediate triplet state scheme. **Right:** Visualization of the proposed active orbitals for the Pd version and the Zn version of the dye used in the single dye intermediate triplet state setup.

Chapter 6

Single molecule electronics

Another fascinating aspect of the discrete energy levels present in molecules is the possibility to manipulate the properties of molecular junctions. As an example of this, the current through a molecular junction can be controlled by simply shifting up or down the molecular levels relative to the Fermi levels of the leads using *e.g.* a gate electrode. In this way the molecular junction is effectively transformed into a molecular transistor. However, in order to use this type of molecular transistor in practice, it is necessary to obtain a very high gate controlled current on/off ratio. Unfortunately, simply tuning the molecular energy levels in and out of resonance with the Fermi level of the leads may not always give a sufficiently low off state current due to electron tunnelling. Hence, additional chemical or physical mechanisms are usually needed to obtain the desired current on/off ratio.

In the following, two different approaches towards controlling the current and achieving a large current on/off ratio are investigated. In Section 6.1 the results from Paper V are presented outlining a way to use electrochemistry to turn quantum interference (QI) on and off while Section 6.2 focuses on the results from Paper VI in which the current is controlled by chemical controlled anchoring of the molecule to the leads. Please note that in the following sections the word *transmission* is used for the computationally calculated transmission function, $T(\varepsilon)$, which at low temperature and bias relates to the experimentally measured *conductance*, G, through the relation [112]

$$G = G_0 T(\varepsilon_F) \tag{6.1}$$

where $G_0 = \frac{2e^2}{h}$ is a constant, allowing for a direct comparison between experimental and computational values.

6.1 Electrochemically controlled transmission

Using the concept of Quantum Interference (QI) described in Section 4.4 provides a way to obtain a very low conductance and hence an effective off state in a molecular transistor. Having to physically exchange the molecule in the junction in order to turn the current on is however quite impractical and it is thus desirable to have *in situ* ways of switching the QI phenomena on/off. A possible approach to this is to use anthraquinone based molecules, where several conformers are predicted to exhibit QI. [118;168] Additionally, reducing the oxo groups in these anthraquinones breaks the cross conjugation* from which the QI origins. Hence, the conductance through these molecules may be controlled electrochemically.

In the following, this possible electrochemical control of the conductance is investigated by synthesizing two different anthraquinone molecules and inserting them into molecular junctions. The electron transport through these junctions is then investigated using both experimental and computational methods. Illustrations of the oxidized and reduced versions of the two molecules are given in the left part of Figure 6.1.

The right part of Figure 6.1 illustrates the electron transport path through the central part

*Cross conjugation is when, in a set of three π-bonds, only two interact with each other through conjugation. This is *e.g.* the situation at the carbon atoms with the oxo groups in the oxidized anthraquinone backbone.

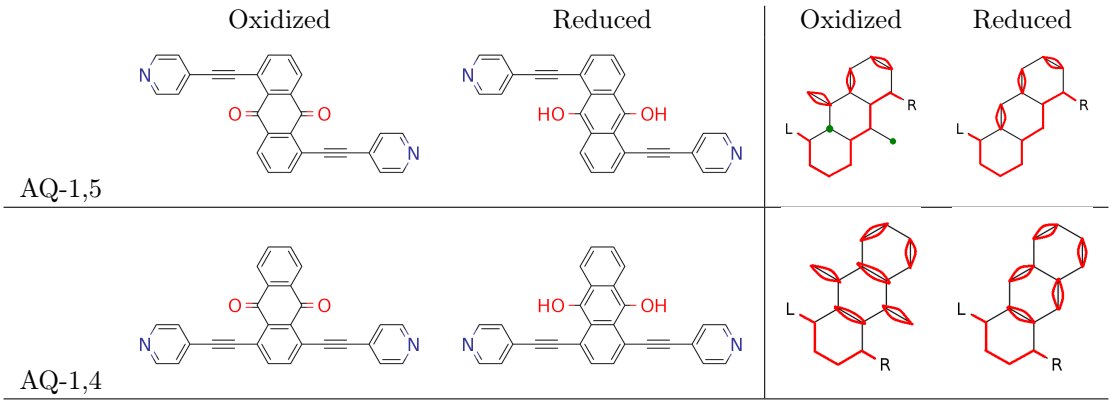

Figure 6.1: **Left:** Oxidized and reduced versions of the AQ-1,5 (top) and AQ-1,4 (bottom) molecules used in the molecular junctions. **Right:** Illustration of the electron transport paths through the central part of the molecules. The graphical rules for Quantum interference (QI) discussed in Section 4.4 are indicated, showing that QI is only expected for the oxidized form of AQ-1,5.

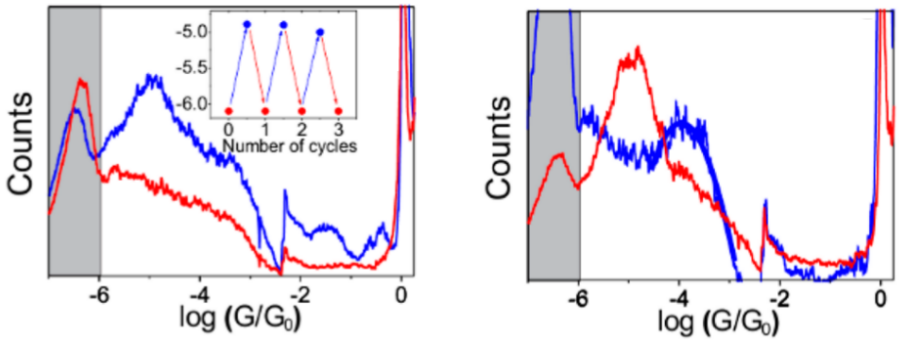

Figure 6.2: 1D conductance histograms generated from 1100 individual curves without any data selection for **left:** oxidized (red) and reduced (blue) AQ-1,5 and **right:** oxidized (red) and reduced (blue) AQ-1,4. The gray areas indicate the noise levels and the inset in the left panel illustrates the reversible switching between oxidized and reduced AQ-1,5 and the measured most probable conductance.

of the molecules with focus on the graphical rules outlined in Section 4.4 and Figure 4.3.[118] Using these rules, it is only the oxidized version of AQ-1,5 that should exhibit QI and the conductance through this molecule should thus be significant lower than the conductance through both the reduced form of AQ-1,5 and both forms of AQ-1,4. The measured conductance histograms from break junction experiments[169] with both the reduced and oxidized forms of AQ-1,4 and AQ-1,5 are given in Figure 6.2. Here, it is observed that the conductance for the oxidized form of AQ-1,5 is indeed significantly lower than the conductance of the other investigated molecules. In fact, the conductance is so low that the noise level made it very challenging to measure. The measured on/off ratio for the AQ-1,5 is around 1.5 orders of magnitude which is a bit lower than desired. However, as shown in the inset of the left part of Figure 6.2 the on/off switch is reversible upon continuous switching the redox state by changing the gate voltage.

To further investigate the experimentally measured conductance shift of the two molecules upon changing redox state, the transmission through the molecular junctions were calculated using the formalism outlined in Chapter 4. Here, all the calculations were performed using Density Functional Theory (DFT)[85] with the PBE[86] exchange-correlation functional and a basis set of numerical atomic orbitals[89] (LCAO mode) with a double-ζ polarized basis set as implemented in the GPAW code.[88] The gold electrodes are modelled by 4x6 gold slabs in the (111) direction and the molecular structures are relaxed until the residual forces are below 0.01 eV/Å. To overcome the problems in DFT to describe molecular energy levels (see Section 2.6) we have used the DFT+Σ

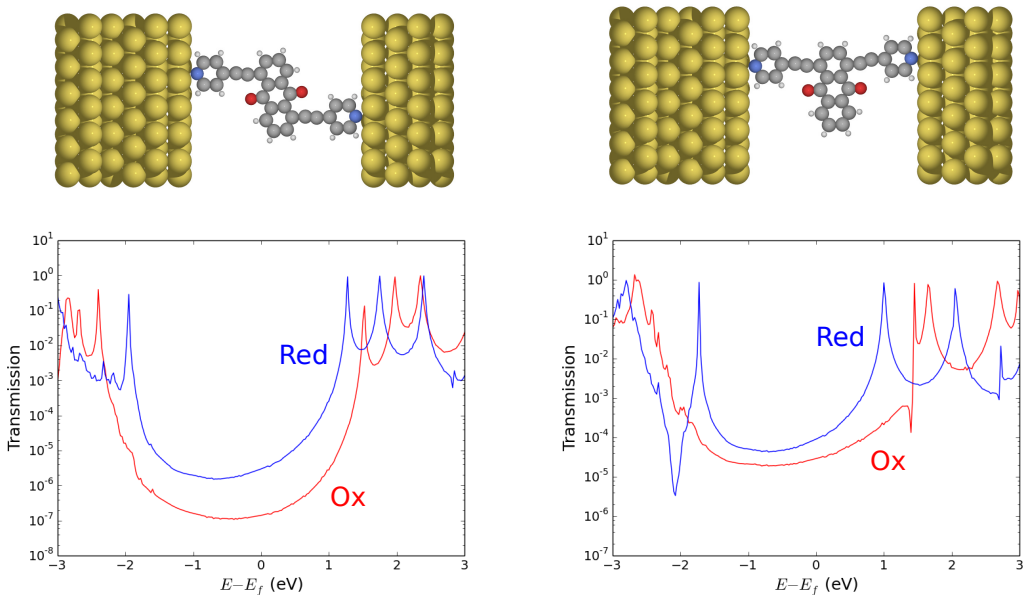

Figure 6.3: Calculated transmission function for the two redox states of AQ-1,5 (left) and AQ-1,4 (right) including illustrations of the supercells used for the transport calculations. The energy scale is relative to the Au Fermi level.

scheme described in Section 4.3 to correct the Kohn-Sham eigenvalues. An illustration of the junctions and the calculated transmission functions are shown in Figure 6.3. Taking the transmission at the Fermi level of gold, the experimental conductance ratio between the redox states of both AQ-1,4 and AQ-1,5 are seen to be reproduced nicely by the calculations.

As the main point of the study is to investigate the conductance through the junctions as a function of the gate potential (and subsequent electrochemistry), it is however advantageous to convert the energy scale of the calculated transmission function to a potential scale allowing for direct comparison between theory and experiments. To convert the energy scale to a potential scale relative to the saturated calomel electrode (SCE), we use that $E_{\mathrm{SCE}} = 4.68\,\mathrm{V}$ *vs.* vacuum [170] and the work function of gold $\Phi(\mathrm{Au}) = 5.25$ eV. Thus the Fermi level is located at $E_{\mathrm{fermi}} = -5.25$ eV and, since having a more positive potential corresponds to having a more negative energy, this corresponds to $E_{\mathrm{fermi}} = 0.57\,\mathrm{V}$ *vs.* SCE. Converting the scale gives the calculated transmission function shown in the bottom two panels in Figure 6.4. The two panels in the top part of the figure show the measured conductance at different potentials around the redox potential indicated by a vertical line. A sharp shift in conductance for both molecules is here observed when crossing the redox potential hence switching the redox state. In this way a small change in gate potential of around 0.1 V is sufficient to switch the conductance on or off which is very promising in terms of a molecular transistor. However, the on/off ratio is still only of around 1.5 orders of magnitude which should be increased for having an effective transistor. Comparing the experimental conductance with the calculated results, a striking qualitative similarity is observed. Especially, the rise in conductance for the reduced state of AQ-1,4 upon lowering the potential towards the redox potential is well reproduced. This indicates that the location of the LUMO in the calculation is in very good agreement with the experiments, validating the DFT+Σ method for this system. Since the computational cost of this method is relatively low, the qualitative agreement between experiments and computations encourage the use of computational methods to assist in the search for redox active molecules to be used in this type of electrochemically controlled molecular transistors.

An important point is however still that the computations of the reduced state of AQ-1,4 at -0.4 V *vs.* SCE predicts the crossing of the LUMO with resonant transmission close to unity. While the experimental curve also shows a sharp increase in conductance at the same potential, the conductance stays below $10^{-3}G_0$. In this case, the lower conductance seen in the experiments could be due to a break down of the phase-coherent transmission assumed in the calculations. Close to

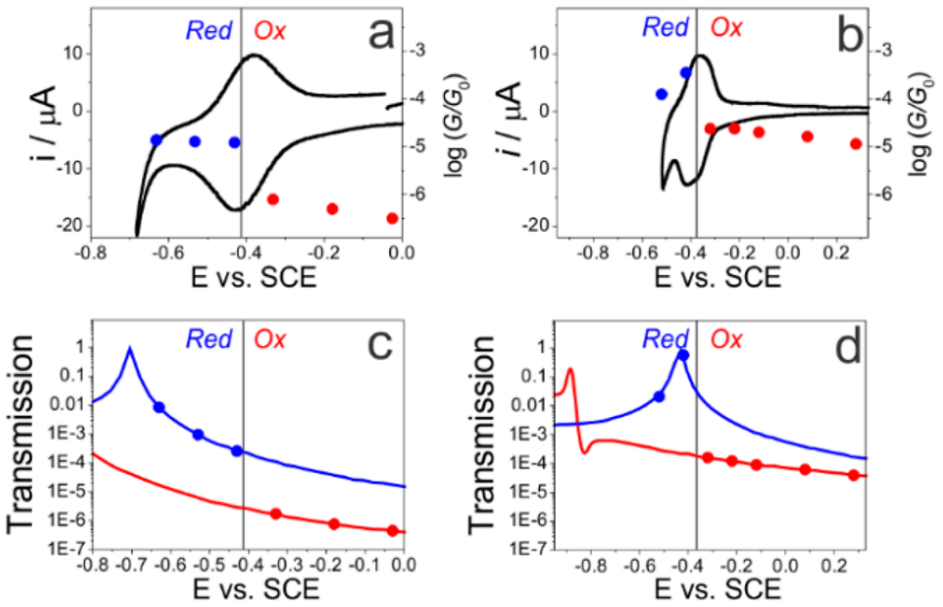

Figure 6.4: Experimental (top) and calculated (bottom) molecular conductance as a function of the applied gating potential *vs.* SCE for AQ-1,5 (a, c) and AQ-1,4 (b, d). The vertical gray line indicates the measured redox potential for the two molecules. The reduced state is favoured at potentials lower than the redox potential and the oxidized state is favoured at potentials higher than the redox potential. The transmission curves shown in the bottom two panels are the same as in Figure 6.3, but are here plotted on the electrochemical potential scale relative to SCE. The black curves in the upper two panels are experimentally obtained cyclic voltammograms spiking at potentials where the redox state switches.

the resonance, the electron spends longer time on the molecule and this enhances the probability of interacting with other molecular degrees of freedom, hence reducing the conductance.

The low on/off ratio for AQ-1,5 may be due to the reduced state only having a weak QI character. This is indicated by the observed very smooth and flat decrease in the transmission around the Fermi level (see Figure 6.3) where strong QI is usually rather characterized by a much more steep decrease.[118] As the graphical model used to predict QI is based on a very simple Hückel model, it should be expected to break down for molecules where the transport can not be described solemnly by the conjugated p_z orbitals. However, using the graphical model is still a very good first approach to finding new molecules with QI. This can then be combined with a simple DFT calculation of the transmission to decide whether the molecule should be synthesized and tested experimentally.

In connection with this, it may be noted that other anthraquinone based molecules with a sharper QI feature have been identified and synthesized. Final experimental studies of the conductance including the reversibility of the electrochemical switching for these molecules are pending.

6.2 Switching the transmission through anchor group selectivity

Another way to control the conductance through a molecular junction is to manipulate the geometry of the junction. This can *e.g.* be achieved through designing a molecule with two sets of anchor groups and then chemically controlling which anchor groups are used for binding to the leads. This concept is illustrated in Figure 6.5. Here, the molecule is initially prepared with both a set of pyridyl anchor groups and a set of acetylide anchor groups. Pacifying the latter set of anchor groups with triisopropylsilyl (TIPS) leaves only the pyridyl anchor groups available for binding to the gold electrodes which gives rise to the M1-N junction. Removing the TIPS groups by

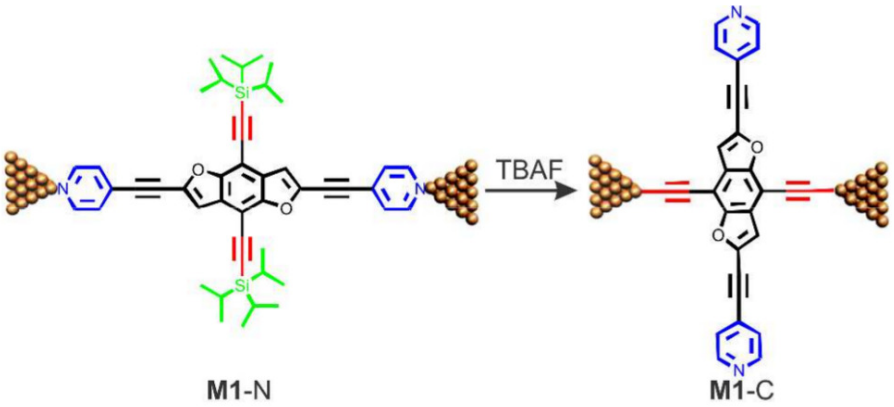

Figure 6.5: The two junction configurations investigated in this study. *In situ* addition of tetrabutylammonium fluoride (TBAF) removes the triisopropylsilyl (TIPS) protection group (green) exposing the acetylide groups (red). Due to a higher binding energy of the acetylide group compared to the pyridyl group (blue), this leads to a shift from the formation of M1-N junctions towards the formation of M1-C junctions.

in situ addition of tetrabutylammonium fluoride (TBAF) exposes the acetylide anchor groups allowing these to bind to gold. As the binding strength of the pyridyl and acetylide groups on the Au electrodes are calculated to be 0.6 eV and 3.2 eV, respectively, the removal of the TIPS protection group should lead to a shift from the formation of M1-N junctions towards the formation of M1-C junctions. In order to confirm this, the molecular junctions formed before and after addition of TBAF have been investigated experimentally and computationally. Here, the computational methodology used is similar to the one used in the previous section with the exception of the above mentioned binding energies which have been calculated using a real space grid basis.

To verify the change from M1-N junctions to M1-C junctions, the Au tip to Au tip distance, z, has been measured giving $z = 2.2$ nm before adding TBAF and $z = 1.2$ nm after. In comparison, the calculated z values for the M1-N and M1-C junctions are 2.4 nm and 1.2 nm respectively. This clearly indicates that the M1-N junctions are only formed before adding TBAF after which the M1-C junctions dominate.

Having a way to control the junction geometries, the subsequent change in conductance is investigated using break junction experiments.[169] The results from these experiments are summarized in the left part of Figure 6.6 giving the 1D conductance histograms for M1-N junctions and M1-C junctions. Here, a significant increase of around an order of magnitude in the conductance is observed upon going from the M1-N to the M1-C junctions. This shift in conductance is in good agreement with the calculated transmission for the two model systems given in the right part of Figure 6.6.

The significant change in conductance illustrates that this chemically controlled junction geometry is a viable alternative to *e.g.* electrochemical controlled conductance for switching the conductance through a molecular junction on or off. However, the relatively small on/off ratio of only a single order of magnitude should be increased for real life applications. Here, it is also important to note that the geometry change has not yet been obtained reversible. Hence, it is so far only possible to go from M1-N junctions to M1-C junctions and not back again. The search for more similar molecules with a larger on/off ratio is however ongoing.[171]

The above presented study again underlines the symbiosis between experiments and computational analysis as the computed binding energies and z values essentially confirmed the proposed mechanism for changing the junction geometry. Hence, by exploiting the strengths of both experiments and computations it is possible to intensify the search for future molecular-sized electronic components.

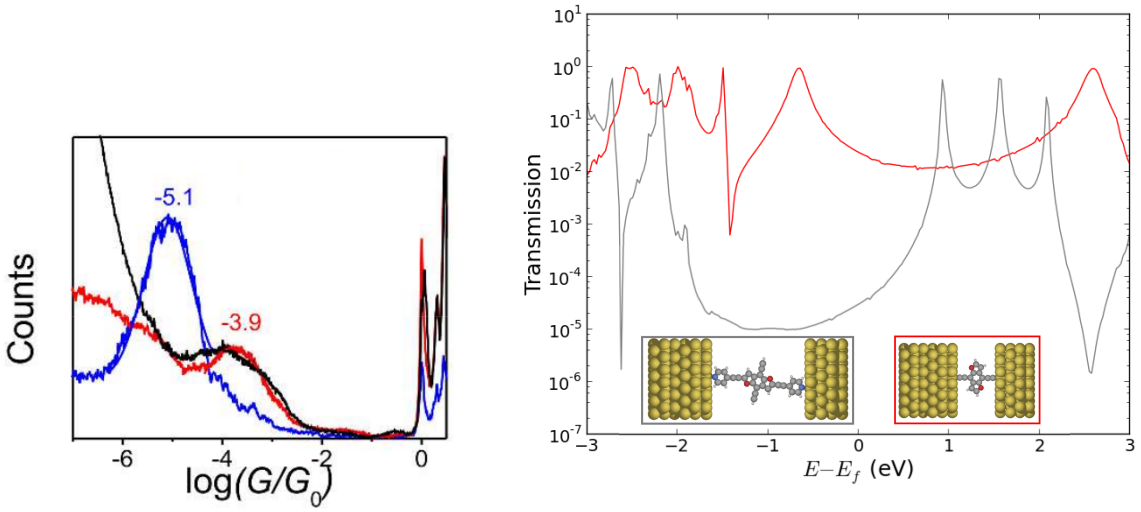

Figure 6.6: **Left:** 1D conductance histograms for M1-N junctions (blue) and M1-C junctions (red). The black curve is the conductance of a reference junction not considered here. **Right:** Calculated transmission function for a M1-N type (gray) and M1-C type (red) junction including illustrations of the supercells used for the computations.

Chapter 7

Concluding remarks

The previous chapters have shown how, often simple, computational approaches can be used to search through a very large set of molecules and identify promising candidates for *e.g.* a dye sensitized solar cell (DSSC). Combining these approaches with more detailed calculations and experimental data furthermore increases the detail level of the knowledge gained. In the DSSC project this leads to a weighted level alignment quality rediscovering well-known high efficiency dyes and proposing more experimental studies of porphyrins with a titanium metal center, possibly in combination with new redox mediators with a low internal reorganization energy. Furthermore, we found that combining dyes into different tandem schemes may significantly improve the open-circuit voltage and possibly boost the DSSC efficiency. In the molecular junction project, we verified the experimental findings and constructed a simple model to predict the gate potential dependent transmission for a redox active anthraquinone based molecule. For a molecule with two sets of anchor groups it was furthermore possible to confirm the hypothesis that the different binding strength of the anchors determines the junction geometry and hence the transmission.

In general, there are two possible goals for a computational study, which can be aimed at either explaining an experimental observation or used as a tool for predicting certain properties of a molecule, not yet experimentally characterized. Both these objectives are important in research, but where the explanatory goal is inherently verifiable, the predictive power of a model is harder to asses. It is of course still possible to apply the model to known systems, compare with experimental data and then assume that the correlation holds for *e.g.* a similar class of molecules. The latter corresponds to the approach used in this thesis in connection with the screening of functionalized porphyrin dyes for DSSCs. As discussed in Chapter 5, the trends for the frontier orbitals of functionalized porphyrins are probably well captured by a simple Density Functional Theory based approach. However, there is still a long way to the prediction of an actual DSSC efficiency. On the other hand, we have come a step closer to this goal by first defining the level alignment quality and then correcting this for the regeneration reaction free energy barrier. Many physical aspects of an actual device are however still not included and, given that they can all be identified, some of these may be very computationally expensive and difficult to model accurately.

Forgetting all about the physical aspects of a device, it is in fact possible to turn the predictive problem upside down and use different machine learning based fitting schemes to extrapolate experimental data from actual devices. In this way, statistical routines decides on the often complex variables used in the fitting and the physical characteristics of a high performance device can then be extracted by analysing these variables. This approach can be combined with computationally obtainable data as illustrated in a study by Ip *et al.*[172] Here, they find a correlation between different computational parameters and the experimental efficiency of DSSCs. Their conclusion is that two of the most important variables in a DSSC are the oxidation potential and reorganization energy of the dyes, which is very encouraging with respect to the predictive power of our weighted level alignment quality. Hence, there should be a great perspective in improving on our model *e.g.* in terms of accuracy of the reorganization energies and optical spectra used. Returning to the machine learning approach, Ip *et al.* furthermore states that one of the most serious limitations of the fitting schemes is the absence of published data for poorly performing devices. This puts a bias on the statistical data, leaving only the question of how to improve on an already well performing DSSC answerable.

In conclusion, it is worth commenting on the future impact on society in general of the two projects included in this thesis. For the molecular junction project, the construction of a commercial molecular transistor is a great challenge that requires new and refined experimental ways of constructing the molecular junction. However, the great interest in increasing *e.g.* computer power, and the financial power behind this interest, should lead to realizable commercial devices. Hence, more research into efficient ways of tuning the conductance should be prioritized. Concerning DSSCs, the future is more unclear. Recently, the fierce pursuit for higher efficiency has shifted the focus from cells with molecular dyes towards cells with, often toxic, perovskites.[173] This is however not a certain death sentence for the conventional molecular DSSC, as the future for this device is not necessarily dependent on obtaining a record high efficiency. In fact, real-life modules only have an efficiency of 8.2%, but there is still much interest in incorporating DSSCs into *e.g.* windows, leading to a trade off in efficiency in exchange for transparency.[174] Furthermore, the DSSC has never been suitable for large scale electricity, but it is perfect for indoor use where it outperforms silicon based technologies.[10;175] Hence, the DSSC is a cheap solar harvesting technology which is perfect for *e.g.* solar driven battery chargers or cheap light sources for use in developing countries. In this light, the research into molecular dye based DSSCs should probably turn more towards lowering the cost and toxicity of the devices rather than increasing the obtainable efficiency.

Bibliography

[1] Ki-moon, B. Remarks for the event on "Clean Industrial Revolution" in Durban, South Africa. 2011; http://www.un.org/press/en/2011/sgsm13998.doc.htm, accessed 15/06-2015.

[2] Hagfeldt, A.; Boschloo, G.; Sun, L.; Kloo, L.; Pettersson, H. *Chem. Rev.* **2010**, *110*, 6595–6663.

[3] Service, R. F. *Science* **2005**, *309*, 548–551.

[4] Reddy, K. G.; Deepak, T. G.; Anjusree, G. S.; Thomas, S.; Vadukumpully, S.; Subramanian, K. R. V.; Nair, S. V.; Nair, A. S. *Phys. Chem. Chem. Phys.* **2014**, *16*, 6838–6858.

[5] McFarland, E. W. *Energy Environ. Sci.* **2014**, *7*, 846–854.

[6] Feldman, D.; Barbose, G.; Margolis, R.; James, T.; Weaver, S.; Darghouth, N.; Fu, R.; Davidson, C.; Booth, S.; Wiser, R. *Photovoltaic system pricing trends*; 2014; National Renewable Energy Laboratory, NREL/PR-6A20-62558.

[7] Ørnsø, K. B.; Garcia-Lastra, J. M.; Thygesen, K. S. *Phys. Chem. Chem. Phys.* **2013**, *15*, 19478–19486.

[8] O'Regan, B.; Grätzel, M. *Nature* **1991**, *353*, 737–740.

[9] Hardin, B. E.; Snaith, H. J.; McGehee, M. D. *Nat. Photon.* **2012**, *6*, 162–169.

[10] Jung, H. S.; Lee, J.-K. *J. Phys. Chem. Lett.* **2013**, *4*, 1682–1693.

[11] Ishihara, S.; Labuta, J.; Van Rossom, W.; Ishikawa, D.; Minami, K.; Hill, J. P.; Ariga, K. *Phys. Chem. Chem. Phys.* **2014**, *16*, 9713–9746.

[12] Auwarter, W.; Ecija, D.; Klappenberger, F.; Barth, J. V. *Nat. Chem.* **2015**, *7*, 105–120.

[13] Higashino, T.; Imahori, H. *Dalton Trans.* **2015**, *44*, 448–463.

[14] Urbani, M.; Grätzel, M.; Nazeeruddin, M. K.; Torres, T. *Chem. Rev.* **2014**, *114*, 12330–12396.

[15] Li, L.-L.; Diau, E. W.-G. *Chem. Soc. Rev.* **2013**, *42*, 291–304.

[16] Campbell, W. M.; Burrell, A. K.; Officer, D. L.; Jolley, K. W. *Coord. Chem. Rev.* **2004**, *248*, 1363–1379.

[17] Bessho, T.; Zakeeruddin, S. M.; Yeh, C.-Y.; Diau, E. W.-G.; Grätzel, M. *Angew. Chem. Int. Ed.* **2010**, *49*, 6646–6649.

[18] Moore, G. F.; Konezny, S. J.; Song, H.; Milot, R. L.; Blakemore, J. D.; Lee, M. L.; Batista, V. S.; Schmuttenmaer, C. A.; Crabtree, R. H.; Brudvig, G. W. *J. Phys. Chem. C* **2012**, *116*, 4892–4902.

[19] Liu, B.; Zhu, W.; Wang, Y.; Wu, W.; Li, X.; Chen, B.; Long, Y.-T.; Xie, Y. *J. Mater. Chem.* **2012**, *22*, 7434–7444.

[20] Rangan, S.; Coh, S.; Bartynski, R. A.; Chitre, K. P.; Galoppini, E.; Jaye, C.; Fischer, D. *J. Phys. Chem. C* **2012**, *116*, 23921–23930.

[21] Masi Reddy, N.; Pan, T.-Y.; Christu Rajan, Y.; Guo, B.-C.; Lan, C.-M.; Wei-Guang Diau, E.; Yeh, C.-Y. *Phys. Chem. Chem. Phys.* **2013**, *15*, 8409–8415.

[22] Luo, J.; Xu, M.; Li, R.; Huang, K.-W.; Jiang, C.; Qi, Q.; Zeng, W.; Zhang, J.; Chi, C.; Wang, P.; Wu, J. *J. Am. Chem. Soc.* **2013**, *136*, 265–272.

[23] He, H.; Gurung, A.; Si, L.; Sykes, A. G. *Chem. Commun.* **2012**, *48*, 7619–7621.

[24] Liu, Y.; Lin, H.; Li, J.; Dy, J. T.; Tamaki, K.; Nakazaki, J.; Nakayama, D.; Nishiyama, C.; Uchida, S.; Kubo, T.; Segawa, H. *Phys. Chem. Chem. Phys.* **2012**, *14*, 16703–16712.

[25] Wang, C.-L.; Hu, J.-Y.; Wu, C.-H.; Kuo, H.-H.; Chang, Y.-C.; Lan, Z.-J.; Wu, H.-P.; Wei-Guang Diau, E.; Lin, C.-Y. *Energy Environ. Sci.* **2014**, *7*, 1392–1396.

[26] Ragoussi, M.-E.; de la Torre, G.; Torres, T. *Eur. J. Org. Chem.* **2013**, *2013*, 2832–2840.

[27] Yella, A.; Lee, H.-W.; Tsao, H. N.; Yi, C.; Chandiran, A. K.; Nazeeruddin, M. K.; Diau, E. W.-G.; Yeh, C.-Y.; Zakeeruddin, S. M.; Grätzel, M. *Science* **2011**, *334*, 629–634.

[28] Sreenivasu, M.; Suzuki, A.; Adachi, M.; Kumar, C. V.; Srikanth, B.; Rajendar, S.; Rambabu, D.; Kumar, R. S.; Mallesham, P.; Rao, N. V. B.; Kumar, M. S.; Reddy, P. Y. *Chem. Eur. J.* **2014**, *20*, 14074–14083.

[29] Jia, H.-L.; Ju, Z.-M.; Sun, H.-X.; Ju, X.-H.; Zhang, M.-D.; Zhou, X.-F.; Zheng, H.-G. *J. Mater. Chem. A* **2014**, *2*, 20841–20848.

[30] Pelado, B.; de la Cruz, P.; Gonzalez-Pedro, V.; Barea, E. M.; Langa, F. *Tetrahedron Lett.* **2012**, *53*, 6665–6669.

[31] Hamamura, T.; Dy, J. T.; Tamaki, K.; Nakazaki, J.; Uchida, S.; Kubo, T.; Segawa, H. *Phys. Chem. Chem. Phys.* **2014**, *16*, 4551–4560.

[32] Nikolaou, V.; Angaridis, P. A.; Charalambidis, G.; Sharma, G. D.; Coutsolelos, A. G. *Dalton Trans.* **2015**, *44*, 1734–1747.

[33] Zegkinoglou, I.; Ragoussi, M.-E.; Pemmaraju, C. D.; Johnson, P. S.; Pickup, D. F.; Ortega, J. E.; Prendergast, D.; de la Torre, G.; Himpsel, F. J. *J. Phys. Chem. C* **2013**, *117*, 13357–13364.

[34] Ørnsø, K. B.; Pedersen, C. S.; Garcia-Lastra, J. M.; Thygesen, K. S. *Phys. Chem. Chem. Phys.* **2014**, *16*, 16246–16254.

[35] Mathew, S.; Yella, A.; Gao, P.; Humphry-Baker, R.; Curchod, B. F. E.; Ashari-Astani, N.; Tavernelli, I.; Rothlisberger, U.; Nazeeruddin, M. K.; Grätzel, M. *Nat. Chem.* **2014**, *6*, 242–247.

[36] Cook, P. L.; Yang, W.; Liu, X.; Garcia-Lastra, J. M.; Rubio, A.; Himpsel, F. J. *J. Chem. Phys.* **2011**, *134*, 204707.

[37] Garcia-Lastra, J. M.; Cook, P. L.; Himpsel, F. J.; Rubio, A. *J. Chem. Phys.* **2010**, *133*, 151103.

[38] de Oteyza, D. G.; El-Sayed, A.; Garcia-Lastra, J. M.; Goiri, E.; Krauss, T. N.; Turak, A.; Barrena, E.; Dosch, H.; Zegenhagen, J.; Rubio, A.; Wakayama, Y.; Ortega, J. E. *J. Chem. Phys.* **2010**, *133*, 214703.

[39] Pickup, D. F.; Zegkinoglou, I.; Ballesteros, B.; Ganivet, C. R.; Garcia-Lastra, J. M.; Cook, P. L.; Johnson, P. S.; Rogero, C.; de Groot, F.; Rubio, A.; de la Torre, G.; Ortega, J. E.; Himpsel, F. J. *J. Phys. Chem. C* **2013**, *117*, 4410–4420.

[40] Wu, J.; Lan, Z.; Lin, J.; Huang, M.; Huang, Y.; Fan, L.; Luo, G. *Chem. Rev.* **2015**, *115*, 2136–2173.

[41] Cong, J.; Yang, X.; Kloo, L.; Sun, L. *Energy Environ. Sci.* **2012**, *5*, 9180–9194.

[42] Sun, Z.; Liang, M.; Chen, J. *Acc. Chem. Res.* **2015**, *48*, 1541–1550.

[43] Feldt, S. M.; Gibson, E. A.; Gabrielsson, E.; Sun, L.; Boschloo, G.; Hagfeldt, A. *J. Am. Chem. Soc.* **2010**, *132*, 16714–16724.

[44] Ahmad, S.; Bessho, T.; Kessler, F.; Baranoff, E.; Frey, J.; Yi, C.; Grätzel, M.; Nazeeruddin, M. K. *Phys. Chem. Chem. Phys.* **2012**, *14*, 10631–10639.

[45] Omata, K.; Kuwahara, S.; Katayama, K.; Qing, S.; Toyoda, T.; Lee, K.-M.; Wu, C.-G. *Phys. Chem. Chem. Phys.* **2015**, *17*, 10170–10175.

[46] Murakami, T. N.; Koumura, N.; Kimura, M.; Mori, S. *Langmuir* **2014**, *30*, 2274–2279.

[47] Perera, I. R.; Gupta, A.; Xiang, W.; Daeneke, T.; Bach, U.; Evans, R. A.; Ohlin, C. A.; Spiccia, L. *Phys. Chem. Chem. Phys.* **2014**, *16*, 12021–12028.

[48] Pazoki, M.; Lohse, P. W.; Taghavinia, N.; Hagfeldt, A.; Boschloo, G. *Phys. Chem. Chem. Phys.* **2014**, *16*, 8503–8508.

[49] Johansson, V.; Ellis-Gibbings, L.; Clarke, T.; Gorlov, M.; Andersson, G. G.; Kloo, L. *Phys. Chem. Chem. Phys.* **2014**, *16*, 711–718.

[50] Cong, J.; Hao, Y.; Boschloo, G.; Kloo, L. *ChemSusChem* **2015**, *8*, 264–268.

[51] Wang, M.; Chamberland, N.; Breau, L.; Moser, J.-E.; Humphry-Baker, R.; Marsan, B.; Zakeeruddin, S. M.; Grätzel, M. *Nat. Chem.* **2010**, *2*, 385–389.

[52] Xu, X.; Cao, K.; Huang, D.; Shen, Y.; Wang, M. *J. Phys. Chem. C* **2012**, *116*, 25233–25241.

[53] Burschka, J.; Brault, V.; Ahmad, S.; Breau, L.; Nazeeruddin, M. K.; Marsan, B.; Zakeeruddin, S. M.; Grätzel, M. *Energy Environ. Sci.* **2012**, *5*, 6089–6097.

[54] Wu, M.; Lin, X.; Wang, Y.; Wang, L.; Guo, W.; Qi, D.; Peng, X.; Hagfeldt, A.; Grätzel, M.; Ma, T. *J. Am. Chem. Soc.* **2012**, *134*, 3419–3428.

[55] Martsinovich, N.; Troisi, A. *Energy Environ. Sci.* **2011**, *4*, 4473–4495.

[56] Chaitanya, K.; Ju, X.-H.; Heron, B. M. *RSC Adv.* **2014**, *4*, 26621–26634.

[57] Lee, M.-J.; Balanay, M. P.; Kim, D. H. *Theor. Chem. Acc.* **2012**, *131*, 1–12.

[58] Santhanamoorthi, N.; Lo, C.-M.; Jiang, J.-C. *J. Phys. Chem. Lett.* **2013**, *4*, 524–530.

[59] Patrick, C. E.; Giustino, F. *Phys. Rev. Lett.* **2012**, *109*, 116801.

[60] Gonzalez-Vazquez, J. P.; Oskam, G.; Anta, J. A. *J. Phys. Chem. C* **2012**, *116*, 22687–22697.

[61] De Angelis, F.; Fantacci, S.; Selloni, A.; Nazeeruddin, M. K.; Grätzel, M. *J. Phys. Chem. C* **2010**, *114*, 6054–6061.

[62] Feng, J.; Jiao, Y.; Ma, W.; Nazeeruddin, M. K.; Grätzel, M.; Meng, S. *J. Phys. Chem. C* **2013**, *117*, 3772–3778.

[63] Meng, S.; Kaxiras, E. *Nano Lett.* **2010**, *10*, 1238–1247.

[64] Le Bahers, T.; Pauporte, T.; Laine, P. P.; Labat, F.; Adamo, C.; Ciofini, I. *J. Phys. Chem. Lett.* **2013**, *4*, 1044–1050.

[65] Johannesson, G. H.; Bligaard, T.; Ruban, A. V.; Skriver, H. L.; Jacobsen, K. W.; Nørskov, J. K. *Phys. Rev. Lett.* **2002**, *88*, 255506.

[66] Franceschetti, A.; Zunger, A. *Nature* **1999**, *402*, 60–63.

[67] Ceder, G.; Chiang, Y.-M.; Sadoway, D. R.; Aydinol, M. K.; Jang, Y.-I.; Huang, B. *Nature* **1998**, *392*, 694–696.

[68] Setyawan, W.; Gaume, R. M.; Lam, S.; Feigelson, R. S.; Curtarolo, S. *ACS Comb. Sci.* **2011**, *13*, 382–390.

[69] Hachmann, J.; Olivares-Amaya, R.; Atahan-Evrenk, S.; Amador-Bedolla, C.; Sachez-Carrera, R. S.; Gold-Parker, A.; Vogt, L.; Brockway, A. M.; Aspuru-Guzik, A. *J. Phys. Chem. Lett.* **2011**, *2*, 2241–2251.

[70] Olivares-Amaya, R.; Amador-Bedolla, C.; Hachmann, J.; Atahan-Evrenk, S.; Sanchez-Carrera, R. S.; Vogt, L.; Aspuru-Guzik, A. *Energy Environ. Sci.* **2011**, *4*, 4849–4861.

[71] O'Boyle, N. M.; Campbell, C. M.; Hutchison, G. R. *J. Phys. Chem. C* **2011**, *115*, 16200–16210.

[72] Kanal, I. Y.; Owens, S. G.; Bechtel, J. S.; Hutchison, G. R. *J. Phys. Chem. Lett.* **2013**, *4*, 1613–1623.

[73] Hachmann, J.; Olivares-Amaya, R.; Jinich, A.; Appleton, A. L.; Blood-Forsythe, M. A.; Seress, L. R.; Roman-Salgado, C.; Trepte, K.; Atahan-Evrenk, S.; Er, S.; Shrestha, S.; Mondal, R.; Sokolov, A.; Bao, Z.; Aspuru-Guzik, A. *Energy Environ. Sci.* **2014**, *7*, 698–704.

[74] Castelli, I. E.; Olsen, T.; Datta, S.; Landis, D. D.; Dahl, S.; Thygesen, K. S.; Jacobsen, K. W. *Energy Environ. Sci.* **2012**, *5*, 5814–5819.

[75] Castelli, I. E.; Landis, D. D.; Thygesen, K. S.; Dahl, S.; Chorkendorff, I.; Jaramillo, T. F.; Jacobsen, K. W. *Energy Environ. Sci.* **2012**, *5*, 9034–9043.

[76] Isayev, O.; Fourches, D.; Muratov, E. N.; Oses, C.; Rasch, K.; Tropsha, A.; Curtarolo, S. *Chem. Mater.* **2015**, *27*, 735–743.

[77] Aviram, A.; Ratner, M. A. *Chem. Phys. Lett.* **1974**, *29*, 277–283.

[78] Aradhya, S. V.; Venkataraman, L. *Nat. Nanotechnol.* **2013**, *8*, 399–410.

[79] Staykov, A.; Watanabe, M.; Ishihara, T.; Yoshizawa, K. *J. Phys. Chem. C* **2014**, *118*, 27539–27548.

[80] Jensen, F. *Introduction to Computational Chemistry*, 2nd ed.; John Wiley & Sons, Ltd, 2007.

[81] Atkins, P.; Friedman, R. *Molecular Quantum Mechanics*; Oxford University Press, 2005.

[82] Ballentine, L. E. *Quantum Mechanics - A Modern Development*; World Scientific Publishing, 1998.

[83] Helgarker, T.; Jørgensen, P.; Olsen, J. *Molecular Electronic-Structure Theory*, 1st ed.; John Wiley & Sons, Ltd, 2000.

[84] Hohenberg, P.; Kohn, W. *Phys. Rev.* **1964**, *136*, B864–B871.

[85] Kohn, W.; Sham, L. J. *Phys. Rev.* **1965**, *140*, A1133–A1138.

[86] Perdew, J. P.; Burke, K.; Ernzerhof, M. *Phys. Rev. Lett.* **1996**, *77*, 3865–3868.

[87] Mortensen, J. J.; Hansen, L. B.; Jacobsen, K. W. *Phys. Rev. B* **2005**, *71*, 035109.

[88] Enkovaara, J. et al. *J. Phys.: Condens. Matter* **2010**, *22*, 253202–1–24.

[89] Larsen, A. H.; Vanin, M.; Mortensen, J. J.; Thygesen, K. S.; Jacobsen, K. W. *Phys. Rev. B* **2009**, *80*, 195112–1–10.

[90] Baerends, E. J.; Gritsenko, O. V.; van Meer, R. *Phys. Chem. Chem. Phys.* **2013**, *15*, 16408–16425.

[91] Kuznetsov, A. M.; Ulstrup, J. *Electron transfer in chemistry and biology: An introduction to the theory*; John Wiley & Sons, Inc., 1999.

[92] Henriksen, N. E.; Hansen, F. Y. *Theories of Molecular Reaction Dynamics*, 1st ed.; Oxford University Press, 2008.

[93] Marcus, R. A. *J. Chem. Phys.* **1956**, *24*, 966–978.

[94] Marcus, R. A. *J. Chem. Phys.* **1956**, *24*, 979–989.

[95] Marcus, R. A. *J. Chem. Phys.* **1957**, *26*, 867–871.

[96] Marcus, R. A. *J. Chem. Phys.* **1957**, *26*, 872–877.

[97] Marcus, R. A. *J. Chem. Phys.* **1965**, *43*, 679–701.

[98] Warshel, A. *J. Phys. Chem.* **1982**, *86*, 2218–2224.

[99] Tachiya, M. *J. Phys. Chem.* **1989**, *93*, 7050–7052.

[100] King, G.; Warshel, A. *J. Chem. Phys.* **1990**, *93*, 8682–8692.

[101] Closs, G. L.; Calcaterra, L. T.; Green, N. J.; Penfield, K. W.; Miller, J. R. *J. Phys. Chem.* **1986**, *90*, 3673–3683.

[102] Schuster, D. I.; Cheng, P.; Jarowski, P. D.; Guldi, D. M.; Luo, C.; Echegoyen, L.; Pyo, S.; Holzwarth, A. R.; Braslavsky, S. E.; Williams, R. M.; Klihm, G. *J. Am. Chem. Soc.* **2004**, *126*, 7257–7270.

[103] Liang, N.; Miller, J. R.; Closs, G. L. *J. Am. Chem. Soc.* **1990**, *112*, 5353–5354.

[104] Feldt, S. M.; Lohse, P. W.; Kessler, F.; Nazeeruddin, M. K.; Grätzel, M.; Boschloo, G.; Hagfeldt, A. *Phys. Chem. Chem. Phys.* **2013**, *15*, 7087–7097.

[105] Jónsson, E. O. Computational approach to electron charge transfer reactions. Ph.D. thesis, Technical University of Denmark, 2014.

[106] van Gunsteren, W.; Berendsen, H. *Mol. Phys.* **1982**, *45*, 637–647.

[107] Bussi, G.; Parrinello, M. *Phys. Rev. E* **2007**, *75*, 056707–.

[108] Souaille, M.; Roux, B. *Comp. Phys. Comm.* **2001**, *135*, 40–57.

[109] Ferrenberg, A. M.; Swendsen, R. H. *Phys. Rev. Lett.* **1989**, *63*, 1195–1198.

[110] Kumar, S.; Rosenberg, J. M.; Bouzida, D.; Swendsen, R. H.; Kollman, P. A. *J. Comp. Chem.* **1992**, *13*, 1011–1021.

[111] Bell, R. P. *The Tunnel Effect in Chemistry*, 1st ed.; Chapman and Hall, 1980.

[112] Thygesen, K. S. Structure and transport in nano-scale contacts. Ph.D. thesis, Technical University of Denmark, 2005.

[113] Meir, Y.; Wingreen, N. S. *Phys. Rev. Lett.* **1992**, *68*, 2512–2515.

[114] Garcia-Lastra, J. M.; Rostgaard, C.; Rubio, A.; Thygesen, K. S. *Phys. Rev. B* **2009**, *80*, 245427.

[115] Mowbray, D. J.; Jones, G.; Thygesen, K. S. *J. Chem. Phys.* **2008**, *128*, 111103.

[116] Quek, S. Y.; Venkataraman, L.; Choi, H. J.; Louie, S. G.; Hybertsen, M. S.; Neaton, J. B. *Nano Lett.* **2007**, *7*, 3477–3482.

[117] Baghernejad, M.; Zhao, X.; Ørnsø, K. B.; Füeg, M.; Moreno-Garcia, P.; Rudnev, A. V.; Kaliginedi, V.; Vesztergom, S.; Huang, C.; Hong, W.; Broekmann, P.; Wandlowski, T.; Thygesen, K. S.; Bryce, M. R. *J. Am. Chem. Soc.* **2014**, *136*, 17922–17925.

[118] Markussen, T.; Stadler, R.; Thygesen, K. S. *Nano Lett.* **2010**, *10*, 4260–4265.

[119] Bahn, S.; Jacobsen, K. W. *Comput. Sci. Eng.* **2002**, *4*, 56–66.

[120] Frisch, M. J. et al. Gaussian 09 Revision B.01. Gaussian Inc. Wallingford CT 2009.

[121] Werner, H.-J. et al. MOLPRO, version 2010.1, a package of ab initio programs. 2010; see http://www.molpro.net.

[122] Allegrucci, A.; Lewcenko, N. A.; Mozer, A. J.; Dennany, L.; Wagner, P.; Officer, D. L.; Sunahara, K.; Mori, S.; Spiccia, L. *Energy Environ. Sci.* **2009**, *2*, 1069–1073.

[123] Martsinovich, N.; Troisi, A. *Phys. Chem. Chem. Phys.* **2012**, *14*, 13392–13401.

[124] Ronca, E.; Pastore, M.; Belpassi, L.; Tarantelli, F.; De Angelis, F. *Energy Environ. Sci.* **2013**, *6*, 183–193.

[125] Gouterman, M. *J. Mol. Spectrosc.* **1961**, *6*, 138–163.

[126] Bauer, C.; Boschloo, G.; Mukhtar, E.; Hagfeldt, A. *J. Phys. Chem. B* **2002**, *106*, 12693–12704.

[127] Clifford, J. N.; Palomares, E.; Nazeeruddin, M. K.; Grätzel, M.; Durrant, J. R. *J. Phys. Chem. C* **2007**, *111*, 6561–6567.

[128] Kuciauskas, D.; Freund, M. S.; Gray, H. B.; Winkler, J. R.; Lewis, N. S. *J. Phys. Chem. B* **2000**, *105*, 392–403.

[129] Shockley, W.; Queisser, H. J. *J. Appl. Phys.* **1961**, *32*, 510–519.

[130] Zietz, B.; Gabrielsson, E.; Johansson, V.; El-Zohry, A. M.; Sun, L.; Kloo, L. *Phys. Chem. Chem. Phys.* **2014**, *16*, 2251–2255.

[131] Pastore, M.; De Angelis, F. *J. Phys. Chem. Lett.* **2013**, *4*, 956–974.

[132] Lu, H.-P.; Tsai, C.-Y.; Yen, W.-N.; Hsieh, C.-P.; Lee, C.-W.; Yeh, C.-Y.; Diau, E. W.-G. *J. Phys. Chem. C* **2009**, *113*, 20990–20997.

[133] Yum, J.-H.; Baranoff, E.; Kessler, F.; Moehl, T.; Ahmad, S.; Bessho, T.; Marchioro, A.; Ghadiri, E.; Moser, J.-E.; Yi, C.; Nazeeruddin, M. K.; Grätzel, M. *Nat. Commun.* **2012**, *3*, 631–1–8.

[134] Boschloo, G.; Hagfeldt, A. *Acc. Chem. Res.* **2009**, *42*, 1819–1826.

[135] Privalov, T.; Boschloo, G.; Hagfeldt, A.; Svensson, P. H.; Kloo, L. *J. Phys. Chem. C* **2009**, *113*, 783–790.

[136] Boschloo, G.; Gibson, E. A.; Hagfeldt, A. *J. Phys. Chem. Lett.* **2011**, *2*, 3016–3020.

[137] Andersen, H. C. *J. Comp. Phys.* **1983**, *54*, 24–34.

[138] V.-Eijnden, E. and Ciccotti, G., *Chem. Phys. Lett.* **2006**, *429*, 310–316.

[139] Jmol: an open-source Java viewer for chemical structures in 3D. http://www.jmol.org/.

[140] Yaghoobi Nia, N.; Farahani, P.; Sabzyan, H.; Zendehdel, M.; Oftadeh, M. *Phys. Chem. Chem. Phys.* **2014**, *16*, 11481–11491.

[141] Hummer, G.; García, A. E. *J. Chem. Phys.* **1997**, *107*, 9275–9277.

[142] Hünenberger, P. H.; McCammon, J. A. *J. Chem. Phys.* **1999**, *110*, 1856–1872.

[143] Ayala, R.; Sprik, M. *J. Phys. Chem. B* **2008**, *112*, 257–269.

[144] Osuka, A.; Noya, G.; Taniguchi, S.; Okada, T.; Nishimura, Y.; Yamazaki, I.; Mataga, N. *Chem. Eur. J.* **2000**, *6*, 33–46.

[145] Krivokapic, I.; Zerara, M.; Daku, M. L.; Vargas, A.; Enachescu, C.; Ambrus, C.; Tregenna-Piggott, P.; Amstutz, N.; Krausz, E.; Hauser, A. *Coord. Chem. Rev.* **2007**, *251*, 364–378.

[146] Mosconi, E.; Yum, J.-H.; Kessler, F.; Gómez Garcia, C. J.; Zuccaccia, C.; Cinti, A.; Nazeeruddin, M. K.; Grätzel, M.; De Angelis, F. *J. Am. Chem. Soc.* **2012**, *134*, 19438–19453.

[147] Feldt, S. M.; Wang, G.; Boschloo, G.; Hagfeldt, A. *J. Phys. Chem. C* **2011**, *115*, 21500–21507.

[148] Sun, Z.-Z.; Zheng, K.-M.; Li, Q.-S.; Li, Z.-S. *RSC Adv.* **2014**, *4*, 31544–31551.

[149] Luque, A.; Marti, A. *Phys. Rev. Lett.* **1997**, *78*, 5014–5017.

[150] Luque, A.; Marti, A.; Stanley, C. *Nat. Photon.* **2012**, *6*, 146–152.

[151] Ekins-Daukes, N. J.; Schmidt, T. W. *Appl. Phys. Lett.* **2008**, *93*, 063507.

[152] Subbaiyan, N. K.; Wijesinghe, C. A.; DSouza, F. *J. Am. Chem. Soc.* **2009**, *131*, 14646–14647.

[153] Warnan, J.; Pellegrin, Y.; Blart, E.; Odobel, F. *Chem. Commun.* **2012**, *48*, 675–677.

[154] Planells, M.; Pelleja, L.; Ballester, P.; Palomares, E. *Energy Environ. Sci.* **2011**, *4*, 528–534.

[155] He, J.; Lindström, H.; Hagfeldt, A.; Lindquist, S.-E. *J. Phys. Chem. B* **1999**, *103*, 8940–8943.

[156] He, J.; Lindström, H.; Hagfeldt, A.; Lindquist, S.-E. *Sol. Energy Mater. Sol. Cells* **2000**, *62*, 265–273.

[157] Sobus, J.; Ziolek, M. *Phys. Chem. Chem. Phys.* **2014**, *16*, 14116–14126.

[158] Nattestad, A.; Mozer, A. J.; Fischer, M. K. R.; Cheng, Y.-B.; Mishra, A.; Bauerle, P.; Bach, U. *Nat. Mater.* **2010**, *9*, 31–35.

[159] Balasingam, S. K.; Lee, M.; Kang, M. G.; Jun, Y. *Chem. Commun.* **2013**, *49*, 1471–1487.

[160] Vos, A. D. *J. Phys. D: Appl. Phys.* **1980**, *13*, 839–846.

[161] te Velde, G.; Bickelhaupt, F. M.; Baerends, E. J.; Fonseca Guerra, C.; van Gisbergen, S. J. A.; Snijders, J. G.; Ziegler, T. *J. Comput. Chem.* **2001**, *22*, 931–967.

[162] Ørnsø, K. B.; Garcia-Lastra, J. M.; De La Torre, G.; Himpsel, F. J.; Rubio, A.; Thygesen, K. S. *Chem. Sci.* **2015**, *6*, 3018–3025.

[163] DeGraziano, J. M.; Liddell, P. A.; Leggett, L.; Moore, A. L.; Moore, T. A.; Gust, D. *J. Phys. Chem.* **1994**, *98*, 1758–1761.

[164] Liao, M.-S.; Scheiner, S. *J. Comput. Chem.* **2002**, *23*, 1391–1403.

[165] Liao, M.-S.; Scheiner, S. *J. Chem. Phys.* **2002**, *117*, 205–219.

[166] Pettersson, K.; Kilså, K.; Mårtensson, J.; Albinsson, B. *J. Am. Chem. Soc.* **2004**, *126*, 6710–6719.

[167] Wiehe, A.; Stollberg, H.; Runge, S.; Paul, A.; Senge, M. O.; Röder, B. *J. Porphyrins Phthalocyanines* **2001**, *5*, 853–860.

[168] Guedon, C. M.; Valkenier, H.; Markussen, T.; Thygesen, K. S.; Hummelen, J. C.; van der Molen, S. J. *Nat. Nanotechnol.* **2012**, *7*, 305–309.

[169] Huang, C.; Rudnev, A. V.; Hong, W.; Wandlowski, T. *Chem. Soc. Rev.* **2015**, *44*, 889–901.

[170] Trasatti, S. *Pure Appl. Chem.* **1986**, *58*, 955–966.

[171] Parker, C. R. et al. *J. Am. Chem. Soc.* **2014**, *136*, 16497–16507.

[172] Ip, C. M.; Eleuteri, A.; Troisi, A. *Phys. Chem. Chem. Phys.* **2014**, *16*, 19106–19110.

[173] Lee, M. M.; Teuscher, J.; Miyasaka, T.; Murakami, T. N.; Snaith, H. J. *Science* **2012**, *338*, 643–647.

[174] Fakharuddin, A.; Jose, R.; Brown, T. M.; Fabregat-Santiago, F.; Bisquert, J. *Energy Environ. Sci.* **2014**, *7*, 3952–3981.

[175] Sharifi, N.; Tajabadi, F.; Taghavinia, N. *ChemPhysChem* **2014**, *15*, 3902–3927.

Appendices

Appendix A

Atomic units and Dirac notation

In this thesis atomic units have been used, which are defined as

$$e = 1\,\text{a.u.} \approx 1.6022 \cdot 10^{-19}\,\text{C} \tag{A.1}$$

$$m_e = 1\,\text{a.u.} \approx 9.1095 \cdot 10^{-31}\,\text{kg} \tag{A.2}$$

$$\hbar = \frac{h}{2\pi} = 1\,\text{a.u.} \approx 1.0546 \cdot 10^{-34}\,\text{J} \cdot \text{s} \tag{A.3}$$

$$a_0 = \frac{4\pi\varepsilon_0\hbar^2}{m_e e^2} = 1\,\text{a.u.} \approx 5.2918 \cdot 10^{-11}\,\text{m} \tag{A.4}$$

$$4\pi\varepsilon_0 = 1\,\text{a.u.} \approx 1.1127 \cdot 10^{-10}\,\text{J}^{-1}\text{C}^2\text{m}^{-1} \tag{A.5}$$

To ease the notation of wavefunctions and their integrals, the Dirac notation has been used

$$\psi_i = |\psi_i\rangle \tag{A.6}$$

$$\psi_i^* = \langle\psi_i| \tag{A.7}$$

$$\int \psi_i^* \psi_j \mathrm{d}\overline{r} = \langle\psi_i|\psi_j\rangle \tag{A.8}$$

$$\int \psi_i^* \hat{\Omega} \psi_j \mathrm{d}\overline{r} = \langle\psi_i|\hat{\Omega}|\psi_j\rangle \tag{A.9}$$

Appendix B

Paper I

Computational screening of functionalized zinc porphyrins for dye sensitized solar cells
K. B. Ørnsø, J. M. Garcia-Lastra and K. S. Thygesen
Phys. Chem. Chem. Phys., **2013**, *15*, 19478-19486

PCCP

RSC Publishing

PAPER

Computational screening of functionalized zinc porphyrins for dye sensitized solar cells†

Cite this: *Phys. Chem. Chem. Phys.*, 2013, **15**, 19478

Kristian B. Ørnsø,*[a] Juan M. Garcia-Lastra[ab] and Kristian S. Thygesen[a]

Received 19th June 2013,
Accepted 30th September 2013

DOI: 10.1039/c3cp54050b

www.rsc.org/pccp

An efficient dye sensitized solar cell (DSSC) is one possible solution to meet the world's rapidly increasing energy demands and associated climate challenges. This requires inexpensive and stable dyes with well-positioned frontier energy levels for maximal solar absorption, efficient charge separation, and high output voltage. Here we demonstrate an extensive computational screening of zinc porphyrins functionalized with electron donating side groups and electron accepting anchoring groups. The trends in frontier energy levels *versus* side groups are analyzed and a no-loss DSSC level alignment quality is estimated. Out of the initial 1029 molecules, we find around 50 candidates with level alignment qualities within 5% of the optimal limit. We show that the level alignment of five zinc porphyrin dyes which were recently used in DSSCs with high efficiencies can be further improved by simple side group substitutions. All frontier energy levels, gaps and level alignment quality values are stored in a database publicly available.

1 Introduction

The limited access to fossil fuels and the CO_2 related climate problems have made the search for efficient sustainable energy sources one of the most important challenges of our time. Since the emergence of the first efficient system in 1991,[1] dye sensitized solar cells (DSSCs) have been intensively researched due to their potential as a cost-efficient and flexible alternative to conventional solar cells.[2] The working mechanisms of a DSSC are illustrated schematically in Fig. 1. Incoming photons from the sun are absorbed by a molecular dye, which is anchored to a semi-conductor nanoparticle (typically TiO_2). The excited electrons on the dye are transferred to the conduction band of the semiconductor in an ultrafast charge separation process, and extracted to an external circuit. In the last step the electron is transferred from the counter electrode back to the dye by an electrolyte. The many steps involved in a DSSC cycle impose several constraints on the properties of the dye molecule. In addition to being stable under illumination and in contact with the often corrosive electrolyte, the alignment of the highest occupied molecular orbital (HOMO) and the lowest unoccupied molecular orbital (LUMO) with the redox potential of the electrolyte and the conduction band of the semiconductor, respectively, as well as a large overlap of the absorption spectrum with the solar spectrum, are crucial properties. The use of porphyrin based dyes has very recently been demonstrated as a very successful path.[3] In addition to the large absorption of visible light, porphyrins are easily customized by introducing side groups. A special scheme for functionalizing porphyrins is the donor–π-acceptor structure in which the HOMO is mainly

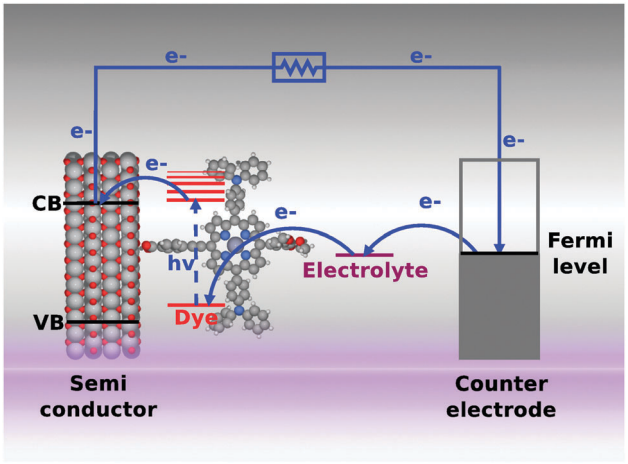

Fig. 1 Schematic overview of the working mechanisms of a dye sensitized solar cell (DSSC).

[a] *Center for Atomic-scale Materials Design, Department of Physics, Technical University of Denmark, 2800 Kgs. Lyngby, Denmark. E-mail: krbt@fysik.dtu.dk*
[b] *Nano-Bio Spectroscopy Group and ETSF Scientific Development Center, University of the Basque Country UPV/EHU, Avenida de Tolosa 72, 20018 San Sebastian, Spain*

† Electronic supplementary information (ESI) available: Method validation, the standard ASTM G-173-03 (AM 1.5 G) solar spectrum, visualization of representative frontier orbitals and a comparison between energy gaps with and without electron–hole interaction. See DOI: 10.1039/c3cp54050b

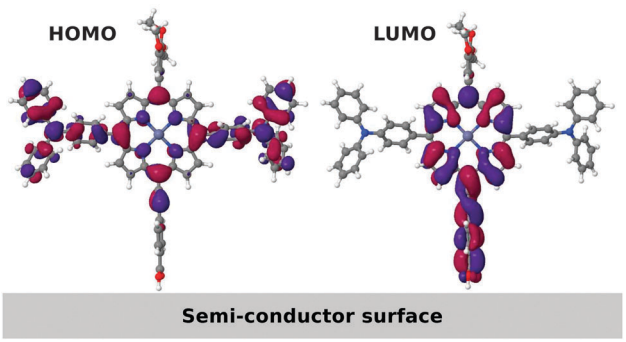

Fig. 2 Visual representation of the calculated HOMO (left) and LUMO (right) of the donor–π-acceptor M3T2P zinc porphyrin dye molecule.

located on the donor side groups while the LUMO is mostly located on the acceptor group. This construction entails a natural separation of the electron and the hole thereby minimizing the recombination rate. Furthermore, if the acceptor acts as an anchoring group to the semi-conductor surface, the rate of electron injection from the dye to the semi-conductor is increased. Using this concept a record efficiency of 12.3% has recently been reported for a zinc porphyrin based DSSC with a cobalt based electrolyte.[4] As an example of a porphyrin-based donor–π–acceptor system, we show the HOMO and the LUMO of the M3T2P dye[5] in Fig. 2. Here the separation of the HOMO and the LUMO is clearly seen.

The tremendous increase of computational power over the last couple of decades, in combination with methodological improvements, has made it possible to guide the development of new materials using first principles quantum mechanical calculations. Previous examples include highly stable metal alloys,[6] semiconductor superlattices with tailored band gaps,[7] battery cathode materials,[8] inorganic scintillator materials[9] as well as molecules for organic photovoltaics[10–13] and materials for photo-catalytic water splitting.[14,15] In this paper, we introduce the use of large-scale computational tools to search for optimal donor–π–acceptor porphyrin based dyes. We present the calculated frontier energy levels, orbitals, and optical gaps for 1029 functionalized zinc porphyrin dye candidates. Based on this we investigate trends in the selective tuning of energy levels and orbital shapes and estimate a (loss-less) DSSC level alignment quality of the candidate molecules. As a concrete example we suggest how the level alignment of five experimentally investigated dyes can be improved. All calculated data are available in the database Computational Materials Repository at the web address http://cmr.fysik.dtu.dk/.

2 Methods

In this screening project we investigate zinc porphyrins functionalized by different side groups and anchor groups. The zinc porphyrin backbone is shown in Fig. 3, where the R1, R2 and R3 labels denote side group locations and A denotes the anchor group location. A total of seven different side groups (see Fig. 4) and three different anchor groups (see Fig. 5) have been chosen for this study. The TPA, MOTPA and TMP side groups as well as

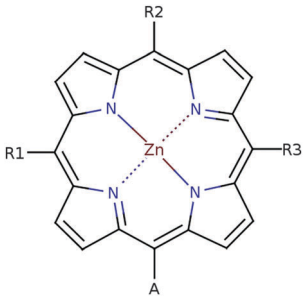

Fig. 3 Labeling of positions in the zinc porphyrin backbone structure.

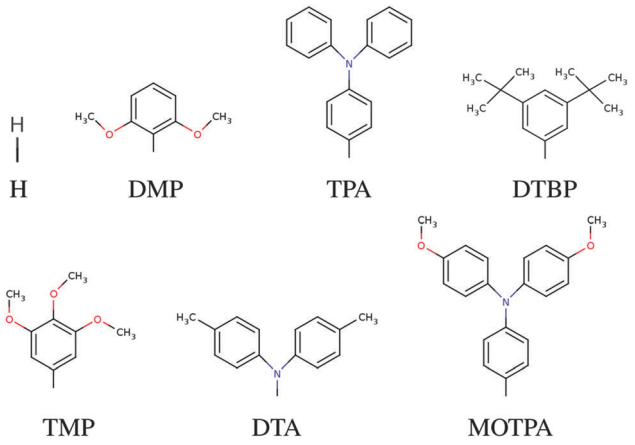

Fig. 4 The donor groups investigated in this work.

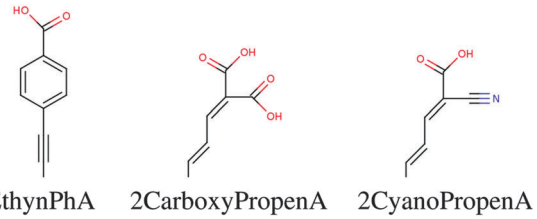

Fig. 5 The accepting anchor groups investigated in this work.

the EthynPhA anchor group have been investigated experimentally by Liu *et al.*,[5] the DMP, DTBP and DTA side groups are modified versions of those investigated experimentally by Yella *et al.*[4] and the 2CarboxyPropenA and 2CyanoPropenA anchor groups have been investigated theoretically by Lee *et al.*[16] The groups have generally been chosen to represent well-known building blocks that should be experimentally available. An example of this is the choice of the EthynPhA anchor group which is a commonly used group. The last two anchoring groups have been chosen to offer a comparison to the EthynPhA group. Furthermore, the donating side groups have been chosen to include comparable groups offering a wide spectra in size. All quantum mechanical calculations are performed using density functional theory (DFT)[17] with the PBE[18,19] exchange–correlation functional as implemented in the GPAW code.[20] For all standard calculations we have used a basis set of numerical atomic orbitals[21] (LCAO mode) with a double-ζ polarized basis set, a grid-spacing of 0.18 and a unit cell

with 5.0 Å vacuum added on both sides of the molecule in all directions. All structures have been optimized using the BFGS method as implemented in the Atomic Simulation Environment (ASE)[22] until all forces are below 0.05 eV Å^{-1}. After the geometry optimization the location of the HOMO, E_{HOMO} and LUMO, E_{LUMO}, is calculated as the ionization potential I_P and electron affinity E_A of the molecule. Thus the resulting gap, E_{gap}, is given by:

$$\begin{aligned} E_{gap} &= E_{LUMO} - E_{HOMO} \\ &= (E[-1] - E[0]) - (E[0] - E[+1]) \\ &= I_P - E_A \end{aligned} \quad (1)$$

where $E[0]$ is the ground state total energy and $E[-1]$ and $E[+1]$ is the total energy of the negatively and positively charged ions of the molecule, respectively. This definition of E_{gap} avoids the use of Kohn–Sham eigenvalues which are well-known to be inaccurate within PBE. The choice of level of theory reflects the large amount of calculations necessary to perform this study. It can be noted that the obtained E_{HOMO} values are in good agreement with results obtained from PBE calculations with the all-electron Gaussian09 program suite[23] and the high-end Coupled-Cluster results obtained using the Molpro program suite.[24] For the E_{LUMO} the agreement is worse with differences up to $\approx$0.2 eV between PBE and both the Gaussian09 DFT and Coupled-Cluster values. However, as will be discussed later, the LUMO energy will not be used for the final level alignment quality calculations. For more details see Tables S1 and S2 in the ESI.† To investigate the quality of the GGA type PBE functional, a comparison between results obtained using the hybrid B3LYP[25–27] and results obtained using PBE for a wide range of zinc porphyrins is given in the ESI† (see Fig. S1–S3). Here a constant shift of up to 0.5 eV is observed for E_{HOMO} and E_{gap}. However, since the shift is constant, the trends for both levels of theory are the same and thus we expect that using PBE will be sufficient. In addition to the fundamental gap, the optical gaps, E_1, which include the electron–hole interactions, are calculated. This is done by forcing the molecule to the triplet groundstate by fixing the magnetic moment, and thus promoting one of the two electrons in the HOMO to the LUMO. We denote this method triplet ΔSCF. Note that this is not the same as the normal singlet ΔSCF method implemented in GPAW.[28] The latter provides a more realistic description of the optical transition (which does not involve spin flip), but is less robust and can be difficult to converge for some of the molecules investigated. The excitation energies calculated by the singlet ΔSCF method are observed to be up to 0.3 eV (see Table S3 in the ESI†) higher than those predicted by the triplet ΔSCF method. However, the robustness problems of the singlet ΔSCF force us to use the triplet ΔSCF method.

A comparison between the calculated E_{HOMO}, E_{gap} and E_1 energies and corresponding experimental values obtained by Liu *et al.*[5] is given in Table 1. The experimental data have been obtained for dyes on a TiO_2 film in acetonitrile and the values have been converted to a vacuum scale using a value for the Normal Hydrogen Electrode (NHE) of −4.5 eV *versus* vacuum.[29–31] For the T2P, MT2P and M3T2P species an excellent agreement between calculations and experimental values are observed, while the agreement is slightly worse for the T3P and MT3P species. We stress that the effect of hybridization and image charge screening[32] by the TiO_2 surface as well as the effect of solvent on the HOMO energies have not been included in the calculations. The trends for the calculated optical gaps, E_1, are in good agreement with the measured values, however, with the tendency that the calculated values are approximately 0.3–0.4 eV too low. Part of this discrepancy can be explained by the approximately 0.2 eV underestimation coming from the use of the triplet rather than singlet excitation (see ESI†). Furthermore, the experimental E_1 values are obtained from the absorption edge of the adsorbed dyes and can thus in addition to the simple HOMO → LUMO transition also include higher energy transitions. In fact, the main features in the absorption spectrum of porphyrins are known to involve higher lying transitions.[33] Based on these observations, we conclude that our method can be used to predict general tendencies for changes in E_{HOMO}, E_{LUMO} and E_1 upon functionalizing zinc porphyrins at a semi-quantitative level.

In order to identify the optimal electronic spectrum of the dyes relative to the semiconductor conduction band edge, we have defined a level alignment quality of a DSSC:

$$\eta = \frac{V_{oc}\int_{E_c-E_H}^{\infty} \Theta(E-E_1)\cdot I_{solar}(E)\mathrm{d}E}{\int_0^{\infty} E\cdot I_{solar}(E)\mathrm{d}E} \quad (2)$$

where:

$$\Theta(E-E_1) = \begin{cases} 1 & \text{for} \quad E-E_1 \geq 0 \\ 0 & \text{for} \quad E-E_1 < 0 \end{cases}$$

Here $E_c - E_H$ is the distance from the HOMO level to the conduction band, E_1 is the optical gap of the dye, $\Theta(E-E_1)$ is a step function representing the absorption of the dye molecules, $I_{solar}(E)$ is the photon flux of the ASTM G-173-03 (AM 1.5 G) solar spectrum (see Fig. S4 in ESI†), and V_{oc} is the open-circuit

Table 1 Comparison between calculated E_{HOMO}, E_{gap} and E_1 and experimental E_{HOMO} and E_1 obtained by Liu *et al.*[5] for a set of zinc porphyrins with the EthynPhA anchor group. The experimental data are obtained for dyes on a TiO_2 film in acetonitrile

Name[a]	R1	R2	R3	E_{HOMO} (eV)	exp. E_{HOMO}[b] (eV)	E_{gap} (eV)	E_1 (eV)	exp. E_1 (eV)
T2P	TPA	H	TPA	−5.63	−5.60	3.88	1.54	1.84
T3P	TPA	TPA	TPA	−5.38	−5.59	3.57	1.41	1.79
MT2P	MOTPA	H	MOTPA	−5.29	−5.26	3.62	1.49	1.83
MT3P	MOTPA	MOTPA	MOTPA	−5.01	−5.25	3.30	1.35	1.78
M3T2P	TPA	TMP	TPA	−5.47	−5.49	3.73	1.46	1.82

[a] Name used by Liu *et al.*[5] [b] Experimental potentials modified to be relative to vacuum using the potential of NHE *vs.* vacuum of −4.5 eV.[29–31]

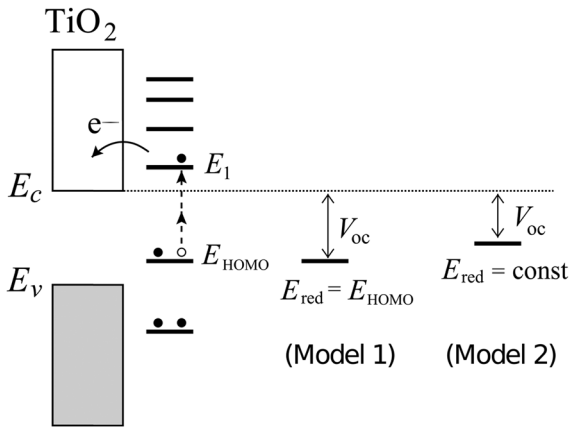

Fig. 6 Diagram visualizing the $E_c - E_H$ and E_1 energies relative to the HOMO of the dye. In the model the V_{oc} has been defined for either a perfectly aligned redox potential (model 1) where $V_{oc} = E_c - E_H$ or for a fixed redox potential (model 2) with $V_{oc} = 1$ V.

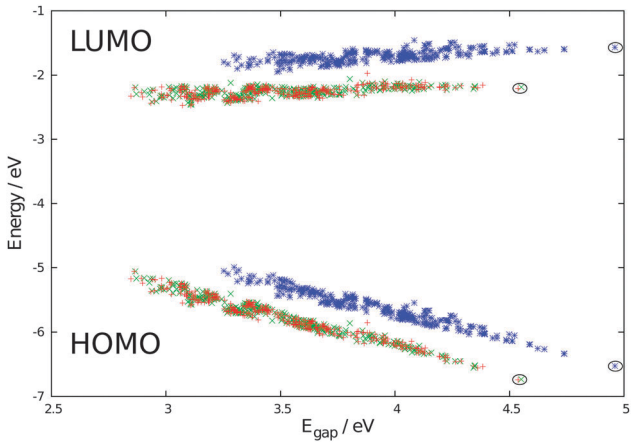

Fig. 7 Calculated corresponding E_{HOMO} and E_{LUMO} relative to vacuum ordered by the resulting E_{gap} of functionalized zinc porphyrins with the EthynPhA (blue star), 2CarboxyPropenA (green ×) and 2CyanoPropenA (red cross) anchor groups. The black circles indicate the porphyrins with only hydrogen side groups.

voltage. The level alignment quality is normalized by the solar effect: $\int_0^\infty E \cdot I_{solar}(E)\mathrm{d}E = 1000\ \mathrm{W\ m^{-2}}$. A visual representation of $E_c - E_H$ and E_1 is given in Fig. 6. The use of the $\Theta(E - E_1)$ step function to represent the dye absorption is based on the assumption that all solar photons with an energy higher than E_1 of the dye are absorbed by the dye molecules. This is a reasonable assumption for strongly absorbing porphyrin based dyes[3] in the usual DSSC setup where the effective area of dyes on the nanostructured semiconductor surface corresponds to several monolayers. Variations in the absorption spectrum of the different porphyrins may still influence the realistically obtainable level alignment quality. However, calculation of these features is not possible for a large screening project due to the high computational cost. We note that the level alignment quality is comparable to a DSSC efficiency where all losses have been neglected. In reality, however, many other critical factors have an influence on the overall efficiency of a DSSC and it should be stressed that we do not claim to include these in the present study. Our emphasis is only on the possibility of systematically improving the level alignment.

3 Results and discussion

3.1 Trends in energy levels

The calculated values of E_{HOMO} and E_{LUMO} plotted against E_{gap} are shown in Fig. 7. It is observed that the variation in E_{gap}, for a fixed anchor group, to a large extent is caused by a shift in the HOMO energy for the differently functionalized porphyrins. The LUMO is determined by the anchor group. In Table 2 we list the molecules showing the largest and smallest values of the three quantities E_{HOMO}, E_{LUMO} and E_{gap}, respectively. It can be seen that the maximum difference in E_{LUMO} is $\sim$1.0 eV while the maximum difference in E_{HOMO} is $\sim$1.7 eV. This leads to the possibility of tuning E_{gap} by up to $\sim$2.1 eV and demonstrates the great flexibility in energy level design offered by functionalized porphyrins.

Table 2 E_{HOMO}, E_{LUMO} and E_{gap} for selected zinc porphyrins

A	R1	R2	R3	E_{HOMO} (eV)	E_{LUMO} (eV)	E_{gap} (eV)
EthynPhA	H	H	H	−6.53	−1.57	4.96[a]
2CyanoPropenA	MOTPA	DTA	MOTPA	−5.17	−2.33	2.85[b]
EthynPhA	MOTPA	MOTPA	MOTPA	−4.99[a]	−1.69	3.30
2CyanoPropenA	H	H	H	−6.74[b]	−2.21	4.54
EthynPhA	TMP	TMP	TMP	−5.54	−1.46[a]	4.08
2CyanoPropenA	DTA	DTA	DTA	−5.58	−2.47[b]	3.11

[a] Largest value of all candidates. [b] Smallest value of all candidates.

The zinc porphyrins with the MOTPA, DTA and TPA side groups exhibit particularly small energy gaps. A simple explanation for this trend can be obtained by comparing E_{HOMO} of the pure zinc porphyrin with E_{HOMO} of the protonated side groups given in Table 3. According to first order perturbation theory, the interaction between the HOMO of the pure zinc porphyrin and the side group HOMO should be proportional to the inverse of the energy difference and thus the smallest energy differences should result in the largest interactions. From the table it follows that it is indeed the HOMOs of the MOTPA, DTA and TPA side groups that are closest in energy to

Table 3 E_{HOMO} and E_{LUMO} for the pure zinc porphyrin backbone and the protonated side and anchor groups

Group	E_{HOMO} (eV)	E_{LUMO} (eV)
DMP	−7.65	2.08
TPA	−6.75	0.42
MOTPA	−6.49	0.58
TMP	−7.04	2.23
DTA	−6.70	0.99
DTBP	−8.22	1.61
EthynPhA	−8.56	−0.24
2CarboxyPropenA	−9.24	−1.04
2CyanoPropenA	−9.37	−1.03
Backbone ZnP	−6.79	−1.35

the HOMO of the pure zinc porphyrin, and thus our findings are in agreement with the expectations from perturbation theory. This suggests that future selection of side groups to be investigated could be guided by E_{HOMO} for the protonated side group.

Since the energy differences between the LUMOs of the side groups and the LUMO in the pure zinc porphyrin are significantly larger than the energy differences for the HOMOs (see Table 3) we can furthermore understand why E_{LUMO} is shifted less than E_{HOMO} upon functionalization of the porphyrins with the donating side groups. Visual inspection of the frontier orbitals of the pure porphyrin and two representative functionalized porphyrins is given in Fig. S5 in the ESI.† From these plots it follows that the change in the spatial shape of the HOMO/LUMO orbitals follows the trend observed for the energy shifts. Specifically, the HOMO of the DMP functionalized porphyrin is very similar to that of the pure zinc porphyrin, while the HOMO of the DTA functionalized porphyrin is pulled towards the side group. The differences in the LUMO orbitals for the three zinc porphyrins are also found to be minor compared to the differences in the HOMOs, which is again consistent with previously discussed results.

Exactly the same trends found for the donating side groups apply to the accepting anchor groups. Table 3 shows that the LUMO of the protonated 2CarboxyPropenA and 2CyanoPropenA anchor groups matches the LUMO of the zinc porphyrin much better than the LUMO of the protonated EthynPhA. This is consistent with the observation that functionalization of the zinc porphyrin by the two former anchor groups has the largest effect on the LUMO (by around −0.5 eV).

It is important to note that E_{gap} corresponds to the differences between the HOMO and the LUMO, *i.e.* the fundamental energy gap. In optical absorption, the attraction between the electron and the hole left behind (the electron–hole interaction) will allow for absorption of photons with energy less than E_{gap}. In Fig. S6 in the ESI,† we show that E_{gap} is essentially linearly correlated with the optical gap, E_1. The range of variation of E_1, however, is decreased from 2.1 eV observed for E_{gap} to approximately 0.6 eV. This is as expected since the Coulombic attraction between the electron and the hole depends strongly on the distance between the charges. Since the porphyrins with the largest E_{gap} have both the HOMO and the LUMO located on the porphyrin backbone, these porphyrins have a higher electron–hole interaction than porphyrins with smaller E_{gap} thus decreasing the range of E_1.

3.2 Level alignment quality

To calculate the level alignment quality as defined in eqn 2, we use two different models for the open circuit voltage, see Fig. 6. The first model assumes a perfect alignment of the dye HOMO with the redox level of the electrolyte and thus sets $V_{oc} = E_c - E_H$. This assumption is mostly used to illustrate the clean effect of the choice of dyes since a realistic cell will have a specific electrolyte and thus a fixed theoretical V_{oc}. However, the assumption of a perfect alignment may soon be very relevant to the emergence of high-efficiency DSSCs incorporating a variety of cobalt- and sulfur-based electrolytes.[4,34–36] Fig. 8 gives the level

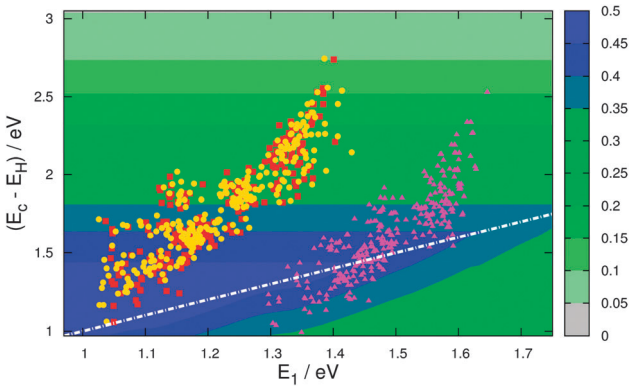

Fig. 8 η as a function of $E_c - E_H$ and E_1 with $V_{oc} = E_c - E_H$ (model 1). The points in the plot indicate the location of the investigated zinc porphyrins with the EthynPhA (purple triangle), 2CarboxyPropenA (red square) and 2CyanoPropenA (yellow circle) anchor groups using triplet ΔSCF values for E_1 and assuming TiO_2 as the semi-conductor with a conduction band located at −4.0 eV relative to vacuum. The white dotted line indicates the location where $E_c - E_H = E_1$.

alignment quality as a function of $E_c - E_H$ and E_1 under this assumption. The $E_c - E_H$ value is determined as the energy difference between the HOMO and the conduction band position of TiO_2, which is set to −4.0 eV relative to vacuum.[5] Using a single value for the conduction band position of TiO_2 is an assumption since the titania films used in DSSCs are typically amorphous films made from sintered nanoparticles of TiO_2 and can therefore be expected to display a band structure that deviates significantly from that of a crystalline semiconductor. Furthermore it can be noted that the charge injection rates differ depending on which crystallographic surface of TiO_2 is exposed.[37] However, having constructed the database the level alignment quality of the candidate dyes can always be re-ranked by using different input parameters, *e.g.* one might use an acid surface treatment to shift the quasi-Fermi level of the titania film.[38] However, using the value of −4.0 eV for the conduction band position, the predicted values for the investigated zinc porphyrins with the EthynPhA anchor group (purple triangle) are in general seen to be close to the maximum level alignment quality. Especially the candidates with an intermediate modification of the HOMO and thus intermediate E_1 and $E_c - E_H$, are within a predicted high-quality zone. To obtain a higher level alignment quality it is however desired to have a shift to lower E_1 values while retaining a fixed HOMO position. This can be achieved by tuning only the LUMO level, which is done by changing the anchor group. The desired shift is exactly observed for the zinc porphyrins with the 2CarboxyPropenA (red squares) and 2CyanoPropenA (yellow circles) anchor groups. Several of these candidates have values lying almost perfectly in the predicted highest level alignment quality zone with the best candidates having optical gaps (E_1) in the range 1.0–1.1 eV and HOMO levels positioned around 1.2 eV below E_c.

Another more experimentally realistic definition of V_{oc} can be obtained by assuming the use of the I^-/I_3^- redox pair, which remains the most common choice of DSSC electrolyte. Under such conditions V_{oc} will not be dictated by $E_c - E_H$ but rather by the dye independent $E_c - E_{red}$ where E_{red} is the redox potential

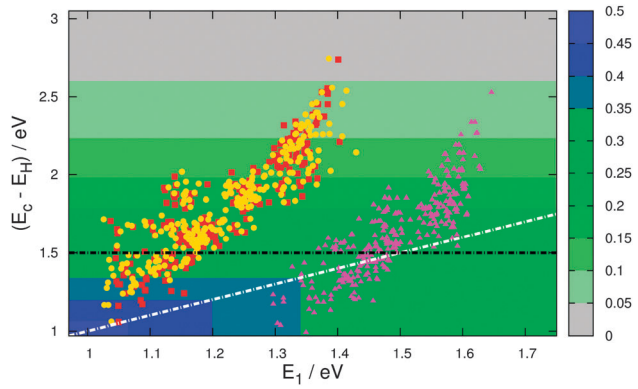

Fig. 9 η as a function of $E_c - E_H$ and E_1 with a constant value of V_{oc} = 1.0 V (model 2). The points in the plot indicate the location of the investigated zinc porphyrins with the EthynPhA (purple triangle), 2CarboxyPropenA (red square) and 2CyanoPropenA (yellow circle) anchor groups using triplet ΔSCF values for E_1 and assuming TiO_2 as the semi-conductor with a conduction band located at −4.0 eV relative to vacuum. The black dotted line indicates the lower limit of $E_c - E_H$ for dyes to be used with the I^-/I_3^- electrolyte (see text) and the white dotted line indicates the location where $E_c - E_H = E_1$.

of the electrolyte. A modified version of Fig. 8 where a constant V_{oc} = 1 V (model 2 in Fig. 6) has been used is presented in Fig. 9. One of the largest differences between Fig. 8 and 9 is the lowering of the optimal $E_c - E_H$ due to the removal of the linear relationship between the HOMO position and η. This effect is also the reason for the general reduction in the level alignment quality. As a consequence, the zinc porphyrins with the EthynPhA anchor group now all lie outside the highest level alignment quality zone. However, the porphyrins with the other two anchor groups and low $E_c - E_H$ and E_1 values are still predicted to be promising candidates. In general, the observed decrease in level alignment quality of model 2 compared to model 1 shows the importance of investigating new electrolytes with redox levels tailored to the dye molecules. In Fig. 8 and 9, a white dotted line indicating $E_c - E_H = E_1$ is added since excited electrons in molecules where $E_c - E_H > E_1$, due to thermal relaxation, can get trapped below the conduction band of the semi-conductor. However, since we in this study operate with a relatively high uncertainty we will not exclude any candidates from our investigation based on this criteria and the lines thus only serve as an indicator for the readers. Table 4 shows η for the ten best zinc porphyrin candidates with $V_{oc} = E_c - E_H$ (model 1). In the table a preference for porphyrins with the lowest possible values for E_1 is a striking feature. This can be explained by the fact that E_1 sets the lower limit of absorption and a lowering of this value thus leads to an increase in the range where the solar photons are converted to DSSC electrons. To further maximize the level alignment quality, an alignment of the E_1 and the $E_c - E_H$ energies is also favorable, since only excitation of the dye to a level above the conduction band of the semiconductor will give rise to the creation of a DSSC electron (see Fig. 6). However, a competition between this alignment and the linear dependence of the open-circuit voltage leads to a preference for a slightly higher $E_c - E_H$ energy for the model 1 case ($V_{oc} = E_c - E_H$). It can be noted that the value η_{dyn} = 0.49 obtained at $V_{oc} = E_1$ = 1.1 eV agrees well with the ultimate efficiency without recombination, u = 0.44 at E_1 = 1.1 eV, reported by Shockley and Queisser.[39] In the referred study they used black-body radiation for the solar spectrum in contrast to our use of the AM 1.5 G solar spectrum, which causes the small discrepancy. The recombination for a specific dye candidate is highly dependent on the overlap between the LUMO and the HOMO and an evaluation of this effect is beyond the scope of this paper.

Using the common I^-/I_3^- electrolyte, a theoretical $V_{oc} = E_c - E_{red}$ of around 0.9 V is obtainable.[5] However, since the dye regeneration by this electrolyte is only efficient with a potential difference between the redox-potential of the electrolyte and the HOMO of the dye of more than 0.6 V,[2,40–42] a value of $E_c - E_H \geq 1.5$ eV is required for an efficient regeneration of the dye candidates. A list of the ten best candidates with this restriction is given in Table 5. Here the preference for low values of E_1 and matching of E_1 and $E_c - E_H$ is again observed, but the predicted level alignment qualities (with V_{oc} = 1 V) are significantly lower compared to the case with no restriction on the $E_c - E_H$ energy, which clearly illustrates the short-comings of the iodide based electrolyte. On the other hand, a more diverse set of dyes employing all three anchor groups is predicted to possess high level alignment quality under these conditions. This leaves room for considering more practically oriented issues when choosing an anchor group. In Table 6 we present calculated $E_c - E_H$, E_1 and η values for five experimentally investigated dyes.[4,5] In general these dyes possess relatively high η values, but none of them lie within our calculated top ten

Table 4 The ten best zinc porphyrin candidates measured on η using a dynamic $V_{oc} = E_c - E_H$ (model 1)

A	R1	R2	R3	$(E_c - E_H)$ (eV)	E_1 (eV)	η_{con} [a]	η_{dyn} [b]
2CarboxyPropenA	DTA	MOTPA	MOTPA	1.16	1.05	0.42	0.49
2CyanoPropenA	TPA	MOTPA	MOTPA	1.17	1.03	0.42	0.49
2CyanoPropenA	DTA	MOTPA	MOTPA	1.17	1.03	0.42	0.49
2CarboxyPropenA	MOTPA	TPA	MOTPA	1.17	1.09	0.41	0.49
2CarboxyPropenA	TPA	MOTPA	MOTPA	1.20	1.09	0.40	0.48
2CarboxyPropenA	MOTPA	MOTPA	MOTPA	1.06	1.05	0.45	0.48
2CyanoPropenA	MOTPA	MOTPA	MOTPA	1.06	1.04	0.45	0.48
2CyanoPropenA	TMP	MOTPA	MOTPA	1.24	1.06	0.38	0.47
2CarboxyPropenA	MOTPA	TMP	MOTPA	1.24	1.15	0.38	0.47
2CarboxyPropenA	TMP	MOTPA	MOTPA	1.24	1.06	0.38	0.47

[a] V_{oc} = 1 V. [b] $V_{oc} = E_c - E_H$.

Table 5 The ten best zinc porphyrin candidates with $E_c - E_H \geq 1.5$ eV measured on η

A	R1	R2	R3	$(E_c - E_H)$ (eV)	E_1 (eV)	η_{con} [a]	η_{dyn} [b]
EthynPhA	H	MOTPA	TMP	1.50	1.45	0.29	0.43
EthynPhA	H	TMP	MOTPA	1.51	1.49	0.29	0.43
2CarboxyPropenA	TPA	TPA	DTA	1.51	1.12	0.29	0.43
2CyanoPropenA	TPA	MOTPA	H	1.50	1.17	0.29	0.43
EthynPhA	DMP	DMP	MOTPA	1.51	1.46	0.29	0.43
2CarboxyPropenA	MOTPA	DTA	H	1.51	1.09	0.29	0.43
EthynPhA	TMP	DTA	TPA	1.51	1.41	0.29	0.43
EthynPhA	TPA	H	TPA	1.51	1.47	0.29	0.43
EthynPhA	TPA	DMP	DTA	1.51	1.44	0.29	0.43
2CyanoPropenA	DTA	DTA	TPA	1.51	1.12	0.29	0.43

[a] $V_{oc} = 1$ V. [b] $V_{oc} = E_c - E_H$.

Table 6 Calculated $E_c - E_H$, E_1 and η values for five experimentally investigated dyes

Name	A	R1	R2	R3	$(E_c - E_H)$ (eV)	E_1 (eV)	η_{con} [a]	η_{dyn} [b]
T2P[c]	EthynPhA	TPA	H	TPA	1.51	1.47	0.29	0.43
T3P[c]	EthynPhA	TPA	TPA	TPA	1.45	1.46	0.30	0.44
MT3P[c]	EthynPhA	MOTPA	MOTPA	MOTPA	0.99	1.35	0.35	0.34
M3T2P[c]	EthynPhA	TPA	TMP	TPA	1.46	1.45	0.31	0.45
YD2-o-C8[d]	EthynPhA	DMP	DTA	DMP	1.77	1.48	0.20	0.36

[a] $V_{oc} = 1$ V. [b] $V_{oc} = E_c - E_H$. [c] Dyes reported by Liu *et al.*[5] [d] Modified version of the dye reported by Yella *et al.*[4]

candidates (model 1 in Table 4), which is mainly due to the high E_1 values predicted for these dyes. All dyes have the EthynPhA anchor group and an easy way to lower the E_1 values would be substituting this anchor group with the 2CarboxyPropenA or the 2CyanoPropenA anchor groups. Doing this for *e.g.* the MT3P dye, increases η_{dyn} from 0.34 to 0.48. Considering model 2 with the iodide induced restriction of $E_c - E_H \geq 1.5$ eV only the T2P and YD2-o-C8 dyes are relevant. To improve the level alignment quality of the rest of the candidates, a replacement of some of the side groups with *e.g.* the DTBP or H side groups may shift down the HOMO in energy thus increasing $E_c - E_H$. Substituting the center TMP group in M3T2P with the DTBP group *e.g.* increases $E_c - E_H$ from 1.46 eV to 1.61 eV. Thus some relatively simple substitutions of side and anchor groups can lead to a better level alignment for these five dyes.

4 Conclusions

We have presented a computational screening study of functionalized zinc porphyrins for use in dye sensitized solar cells. The screening procedure is based on DFT calculations providing an optimal balance between accuracy and computational cost. Specifically, the frontier energy levels and orbitals, together with the first optical excitation were calculated for 1029 zinc porphyrins with different electron donating sidegroups and electron accepting anchor groups. It was shown that this donor–π-acceptor architecture allows for selective tuning of the highest occupied (HOMO) and lowest unoccupied (LUMO) molecular orbitals by up to 2.1 eV, by varying the functional groups. The performance of the dyes was benchmarked by evaluating a loss-less DSSC level alignment quality with two different energy level alignment scenarios: (i) perfect matching of the electrolyte redox potential and the dye HOMO level, and (ii) a fixed redox potential and an overpotential of 0.6 eV corresponding to the conditions for the standard iodide electrolyte. We have furthermore investigated five experimentally used dyes and found that simple substitution of one side or one anchor group may improve the level alignment of these dyes. All investigated molecules and their calculated frontier energy levels are available in the database Computational Materials Repository at the web address http://cmr.fysik.dtu.dk/.

The fact that the estimated level alignment qualities are rather high with the best candidates lying very close to the maximum limit, indicates that losses, such as recombination losses and overpotentials associated with the redox charge transfer reactions, would be important to include as part of the screening in the future. On the other hand, with the present approach one can identify a small family of dye candidates with specific energy levels and orbital properties which could then be further assessed with respect to losses, stability, synthetic- or device-related considerations. In the future it may be interesting to investigate porphyrins with other side groups and metal centers as well as different π-spacers between the backbone and the anchor group and we plan to expand the database to include several of these. Furthermore the inclusion of two or more porphyrin backbones may also be included in the search for better dyes.

Acknowledgements

The authors would like to thank Angel Rubio and Franz Himpsel for inspiring discussions. KBØ and KST would further like to thank the Danish Council for Independent Research DFF-Sapere Aude program (grant no. 11-1051390) for financial support. JMGL acknowledges support from the Spanish Ministry of Economy and Competitiveness under Projects FIS2009-07083,

FIS2010-21282-C02-01 and FIS2012-30996 and through Ramon y Cajal grant RYC-2011-07782.

References

1 B. O'Regan and M. Grätzel, *Nature*, 1991, **353**, 737–740.
2 A. Hagfeldt, G. Boschloo, L. Sun, L. Kloo and H. Pettersson, *Chem. Rev.*, 2010, **110**, 6595–6663.
3 L.-L. Li and E. W.-G. Diau, *Chem. Soc. Rev.*, 2013, **42**, 291–304.
4 A. Yella, H.-W. Lee, H. N. Tsao, C. Yi, A. K. Chandiran, M. K. Nazeeruddin, E. W.-G. Diau, C.-Y. Yeh, S. M. Zakeeruddin and M. Grätzel, *Science*, 2011, **334**, 629–634.
5 B. Liu, W. Zhu, Y. Wang, W. Wu, X. Li, B. Chen, Y.-T. Long and Y. Xie, *J. Mater. Chem.*, 2012, **22**, 7434–7444.
6 G. H. Johannesson, T. Bligaard, A. V. Ruban, H. L. Skriver, K. W. Jacobsen and J. K. Nørskov, *Phys. Rev. Lett.*, 2002, **88**, 255506.
7 A. Franceschetti and A. Zunger, *Nature*, 1999, **402**, 60–63.
8 G. Ceder, Y.-M. Chiang, D. R. Sadoway, M. K. Aydinol, Y.-I. Jang and B. Huang, *Nature*, 1998, **392**, 694–696.
9 W. Setyawan, R. M. Gaume, S. Lam, R. S. Feigelson and S. Curtarolo, *ACS Comb. Sci.*, 2011, **13**, 382–390.
10 J. Hachmann, R. Olivares-Amaya, S. Atahan-Evrenk, C. Amador-Bedolla, R. S. Snchez-Carrera, A. Gold-Parker, L. Vogt, A. M. Brockway and A. Aspuru-Guzik, *J. Phys. Chem. Lett.*, 2011, **2**, 2241–2251.
11 R. Olivares-Amaya, C. Amador-Bedolla, J. Hachmann, S. Atahan-Evrenk, R. S. Sanchez-Carrera, L. Vogt and A. Aspuru-Guzik, *Energy Environ. Sci.*, 2011, **4**, 4849–4861.
12 N. M. O'Boyle, C. M. Campbell and G. R. Hutchison, *J. Phys. Chem. C*, 2011, **115**, 16200–16210.
13 I. Y. Kanal, S. G. Owens, J. S. Bechtel and G. R. Hutchison, *J. Phys. Chem. Lett.*, 2013, **4**, 1613–1623.
14 I. E. Castelli, T. Olsen, S. Datta, D. D. Landis, S. Dahl, K. S. Thygesen and K. W. Jacobsen, *Energy Environ. Sci.*, 2012, **5**, 5814–5819.
15 I. E. Castelli, D. D. Landis, K. S. Thygesen, S. Dahl, I. Chorkendorff, T. F. Jaramillo and K. W. Jacobsen, *Energy Environ. Sci.*, 2012, **5**, 9034–9043.
16 M.-J. Lee, M. P. Balanay and D. H. Kim, *Theor. Chem. Acc.*, 2012, **131**, 1–12.
17 W. Kohn and L. J. Sham, *Phys. Rev.*, 1965, **140**, A1133–A1138.
18 J. P. Perdew, K. Burke and M. Ernzerhof, *Phys. Rev. Lett.*, 1996, **77**, 3865–3868.
19 J. P. Perdew, K. Burke and M. Ernzerhof, *Phys. Rev. Lett.*, 1997, **78**, 1396.
20 J. Enkovaara, C. Rostgaard, J. J. Mortensen, J. Chen, M. Dulak, L. Ferrighi, J. Gavnholt, C. Glinsvad, V. Haikola, H. A. Hansen, H. H. Kristoffersen, M. Kuisma, A. H. Larsen, L. Lehtovaara, M. Ljungberg, O. Lopez-Acevedo, P. G. Moses, J. Ojanen, T. Olsen, V. Petzold, N. A. Romero, J. Stausholm-Møller, M. Strange, G. A. Tritsaris, M. Vanin, M. Walter, B. Hammer, H. Häkkinen, G. K. H. Madsen, R. M. Nieminen, J. K. Nørskov, M. Puska, T. T. Rantala, J. Schiøtz, K. S. Thygesen and K. W. Jacobsen, *J. Phys.: Condens. Matter*, 2010, **22**, 253202.
21 A. H. Larsen, M. Vanin, J. J. Mortensen, K. S. Thygesen and K. W. Jacobsen, *Phys. Rev. B: Condens. Matter Mater. Phys.*, 2009, **80**, 195112.
22 S. Bahn and K. W. Jacobsen, *Comput. Sci. Eng.*, 2002, **4**, 56–66.
23 M. J. Frisch, G. W. Trucks, H. B. Schlegel, G. E. Scuseria, M. A. Robb, J. R. Cheeseman, G. Scalmani, V. Barone, B. Mennucci, G. A. Petersson, H. Nakatsuji, M. Caricato, X. Li, H. P. Hratchian, A. F. Izmaylov, J. Bloino, G. Zheng, J. L. Sonnenberg, M. Hada, M. Ehara, K. Toyota, R. Fukuda, J. Hasegawa, M. Ishida, T. Nakajima, Y. Honda, O. Kitao, H. Nakai, T. Vreven, J. A. Montgomery Jr, J. E. Peralta, F. Ogliaro, M. Bearpark, J. J. Heyd, E. Brothers, K. N. Kudin, V. N. Staroverov, R. Kobayashi, J. Normand, K. Raghavachari, A. Rendell, J. C. Burant, S. S. Iyengar, J. Tomasi, M. Cossi, N. Rega, J. M. Millam, M. Klene, J. E. Knox, J. B. Cross, V. Bakken, C. Adamo, J. Jaramillo, R. Gomperts, R. E. Stratmann, O. Yazyev, A. J. Austin, R. Cammi, C. Pomelli, J. W. Ochterski, R. L. Martin, K. Morokuma, V. G. Zakrzewski, G. A. Voth, P. Salvador, J. J. Dannenberg, S. Dapprich, A. D. Daniels, O. Farkas, J. B. Foresman, J. V. Ortiz, J. Cioslowski and D. J. Fox, *Gaussian 09 Revision B.01*, Gaussian Inc., Wallingford, CT, 2009.
24 H.-J. Werner, P. J. Knowles, G. Knizia, F. R. Manby, M. Schütz, P. Celani, T. Korona, R. Lindh, A. Mitrushenkov, G. Rauhut, K. R. Shamasundar, T. B. Adler, R. D. Amos, A. Bernhardsson, A. Berning, D. L. Cooper, M. J. O. Deegan, A. J. Dobbyn, F. Eckert, E. Goll, C. Hampel, A. Hesselmann, G. Hetzer, T. Hrenar, G. Jansen, C. Köppl, Y. Liu, A. W. Lloyd, R. A. Mata, A. J. May, S. J. McNicholas, W. Meyer, M. E. Mura, A. Nicklass, D. P. O'Neill, P. Palmieri, K. Pflüger, R. Pitzer, M. Reiher, T. Shiozaki, H. Stoll, A. J. Stone, R. Tarroni, T. Thorsteinsson, M. Wang and A. Wolf, *MOLPRO, version 2010.1*, a package of *ab initio* programs, 2010, see http://www.molpro.net.
25 C. Lee, W. Yang and R. G. Parr, *Phys. Rev. B: Condens. Matter Mater. Phys.*, 1988, **37**, 785–789.
26 A. D. Becke, *J. Chem. Phys.*, 1993, **98**, 5648–5652.
27 P. J. Stephens, F. J. Devlin, C. F. Chabalowski and M. J. Frisch, *J. Phys. Chem.*, 1994, **98**, 11623–11627.
28 J. Gavnholt, T. Olsen, M. Engelund and J. Schiøtz, *Phys. Rev. B: Condens. Matter Mater. Phys.*, 2008, **78**, 075441.
29 E. Skulason, G. S. Karlberg, J. Rossmeisl, T. Bligaard, J. Greeley, H. Jonsson and J. K. Norskov, *Phys. Chem. Chem. Phys.*, 2007, **9**, 3241–3250.
30 J. E. B. Randles, *Trans. Faraday Soc.*, 1956, **52**, 1573–1581.
31 E. Kötz, H. Neff and K. Müller, *J. Electroanal. Chem.*, 1986, **215**, 331–344.
32 J. M. Garcia-Lastra, C. Rostgaard, A. Rubio and K. S. Thygesen, *Phys. Rev. B: Condens. Matter Mater. Phys.*, 2009, **80**, 245427.
33 M. Gouterman, *J. Mol. Spectrosc.*, 1961, **6**, 138–163.
34 J.-H. Yum, E. Baranoff, F. Kessler, T. Moehl, S. Ahmad, T. Bessho, A. Marchioro, E. Ghadiri, J.-E. Moser, C. Yi, M. K. Nazeeruddin and M. Grätzel, *Nat. Commun.*, 2012, **3**, 631.
35 M. Wang, N. Chamberland, L. Breau, J.-E. Moser, R. Humphry-Baker, B. Marsan, S. M. Zakeeruddin and M. Grätzel, *Nat. Chem.*, 2010, **2**, 385–389.

36 X. Xu, K. Cao, D. Huang, Y. Shen and M. Wang, *J. Phys. Chem. C*, 2012, **116**, 25233–25241.
37 N. Martsinovich and A. Troisi, *Phys. Chem. Chem. Phys.*, 2012, **14**, 13392–13401.
38 A. Allegrucci, N. A. Lewcenko, A. J. Mozer, L. Dennany, P. Wagner, D. L. Officer, K. Sunahara, S. Mori and L. Spiccia, *Energy Environ. Sci.*, 2009, **2**, 1069–1073.
39 W. Shockley and H. J. Queisser, *J. Appl. Phys.*, 1961, **32**, 510–519.
40 C. Bauer, G. Boschloo, E. Mukhtar and A. Hagfeldt, *J. Phys. Chem. B*, 2002, **106**, 12693–12704.
41 J. N. Clifford, E. Palomares, M. K. Nazeeruddin, M. Grätzel and J. R. Durrant, *J. Phys. Chem. C*, 2007, **111**, 6561–6567.
42 D. Kuciauskas, M. S. Freund, H. B. Gray, J. R. Winkler and N. S. Lewis, *J. Phys. Chem. B*, 2000, **105**, 392–403.

Appendix C

Paper II

Optimizing porphyrins for dye sensitized solar cells using large-scale *ab initio* calculations
K. B. Ørnsø, C. S. Pedersen, J. M. Garcia-Lastra and K. S. Thygesen
Phys. Chem. Chem. Phys., **2014**, *16*, 16246-16254

PCCP

PAPER

Optimizing porphyrins for dye sensitized solar cells using large-scale *ab initio* calculations†

Cite this: *Phys. Chem. Chem. Phys.*, 2014, **16**, 16246

Kristian B. Ørnsø,*[a] Christian S. Pedersen,[a] Juan M. Garcia-Lastra[ab] and Kristian S. Thygesen[a]

Received 25th March 2014,
Accepted 13th June 2014

DOI: 10.1039/c4cp01289e

www.rsc.org/pccp

In the search for sustainable energy sources, dye sensitized solar cells (DSSCs) represent an attractive solution due to their low cost, relatively high efficiencies, and flexible design. Porphyrin-based dyes are characterized by strong absorption in the visible part of the spectrum and easy customization allowing their electronic properties to be controlled by structural variations. Here we present a computational screening study of more than 5000 porphyrin-based dyes obtained by modifying the porphyrin backbone (metal center and axial ligands), substituting hydrogen by fluorine, and adding different side and anchoring groups. Based on the calculated frontier orbital energies and optical gaps we quantify the energy level alignment with the TiO_2 conduction band and different redox mediators. An analysis of the energy level–structure relationship reveals a significant structural diversity among the dyes with the highest level alignment quality, demonstrating the large degree of flexibility in porphyrin dye design. As a specific example of dye optimization, we show that the level alignment of the high efficiency record dye YD2-o-C8 [Yella *et al.*, *Science*, 2011, **334**, 629–634] can be significantly improved by modest structural variations. All the presented data have been stored in a publicly available database.

1 Introduction

As the negative environmental consequences of fossil energy production and use are growing, the search for new efficient technologies enabling harvesting and conversion of solar photons into electrical or chemical energy is becoming increasingly important. Since the emergence of the first efficient system in 1991,[1] dye sensitized solar cells (DSSCs)[2] have been considered promising and cost-efficient candidates for photovoltaic energy conversion. Compared to conventional solar cell systems, some of the unique properties of DSSCs are their simple fabrication and low material cost, flexibility, both in terms of mechanical properties and architectural design, and high efficiency under low illumination conditions.[3]

A (standard) DSSC is a photoelectrochemical system which converts photons from the sun into electrical work in a three-step process. First, the photons are absorbed by a molecular dye which is anchored to a semi-conductor nanoparticle (typically TiO_2). Next, the excited electrons on the dye are transferred to the conduction band of the semiconductor and extracted to an external circuit. In the last step the electron is transferred from the counter electrode and back to the dye using an electrolyte. For a dye to yield a high efficiency in this type of setup there are three essential requirements which should be fullfilled: (i) the energy of the highest occupied molecular orbital (HOMO) should be smaller than the redox potential of the electrolyte. (ii) The lowest unoccupied molecular orbital (LUMO) should lie above the conduction band edge of the semiconductor. (iii) The absorption spectrum of the dye should have a large overlap with the solar spectrum. In addition to these level alignment criteria, the efficiency of the DSSC depends on a number of other processes including the charge injection from the dye to the semiconductor, the regeneration of the oxidized dye by the electrolyte, losses due to charge transport and recombination *etc.* In the present study we shall focus on the criteria (i)–(iii).

The high absorption of visible light in combination with the many possibilities of functionalizing porphyrins makes these dyes excellent candidates for use in DSSCs.[4–15] In particular, the so-called donor–π–acceptor scheme in which the HOMO of the functionalized porphyrin dye is located on the donor side groups while the LUMO is mostly located on the accepting anchor group has led to DSSCs with very high efficiencies including a record efficiency of 12.3%.[16] To improve the efficiency of DSSCs further it is natural to resort to computational methods that allow for

[a] *Center for Atomic-scale Materials Design, Department of Physics, Technical University of Denmark, Fysikvej, 2800 Kgs. Lyngby, Denmark. E-mail: krbt@fysik.dtu.dk*

[b] *Department of Energy Conversion, Technical University of Denmark, Frederiksborgvej 399, 4000 Roskilde, Denmark*

† Electronic supplementary information (ESI) available: Detailed figures showing the calculated level alignment quality, orbital visualizations, figures giving the trends in frontier orbital energies of all anchor groups and details of dyes with the highest/lowest values of the different properties investigated. See DOI: 10.1039/c4cp01289e

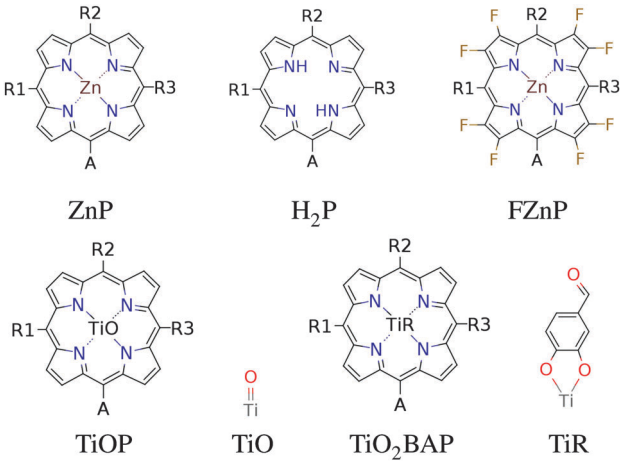

Fig. 1 The porphyrin backbones investigated in this work. The axial ligands used for TiOP and TiO_2BAP are shown next to the backbones.

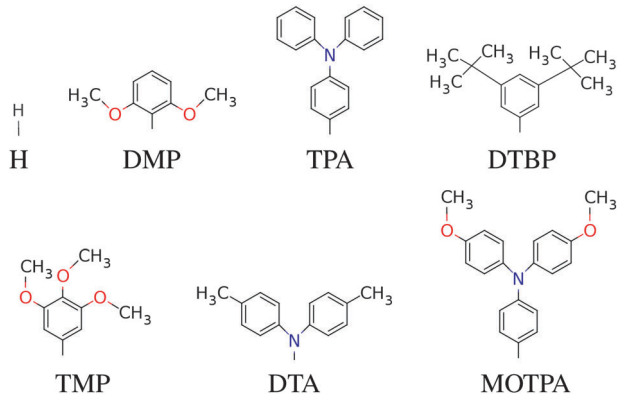

Fig. 2 The donor groups investigated in this work. Note that when the fluorinated FZnP backbone is used, the H side group is replaced by the F group consisting of a fluorine atom.

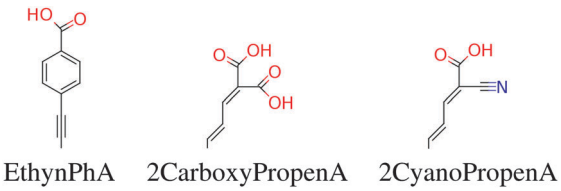

Fig. 3 The accepting anchor groups investigated in this work.

fast exploration of the vast space of molecular structures. Thanks to the enormous growth in computer power, high-throughput computational screening is rapidly becoming an essential tool for accelerated materials discovery and has recently been applied in a wide range of areas.[17–27]

We have previously reported a computational screening study of zinc porphyrin based dyes,[28] in which we investigated the effect of changing side and anchor groups. However, modifying the backbone by exchanging zinc as the metal center can alter the electronic structure of the dye significantly.[29,30] In addition, replacing hydrogen with fluorine in copper-phthalocyanine has been shown to produce a significant lowering of the frontier orbital energies.[31] Furthermore, using a Ti^{4+}metal center in the porphyrin allows for the use of axial ligands. As shown by Pickup *et al.* for titanium phthalocyanines this can have a large impact on the frontier orbitals.[32] Inspired by these results, we have performed extensive electronic structure calculations to systematically explore the effect of fluorination of the zinc porphyrins as well as the effect of changing the metal center of the porphyrin dyes including titanium with the two axial ligands investigated by Pickup *et al.*[32] We explore the systematic trends in frontier orbital energies, optical gaps and level alignment quality essential for the DSSC performance for a total of 5145 different porphyrin based dyes with a high structural diversity. All calculated data are available in the public database Computational Materials Repository at the web address http://cmr.fysik.dtu.dk/.

2 Methods

In this paper we have calculated the frontier orbital energies, lowest optical excitation energies and level alignment quality for porphyrins with different metal centers and functionalized by different side groups and anchor groups. The investigated metal centers are Zn and Ti which are also compared to using the metal-free porphyrin. The use of a Ti^{4+} metal center leads to the requirement of having an axial anionic ligand bound directly to the metal center in order to obtain a neutral porphyrin molecule. In this study we have chosen to use the simple O^{2-} ligand and the more complicated $OCHC_6H_3OO^{2-}$ ligand as axial ligands. This leads to the five different porphyrin backbones shown in Fig. 1. In the figure, for all backbones, the R1, R2 and R3 labels denote side group locations and A denotes the anchor group location. A total of seven different side groups (see Fig. 2) and three different anchor groups (see Fig. 3) have been chosen for this study.[8,10,16,28] Note that when the fluorinated FZnP backbone is used, the H side group is replaced by the F group consisting of a fluorine atom. Apart from accepting electrons, the anchor groups should also be able to bind to the semi-conductor surface, which is achieved by using anchor groups with carboxylic acid groups. All quantum mechanical calculations are performed using density functional theory (DFT)[33] with the Perdew–Burke–Ernzerhof (PBE)[34] exchange–correlation functional as implemented in the GPAW code.[35] For all standard calculations we have used a basis set of numerical atomic orbitals[36] (LCAO mode) with a double-ζ polarized basis set, a grid-spacing of 0.18 Å and a unit cell with a 5.0 Å vacuum added on both sides of the molecule in all directions. All structures have been optimized using the Broyden–Fletcher–Goldfarb–Shanno (BFGS) method as implemented in the Atomic Simulation Environment (ASE)[37] until all forces are below 0.05 eV $Å^{-1}$. After the geometry optimization the locations of the HOMO, E_{HOMO}, and LUMO, E_{LUMO} are calculated as the ionization potential I_P and electron affinity E_A of the molecule. Thus the the resulting gap, E_{gap}, is given by:

$$\begin{aligned} E_{gap} &= E_{LUMO} - E_{HOMO} \\ &= (E[-1] - E[0]) - (E[0] - E[+1]) \\ &= I_P - E_A \end{aligned} \quad (1)$$

where $E[0]$ is the ground state total energy and $E[-1]$ and $E[+1]$ is the total energy of the negatively and positively charged ions of the molecule in the ground state geometry, respectively. This definition of E_{gap} avoids the use of Kohn–Sham eigenvalues which are well-known to be inaccurate within PBE. In addition to the fundamental gap, the optical gap, E_1, which includes the electron–hole interaction, has been calculated. The calculation of E_1 is done by forcing the molecule to the triplet groundstate by fixing the magnetic moment, and thus promoting one of the two electrons in the HOMO to the LUMO. We use the triplet excitation energy rather than the singlet excitation because this is technically simpler to compute. We have previously shown for a number of Zn-porhyrins that the singlet and triplet excitations are within 0.3 eV and that their dependence on the molecular structure is very similar.[28] In the same study we furthermore showed that computed E_{HOMO} and E_1 values compared well to experimental values.[8,28] However, we underline that it is the presented trends rather than the absolute values which are the main focus of this paper. We also stress that the effect of hybridization and image charge screening by the TiO_2 surface as well as the effect of the solvent on the HOMO energies have not been included in the calculations.[38–41] However, we do not believe that this will have a significant impact on the qualitative trends. In order to identify the optimal electronic spectrum of the dyes relative to the semiconductor conduction band edge, we have previously defined a loss-less level alignment quality of a DSSC:[28]

$$\eta = \frac{eV_{oc}\int_{E_c-E_H}^{\infty} \Theta(E-E_1)\cdot I_{solar}(E)\mathrm{d}E}{\int_0^{\infty} E\cdot I_{solar}(E)\mathrm{d}E} \qquad (2)$$

where

$$\Theta(E-E_1) = \begin{cases} 1 & \text{for} \quad E-E_1 \geq 0 \\ 0 & \text{for} \quad E-E_1 < 0 \end{cases}$$

Here E_c–E_H is the distance from the HOMO level to the conduction band, E_1 is the optical gap of the dye, $\Theta(E-E_1)$ is a step function representing the absorption of the dye molecules, $I_{solar}(E)$ is the photon flux of the ASTM G-173-03 (AM 1.5 G) solar spectrum, and eV_{oc} is the open-circuit voltage multiplied with the charge of the electron. In the following we assume that E_c = −4.0 eV and V_{oc} = 1.0 V consistent with using TiO_2 as the semi-conductor and I^-/I_3^- as the redox mediator. We note that using a single value of E_c for all dyes is an assumption, since different dyes will affect the conduction band *via* interface–dipole interactions.[42] Furthermore, using the $\Theta(E-E_1)$ step function to represent the dye absorption is based on the assumption that all solar photons with an energy higher than E_1 of the dye are absorbed by the dye molecules. We thus assume that all investigated dyes regardless of their size cover the nano-structured TiO_2 to effectively form several layers of the dye in the device and that vibrational modes enhance the oscillator strength of any symmetry-forbidden transitions in the dyes.[43] The level alignment quality only describes the alignment between the dye and the semi-conductor and is thus only one component in order to obtain a high efficiency in a DSSC. In reality many other critical factors influence the overall efficiency of a DSSC and it should be stressed that we do not claim to include these in the present study.

3 Results and discussion

Histograms of the computed E_{HOMO} and E_{LUMO} as well as the level alignment quality are shown in Fig. 4 and 5, respectively. (The molecules with the largest and smallest E_{HOMO}, E_{LUMO}, E_{gap} and E_1 are listed in Table S1 in the ESI.†) The entire data set spans a range of 2.3 eV for E_{HOMO}, 1.3 eV for E_{LUMO}, 2.4 eV for E_{gap}, and 0.8 eV for E_1. Furthermore, a great part of the presented dyes are expected to have highly optimal level alignment with respect to the TiO_2 conduction band and the I^-/I_3^- redox mediator as can be seen in Fig. 5. Here, thousands of candidates with a high structural diversity exceed the predicted level alignment quality of the record holding YD2-o-C8[16] dye

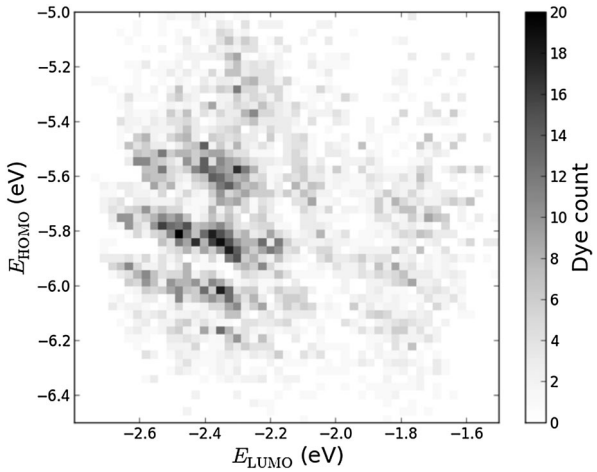

Fig. 4 2D histogram of obtained pairs of E_{HOMO} and E_{LUMO} for all 5145 investigated dyes.

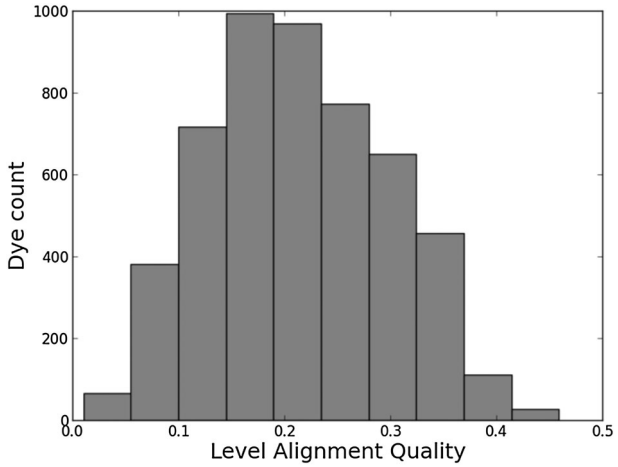

Fig. 5 Level alignment quality histogram for all 5145 investigated dyes. As a reference, the calculated level alignment quality of the record holding YD2-o-C8[16] dye is 0.2.

(η = 0.2). These results demonstrate the large degree of flexibility of the electronic properties of functionalized porphyrins and show that many different design strategies could be followed to control the level alignment. In the following the effects of the different modifications on the frontier orbital energies, lowest optical excitation, and level alignment quality are described in more detail and an overview of the best candidates is provided.

3.1 Porphyrin backbones

The effect of exchanging the central metal atom can be investigated by comparing porphyrin dyes with the ZnP, H_2P and TiOP backbones (see Fig. 1). Fig. 6 shows the frontier orbital energies of the three different porphyrin backbones using the EthynPhA anchoring group and varying the side groups. It can be seen that replacing ZnP by TiOP results in a small red shift of both the HOMO and the LUMO. However, it is also clear that the three backbones exhibit the same trends depending on the side groups. In particular, the side groups affect the HOMO levels in a similar way whereas the LUMO is almost not affected (see Table S2 in ESI†). From Fig. S1 in the ESI† it is further observed that varying the anchor group shifts the LUMO without affecting the HOMO. For the ZnP backbone these trends were explained by first order perturbation theory[28] and more specifically by the match between E_{HOMO} and E_{LUMO} of the bare backbone with E_{HOMO} of the side groups and E_{LUMO} of the anchor groups, respectively. For comparison, E_{HOMO} and E_{LUMO} of the different bare backbone structures are given in Table 1.‡ From the table it is noted that E_{HOMO} and E_{LUMO} of the bare backbones vary only up to 0.3 eV between ZnP, H_2P and TiOP. This suggests that the orbital energy match between the backbone and the side and anchor groups is retained for all three backbones thus explaining the similar trends as shown in Fig. 6.

For two specific dyes, Fig. S2 and S3 in the ESI† give a visual impression of the effect on the HOMO wave functions upon changing the metal center. In the figures it can be seen that substituting the Zn core atom for H_2 only makes little difference in terms of the spatial distribution of the HOMO as the metal core atoms carry no weight of the molecular orbital. On the other hand, an interesting effect appears when substituting with the TiO center. In this case the O atom, as opposed to the metal centres, does carry part of the HOMO. This may explain the lower E_{HOMO} of the TiOP backbone relative to ZnP and H_2P as shown in Table 1, and indicates that the frontier orbitals of the titanium porphyrins may be altered by modifying the axial ligand as will be discussed in greater details later.

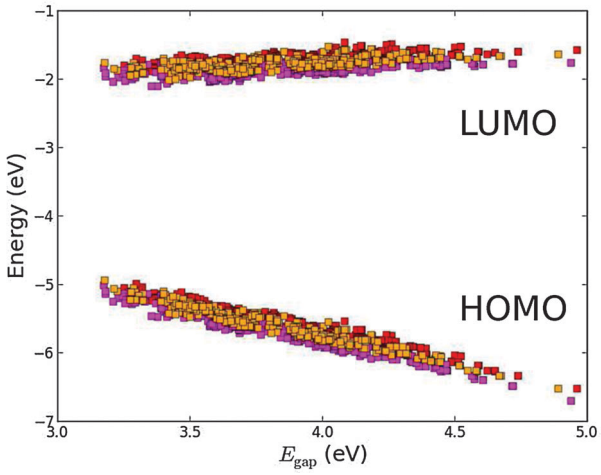

Fig. 6 Calculated E_{HOMO} and E_{LUMO} relative to vacuum ordered by the resulting E_{gap} of functionalized porphyrins with the EthynPhA anchor group and the ZnP (red), H_2P (orange) and TiOP (magenta) backbones.

Table 1 E_{HOMO} and E_{LUMO} for the bare ZnP, H_2P, TiOP, TiO_2BAP and FZnP backbones

Backbone	E_{HOMO}	E_{LUMO}
ZnP	−6.71	−1.10
H_2P	−6.72	−1.20
TiOP	−6.88	−1.37
TiO_2BAP	−6.56	−1.80
FZnP	−7.20	−1.85

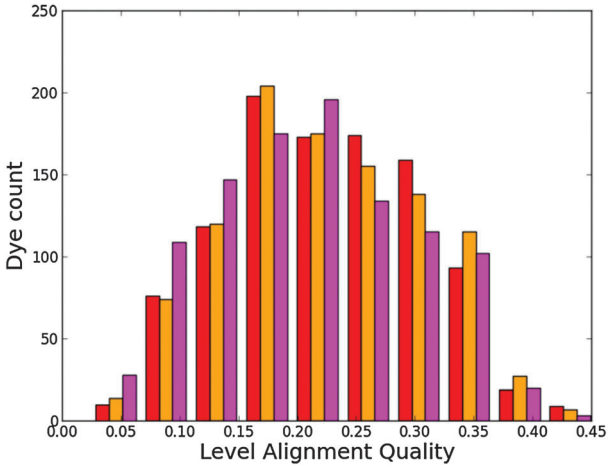

Fig. 7 Level alignment quality histogram for functionalized porphyrins with the ZnP (red), H_2P (orange) and TiOP (magenta) backbones.

Fig. 7 gives a histogram for the level alignment quality of all molecules using either of the three backbones. Clearly, it is possible to obtain very high level alignment qualities for several dyes using any of the three backbones. However, for the three backbones, the best level alignment quality is generally obtained for different side and anchor groups. This is visualized in Fig. S4 in the ESI† where the level alignment quality for all combinations of dyes with the three backbones as a function of the optical gap, E_1, and the energy difference between the conduction band of TiO_2 and the HOMO level of the dyes, $E_c - E_H$, are visualized. Here, it is observed that for all backbones, in order to yield a high level alignment quality, it is necessary to use highly donating side groups giving a low $E_c - E_H$ value. To further optimize the level alignment quality it is necessary to have a low E_1 value, which is mainly influenced

‡ Note that E_{HOMO} and E_{LUMO} of ZnP differ slightly from the previously published values as those values were calculated using a different basis set.

by the LUMO position. The latter is controlled by the anchor group and it is generally observed that using the 2CarboxyPropenA or 2CyanoPropenA anchor groups yields more dyes with a high level alignment quality. This observation is especially concerned with dyes with the ZnP backbone for which the use of the popular EthynPhA anchor group significantly lowers the number of dyes with a high level alignment quality. Thus, it may be beneficial for these dyes to replace the zinc atom to obtain a better level alignment quality.

3.2 Axial ligands

By employing a Ti^{4+} metal center we introduce the possibility of using axial ligands directly bound to the titanium metal center. As discussed, using a double bonded oxygen to form the TiOP backbone shifts the weight of the HOMO towards the axial ligand. Thus, we now investigate the effect of replacing the oxygen with the O_2BA ligand. Fig. 8 shows a plot of the frontier orbital energies of the TiOP and TiO_2BAP porphyrin backbones using the EthynPhA anchoring group and varying the side groups (see Fig. S5 in the ESI† for results with all anchor groups). It is observed that the general trends discussed previously are retained and that the fundamental gaps of the dyes with the TiO_2BAP backbone are lower due to generally lower E_{LUMO} values. Furthermore, a significant decrease in the range of E_{gap} is observed for TiO_2BAP compared to TiOP. This is seen to be due to the lower range of E_{HOMO} values indicating a smaller interaction between the side groups and the backbone. This effect may in turn be explained by looking at the spatial shape of the HOMOs for similar dyes with different backbones shown in Fig. S6 and S7 in the ESI.† Here, it is observed that for the TiO_2BAP backbone the HOMO is mostly located at the O_2BA axial ligand and thus the interaction between the side groups and the backbone is reduced. Apart from modifying the energy of the frontier orbitals of the dye, the relatively large weight of the HOMO on the axial ligand can further influence the regeneration of the dye, since this involves interaction between the redox mediator and the HOMO.

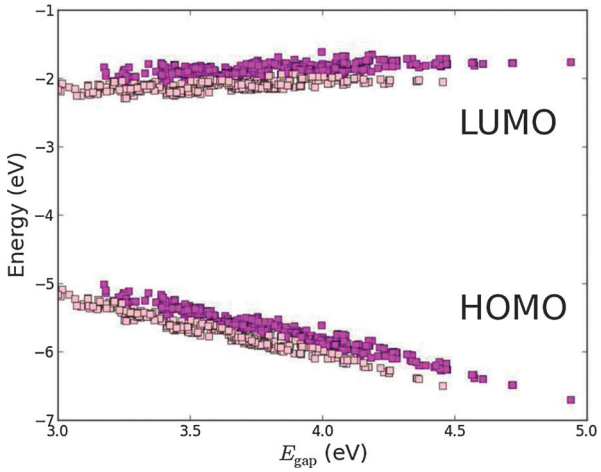

Fig. 8 Calculated E_{HOMO} and E_{LUMO} relative to vacuum ordered by the resulting E_{gap} of functionalized porphyrins with the EthynPhA anchor group and the TiOP (magenta) and TiO_2BAP (pink) backbones.

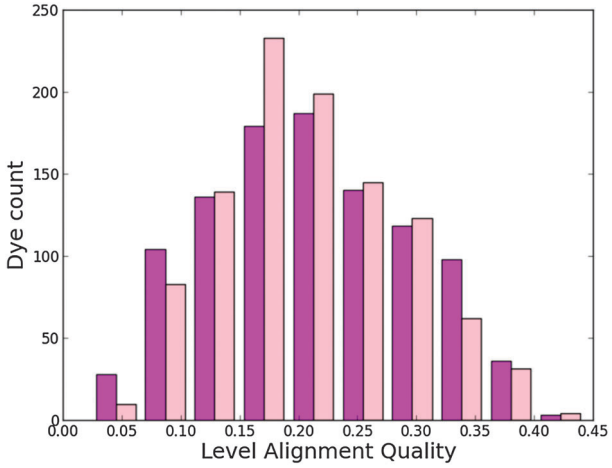

Fig. 9 Level alignment quality histogram for functionalized porphyrins with the TiOP (magenta) and TiO_2BAP (pink) backbones.

Fig. 9 shows a histogram of the level alignment quality using either of the two backbones. It can be seen that the TiOP backbone yields slightly more candidates with high level alignment quality, but in general it is possible to obtain a high level alignment quality using either of the axial ligands introducing more flexibility in designing dyes. The optimal choice of side and anchor groups needed to obtain a high level alignment quality is very similar for the two backbones. This is visualized in Fig. S8 in the ESI,† which shows the calculated level alignment quality for all dye combinations with the two backbones as a function of E_1 and $E_c - E_H$. For both backbones the highest level alignment quality values are found for dyes with highly donating side groups in combination with either 2CarboxyPropenA or 2CyanoPropenA anchor groups. The main difference between the two backbones concerning the level alignment quality is found when using the EthynPhA anchor group. Here, using the TiO_2BAP backbone yields a greater number of dyes with a high level alignment quality.

3.3 Substitution of hydrogen with fluorine

A third method for tweaking the electronic structure of the porphyrin dyes is to replace the hydrogen atoms in the porphyrin backbone with fluorine atoms. Here, the electron transfer from the backbone to the fluorine atoms is expected to generate an electrostatic potential that shifts down the energy of the orbitals localized on the backbone.[31,44] This effect is shown in Fig. 10 which shows the frontier orbital energies of the ZnP and FZnP porphyrin backbones using the EthynPhA anchor group and varying the side groups (see Fig. S9 in the ESI† for results with all anchor groups). Apart from exhibiting the same trends as discussed for all other backbones, the fluorinated dyes have significantly lower E_{LUMO} values. As the LUMO is mostly localized on the backbone (and the anchor group) this decrease can be ascribed to the electrostatic potential generated by the fluorine atoms. For the E_{HOMO} values the picture is more complicated as

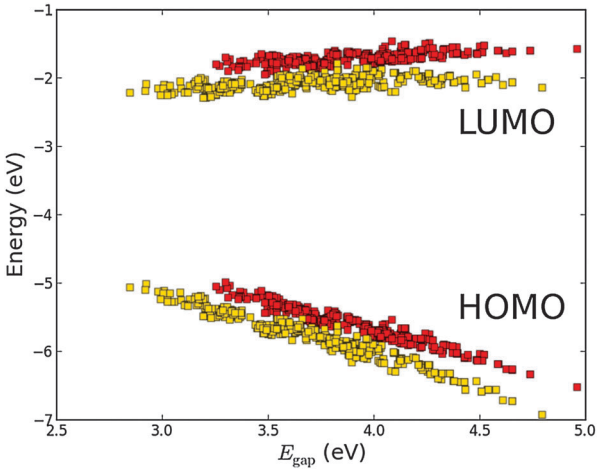

Fig. 10 Calculated E_{HOMO} and E_{LUMO} relative to vacuum ordered by the resulting E_{gap} of functionalized porphyrins with the EthynPhA anchor group and the ZnP (red) and FZnP (yellow) backbones.

only dyes with a large fundamental gap have HOMOs which are localized on the backbone whereas dyes with more donating side groups have HOMOs which are localized more on the side groups.[28] Thus, it can be expected that the E_{HOMO} values for fluorinated dyes with large E_{gap} will be more affected than those with a small E_{gap}. This is indeed shown in Fig. 10. From Fig. S10 and S11 in the ESI,† which show the HOMO and LUMO wave functions for both fluorinated and non-fluorinated dyes, it is observed that the change in shape of the orbitals upon fluorination is negligible and thus the altered electrostatic potential must be the main effect of the fluorination.

Fig. 11 shows a histogram for the level alignment quality of all dyes with either hydrogen or fluorine in the porphyrin backbone. From the figure it is clear that the FZnP backbone yields slightly more candidates with high level alignment quality, but also dramatically increases the number of candidates with very low level alignment quality. Fluorination thus

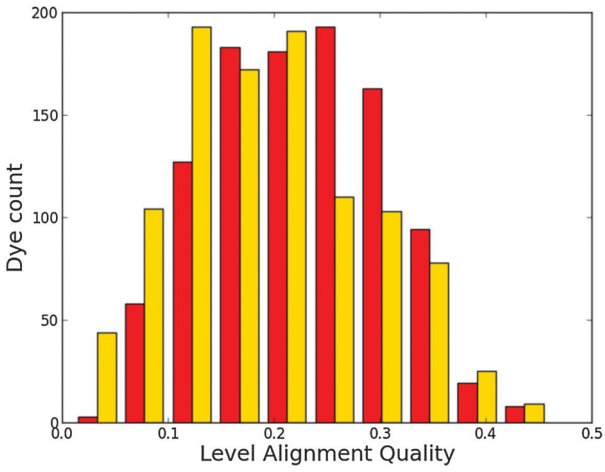

Fig. 11 Level alignment quality histogram for functionalized porphyrins with the ZnP (red) and FZnP (yellow) backbones.

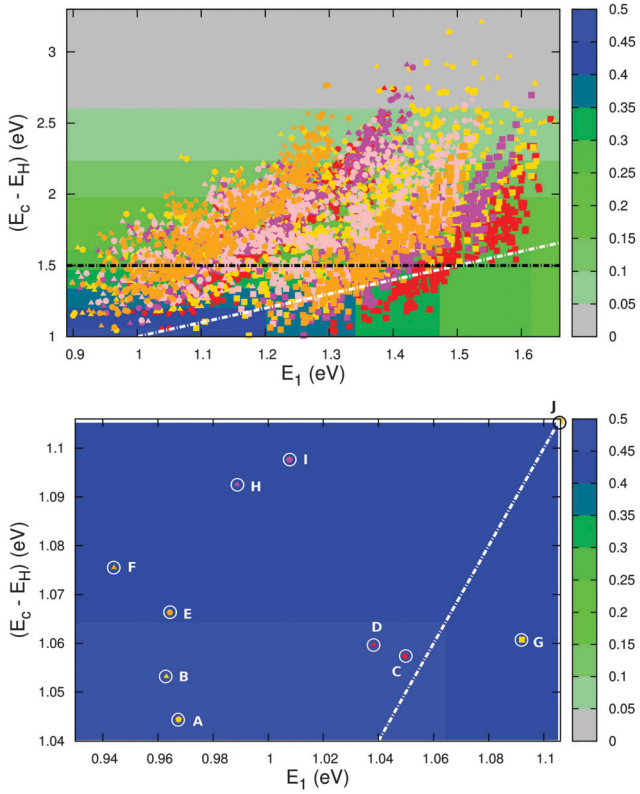

Fig. 12 Top: calculated level alignment quality as a function of the optical gap, E_1, and the energy difference between the conduction band of TiO_2 and the HOMO level of the dyes, $E_c - E_H$, for candidates with the ZnP (red), H_2P (orange), TiOP (magenta), TiO_2BAP (pink) and FZnP (yellow) backbones and the EthynPhA (square), 2CarboxyPropenA (circle) and 2CyanoPropenA (triangle) anchor groups. The black dotted line indicates the lower limit of $E_c - E_H$ for dyes to be used with the I^-/I_3^- electrolyte and the white dotted line indicates where $E_c - E_H = E_1$. Bottom: zoom of the above figure onto the region with the highest level alignment quality. The letters identify the top ten candidates and correspond to the letters given in Table 2.

have a significant impact on specific dyes and the resulting level alignment quality. This can be further understood from Fig. S12 in the ESI† in which the level alignment quality is given as a function of E_1 and $E_c - E_H$. Here, highly donating side groups as discussed for all backbones lead to the highest level alignment quality. However, in contrast to dyes with the ZnP backbone, the number of dyes with a high level alignment quality employing the FZnP backbones is similar for all anchor groups leading to more structural flexibility.

3.4 Optimizing level alignment

Fig. 12 (top) shows the calculated level alignment quality for all 5145 dye candidates presented in this study as a function of E_1 and the energy difference between the conduction band of TiO_2 and the HOMO level of the dyes, $E_c - E_H$. The black dotted line indicates where $E_{HOMO} = -5.50$ eV which corresponds to the upper limit of E_{HOMO} for dyes used in a DSSC with the I^-/I_3^- redox pair. This strict limit stems from the need to have a 0.6 V potential difference between E_{HOMO} and the redox potential of the I^-/I_3^- redox pair in order to drive the charge transfer.[2,45–47]

Table 2 Top ten candidates measured by the level alignment quality under the assumption that $E_c = -4.0$ eV and $V_{oc} = 1.0$ V. The letters correspond to the letters in the bottom part of Fig. 12

Dye	Backbone	A	R1	R2	R3	E_{HOMO} (eV)	E_1 (eV)	η
A	FZnP	2CarboxyPropenA	MOTPA	MOTPA	MOTPA	−5.04	0.97	0.46
B	FZnP	2CyanoPropenA	MOTPA	MOTPA	MOTPA	−5.05	0.96	0.45
C	ZnP	2CarboxyPropenA	MOTPA	MOTPA	MOTPA	−5.06	1.05	0.45
D	ZnP	2CyanoPropenA	MOTPA	MOTPA	MOTPA	−5.06	1.04	0.45
E	H_2P	2CarboxyPropenA	MOTPA	MOTPA	MOTPA	−5.07	0.96	0.45
F	H_2P	2CyanoPropenA	MOTPA	MOTPA	MOTPA	−5.08	0.94	0.45
G	FZnP	EthynPhA	DTA	MOTPA	MOTPA	−5.06	1.09	0.44
H	TiOP	2CyanoPropenA	MOTPA	MOTPA	MOTPA	−5.09	0.99	0.44
I	TiOP	2CarboxyPropenA	MOTPA	MOTPA	MOTPA	−5.10	1.01	0.44
J	FZnP	EthynPhA	MOTPA	DTA	MOTPA	−5.11	1.11	0.44

Table 3 Using the YD2-o-C8[16] dye as a starting point the level alignment quality is optimized by varying 1 or 2 structural parameters

No. of optimized parameters	Backbone	A	R1	R2	R3	E_{HOMO} (eV)	E_1 (eV)	η
0 parameters	ZnP	EthynPhA	DMP	DTA	DMP	−5.77	1.48	0.20
1 parameter[a]	ZnP	EthynPhA	DMP	DTA	TPA	−5.54	1.40	0.27
1 parameter[b]	ZnP	EthynPhA	MOTPA	DTA	DMP	−5.40	1.40	0.33
2 parameters[a]	ZnP	EthynPhA	DMP	DMP	MOTPA	−5.51	1.46	0.29
2 parameters[b]	ZnP	EthynPhA	TPA	DTA	TPA	−5.36	1.34	0.34

[a] The optimization is performed under the constraint that $E_{HOMO} \leq -5.50$ eV corresponding to the requirement of using the I^-/I_3^- redox pair.[2,45–47] [b] The optimization is performed under the constraint that $E_{HOMO} \leq -5.36$ eV corresponding to the requirement of using the $[Co^{II/III}(bpy\text{-}pz)_2]$ redox pair.[48]

The white dotted line indicates where $E_c - E_H = E_1$. Above this line, photoexcited electrons on the dye could in principle be trapped below the conduction band if the thermal relaxation in the molecule is fast compared to the charge injection time.

The bottom part of Fig. 12 shows a zoom of the region with the highest level alignment quality and identifies the ten dyes with the highest η values. The structure of these candidates can be found in Table 2. The common feature of the top ten candidates is that they have an E_1 value of around 1.0 eV and an E_{HOMO} value of around −5.1 eV (corresponding to an $E_c - E_H$ value of around 1.1 eV). For similar values of E_1 and $E_c - E_H$ all the photoexcited electrons on the dye contribute to the photocurrent. The optimal value of 1.1 eV is in agreement with the optimal value predicted for semi-conductor solar cells by Shockley and Queisser.[49] Out of the top ten candidates only two contain the common ZnP backbone. Thus, by changing the backbone we have found eight new candidates for the top ten relative to our recent screening of zinc porphyrins.[28] However, none of the top ten candidates have E_{HOMO} values below −5.50 eV, which is the requirement for using the I^-/I_3^- redox pair. Thus, a different redox mediator must be used for these dyes. Fig. S13 in the ESI† shows the TD-DFT predicted UV-VIS spectra of the top five dyes. These results verify that with a sufficient amount of dye layers present in the device due to the meso-porous TiO_2 nano-particles, all dyes will have a step-function absorption spectrum above the absorption edge since the absorption here is non-zero for all dyes. The absorption edge is however poorly predicted by TD-DFT due to the charge-transfer character of donor–π–acceptor porphyrin dyes.

Using our computational database it is possible to optimize the level alignment quality of a given dye by varying one or more structural parameters (side groups, anchor groups and backbones). In Table 3 we have optimized the level alignment quality of the high efficiency record holding YD2-o-C8 dye[16] by varying 1 or 2 structural parameters under the constraint $E_{HOMO} \leq -5.50$ eV corresponding to the requirement imposed by the I^-/I_3^- redox pair and the constraint $E_{HOMO} \leq -5.36$ eV corresponding to the requirement imposed by the $[Co^{II/III}(bpy\text{-}pz)_2]$ redox pair,[48] respectively. From the table it can be seen that changing the side groups has the largest impact on the level alignment quality for this particular dye. In fact, by substituting a single side group, the level alignment quality is expected to increase significantly. Since the structural change is negligible this could lead to a higher efficiency of an actual DSSC.

4 Conclusions

We have presented a computational screening study of 5145 functionalized porphyrin dyes composed of a set of five different backbones, seven different donating side groups and three different accepting anchor groups. Replacing the commonly used zinc metal center with H_2 was found to alter the electronic structure of the dyes only slightly. On the other hand, introducing the Ti^{4+} metal center enables the use of axial ligands. For dyes containing only weakly donating side groups, these ligands can have a large influence on both the frontier energy levels and the shape of the HOMO. The latter effect could be important for the dye regeneration process. Both of the investigated axial ligands produced many dyes with a high level alignment quality and thus the use of a Ti^{4+} center with axial ligands introduces more flexibility in the design of porphyrin

based dyes. By fluorinating the standard zinc porphyrin based dyes we found a dramatic impact on the LUMO energy and, for dyes without very donating side groups, also on the HOMO energy. This suggests fluorination as an effective method to control the electronic structure of the porphyrins. For all types of structural modifications we generally found a large number of dye candidates with a high level alignment quality, exceeding those of well known high efficiency dyes. These results suggest that there is plenty of room for improving dye sensitized solar cells by optimization of the porphyrin dyes. Despite the observed qualitative trends, we do not observe any simple additive quantitative relation between the structure and energy levels. We are currently investigating whether this relation between orbital energies and structural changes can be predicted using a model based on perturbation theory. In parallel with this we also plan to include the alignment with the redox mediator in the definition of the level alignment quality in a future study.

Acknowledgements

The authors would like to thank A. Rubio and F. J. Himpsel for inspiring discussions and J. J. Mortensen for help with setting up an efficient database. KBØ and KST would further like to thank the Danish Council for Independent Research's DFF-Sapere Aude program (grant no. 11-1051390) for financial support. JMGL acknowledges support from the Spanish Ministry of Economy and Competitiveness under Projects FIS2009-07083, FIS2010-21282-C02-01 and FIS2012-30996 and through Ramon y Cajal grant RYC-2011-07782.

References

1 B. O'Regan and M. Grätzel, *Nature*, 1991, **353**, 737–740.
2 A. Hagfeldt, G. Boschloo, L. Sun, L. Kloo and H. Pettersson, *Chem. Rev.*, 2010, **110**, 6595–6663.
3 H. S. Jung and J.-K. Lee, *J. Phys. Chem. Lett.*, 2013, **4**, 1682–1693.
4 L.-L. Li and E. W.-G. Diau, *Chem. Soc. Rev.*, 2013, **42**, 291–304.
5 W. M. Campbell, A. K. Burrell, D. L. Officer and K. W. Jolley, *Coord. Chem. Rev.*, 2004, **248**, 1363–1379.
6 T. Bessho, S. M. Zakeeruddin, C.-Y. Yeh, E. W.-G. Diau and M. Grätzel, *Angew. Chem., Int. Ed.*, 2010, **49**, 6646–6649.
7 G. F. Moore, S. J. Konezny, H. Song, R. L. Milot, J. D. Blakemore, M. L. Lee, V. S. Batista, C. A. Schmuttenmaer, R. H. Crabtree and G. W. Brudvig, *J. Phys. Chem. C*, 2012, **116**, 4892–4902.
8 B. Liu, W. Zhu, Y. Wang, W. Wu, X. Li, B. Chen, Y.-T. Long and Y. Xie, *J. Mater. Chem.*, 2012, **22**, 7434–7444.
9 S. Rangan, S. Coh, R. A. Bartynski, K. P. Chitre, E. Galoppini, C. Jaye and D. Fischer, *J. Phys. Chem. C*, 2012, **116**, 23921–23930.
10 M.-J. Lee, M. P. Balanay and D. H. Kim, *Theor. Chem. Acc.*, 2012, **131**, 1–12.
11 N. Masi Reddy, T.-Y. Pan, Y. Christu Rajan, B.-C. Guo, C.-M. Lan, E. Wei-Guang Diau and C.-Y. Yeh, *Phys. Chem. Chem. Phys.*, 2013, **15**, 8409–8415.
12 N. Santhanamoorthi, C.-M. Lo and J.-C. Jiang, *J. Phys. Chem. Lett.*, 2013, **4**, 524–530.
13 J. Luo, M. Xu, R. Li, K.-W. Huang, C. Jiang, Q. Qi, W. Zeng, J. Zhang, C. Chi, P. Wang and J. Wu, *J. Am. Chem. Soc.*, 2013, **136**, 265–272.
14 H. He, A. Gurung, L. Si and A. G. Sykes, *Chem. Commun.*, 2012, **48**, 7619–7621.
15 Y. Liu, H. Lin, J. Li, J. T. Dy, K. Tamaki, J. Nakazaki, D. Nakayama, C. Nishiyama, S. Uchida, T. Kubo and H. Segawa, *Phys. Chem. Chem. Phys.*, 2012, **14**, 16703–16712.
16 A. Yella, H.-W. Lee, H. N. Tsao, C. Yi, A. K. Chandiran, M. K. Nazeeruddin, E. W.-G. Diau, C.-Y. Yeh, S. M. Zakeeruddin and M. Grätzel, *Science*, 2011, **334**, 629–634.
17 G. H. Johannesson, T. Bligaard, A. V. Ruban, H. L. Skriver, K. W. Jacobsen and J. K. Nørskov, *Phys. Rev. Lett.*, 2002, **88**, 255506.
18 A. Franceschetti and A. Zunger, *Nature*, 1999, **402**, 60–63.
19 G. Ceder, Y.-M. Chiang, D. R. Sadoway, M. K. Aydinol, Y.-I. Jang and B. Huang, *Nature*, 1998, **392**, 694–696.
20 W. Setyawan, R. M. Gaume, S. Lam, R. S. Feigelson and S. Curtarolo, *ACS Comb. Sci.*, 2011, **13**, 382–390.
21 J. Hachmann, R. Olivares-Amaya, S. Atahan-Evrenk, C. Amador-Bedolla, R. S. Snchez-Carrera, A. Gold-Parker, L. Vogt, A. M. Brockway and A. Aspuru-Guzik, *J. Phys. Chem. Lett.*, 2011, **2**, 2241–2251.
22 R. Olivares-Amaya, C. Amador-Bedolla, J. Hachmann, S. Atahan-Evrenk, R. S. Sanchez-Carrera, L. Vogt and A. Aspuru-Guzik, *Energy Environ. Sci.*, 2011, **4**, 4849–4861.
23 N. M. O'Boyle, C. M. Campbell and G. R. Hutchison, *J. Phys. Chem. C*, 2011, **115**, 16200–16210.
24 I. Y. Kanal, S. G. Owens, J. S. Bechtel and G. R. Hutchison, *J. Phys. Chem. Lett.*, 2013, **4**, 1613–1623.
25 J. Hachmann, R. Olivares-Amaya, A. Jinich, A. L. Appleton, M. A. Blood-Forsythe, L. R. Seress, C. Roman-Salgado, K. Trepte, S. Atahan-Evrenk, S. Er, S. Shrestha, R. Mondal, A. Sokolov, Z. Bao and A. Aspuru-Guzik, *Energy Environ. Sci.*, 2014, **7**, 698–704.
26 I. E. Castelli, T. Olsen, S. Datta, D. D. Landis, S. Dahl, K. S. Thygesen and K. W. Jacobsen, *Energy Environ. Sci.*, 2012, **5**, 5814–5819.
27 I. E. Castelli, D. D. Landis, K. S. Thygesen, S. Dahl, I. Chorkendorff, T. F. Jaramillo and K. W. Jacobsen, *Energy Environ. Sci.*, 2012, **5**, 9034–9043.
28 K. B. Ørnsø, J. M. Garcia-Lastra and K. S. Thygesen, *Phys. Chem. Chem. Phys.*, 2013, **15**, 19478–19486.
29 P. L. Cook, W. Yang, X. Liu, J. M. Garcia-Lastra, A. Rubio and F. J. Himpsel, *J. Chem. Phys.*, 2011, **134**, 204707.
30 J. M. Garcia-Lastra, P. L. Cook, F. J. Himpsel and A. Rubio, *J. Chem. Phys.*, 2010, **133**, 151103.
31 D. G. de Oteyza, A. El-Sayed, J. M. Garcia-Lastra, E. Goiri, T. N. Krauss, A. Turak, E. Barrena, H. Dosch, J. Zegenhagen, A. Rubio, Y. Wakayama and J. E. Ortega, *J. Chem. Phys.*, 2010, **133**, 214703.

32 D. F. Pickup, I. Zegkinoglou, B. Ballesteros, C. R. Ganivet, J. M. Garca-Lastra, P. L. Cook, P. S. Johnson, C. Rogero, F. de Groot, A. Rubio, G. de la Torre, J. E. Ortega and F. J. Himpsel, *J. Phys. Chem. C*, 2013, **117**, 4410–4420.

33 W. Kohn and L. J. Sham, *Phys. Rev.*, 1965, **140**, A1133–A1138.

34 J. P. Perdew, K. Burke and M. Ernzerhof, *Phys. Rev. Lett.*, 1996, **77**, 3865–3868.

35 J. Enkovaara, C. Rostgaard, J. J. Mortensen, J. Chen, M. Dulak, L. Ferrighi, J. Gavnholt, C. Glinsvad, V. Haikola, H. A. Hansen, H. H. Kristoffersen, M. Kuisma, A. H. Larsen, L. Lehtovaara, M. Ljungberg, O. Lopez-Acevedo, P. G. Moses, J. Ojanen, T. Olsen, V. Petzold, N. A. Romero, J. Stausholm-Møller, M. Strange, G. A. Tritsaris, M. Vanin, M. Walter, B. Hammer, H. Häkkinen, G. K. H. Madsen, R. M. Nieminen, J. K. Nørskov, M. Puska, T. T. Rantala, J. Schiøtz, K. S. Thygesen and K. W. Jacobsen, *J. Phys.: Condens. Matter*, 2010, **22**, 253202.

36 A. H. Larsen, M. Vanin, J. J. Mortensen, K. S. Thygesen and K. W. Jacobsen, *Phys. Rev. B: Condens. Matter Mater. Phys.*, 2009, **80**, 195112.

37 S. Bahn and K. W. Jacobsen, *Comput. Sci. Eng.*, 2002, **4**, 56–66.

38 C. E. Patrick and F. Giustino, *Phys. Rev. Lett.*, 2012, **109**, 116801.

39 J. M. Garcia-Lastra, C. Rostgaard, A. Rubio and K. S. Thygesen, *Phys. Rev. B: Condens. Matter Mater. Phys.*, 2009, **80**, 245427.

40 A. Allegrucci, N. A. Lewcenko, A. J. Mozer, L. Dennany, P. Wagner, D. L. Officer, K. Sunahara, S. Mori and L. Spiccia, *Energy Environ. Sci.*, 2009, **2**, 1069–1073.

41 N. Martsinovich and A. Troisi, *Phys. Chem. Chem. Phys.*, 2012, **14**, 13392–13401.

42 E. Ronca, M. Pastore, L. Belpassi, F. Tarantelli and F. De Angelis, *Energy Environ. Sci.*, 2013, **6**, 183–193.

43 M. Gouterman, *J. Mol. Spectrosc.*, 1961, **6**, 138–163.

44 M.-S. Liao and S. Scheiner, *J. Chem. Phys.*, 2002, **117**, 205–219.

45 C. Bauer, G. Boschloo, E. Mukhtar and A. Hagfeldt, *J. Phys. Chem. B*, 2002, **106**, 12693–12704.

46 J. N. Clifford, E. Palomares, M. K. Nazeeruddin, M. Grätzel and J. R. Durrant, *J. Phys. Chem. C*, 2007, **111**, 6561–6567.

47 D. Kuciauskas, M. S. Freund, H. B. Gray, J. R. Winkler and N. S. Lewis, *J. Phys. Chem. B*, 2000, **105**, 392–403.

48 J.-H. Yum, E. Baranoff, F. Kessler, T. Moehl, S. Ahmad, T. Bessho, A. Marchioro, E. Ghadiri, J.-E. Moser, C. Yi, M. K. Nazeeruddin and M. Grätzel, *Nat. Commun.*, 2012, **3**, 631.

49 W. Shockley and H. J. Queisser, *J. Appl. Phys.*, 1961, **32**, 510–519.

Appendix D

Paper III

Importance of the reorganization energy barrier in computational design of porphyrin-based solar cells with cobalt-based redox mediators
K. B. Ørnsø, E. Ö. Jónsson, K. W. Jacobsen and K. S. Thygesen
J. Phys. Chem. C, **2015**, *119*, 12792-12800

THE JOURNAL OF PHYSICAL CHEMISTRY C

Article

pubs.acs.org/JPCC

Importance of the Reorganization Energy Barrier in Computational Design of Porphyrin-Based Solar Cells with Cobalt-Based Redox Mediators

Kristian B. Ørnsø,[†] Elvar Ö. Jónsson,[†,‡] Karsten W. Jacobsen,[†] and Kristian S. Thygesen*,[†]

[†]Center for Atomic-scale Materials Design, Department of Physics, Technical University of Denmark, Fysikvej, 2800 Kongens Lyngby, Denmark

Supporting Information

ABSTRACT: The shift from iodide-based redox mediators in dye-sensitized solar cells toward octahedral cobalt complexes has led to a significant increase in the efficiency. However, due to the nature of this type of complexes the driving force required for the regeneration of the dye is very high, and this limits the achievable efficiency. Here we show that the large driving force is a direct consequence of the large reorganization energy of the dye regeneration reaction. The reorganization energies for charge transfer between a simple zinc porphyrin dye and two popular cobalt-based redox mediators is calculated using ab initio molecular dynamics with explicit solvent. These results are then combined with a Marcus-based extrapolation scheme to obtain the reorganization energies of more than 5000 porphyrin-based dyes. We propose a scheme for scoring the performance of the porphyrin dyes, which is able to identify already known high-performance dyes in addition to a number of even better candidates. Our analysis shows that the large internal reorganization energy of the Co-based redox mediators is an obstacle for achieving higher efficiencies.

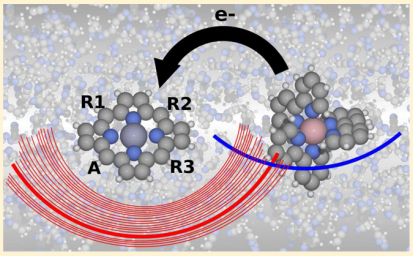

INTRODUCTION

As the search for sustainable energy sources is intensified, focus is put on exploiting the vast energy in sunlight. For this purpose, dye-sensitized solar cells (DSSC)[1] have since the emergence of the first efficient system in 1991[2] been considered promising candidates. In particular, the low material cost, flexibility, and high efficiency under low illumination conditions[3] of DSSCs make these stand out from the conventional semiconductor-based solar cells. In a standard DSSC the photons are absorbed by a molecule with a high absorption in the visible part of the solar spectrum. This creates a photoexicted electron in the dye which is transferred to the conduction band of a semiconductor nanoparticle (usually TiO_2) on which the dye is anchored. Following this, the electron is extracted to an external circuit and reintroduced into the cell via a counter electrode (usually Pt). In the last two steps, the electron is transferred from the counter electrode to a redox mediator and then from the redox mediator back to the dye completing the circuit. To improve the efficiency of DSSCs, much focus has been put on choosing the correct dye. Here, several factors are important including the correct level alignment of the dye orbitals with the semiconductor conduction band and the redox potential of the redox mediator, a large overlap between the dye absorption spectrum and the solar spectrum, the charge injection from the dye to the semiconductor, the regeneration of the oxidized dye by the redox mediator, losses due to charge transport and recombination, etc. More recently, functionalized porphyrins have gained interest as dyes in DSSCs due to their high absorption of visible light and high customizability.[4−13] The highest efficiencies obtained for DSSCs of 12.3%[14] and 13.0%[15] have both been obtained using porphyrin-based dyes. We previously reported a computational screening study of porphyrin-based dyes,[16,17] in which we investigated the effect of changing side and anchor groups for a range of different porphyrin backbones. In these studies we scored the dyes by computing a level alignment quality based only on the level alignment between the dye orbitals and the conduction band of TiO_2, while the redox potential of the redox mediator was treated as a simple variable. However, the reorganization energy associated with the electron transfer from the redox mediator to the oxidized dye is also an essential component to obtain a high DSSC efficiency. To include this effect in the level alignment quality, we here present a computational study in which we apply Marcus theory[18−22] to evaluate the solvent reorganization barrier for the regeneration reactions of functionalized porphyrins by two cobalt-based redox mediators. The cobalt-based redox mediators are chosen here since they are presently considered the most promising redox molecules[14,23] and the electron transfer is believed to be a simple outer-sphere process.

A schematic overview of the energetics associated with the regeneration reaction is given in Figure 1 (left). The regeneration process itself is defined as the electron transfer from a cobalt-based redox mediator to the oxidized dye

$$D^+ + [Co(red)]^{2+} \rightarrow D + [Co(red)]^{3+} \quad (1)$$

Received: December 18, 2014
Revised: March 24, 2015
Published: May 12, 2015

DOI: 10.1021/jp512627e
J. Phys. Chem. C 2015, 119, 12792−12800

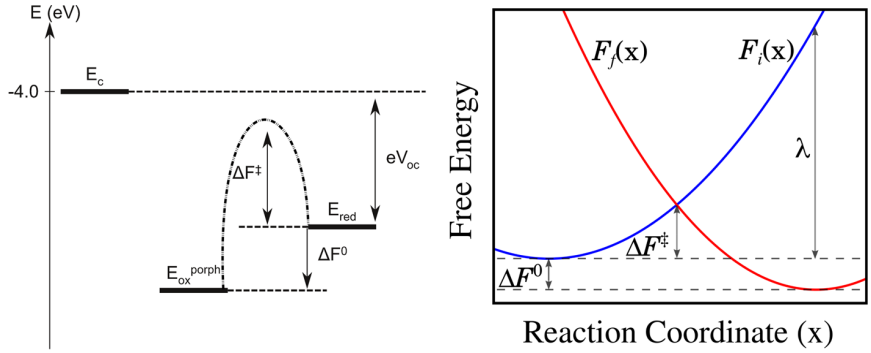

Figure 1. (Left) Scheme of the energetics associated with the regeneration reaction. Here, E_c is the conduction band edge of TiO_2, E_{ox}^{porph} is the oxidation potential of the porphyrin-based dyes, E_{red} is the redox potential of the cobalt-based redox mediator, ΔF^0 is the driving force for the regeneration reaction, $\Delta F^{\ddagger}$ is the barrier associated with the electron transfer, and eV_{oc} is the open-circuit voltage multiplied with the electronic charge. (Right) Schematic illustration of the free energy function for the initial, $F_i(x)$, and final, $F_f(x)$, electronic states. The reaction coordinate, $x = \Delta E(R^N)$ (see eq 3), is the vertical energy gap between the two electronic configurations corresponding to the left- and right-hand sides of eq 1. The gap collectively represents all fluctuations of the nuclear degrees of freedom of both the solute and the solvent environment, R^N. Running MD based solely on the initial and final electronic states gives information for their respective equilibrium values (the region around the minimum of the two curves). To achieve sampling in the intermediate region where the free energy barrier is defined our MD is based on the coupling parameter scheme (eq 6). Knowing one function the free energy change, barrier, and reorganization energy relative to the initial state can readily be solved for $\Delta F^0 = F_f(x_{f,min}) - F_i(x_{i,min})$, $\Delta F^{\ddagger} = F_i(x^{\ddagger}) - F_i(x_{i,min})$ and $\lambda = F_i(x_{f,min}) - F_i(x_{i,min})$, respectively. Here, $x^{\ddagger}$ and $x_{j,min}$ denote the reaction coordinate value at the crossing and minimum of the free energy functions. The parabolas presented here are an idealized case, which is realized under certain conditions, namely, linear response (see eq 14 and the section on Marcus Theory).

where D/D^+ is the neutral/oxidized dye and $[Co(red)]^{2+}/[Co(red)]^{3+}$ is the reduced/oxidized cobalt-based redox mediator. In Marcus theory the charge transfer rate between two species is expressed in terms of a pre-exponential factor (taking into account the donor−acceptor electronic state overlap factor) and an exponential term which accounts for the thermodynamic free energy that must be overcome to facilitate electron transfer. The latter term includes the redox potentials as well as the nuclear and electronic response of the solvent and solute to the transferred electron.

In this study we focus only on the exponential term in the Marcus rate expression from which we explicitly calculate the barrier for the smallest porphyrin dye. We then introduce a Marcus-based extrapolation scheme to estimate the barrier for more than 5000 porphyrin dyes present in our database.[16,17] In this way we combine large-scale computational screening with a more in-depth study of the simplest zinc porphyrin (ZnP) to improve the scoring of the dyes by introducing a correction term to the level alignment quality and at the same time identify parameters acting as obstacles for improving the efficiency of DSSCs.

METHODS

We used density functional theory (DFT)-based molecular dynamics (MD) calculations in combination with Marcus theory to calculate the solvent barrier associated with the regeneration (see eq 1) of unsubstituted zinc porphyrin by two different cobalt-based redox mediators. These calculations are extrapolated using a continuum model for the reorganization energy for more than 5000 functionalized porphyrins to provide an estimate of the overpotential related to the regeneration process. The two cobalt redox mediators investigated are the commonly used $[Co^{II/III}(bpy)_3]$ and $[Co^{II/III}(bpy\text{-}pz)_2]$ (bpy-pz = 6-(1*H*-pyrazol-1-yl)-2,2′-bipyridine).[23,24] The chemical structures of the two redox mediators and the functionalized porphyrin dyes are shown in Figure 2. In the figure for the porphyrin the R1, R2, and R3 labels denote side group locations, A denotes the anchor group location, and

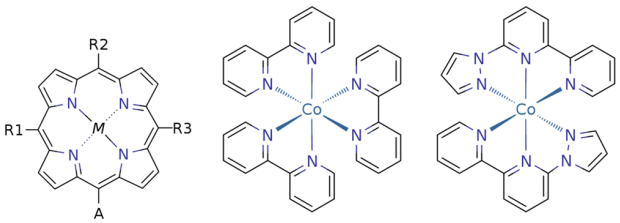

Figure 2. Molecules investigated in this work. (Left) Functionalized porphyrin dye with side groups (R1−R3) and acceptor group (A). (Middle) $[Co^{II/III}(bpy)_3]$ redox mediator. (Right) $[Co^{II/III}(bpy\text{-}pz)_2]$ redox mediator.

M denotes the metal center. The different metal centers, side, and anchor groups used in this study are described in detail in recent publications[16,17] and shown in Figures S2−S4, Supporting Information. In the following we briefly introduce the methods used in this study.

Free Energy Function. In order to address the free energy barrier we use the free energy function, defined by the restricted partition function of the vertical (potential) energy gap between the initial and the final state[25]

$$F_i(x) = -\frac{1}{\beta}\ln\int dR^N \delta(x - \Delta E(R^N)) e^{-\beta E_i(R^N)} = -\frac{1}{\beta}\ln[P_i(x)] + F_i^* \quad (2)$$

where the gap $\Delta E(R^N)$ is given by

$$\Delta E(R^N) = E_i(R^N) - E_f(R^N) \quad (3)$$

and i and f refer to the initial and final electronic states (i.e., left- and right-hand side of eq 1)

$$E_i = E[D^+ + [Co(red)]^{2+}]$$

$$E_f = E[D + [Co(red)]^{3+}]$$

DOI: 10.1021/jp512627e
J. Phys. Chem. C 2015, 119, 12792−12800

$P_i(x)$ denotes the probability distribution of the reaction coordinate, $x = \Delta E(R^N)$, for the initial state

$$P_i(x) = \frac{\int dR^N \delta(x - \Delta E(R^N)) e^{-\beta E_i(R^N)}}{\int dR^N e^{-\beta E_i(R^N)}} \quad (4)$$

Finally, F_i^* denotes the (absolute) free energy of the initial state. This quantity is not well defined; however, the expressions above completely define relative differences of the free energy function of the initial and final state. For example, rearranging eq 3 to $E_i(R^N) - \Delta E(R^N) = E_f(R^N)$ and inserting into the analogous expression for $F_f(x)$ one can show that $F_f(x) = F_i(x) - x$ (see Derivation 1, Supporting Information). In particular, the reorganization energy and free energy barrier can be determined from just one of the free energy curves (see Figure 1).

Sampling and Optimization. An accurate treatment of the integral expressions above requires knowledge of both equilibrium and nonequilibrium configurations, relevant for both the initial and the final electronic states. To achieve a proper sampling in the crossing region one defines intermediate states, α, as

$$\begin{aligned} E_\alpha(R^N) &= (1 - \chi_\alpha) E_i(R^N) + \chi_\alpha E_f(R^N) \\ &= E_i(R^N) - \chi_\alpha \Delta E(R^N) \end{aligned} \quad (5)$$

which connects the two states in a straightforward manner. The MD sampling of the relevant phase spaces are then based on a simple linear combination of the forces

$$\mathbf{F}_\alpha(R^N) = (1 - \chi_\alpha)\mathbf{F}_i(R^N) + \chi_\alpha \mathbf{F}_f(R^N) \quad (6)$$

where $\mathbf{F}_i$ and $\mathbf{F}_f$ are the force vectors for the initial and final states, respectively. The coupling parameter $\{\chi_\alpha : 0 \leq \chi_\alpha \leq 1\}$ is sampled at equally spaced intervals between 0 and 1, which obviously brings the system from the initial electronic charge state to the final electronic charge state. This ensures sampling of R^N in and out of equilibrium for either state, giving information for the free energy functions in the intermediate region, which is important for an accurate estimate of the free energy barrier, $\Delta F^{\ddagger}$ (see Figure 1). Note that the MD sampling employed here is further enhanced by constraining high-frequency degrees of freedom (hydrogen bonds) to allow for larger time steps when solving for the equations of motion. R^N, in all expression, denotes the active degrees of freedom present in the simulations which means that the Boltzmann factor, $\beta = (1/(k_B T))$, is scaled accordingly.

Employing the coupling parameter method as outlined above produces biased probabilities, $P_\alpha^b(\Delta E(R^N))$, which need to be corrected for the bias $-\chi_\alpha \Delta E(R^N)$, and subsequently combined to give the total probability curve for the initial state. To this end we use the weighted histogram analysis method (WHAM)[26−28] following the formulation of Souaille and Roux.[26]

In WHAM the unbiased probability is given by

$$P_\alpha^u(\Delta E(R^N)) = e^{\beta[-\chi_\alpha \Delta E(R^N) - f_\alpha]} P_\alpha^b(\Delta E(R^N)) \quad (7)$$

where f_α corresponds to the free energy change in the system due to the bias $-\chi_\alpha \Delta E(R^N)$ and is determined in a self-consistent fashion. The sampling is performed for N_α values of α, so the total probability curve for the initial state is written as

$$P_i(\Delta E(R^N)) = C \sum_{\alpha=1}^{N_\alpha} p_\alpha(\Delta E(R^N)) P_\alpha^u(\Delta E(R^N)) \quad (8)$$

where C is a normalization constant and $p_\alpha(\Delta E(R^N))$ are the weights of the sampling windows for a given value of the vertical potential energy gap $\Delta E(R^N)$. Now, requiring the weights to be normalized and minimize the statistical error in the sampling results in[26,27]

$$P_i(\Delta E(R^N)) = C \sum_{\alpha=1}^{N_\alpha} \frac{n_\alpha}{\sum_{\kappa=1}^{N_\alpha} n_\kappa e^{-\beta[-\chi_\kappa \Delta E(R^N) - f_\kappa]}} P_\alpha^b(\Delta E(R^N)) \quad (9)$$

where n_α is the number of samples in the window α. The unknown free energy change due to the bias can be solved in a self-consistent manner using

$$e^{-\beta f_\nu} = C \int dR^N \sum_{\alpha=1}^{N_\alpha} \frac{n_\alpha e^{-\beta[-\chi_\alpha \Delta E(R^N)]}}{\sum_{\kappa=1}^{N_\alpha} e^{-\beta[-\chi_\kappa \Delta E(R^N) - f_\kappa]}} P_\alpha^b(\Delta E(R^N)) \quad (10)$$

The expression above is solved using all available data points and is the most time-consuming step in the WHAM procedure, both because of the shear number of data points as well as strict convergence criteria. Furthermore, subtracting the value corresponding to the initial state, f_i, from all f_α ensures that eq 9 is normalized (C). As a last step we also introduce the normalized histograms into eq 9 to give a manageable number of data points for the construction and fitting of the free energy function (eq 2).

$$P_\alpha^b(x) = \frac{1}{n_\alpha} \sum_{l=1}^{n_\alpha} \delta(x - \Delta E(R_{\alpha,l}^N)) \quad (11)$$

Marcus Theory. In Marcus theory it is customary to split the total reorganization energy into internal and outer contributions

$$\lambda = \lambda^{in} + \lambda^{out} \quad (12)$$

The internal reorganization energy can be approximated as the energy difference of the solute species in the initial electronic state evaluated at the relaxed structures corresponding to the initial and final electronic states in vacuum. The outer reorganization energy is associated with the solvent structural response to the change in electronic charge on the solute species. This term was recognized by Marcus as the key factor in determining the rate of outer-sphere electron charge transfer reactions.[18−22]

In terms of a continuum model representing the solvent surrounding two solute species A and D represented as charged spheres of radius r_A and r_D, respectively, the outer reorganization energy in atomic units can be expressed as[18]

$$\lambda^{out} = (\Delta q^2)\left(\frac{1}{\epsilon^\infty} - \frac{1}{\epsilon^{st}}\right)\left(\frac{1}{2r_A} + \frac{1}{2r_D} - \frac{1}{R_{AD}}\right) \quad (13)$$

where ϵ^∞ and ϵ^{st} are the high-frequency and static dielectric constants of the solvent and Δq the total charge transferred. The last term on the right-hand side is the screened Coulomb interaction between the donor and the acceptor, where R_{AD} is the distance between the two solute species. Assuming that the charge transfer occurs when the two spheres come in contact R_{AD} is simply given by the sum of two solute species radii.

DOI: 10.1021/jp512627e
J. Phys. Chem. C 2015, 119, 12792−12800

In the linear response regime the sampled vertical energy gaps in the N_α windows display Gaussian statistics, with a relative shift of the mean value directly proportional to the coupling value α.[25,29] Under these conditions the free energy function reduces to a parabola[25,30]

$$F_i(x) = \frac{1}{4\lambda}(x - x_{\min,i})^2 + F_i^* \tag{14}$$

where $x_{\min,i}$ denotes the reaction coordinate associated with the equilibrium configurations of the initial state.

We do not explicitly calculate the reorganization energy of the reaction in eq 1 but split the reaction into two parts

$$D^+ + D \rightarrow D + D^+$$

$$[Co(red)]^{2+} + [Co(red)]^{3+} \rightarrow [Co(red)]^{3+} + [Co(red)]^{2+}$$

which in turn provides us with symmetric free energy curves after solving for the probability curves following the procedure in the preceding section (see Figures S5−S7, Supporting Information). The fully simulated free energy functions are fitted with a parabolic expression (it is easy to show that for this case $F_f(x) = F_i(x) - x$, see Derivation 2, Supporting Information). This in turn gives us the reorganization energy for the individual species which are then combined to give the reorganization energy for the total reaction in eq 1 (see the next section and eq 19).

Extrapolated Barrier Calculations. Due to limited computational resources it has been necessary to only explicitly calculate the reorganization energy for the simplest zinc porphyrin and extrapolate this value to the functionalized porphyrins. Functionalizing porphyrins significantly changes the size of the dye, and to account for this change we used the *Jmol* program suite[31] to obtain a volume of all 5000+ porphyrin dyes using the predefined van der Waals surfaces of the atoms. This volume is then transformed into a radius of a sphere using

$$r = \left(\frac{3V}{4\pi}\right)^{1/3} \tag{15}$$

Having this radius we can use a modified version of eq 13 in which we include a correction for using a finite cell with periodic boundary conditions to obtain the correlation between our chosen convention for r and the explicitly calculated reorganization energy for the simplest zinc porphyrin (see Table S1, Supporting Information)[32−34]

$$\lambda_{PBC}^{out} = (\Delta q)^2 c\left(\frac{1}{2r} + \frac{1}{2L_c}\left(\xi_{Ew} + \frac{4\pi}{3}\left(\frac{r}{L_c}\right)^2 - \frac{16\pi^2}{45}\left(\frac{r}{L_c}\right)^5\right)\right) \tag{16}$$

where λ_{PBC}^{out} is the uncorrected reorganization energy obtained from our MD simulation, L_c is the linearized cell length, $L_c = V^{1/3}$, where V is the volume of the cell, and ξ_{Ew} is the Madelung constant, which for our cell is $\xi_{Ew} = -2.757$. From the above equation we can estimate $c = (1/\epsilon^{\infty}) - (1/\epsilon^{st})$. This fitting was tested for both the "flat" zinc porphyrin species as well as the octahedral $Co(bpy)_3$ species, giving $c = 0.502$ and 0.520, respectively. These values are in good agreement with the inverse of the experimental dielectric constant of acetonitrile, $c \approx 0.53$. Our smaller values reflect an overestimated dielectric response, which PBE is known to do, e.g., for water. For the extrapolation scheme of the zinc porphyrin-based dyes $c = 0.502$ was used throughout.

Having corrected for the finite cell with periodic boundary conditions, we can define the r-dependent outer reorganization energy for the functionalized porphyrins as

$$\lambda_{porph}^{out}(r) = (\Delta q)^2 c\frac{1}{2r} \tag{17}$$

We again note that converting the volumes of porphyrins into spheres is a simplification. Apart from the usually flat structure of porphyrins, the way the dye is connected to the surface further influences the actual radius and accessible surface area of the dye as well as the distance to the redox complex.[35] However, since this approximation only enters the correction to an explicitly computed reorganization energy, we believe that we will obtain the correct trends in the size dependency.

To account for the screened coulomb interaction between the acceptor and the donor we apply a correction based on the $1/R_{AD}$ part of eq 13. Assuming that the electron transfer occurs when the acceptor and donor are right next to each other corresponds to setting $R_{AD} = r + r_{red}$, where r is still the dye radius and r_{red} is the radius of the redox mediator. Using this we obtain a correction to the outer reorganization given by

$$\lambda_R^{out}(r) = -(\Delta q)^2 c\frac{1}{r + r_{red}} \tag{18}$$

Having the size-dependent part of the reorganization energy and the corrections, we can obtain the total reorganization energy for the regeneration reaction as

$$\lambda(r) = \lambda_{porph}^{out}(r) + \lambda_{redox}^{in+out} + \lambda_{porph}^{in} + \lambda_R^{out}(r) \tag{19}$$

where we assume that λ_{porph}^{in} is r independent due to the similarity in chemical structure. The r-independent parts of the above equation are found explicitly from a MD simulation of the diabatic regeneration reaction (eq 1) with the smallest porphyrin in which λ_{redox}^{in+out} have been corrected for the effect of using a finite cell with periodic boundary conditions.

To obtain the electron transfer barrier we need in addition to the reorganization energy also the driving force, ΔF^0, for the regeneration reaction. This quantity is defined as

$$\Delta F^0 = E_{ox}^{porph} - E_{red} \tag{20}$$

where E_{ox}^{porph} is the oxidation potential of the porphyrin dye and E_{red} is the redox potential of the redox mediator. To obtain E_{ox}^{porph} from our calculations we assume that the oxidation potential scales linearly with the vacuum ionization potential calculated from total energy differences, $E_{HOMO} = E_0[N] - E_0[N-1]$, of the dyes with a constant shift due to solvation energies, image charge effects, etc. Fitting our calculations to the experimental oxidation potentials of 5 porphyrin dyes on TiO_2 measured by Liu et al.[7] we obtain the relation

$$E_{ox}^{porph} = E_{HOMO} - 0.11\ \text{eV} \tag{21}$$

We now have ΔF^0 and $\lambda(r)$ for all 5000+ porphyrin dyes, and we can then calculate the barrier height using the Marcus expression (solving for the crossing between initial and final state free energy curves using eq 14)

$$\Delta F^{\ddagger}(\Delta F^0, \lambda) = \frac{(\lambda + \Delta F^0)^2}{4\lambda} \tag{22}$$

DOI: 10.1021/jp512627e
J. Phys. Chem. C 2015, 119, 12792−12800

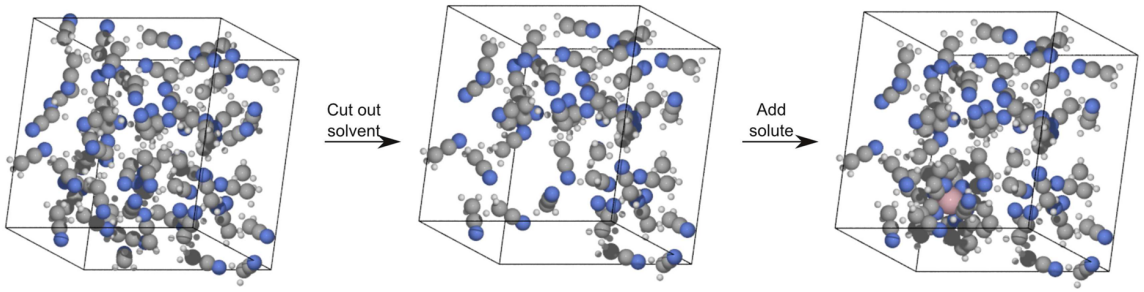

Figure 3. Illustration of the procedure to create the simulation cell for $[Co^{II/III}(bpy)_3]$. A 20 Å × 20 Å × 15 Å unit cell with periodic boundary conditions is filled with acetonitrile and thermalized. After this a hole is cut, and in the last step the desired molecule is inserted.

Weighted Level Alignment Quality. We previously defined the level alignment quality as[16,17]

$$\eta = \frac{eV_{oc}\int_{E_c-E_H}^{\infty}\Theta(E-E_1)\cdot I_{solar}(E)\mathrm{d}E}{\int_0^{\infty}E\cdot I_{solar}(E)\mathrm{d}E} \tag{23}$$

where

$$\Theta(E-E_1)=\begin{cases}1 & \text{for } -E_1\geq 0\\ 0 & \text{for } E-E_1<0\end{cases}$$

Here $E_c - E_H$ is the distance from the HOMO level to the conduction band, E_1 is the optical gap of the dye, $\Theta(E-E_1)$ is a step function representing the absorption of the dye molecules, $I_{solar}(E)$ is the photon flux of the ASTM G-173-03 (AM 1.5 G) solar spectrum, and eV_{oc} is the open-circuit voltage multiplied with the charge of the electron. In the following we assume that $E_c = -4.0$ eV, consistent with using TiO_2 as the semiconductor and $V_{oc} = E_c - E_{red}$. This definition of the level alignment quality neglects all loss mechanisms and only takes the level alignment between semiconductor and the dye molecule into account. An in-depth discussion of the level alignment quality is given in previous publications.[16,17]

Having obtained the regeneration barriers for different dyes and redox mediators it is possible to include this information in a correction factor to correct the level alignment quality. Inspired by the Arrhenius expression we write

$$\eta_{reg}(\Delta F^0, \lambda; T) = C(\Delta F^0, \lambda; T)\cdot\eta \tag{24}$$

where

$$C(\Delta F^0, \lambda; T)=\begin{cases}\exp\left(\dfrac{-\Delta F^{\ddagger}(\Delta F^0, \lambda)}{k_B T}\right) & \text{for } \Delta F^0\leq 0\\ 0 & \text{for } \Delta F^0>0\end{cases} \tag{25}$$

We note that the correction function is highly dependent on the used temperature, and this may be important for solar cells, where the working temperature may be very high under intense sunlight. A flowchart illustrating the steps in calculating the weighted level alignment quality is shown in Figure S8, Supporting Information.

Computational Details. All quantum mechanical calculations were performed using density functional theory (DFT)[36] with the PBE[37] exchange-correlation functional as implemented in the GPAW code.[38] For all standard calculations we used a basis set of numerical atomic orbitals[39] (LCAO mode) with a double-ζ polarized basis set, a grid spacing of 0.18 Å, and a 20 Å × 20 Å × 15 Å unit cell with periodic boundary conditions in all directions. To prepare for the molecular dynamics (MD) simulations, the cell was initially filled with acetonitrile to obtain a density of ρ = 786 mg mL^{-1}, which was thermalized to 300 K with 2.0 fs time steps. This is accomplished with an in-house Langevin integrator employing the RATTLE[40] constraint scheme (algorithm based on the formulation by Eijnden et al.[41]). The constraints introduced consist in the pacification of all C−H bonds, which allows us to take larger time steps and thus decrease the computational time required. Since the role of the C−H bonds in the simulations are very limited we believe that the pacification is justified. After the thermalization, a block of solvent molecules was cut out of the unit cell to make room for the dye or redox mediator molecule (see Figure 3 for an illustration of the procedure). Effectively, this gives a conentration of 0.28 M. Since all boxes are similar in size and only contain one solute molecule, the concentration ratio between all species is unity. The solutes are however electrostatically decoupled from the neighboring cell (resulting from the periodic boundary conditions) through the Ewald method. Thus, we are focusing on a single species, corresponding to the infinite dilution limit. The resulting box, containing the solvated molecule, was then thermalized in the same manner as the initial solvent box. To obtain data for the WHAM method (see discussion above) we created five copies of the thermalized box with the solvated molecule and thermalized them using a linear combination of initial and final state forces with χ_α = 0.0, 0.25, 0.50, 0.75, and 1.00 for each box. After 1.0 ps of thermalization we ran the simulation for an additional 5.0 ps production time, resulting in 2500 data points for every configuration. Combining the data point for the WHAM procedure lead to in total 6.25 million data points for every linear force combination.

RESULTS AND DISCUSSION

The values for all explicitly calculated reorganization energies are given in Tables S2 and S3, Supporting Information, and the constructed Marcus parabolas for the regeneration of the simplest zinc porphyrin dye by $^{LS}[Co^{II/III}(bpy)_3]$ are given in Figure 4. Correcting the calculated λ_{PBC} for the symmetric electron transfer between two porphyrins ($ZnP + ZnP^+ \rightarrow ZnP^+ + ZnP$) for the periodic boundary conditions and the screened coulomb interaction (eq 18) we obtain λ = 0.89 eV. This value is in good agreement with the λ = 0.84 eV reported by Osuka et al.[42] for a comparable electron transfer in porphyrin dyads in DMF. Considering the cobalt-based redox mediators, we note that the energy difference between the high-spin (HS) and the low-spin (LS) states of cobalt(II) species is

DOI: 10.1021/jp512627e
J. Phys. Chem. C 2015, 119, 12792−12800

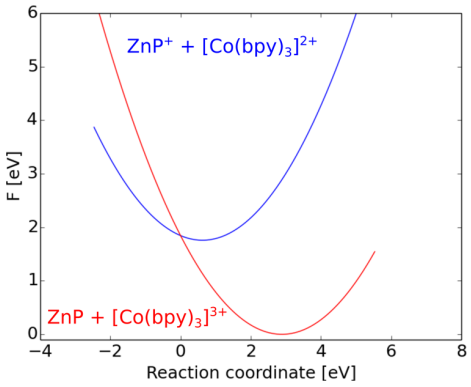

Figure 4. Constructed Marcus parabolas for the regeneration of the simplest zinc porphyrin dye by $^{LS}[Co^{II/III}(bpy)_3]$. The blue curve is $F_i(x)$, and the red curve is $F_f(x)$. ΔF^0 (obtained from eq 21) is −1.76 eV, and the PBC and screened Coulomb interaction-corrected calculated λ is 1.30 eV. Since $-\Delta F^0 > \lambda$ the reaction is predicted to be in the Marcus inverted region.

small.[43] Thus, it may be hard to identify the correct ground spin state using DFT, and we therefore investigated both HS and LS for the two redox mediators in question. In line with previously reported results[44] we here find that the reorganization energy involving the HS is around 1 eV higher than for the LS case. As our calculated and corrected reorganization energies for the regeneration reactions with the LS species resemble the experimental values obtained for the regeneration of an organic dye using different cobalt-based redox mediators reported by Feldt et al.[45,46] we find it likely that these reorganization values give the best representation. We therefore in the following assume that all cobalt species are LS. We further note that our obtained reorganization energies are higher than those recently reported for the cobalt redox mediators using continuum models for the solvent.[44,47] This is expected since we capture the solvent reorientation by including an explicit solvent. Furthermore, we do not include the lowering of the reorganization caused by the immobilization of the dyes introduced by the bonding to the semiconductor. In the following we present the calculated barrier heights associated with the regeneration reaction and the resulting correction function and weighted level alignment quality for all 5000+ porphyrin dyes. It should be noted that in order to obtain high efficiency in a DSSC using cobalt-based redox mediators, it is necessary to have dyes with bulky side groups (e.g., long alkane chains) to prevent electron recombination from TiO_2 to the cobalt species.[14,23] The dyes investigated in this study are however all relatively small due to computational considerations. Using versions with longer alkane chains should not alter the electronic structure of the dyes significantly, and thus, this will only lead to a lowering of the reorganization energy.

Regeneration Barrier Heights. Figure 5 shows the calculated electron transfer barrier (eq 22) as a function of ΔF^0 for all 5000+ porphyrin dyes with both redox mediators. In both figures a clear quadratic dependence on the driving force is observed with minima around $\Delta F^0 = -1.2$ eV for $[Co^{II/III}(bpy)_3]$ and $\Delta F^0 = -1.3$ eV for $[Co^{II/III}(bpy\text{-}pz)_2]$. According to eq 22 the minimum in barrier height is obtained for $\Delta F^0 = -\lambda$, which suggests very high reorganization energies for the regeneration reactions with both redox mediators. In connection with this we note that the deviation from a single parabola for both redox mediators in Figure 5 is negligible. This indicates that the variation in reorganization energy upon functionalizing of the porphyrins is small compared to the total reorganization energy for the regeneration process. Furthermore, the difference in redox potential between the redox mediators (see Table S4, Supporting Information) is clearly observed in the figures as the largest barriers for $[Co^{II/III}(bpy\text{-}pz)_2]$ are obtained for dyes with only a small driving force, while the source of the large barriers for $[Co^{II/III}(bpy)_3]$ can be both a too small and a too large driving force, the latter corresponding to the Marcus inverted region ($-\Delta F^0 > \lambda$).

Weighted Level Alignment Quality. The level alignment quality, η (eq 23), correction factor, $C(\Delta F^0, \lambda; T)$ (eq 25), and weighted level alignment quality, $\eta_{reg} = C(\Delta F^0, \lambda; T)\cdot\eta$, plotted against the driving force, ΔF^0, is shown in Figure 6 for both redox mediators. Here, it is observed that the level alignment quality increases significantly with decreasing driving force. This can be explained by noting that a lowering of the regeneration driving force is equivalent to decreasing the energy difference $E_c - E_H$ in eq 23. At small driving forces the level alignment quality starts to vary more, which can be ascribed to differences in the first excited state, E_1, for the different dyes. Due to the parabolic shape of the Marcus barriers our proposed correction factors are gaussians centered around $-\lambda$ for the regeneration reactions. Thus, multiplying the level alignment qualities and the correction factors results in weighted level alignment qualities peaking around $\Delta F^0 = -\lambda$. The significant dependence on λ and ΔF^0 strongly influences the obtainable weighted level alignment quality for the two different redox mediators. As the $[Co^{II/III}(bpy)_3]$ redox mediator has both a smaller λ and a lower

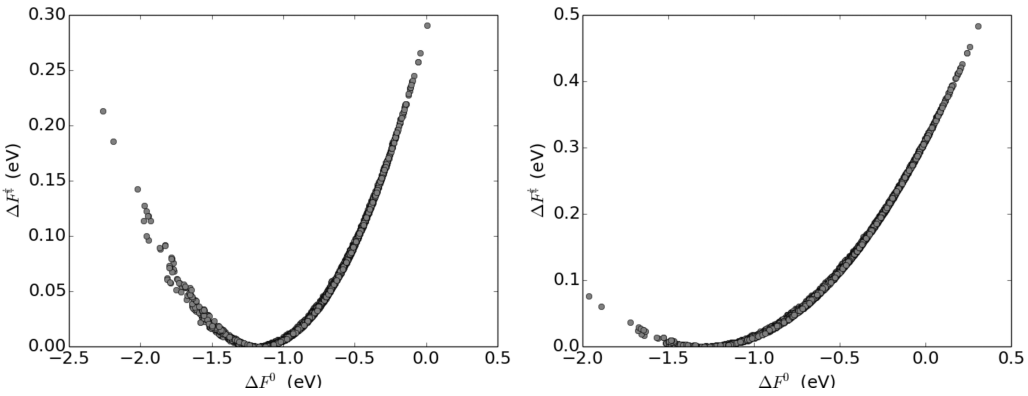

Figure 5. Barrier vs driving force for $[Co^{II/III}(bpy)_3]$ (left) and $[Co^{II/III}(bpy\text{-}pz)_2]$ (right).

DOI: 10.1021/jp512627e
J. Phys. Chem. C 2015, 119, 12792−12800

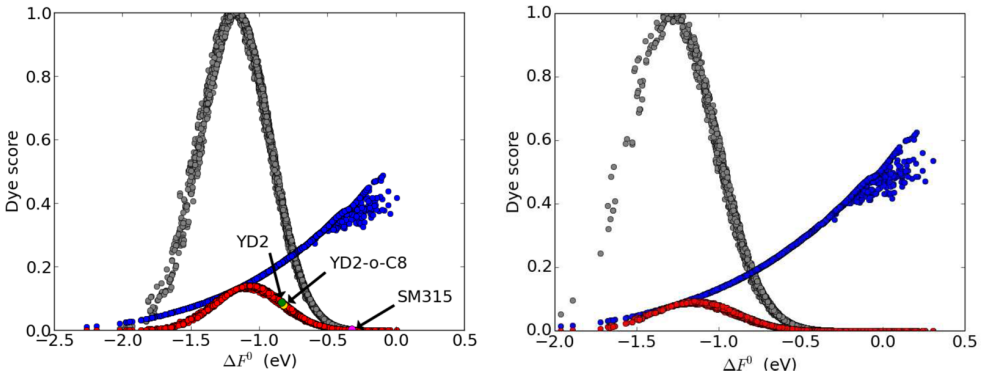

Figure 6. Level alignment quality, η (blue), regeneration correction, $C(\Delta F^0, \lambda)$ (gray), and weighted level alignment quality, $\eta_{reg} = C(\Delta F^0, \lambda; T)\cdot\eta$ (red) for $[Co^{II/III}(bpy)_3]$ (left) and $[Co^{II/III}(bpy\text{-}pz)_2]$ (right) at 298.15 K. For $[Co^{II/III}(bpy)_3]$ the weighted level alignment qualities for the known high-efficiency dyes YD2 (green), YD2-o-C8,[14] (gold) and SM315[15] (magenta) are indicated.

redox potential (higher energy) increasing the driving force of the regeneration reaction we observe significantly higher weighted level alignment qualities using this redox mediator compared to using $[Co^{II/III}(bpy\text{-}pz)_2]$. Here we note that the larger open-circuit voltage obtainable using the latter redox mediator has been taken into account in the level alignment quality, and thus, the V_{oc} is of less importance compared to ΔF^0 and λ.

The top 10 dyes scored on the weighted level alignment quality at room temperature for both redox mediators are given in Tables S5 and S6, Supporting Information. The tables are dominated by dyes having practically no barrier for the regeneration reaction and thus having correction factors very close to unity. This again indicates that the reorganization energy needed for the regeneration reaction overshadows the increase in the level alignment quality obtained by lowering the driving force. In the left part of Figure 6 the calculated weighted level alignment qualities of the known high-efficiency dyes YD2 and YD2-o-C8[14] with the $[Co^{II/III}(bpy)_3]$ redox mediator are indicated. The reported efficiencies for these dyes are 8.4% and 11.9%, respectively,[14] but according to the weighted level alignment quality presented in the figure, the driving force, is slightly too low for these dyes. However, the dyes are still found within our predicted good region of dyes. On the other hand, the record holding SM315[15] dye (reported efficiency of 13.0%) is seen to have even lower weighted level alignment quality due to a very low driving force. As the working temperature of a DSSC can be higher than room temperature due to the exposure to sunlight, we calculated the weighted level alignment for all dyes with both redox mediators at 500 K and presented the top dyes in Tables S7 and S8, Supporting Information. The temperature mainly defines the width of the Gaussian correction function, and thus, dyes with slightly lower regeneration driving force end in the top. The maximum achievable weighted level alignment quality for both redox mediators however only change by 0.01.

The strong dependence of the weighted level alignment quality on the reorganization energy needed for the regeneration reaction inspired us to look at the dependence of η_{reg} on λ for the individual dyes. The results are presented in Figure S9, Supporting Information, for both redox mediators. Here, it is clearly observed that no systematic dependence of η_{reg} on λ can be observed, indicating that it is not the variation in λ for the individual dyes but rather the reorganization energy introduced by the redox mediator which has the greatest impact on the overpotential needed for the regeneration process. In particular, the internal reorganization energy for the two cobalt redox mediators (Table S1, Supporting Information) is a problem which could be expected to be symptomatic for all octahedral transition metal complexes. Using the I^-/I_3^- redox mediator on the other hand introduces significant challenges due to the complicated mechanism for the corresponding regeneration reaction.[48] Thus, the search for new redox mediators with smaller internal reorganization energy and a simple regeneration mechanism must be considered as a very important part of improving the efficiency of DSSCs.

Regeneration versus Recombination. Our definition of the correction factor puts a penalty on all dyes having any barrier associated with the regeneration process. In reality it would however rather be the relationship between the rate of the *regeneration* reaction and the *recombination* reaction (electron transfer from the conduction band of the semiconductor to the oxidized dye) that influences the efficiency. Feldt et al.[45] investigated the regeneration of the organic D35 dye with different cobalt redox mediators and found that a system with λ = 0.8 eV and ΔF^0 = −0.39 eV for the regeneration reaction still had the regeneration reaction dominating over the recombination reaction. Using eq 22, the barrier of this system is $\Delta F^{\ddagger}$ = 0.05 eV. Assuming that regeneration reactions with a barrier equal to or lower than this threshold will be fast enough to dominate over the recombination reaction, we can redefine our correction factor

$$C' = \begin{cases} 1 & \text{for } \Delta F^{\ddagger} \leq 0.05 \text{ eV} \\ \exp\left(\dfrac{-\Delta F^{\ddagger}(\Delta F^0, \lambda) + 0.05 \text{ eV}}{k_B T}\right) & \text{for } F^{\ddagger} > 0.05 \text{ eV} \end{cases} \quad (26)$$

where we still enforce that C' = 0 if $\Delta F^0 > 0$. Using this definition for the $[Co^{II/III}(bpy)_3]$ redox mediator gives the correction factors and weighted level alignment qualities shown in Figure 7. Compared to Figure 6, we here have a large driving force window in which the level alignment quality dominates, shifting the maximum in weighted level alignment quality toward lower driving forces. As indicated in the figure we can further note that we now find the YD2 and YD2-o-C8 dyes within our set of very good candidates, while the record holding SM315 dye still is predicted to have too low driving forces.

A table of the top 10 dyes with this definition of the correction factor can be found in Table S9, Supporting

DOI: 10.1021/jp512627e
J. Phys. Chem. C 2015, 119, 12792−12800

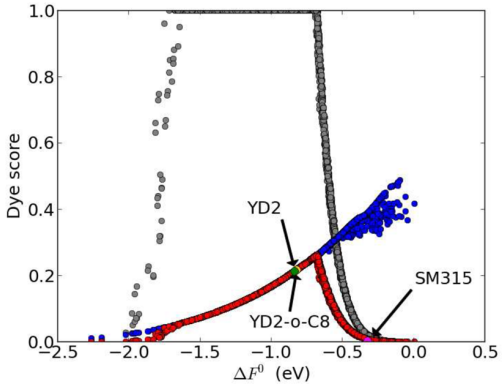

Figure 7. Level alignment quality, η (blue), regeneration correction, $C'(\Delta F^0, \lambda)$ (gray), and weighted level alignment quality, $\eta_{reg} = C'(\Delta F^0, \lambda; T)\cdot\eta$ (red) for $[Co^{II/III}(bpy)_3]$ at 298.15 K using the alternative correction factor C'. The weighted level alignment qualities for the known high-efficiency dyes YD2 (green), YD2-o-C8,[14] (gold) and SM315[15] (magenta) are indicated.

Information. As the table is dominated by dyes having exactly $\Delta F^{\ddagger} = 0.05$ eV, this definition is seen to be extremely sensitive to the chosen threshold value in eq 26, and our choice is thus only one example out of many possibilities. Regardless of the definition of the correction factor, most of the identified top candidates employ a different metal center than the classic zinc center. We therefore believe that our results should encourage exploring, e.g., titanium-based alternatives in the ongoing pursuit for porphyrin-based dyes with high DSSC efficiencies.

CONCLUSIONS

We presented a high-throughput approach to computational design of porphyrin-based dyes for dye-sensitized solar cells. In addition to the energy level alignment and light-harvesting ability of the dyes, the overpotential due to the finite reorganization energy associated with dye regeneration by two commonly used Co redox mediators was taken into account when scoring the dyes. The reorganization energy was calculated using ab initio molecular dynamics for the redox mediators and the simplest Zn−porphyrin dye. These results were then extrapolated to 5000+ functionalized porphyrins using a continuum model for the solvent reorganization energy. We showed that the scheme identifies well-known high-efficiency dyes in addition to a number of new promising candidates. Apart from improving the scoring of the porphyrin dyes, we also identified the reorganization energy of the Co-based redox mediators as an issue to be addressed for improving the efficiency of dye-sensitized solar cells. We propose that new redox mediators with smaller internal reorganization energy than the known octahedral transition metal complexes should be investigated. Here, high-throughput computational methods could be a useful tool.

ASSOCIATED CONTENT

Supporting Information

Derivations, periodic boundary, and finite size corrections; figures with dye backbones, anchor groups, and side groups; tables of explicitly calculated reorganization energies; figures with energy gap distributions and Marcus curves; tables that list of the top 10 dyes based on different scores; figures with weighted level alignment quality as a funtion of the reorganization energy. The Supporting Information is available free of charge on the ACS Publications website at DOI: 10.1021/jp512627e.

AUTHOR INFORMATION

Corresponding Author

*Phone +45 4525 3188. Fax +45 4593 2399. E-mail: thygesen@fysik.dtu.dk.

Present Address

‡Elvar Ö. Jónsson: Department of Applied Physics, Aalto University School of Science, FI-00076 Aalto, Finland.

Notes

The authors declare no competing financial interest.

ACKNOWLEDGMENTS

The authors acknowledge support from the Catalysis for Sustainable Energy (CASE) initiative funded by the Danish Ministry of Science, Technology and Innovation. K.B.Ø. and K.S.T. would further like to thank the Danish Council for Independent Research's DFF-Sapere Aude program (grant no.11-1051390) for financial support.

REFERENCES

(1) Hagfeldt, A.; Boschloo, G.; Sun, L.; Kloo, L.; Pettersson, H. Dye-sensitized solar cells. *Chem. Rev.* **2010**, *110*, 6595−6663.

(2) O'Regan, B.; Grätzel, M. A low-cost, high-efficiency solar cell based on dye-sensitized colloidal TiO_2 films. *Nature* **1991**, *353*, 737−740.

(3) Jung, H. S.; Lee, J.-K. Dye sensitized solar cells for economically viable photovoltaic systems. *J. Phys. Chem. Lett.* **2013**, *4*, 1682−1693.

(4) Li, L.-L.; Diau, E. W.-G. Porphyrin-sensitized solar cells. *Chem. Soc. Rev.* **2013**, *42*, 291−304.

(5) Bessho, T.; Zakeeruddin, S. M.; Yeh, C.-Y.; Diau, E. W.-G.; Grätzel, M. Highly efficient mesoscopic dye-sensitized solar cells based on donor-acceptor-substituted porphyrins. *Angew. Chem., Int. Ed.* **2010**, *49*, 6646−6649.

(6) Moore, G. F.; Konezny, S. J.; Song, H.; Milot, R. L.; Blakemore, J. D.; Lee, M. L.; Batista, V. S.; Schmuttenmaer, C. A.; Crabtree, R. H.; Brudvig, G. W. Bioinspired high-potential porphyrin photoanodes. *J. Phys. Chem. C* **2012**, *116*, 4892−4902.

(7) Liu, B.; Zhu, W.; Wang, Y.; Wu, W.; Li, X.; Chen, B.; Long, Y.-T.; Xie, Y. Modulation of energy levels by donor groups: an effective approach for optimizing the efficiency of zinc-porphyrin based solar cells. *J. Mater. Chem.* **2012**, *22*, 7434−7444.

(8) Masi Reddy, N.; Pan, T.-Y.; Christu Rajan, Y.; Guo, B.-C.; Lan, C.-M.; Wei-Guang Diau, E.; Yeh, C.-Y. Porphyrin sensitizers with [pi]-extended pull units for dye-sensitized solar cells. *Phys. Chem. Chem. Phys.* **2013**, *15*, 8409−8415.

(9) Luo, J.; Xu, M.; Li, R.; Huang, K.-W.; Jiang, C.; Qi, Q.; Zeng, W.; Zhang, J.; Chi, C.; Wang, P.; et al. N-annulated perylene as an efficient electron donor for porphyrin-based dyes: Enhanced light-harvesting ability and high-efficiency Co(II/III)-based dye-sensitized solar cells. *J. Am. Chem. Soc.* **2013**, *136*, 265−272.

(10) He, H.; Gurung, A.; Si, L.; Sykes, A. G. A simple acrylic acid functionalized zinc porphyrin for cost-effective dye-sensitized solar cells. *Chem. Commun.* **2012**, *48*, 7619−7621.

(11) Liu, Y.; Lin, H.; Li, J.; Dy, J. T.; Tamaki, K.; Nakazaki, J.; Nakayama, D.; Nishiyama, C.; Uchida, S.; Kubo, T.; et al. Ethynyl-linked push-pull porphyrin hetero-dimers for near-IR dye-sensitized solar cells: photovoltaic performances versus excited-state dynamics. *Phys. Chem. Chem. Phys.* **2012**, *14*, 16703−16712.

(12) Chaitanya, K.; Ju, X.-H.; Heron, B. M. Theoretical study on the light harvesting efficiency of zinc porphyrin sensitizers for DSSCs. *RSC Adv.* **2014**, *4*, 26621−26634.

(13) Wang, C.-L.; Hu, J.-Y.; Wu, C.-H.; Kuo, H.-H.; Chang, Y.-C.; Lan, Z.-J.; Wu, H.-P.; Wei-Guang Diau, E.; Lin, C.-Y. Highly efficient porphyrin-sensitized solar cells with enhanced light harvesting ability

DOI: 10.1021/jp512627e
J. Phys. Chem. C 2015, 119, 12792−12800

beyond 800 nm and efficiency exceeding 10%. *Energy Environ. Sci.* **2014**, *7*, 1392−1396.
(14) Yella, A.; Lee, H.-W.; Tsao, H. N.; Yi, C.; Chandiran, A. K.; Nazeeruddin, M. K.; Diau, E. W.-G.; Yeh, C.-Y.; Zakeeruddin, S. M.; Grätzel, M. Porphyrin-sensitized solar cells with cobalt (II/III)-based redox electrolyte exceed 12% efficiency. *Science* **2011**, *334*, 629−634.
(15) Mathew, S.; Yella, A.; Gao, P.; Humphry-Baker, R.; Curchod, B. F. E.; Ashari-Astani, N.; Tavernelli, I.; Rothlisberger, U.; Nazeeruddin, M. K.; Grätzel, M. Dye-sensitized solar cells with 13% efficiency achieved through the molecular engineering of porphyrin sensitizers. *Nat. Chem.* **2014**, *6*, 242−247.
(16) Ørnsø, K. B.; Garcia-Lastra, J. M.; Thygesen, K. S. Computational screening of functionalized zinc porphyrins for dye sensitized solar cells. *Phys. Chem. Chem. Phys.* **2013**, *15*, 19478−19486.
(17) Ørnsø, K. B.; Pedersen, C. S.; Garcia-Lastra, J. M.; Thygesen, K. S. Optimizing porphyrins for dye sensitized solar cells using large-scale ab initio calculations. *Phys. Chem. Chem. Phys.* **2014**, *16*, 16246−16254.
(18) Marcus, R. A. On the theory of oxidationreduction reactions involving electron transfer. I. *J. Chem. Phys.* **1956**, *24*, 966−978.
(19) Marcus, R. A. Electrostatic free energy and other properties of states having nonequilibrium polarization. I. *J. Chem. Phys.* **1956**, *24*, 979−989.
(20) Marcus, R. A. On the theory of oxidation-reduction reactions involving electron transfer. II. Applications to data on the rates of isotopic exchange reactions. *J. Chem. Phys.* **1957**, *26*, 867−871.
(21) Marcus, R. A. On the theory of oxidation-reduction reactions involving electron transfer. III. Applications to data on the rates of organic redox reactions. *J. Chem. Phys.* **1957**, *26*, 872−877.
(22) Marcus, R. A. On the theory of electron-transfer reactions. VI. Unified treatment of homogeneous and electrode reactions. *J. Chem. Phys.* **1965**, *43*, 679−701.
(23) Feldt, S. M.; Gibson, E. A.; Gabrielsson, E.; Sun, L.; Boschloo, G.; Hagfeldt, A. Design of organic dyes and cobalt polypyridine redox mediators for high-efficiency dye-sensitized solar cells. *J. Am. Chem. Soc.* **2010**, *132*, 16714−16724.
(24) Yum, J.-H.; Baranoff, E.; Kessler, F.; Moehl, T.; Ahmad, S.; Bessho, T.; Marchioro, A.; Ghadiri, E.; Moser, J.-E.; Yi, C.; et al. A cobalt complex redox shuttle for dye-sensitized solar cells with high open-circuit potentials. *Nat. Commun.* **2012**, *3*, 631−1−8.
(25) Warshel, A. Dynamics of reactions in polar solvents. Semiclassical trajectory studies of electron-transfer and proton-transfer reactions. *J. Phys. Chem.* **1982**, *86*, 2218−2224.
(26) Souaille, M.; Roux, B. Extension to the weighted histogram analysis method: Combining umbrella sampling with free energy calculations. *Comput. Phys. Commun.* **2001**, *135*, 40−57.
(27) Ferrenberg, A. M.; Swendsen, R. H. Optimized Monte Carlo data analysis. *Phys. Rev. Lett.* **1989**, *63*, 1195−1198.
(28) Kumar, S.; Rosenberg, J. M.; Bouzida, D.; Swendsen, R. H.; Kollman, P. A. The weighted histogram analysis method for free-energy calculations on biomolecules. I. The method. *J. Comput. Chem.* **1992**, *13*, 1011−1021.
(29) Tachiya, M. Relation between the electron-transfer rate and the free energy change of reaction. *J. Phys. Chem.* **1989**, *93*, 7050−7052.
(30) King, G.; Warshel, A. Investigation of the free energy functions for electron transfer reactions. *J. Chem. Phys.* **1990**, *93*, 8682−8692.
(31) *Jmol: an open-source Java viewer for chemical structures in 3D*; http://www.jmol.org/, Jmol.org: USA, 2014.
(32) Hummer, G.; García, A. E. Ion sizes and finite-size corrections for ionic-solvation free energies. *J. Chem. Phys.* **1997**, *107*, 9275−9277.
(33) Hünenberger, P. H.; McCammon, J. A. Ewald artifacts in computer simulations of ionic solvation and ionion interaction: A continuum electrostatics study. *J. Chem. Phys.* **1999**, *110*, 1856−1872.
(34) Ayala, R.; Sprik, M. A classical point charge model study of system size dependence of oxidation and reorganization free energies in aqueous solution. *J. Phys. Chem. B* **2008**, *112*, 257−269.
(35) Yaghoobi Nia, N.; Farahani, P.; Sabzyan, H.; Zendehdel, M.; Oftadeh, M. A combined computational and experimental study of the [Co(bpy)3]2+/3+ complexes as one-electron outer-sphere redox couples in dye-sensitized solar cell electrolyte media. *Phys. Chem. Chem. Phys.* **2014**, *16*, 11481−11491.
(36) Kohn, W.; Sham, L. J. Self-consistent equations including exchange and correlation effects. *Phys. Rev.* **1965**, *140*, A1133−A1138.
(37) Perdew, J. P.; Burke, K.; Ernzerhof, M. Generalized Gradient Approximation made simple. *Phys. Rev. Lett.* **1996**, *77*, 3865−3868.
(38) Enkovaara, J.; Rostgaard, C.; Mortensen, J. J.; Chen, J.; Dulak, M.; Ferrighi, L.; Gavnholt, J.; Glinsvad, C.; Haikola, V.; Hansen, H. A.; et al. Electronic structure calculations with GPAW: a real-space implementation of the projector augmented-wave method. *J. Phys.: Condens. Matter* **2010**, *22*, 253202−1−24.
(39) Larsen, A. H.; Vanin, M.; Mortensen, J. J.; Thygesen, K. S.; Jacobsen, K. W. Localized atomic basis set in the projector augmented wave method. *Phys. Rev. B* **2009**, *80*, 195112−1−10.
(40) Andersen, H. C. Rattle: A "velocity" version of the shake algorithm for Molecular Dynamics calculations. *J. Comput. Phys.* **1983**, *54*, 24−34.
(41) V. Eijnden, E.; Ciccotti, G. Second-order integrators for Langevin equations with holonomic constraints. *Chem. Phys. Lett.* **2006**, *429*, 310−316.
(42) Osuka, A.; Noya, G.; Taniguchi, S.; Okada, T.; Nishimura, Y.; Yamazaki, I.; Mataga, N. Energy-gap dependence of photoinduced charge separation and subsequent charge recombination in 1,4-phenylene-bridged zinc-free-base hybrid porphyrins. *Chem.—Eur. J.* **2000**, *6*, 33−46.
(43) Krivokapic, I.; Zerara, M.; Daku, M. L.; Vargas, A.; Enachescu, C.; Ambrus, C.; Tregenna-Piggott, P.; Amstutz, N.; Krausz, E.; Hauser, A. Spin-crossover in cobalt(II) imine complexes. *Coord. Chem. Rev.* **2007**, *251*, 364−378.
(44) Mosconi, E.; Yum, J.-H.; Kessler, F.; Gómez Garcia, C. J.; Zuccaccia, C.; Cinti, A.; Nazeeruddin, M. K.; Grätzel, M.; De Angelis, F. Cobalt electrolyte/dye interactions in dye-sensitized solar cells: A combined computational and experimental study. *J. Am. Chem. Soc.* **2012**, *134*, 19438−19453.
(45) Feldt, S. M.; Wang, G.; Boschloo, G.; Hagfeldt, A. Effects of driving forces for recombination and regeneration on the photovoltaic performance of dye-sensitized solar cells using cobalt polypyridine redox couples. *J. Phys. Chem. C* **2011**, *115*, 21500−21507.
(46) Feldt, S. M.; Lohse, P. W.; Kessler, F.; Nazeeruddin, M. K.; Grätzel, M.; Boschloo, G.; Hagfeldt, A. Regeneration and recombination kinetics in cobalt polypyridine based dye-sensitized solar cells, explained using Marcus theory. *Phys. Chem. Chem. Phys.* **2013**, *15*, 7087−7097.
(47) Sun, Z.-Z.; Zheng, K.-M.; Li, Q.-S.; Li, Z.-S. Rational design of Co-based redox mediators for dye-sensitized solar cells by density functional theory. *RSC Adv.* **2014**, *4*, 31544−31551.
(48) Boschloo, G.; Hagfeldt, A. Characteristics of the iodide/triiodide redox mediator in dye-sensitized solar cells. *Acc. Chem. Res.* **2009**, *42*, 1819−1826.

DOI: 10.1021/jp512627e
J. Phys. Chem. C 2015, 119, 12792−12800

Appendix E

Paper IV

Design of two-photon molecular tandem architectures for solar cells by *ab initio* theory
K. B. Ørnsø, J. M. Garcia-Lastra, G. De La Torre, F. J. Himpsel, A. Rubio and K. S. Thygesen
Chem. Sci., **2015**, *6*, 3018-3025

Chemical Science

EDGE ARTICLE

Cite this: *Chem. Sci.*, 2015, **6**, 3018

Design of two-photon molecular tandem architectures for solar cells by *ab initio* theory†

Kristian B. Ørnsø,*[a] Juan M. Garcia-Lastra,[ab] Gema De La Torre,[c] F. J. Himpsel,[d] Angel Rubio[ef] and Kristian S. Thygesen*[a]

Received 11th December 2014
Accepted 4th March 2015

DOI: 10.1039/c4sc03835e

www.rsc.org/chemicalscience

An extensive database of spectroscopic properties of molecules from *ab initio* calculations is used to design molecular complexes for use in tandem solar cells that convert two photons into a single electron–hole pair, thereby increasing the output voltage while covering a wider spectral range. Three different architectures are considered: the first two involve a complex consisting of two dye molecules with appropriately matched frontier orbitals, connected by a molecular diode. Optimized combinations of dye molecules are determined by taking advantage of our computational database of the structural and energetic properties of several thousand porphyrin dyes. The third design is a molecular analogy of the intermediate band solar cell, and involves a single dye molecule with strong intersystem crossing to ensure a long lifetime of the intermediate state. Based on the calculated energy levels and molecular orbitals, energy diagrams are presented for the individual steps in the operation of such tandem solar cells. We find that theoretical open circuit voltages of up to 1.8 V can be achieved using these tandem designs. Questions about the practical implementation of prototypical devices, such as the synthesis of the tandem molecules and potential loss mechanisms, are addressed.

1 Introduction

As the search for renewable energy sources has intensified, the discovery of efficient and cheap technologies for exploiting the energy from the sunlight has emerged as a key challenge. Important examples of such technologies include organic polymer and small-molecule solar cells, as well as dye sensitized solar cells (DSSCs) which provide inexpensive, flexible, and environmentally friendly alternatives to the more conventional inorganic solar cells.[1–3] One important drawback of the traditional molecular based photovoltaic systems is their inefficiency in capturing the red and infrared part of the solar spectrum. In fact, they are often transparent in the red, suggesting the addition of a second solar cell to intercept that part of the solar spectrum.[4] Such tandem cells have the potential to double the output voltage of a solar cell at the expense of a lower current. As lower currents are associated with smaller losses and higher fill-factors, as observed in experiments under low light intensity,[5,6] trading a high current for a high voltage could boost the efficiency of the cell.

Higher efficiency plays an increasingly important role in making competitive solar cell designs as the price of silicon continues to drop. At present, the actual silicon solar cell accounts for less than 1/4 of the cost of a complete solar panel installation and the cost of the support structure is becoming increasingly important. Higher efficiency reduces the required area and thereby reduces the cost of both the solar cells and their support structure.[7] A way to increase the efficiency of a photovoltaic system is to incorporate the second solar cell into a tandem device. However, pn-type tandem DSSCs have not been able to surpass the efficiency of single DSSCs so far.[8,9] Tandem designs have also been investigated for polymer solar cells[10,11] (for further references on tandem designs in organic photovoltaics see ref. 51–58 in the review by Krebs[12] and ref. 213–232 in the review by Cao and Xue[13]). Furthermore, dye sensitized upconversion has been suggested as a way to exploit infrared light.[14–16]

Conventional tandem solar cells (organic as well as inorganic) combine two or more types of materials that are separated by interfaces where electrons and holes are exchanged. These interfaces are highly critical and inevitably contain defects and other imperfections, which act as scattering and

[a]*Center for Atomic-scale Materials Design, Department of Physics, Technical University of Denmark, 2800 Kgs. Lyngby, Denmark. E-mail: krbt@fysik.dtu.dk; thygesen@fysik.dtu.dk*

[b]*Department of Energy Conversion, Technical University of Denmark, Frederiksborgvej 399, 4000 Roskilde, Denmark*

[c]*Departamento de Quimica Organica, Facultad de Ciencias, Universidad Autonoma de Madrid, Campus de Cantoblanco, 28049 Madrid, Spain*

[d]*Department of Physics, University of Wisconsin-Madison, 1150 University Avenue, Madison, Wisconsin 53706, USA*

[e]*Max Planck Institute for the Structure and Dynamics of Matter, Hamburg, Germany*

[f]*Nano-Bio Spectroscopy Group and ETSF, Universidad del Pais Vasco CFM CSIC-UPV/EHU-MPC & DIPC, 20018 San Sebastian, Spain*

† Electronic supplementary information (ESI) available: Visualizations of molecular orbitals, one-particle mechanisms and a table with Kohn–Sham eigenvalues. See DOI: 10.1039/c4sc03835e

recombination centers for the charge carriers. The problem of controlling the atomic structure of the interface could be circumvented using molecular complexes where molecules absorbing in different parts of the solar spectrum are combined with atomic precision through synthetic chemistry. The design of such complexes is clearly a daunting experimental challenge as successful operation depends sensitively on the relative position of all the involved energy levels. However, using *ab initio* calculations it is now possible to search a large variety of possible materials and identify promising candidates which could be considered experimentally.[17–21] Recently we have constructed a database containing calculations of the frontier orbitals of more than 5000 porphyrin dyes.[22,23] Porphyrins have been widely used in DSSCs[24] including the system with the highest reported efficiency so far.[25] Here we take advantage of this database to propose new porphyrin-based molecular complexes inspired by the tandem[26] and intermediate band[27–29] solar cell schemes. The proposed molecular architectures have the potential to exploit a broader range of the solar spectrum and at the same time obtain very large open-circuit voltages. In addition, the proposed design combines the different photoactive regions through atomically well-defined chemical bonds and thereby eliminates the problems with disorder and defects at the interfaces in conventional tandem devices. We present our idea in the context of a DSSC and show that open-circuit voltages of up to 1.8 V are achievable in molecular complexes that generate a single electron–hole pair from two absorbed photons. Finally, we briefly discuss practical perspectives and challenges related to the realization of the proposed schemes.

2 Methods

The atomic and electronic structures of 5000+ porphyrins are taken from our public database[22,23] (http://cmr.fysik.dtu.dk) containing quantum mechanical calculations based on the use of density functional theory (DFT)[30] with the PBE[31] exchange–correlation functional as implemented in the GPAW code.[32] The calculations use consistently a basis set of numerical atomic orbitals[33] with double-ζ and polarization, a grid-spacing of 0.18 Å and a unit cell with a 5.0 Å vacuum added on all sides of the molecules. The structures have been optimized until all forces were below 0.05 eV $Å^{-1}$. After the geometry optimization the location of the highest occupied molecular orbital (HOMO), E_{HOMO}, and lowest unoccupied molecular orbital (LUMO), E_{LUMO}, were calculated as the ionization potential I_P and electron affinity E_A of the molecule. Thus the resulting energy gap, E_{gap}, is given by:

$$E_{gap} = E_{LUMO} - E_{HOMO} = (E[-1] - E[0]) - (E[0] - E[+1]) = I_P - E_A \quad (1)$$

where $E[0]$ is the ground state total energy and $E[-1]$ and $E[+1]$ is the total energy of the negatively and positively charged ions of the molecule in the ground state geometry, respectively. In the latter case the magnetic moment of the system is fixed to ensure a single unpaired electron. This definition of E_{HOMO} and E_{LUMO} avoids the use of Kohn–Sham (KS) eigenvalues which are well-known to be inaccurate within PBE. In addition we have previously shown that this definition gives good trends compared to experiments[22] and we will therefore use E_{HOMO} and E_{LUMO} calculated from total energy calculations throughout this study. In addition to the fundamental gap, the lowest optical transition energy, E_1, has also been calculated. The calculation of E_1 is done by forcing the molecule to the triplet ground state by fixing the magnetic moment, and thus promoting one of the two electrons in the HOMO to the LUMO. We use the triplet excitation energy rather than the singlet excitation because this is technically simpler to compute. We have previously shown for a number of Zn porphyrins that the singlet and triplet excitations are within 0.3 eV and that their dependence on molecular structure is very similar.[22] In the same study we furthermore showed that computed E_{HOMO} and E_1 values compared well to experimental values.[22,34] For selected dyes we have in this study calculated the singlet excitation energies using the all-electron ADF code with a double-ζ Slater-type basis set with polarization functions[35] and the proposed dyad for the molecular tandem scheme has been investigated using TD-DFT as implemented in Orca[36] with the CAM-B3LYP functional.[37] Full details on the ADF and Orca calculations are given in the ESI.†

3 Molecular two-photon schemes

Inspired by earlier attempts to improve the light absorption in DSSCs by combining the conventional n-type DSSC with a p-type DSSC[38] to construct a tandem pn-DSSC,[26] the intermediate band solar cell design[27,28] and especially the molecular version of this,[29] as well as previous attempts to use supramolecular porphyrin structures to enhance the efficiency,[39–41] we propose three different molecular two-photon schemes, shown in Fig. 1. The different schemes are explained in more detail in the following, where we also propose specific dyes as suitable

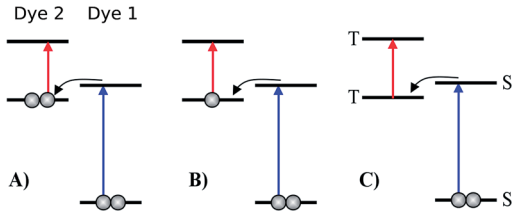

Fig. 1 Various proposed energy level schemes for solar cells based on two dye molecules connected by a molecular diode (molecular linker not shown here, see Fig. 3). The occupancy is given for the ground state. (A) Simplest concept with both HOMOs doubly occupied. Both dye molecules need to be excited at the same time to generate a hole in the upper HOMO that can take up an electron from the lower LUMO. That is unlikely to happen in the same tandem complex. (B) The upper HOMO is partially occupied to allow facile charge transfer between the two dye molecules. Such a situation can be realized in metal–organic dye molecules with an odd number of electrons. This is the analog of an intermediate band solar cell.[27–29] (C) Using singlet (S) and triplet (T) excitations. The long lifetime of the triplet allows a significant electron population to accumulate in the lower triplet level, which can be excited into the upper triplet level. This scheme could also be realized with a single dye molecule.

candidates for experimental realizations of the different schemes.

3.1 Tandem scheme

The first concept we propose is the tandem scheme shown in Fig. 1A in which we exploit the level alignment of two dyes to obtain a higher open-circuit voltage. One of the dyes should be a dye with a low lying HOMO (dye 1) and the second should have a LUMO aligned with the conduction band of TiO_2 (dye 2). To optimize the efficiency of a tandem cell it has been proposed to have one species with an optical gap of 1.0 eV and another with 1.9 eV.[42] However, while this is true for semi-conductors which absorb most photons above the band gap, for dyes with limited absorption it may be better to use two dyes with optical gaps of 1.1 eV in agreement with the Shockley–Queisser limit.[43] Having dyes fulfilling these requirements, the basic idea can be described in six simple steps: I → II: a photon excites an electron from the HOMO of dye 2 to an excited level. II → III: the excited electron on dye 2 is rapidly injected into the conduction band of the semi-conductor. III → IV: a second photon excites an electron from the HOMO of dye 1 to the LUMO of dye 1. IV → V: the excited electron on dye 1 tunnels to fill the hole on the HOMO of dye 2. V → VI: an electron from the redox mediator regenerates the dye by filling the hole on the HOMO of dye 1. VI → I: the electron in the conduction band of the semi-conductor is used for performing electric work after which it is transferred back to the electrolyte *via* the counter electrode as in standard DSSCs.

This mechanism puts some constraints on the two dyes to be used, but using our database of functionalized porphyrins,[22,23] we have identified around 800 suitable dye pairs (see Fig. 2 for an illustration of this process) made from 9 unique dyes for use as dye 2, all functionalized with highly donating side groups. On the other hand, the dyes suitable for use as dye 1 should have less donating side groups in order to have a lower-lying HOMO. From the suitable candidates we have chosen the simplest example and refined the structure to provide an experimentally realizable molecule while retaining the alignment of the molecular levels. The singlet excitation energies and level alignment of the refined individual dyes are given in Table 1. It may be noted that the calculated singlet excitation energies agree within 0.2–0.4 eV to the excitation energies obtained using TD-DFT with B3LYP (see Table S1 in ESI†). To create the tandem scheme, the dyes have been connected from the central side group of dye 2 to the anchor group of dye 1. A scheme of the full tandem scheme is given in Fig. 3. As in a semiconductor tandem cell, the connection between the two dye molecules has to act as a diode in order to suppress recombination of the final electron with the initial hole.[44–46] Any molecular wire can act as diode, as long as it is asymmetric, *i.e.*, the energy levels at the two ends of the wire are different. Many such molecular wires have been investigated, for example by $I(V)$ spectroscopy of break junctions bridged by a molecule or of a molecule connecting the tip of a scanning tunneling microscope to a surface.[47–49] The optimal length of the linker involves a trade-off between fast electron transfer (shorter is better) and preservation of the properties of the individual dyes (longer is better). A useful tool for controlling the charge transfer between the dye molecules is a tunnel junction, which contains a stretch of molecular wire with a significant HOMO–LUMO gap between conducting pi-systems.[50,51] Macroscopic tunnel junctions constitute an important part of inorganic tandem solar cells. To minimize hybridization between the two dyes while ensuring a reasonably short tunneling barrier, we propose to connect the two dyes by an ester bond between the carboxylic acid of dye 1 and a phenolic group linked to the *meso* position of dye 2. The synthesis of the tandem structure is an arduous but realizable task. Two individual face-to-face functionalized porphyrins have to be prepared, showing a similar functionalization pattern to that of push–pull porphyrin dyes with record efficiencies in DSSCs.[25] Each of the crosswise-substituted porphyrins can be obtained by condensation between dipyrromethane and either benzaldehyde (for dye 1) or *N*,*N*-bis(4-methoxyphenyl)-4-aminobenzaldehyde (for dye 2). Following this, bromination of the free *meso* positions of the porphyrins, and sequential Pd-catalyzed cross-coupling reactions, namely, Buchwald, Suzuki or Stille procedures, to incorporate the diphenylamino moiety, 4-ethynylphenol or the anchoring group, respectively, would lead to the target dyes. Finally, both chromophores could be linked together through a final esterification reaction.

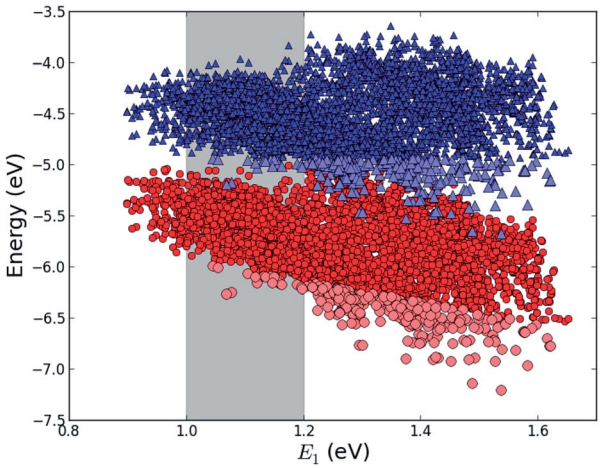

Fig. 2 E_{HOMO} (red circles) and $E_{HOMO} + E_1$ (blue triangles) for all 5000+ porphyrins in our database[22,23] plotted against the lowest optical transition energy, E_1. The light blue and light red points indicate dyes where $E_{HOMO} + E_1$ lies at a lower energy than the maximum value of E_{HOMO} making it a potential candidate for dye 1 in the tandem scheme and the gray shaded area indicates the region of interest around $E_1 = 1.1$ eV.

Table 1 Calculated singlet excitation energies and level alignment of the individual dyes used in the tandem scheme

Species	E_{HOMO} (eV)	$E_{HOMO} + E_1$ (eV)	E_1 (eV)
Dye 1	−5.9	−4.7	1.2
Dye 2	−5.3	−4.1	1.2

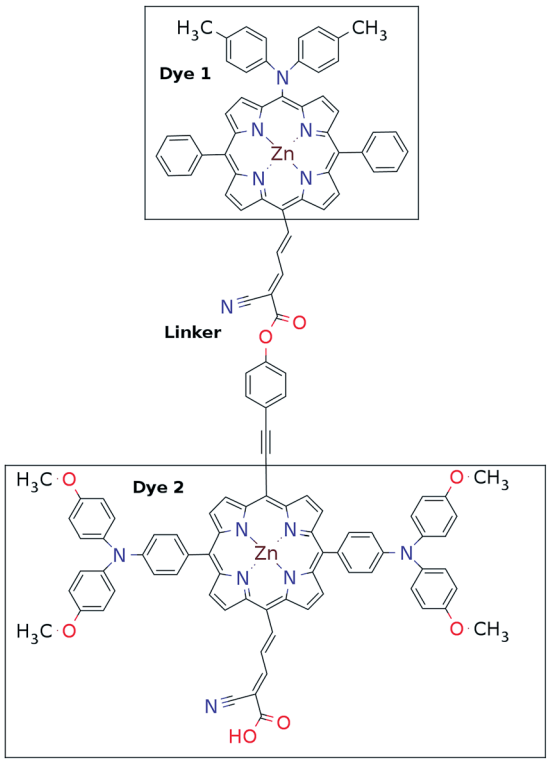

Fig. 3 Chemical structure of one of the molecular tandem schemes used in the present work.

Proof of the lack of hybridization between dyes has been achieved by calculations of the frontier orbitals of the full tandem set up. A visualization of these using, respectively, the PBE and CAM-B3LYP functional are given in Fig. S1 and S2 in the ESI.† It may be noted that the different functionals yield different ordering and spatial weights, but in both figures it is readily seen that the orbitals are highly localized on the individual dyes and resemble the orbitals calculated for these individually. This means that the proposed mechanism effectively transfers an electron from the backbone of dye 1 to the anchor group of dye 2. In this way the tandem scheme achieves excellent charge separation with the electron overlapping with the conduction band of the semi-conductor and the hole located close to the electrolyte. Performing a TD-DFT calculation on the full tandem dyad furthermore reveals a large oscillator strength (see Table S2 in the ESI†) for the local excitations on both parts of the dyad. Additionally, the oscillator strength associated with the charge transfer from dye 2 to dye 1 in the dyad is of comparable size to the local excitations. Thus the charge transfer is possible at least in terms of energetics but the charge transfer integral has yet to be evaluated.[52,53] Using the values from Table 1, and taking TiO_2 as the semi-conductor with the conduction band located at −4.1 eV and an electrolyte with a redox potential aligned 0.3 eV above the HOMO of dye 1, we can construct the detailed energetics given in Fig. 4 where the mechanisms for all six steps are also indicated. In the figure we further assume that the electronic excitations are faster than the structural relaxation of the individual dyes. This leaves us with a mechanism that, apart from the two photo-excitations, is downhill and with a theoretical open-circuit voltage of 1.5 V which is a significant improvement compared to current DSSC devices. However, the low-lying $[Co^{II/III}(bpy\text{–}pz)_2]$ redox pair only has a redox potential of −5.36 eV *vs.* vacuum[54] which limits the theoretical open-circuit voltage of the tandem device to 1.26 V (using $V_{oc} = E_c - E_{red}$). Thus, it is crucial to use an electrolyte with a lower redox potential. This could *e.g.* be achieved by modifying the ligands of the popular cobalt-based redox couple as shown by Feldt *et al.*[55] or by designing completely new redox mediators.

3.2 Intermediate band scheme

In general the lifetimes of the singlet excitation of zinc porphyrins are long (more than 1 ns).[56,57] However, the time-scale on which the excited electron on dye 1 tunnels to the hole on dye 2 is unknown (step IV → V in Fig. 4). Unfortunately, this crucial step is probably highly unlikely, since there are very few photoexcited electrons in the LUMO of dye 1, which have to find one of the very few photo-generated holes which are in the HOMO of dye 2 at the same place and the same time. A possibility to overcome this is to have the HOMO of dye 2 half-filled in the ground state as shown in Fig. 1B as this would give the photoexcited electrons a good chance to find a hole in the HOMO of dye 2. Having this type of scheme would then give the six step shown in Fig. S3 in the ESI.† I → II: a photon excites an electron from the HOMO of dye 1 to the LUMO of dye 1. II → III: the excited electron on dye 1 tunnels to the singly-occupied HOMO of dye 2. III → IV: a second photon excites an electron from the now doubly-occupied HOMO of dye 2 to an exited state on dye 2. IV → V: the excited electron on dye 2 is rapidly injected into the conduction band of the semi-conductor. V → VI: an electron from the redox-mediator regenerates the dye by filling the hole on the HOMO of dye 1. VI → I: the electron in the conduction band of the semi-conductor is used for performing electric work after which it is transferred back to the electrolyte *via* the counter electrode as in standard DSSCs.

A possibility for realizing this scheme could be to use a porphyrin with a transition metal center with an uneven number of electrons such as Fe^{3+} (d^5-system). Performing a calculation of this species confirms in accordance with reported calculations,[58,59] the presence of an unpaired electron located in an orbital similar to the HOMO of the iron(II) porphyrin (see Fig. S4 in ESI† for details).

3.3 Intermediate triplet state scheme

In the single-dye intermediate triplet state scheme we propose to still use two photons but only a single dye. Here the idea is to have a dye with a low lying HOMO, a LUMO located inside the gap of the semi-conductor used and a higher excited state aligned with the semi-conductor conduction band edge. The first photon should thus excite an electron from the HOMO to the LUMO followed by a second photon exciting the electron from the LUMO to the higher excited state. To ensure that the first excitation lives long enough for the second excitation to occur, we can exploit inter-system-crossing (ISC) to prepare the

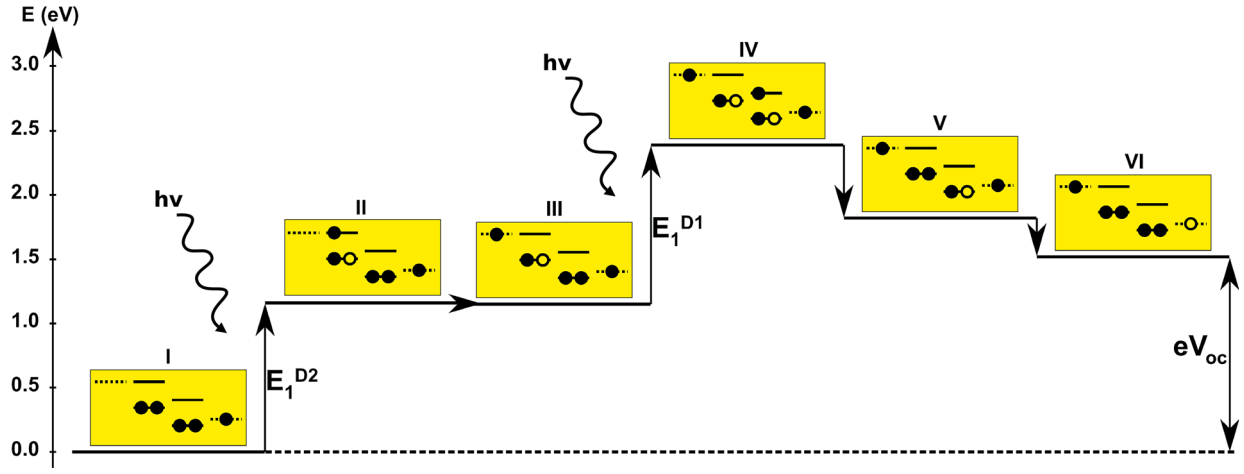

Fig. 4 One-particle state-based sketch of the steps involved in the molecular tandem device proposed here. For each state the energetics are indicated by the *y*-axis while the one-particle mechanism associated with the step is shown in the corresponding yellow box. Here the filled circles represent electrons and the empty circles represents holes. From right to left in each box the dotted state is the redox mediator, the first set of solid lines represents the ground state and excited state of dye 1, the second set of solid lines represents the ground and excited state of dye 2 and the last dotted line represents the conduction band of the semi-conductor.

first excited state in a triplet state with a long lifetime. This is equivalent to the scheme in Fig. 1C. Thus, the idea can be described in six steps: I → II: a photon excites an electron from the HOMO of the dye to the first excited singlet state. II → III: the excited electron undergoes ISC to the first excited triplet state. III → IV: a second photon excites the electron from the first excited triplet state to a higher excited triplet state. IV → V: the excited electron is injected into the conduction band of the semi-conductor. V → VI: an electron from the redox-mediator regenerates the dye by filling the hole on the HOMO of the dye. VI → I: the electron in the conduction band of the semi-conductor is used for performing electric work after which it is transferred back to the electrolyte *via* the counter electrode as in standard DSSCs. By again employing our database,[22,23] we have found a candidate (see Fig. 5) with suitable energy levels as shown in Table 2. Here, the LUMO is located in the band gap of TiO_2 and the triplet is located at a slightly lower energy than the singlet state making it energetically favorable to perform ISC. Furthermore, the triplet LUMO+2 is well aligned with the conduction band of TiO_2 making this level perfect as the second excited state used in this type of scheme. Using these levels in the dye yields the energetics shown in Fig. 6 where the mechanisms for all six steps are also indicated. From the figure it is seen that this scheme yields a V_{oc} around 1.8 V, again significantly exceeding 1.0 V. However, for this approach to be realistic we need a dye with a high ISC. As the fluorescence lifetime of a zinc porphyrin molecule has been reported to be greater than 1.0 ns, indicating no significant ISC,[56] we may need to exchange the Zn metal center with a heavier metal to obtain a higher ISC yield. Here, porphyrins especially with a Pd metal center have previously been shown to undergo efficient ISC with a quantum yield close to unity.[60] Performing a DFT calculation on the closed-shell Pd version of the porphyrin dye reveals that the KS eigenvalues for the frontier orbitals are nearly identical to the eigenvalues for the Zn porphyrin. All eigenvalues are given in Table S3 in the ESI.† A visualization of the relevant orbitals for both species is given in Fig. S5 in the ESI.† From the figure we see that the orbitals are nearly identical for the two species and that the orbitals are very well suited for this type of scheme as the HOMO is located mostly on the backbone and side group whereas the LUMO is located more on the anchor group. This has the consequence that the first excitation obtains a great charge separation limiting the recombination of hole and electron. The shape of the second excited state (LUMO+2) of both porphyrins is very similar to the LUMO yielding a high oscillator strength for the transition. The localization of the

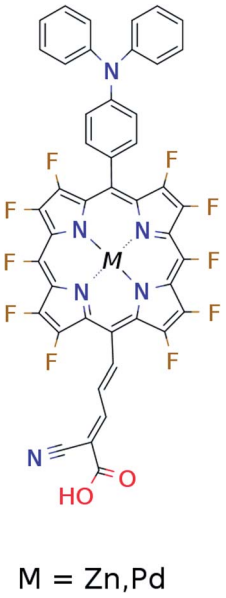

M = Zn,Pd

Fig. 5 Scheme of the proposed dye for the single-dye intermediate triplet state scheme.

Table 2 Calculated singlet and triplet orbital energies for the dye used in the single-dye intermediate triplet state scheme

State	$E_{\text{singlet state}}$ (eV)	$E_{\text{triplet state}}$ (eV)
HOMO	−6.2	—
LUMO	−4.9	−5.0
LUMO+2	—	−4.1

LUMO+2 on the anchor group furthermore ensures a very fast injection of the excited electron into the conduction band of the semi-conductor. Using the Pd species may thus, *via* the high ISC, be a way to obtain the mechanism sketched in Fig. 6. Another approach to obtain the triplet excited state could be to use the concept of singlet fission.[61] To use singlet fission we would however need to meet a number of restrictions such as a large energy gap between the singlet and triplet states, which is not present for the first excited state of the Zn porphyrin and a different type of dye should thus be used. As for the tandem scheme, the redox potential of the commonly-used redox mediators are located at energies too high for this scheme to be efficient. Thus, it is also crucial here to use an electrolyte with a better-aligned redox potential.

4 Conclusions

We have proposed three new two-photon tandem schemes for use in photovoltaics in a pure molecular framework thus avoiding the inherent problems of disorder and defects found for solid state photovoltaics. In all cases, high energy electron–hole pairs are generated by absorption of two photons which allow for higher output voltages while harvesting a broader range of the solar spectrum. The three considered schemes include a two-dye tandem structure, a two-dye intermediate band scheme, and a single-dye intermediate triplet state scheme. For all three schemes, we used an extensive database of porphyrin orbital energies to identify dyes with properly-aligned energy levels to yield open-circuit voltages well beyond 1.0 V. The proposed schemes were substantiated by *ab initio* calculations for the complexes indicating that the energy level alignment is retained upon attaching the molecules *via* a diode. Many possible loss mechanisms and questions regarding *e.g.* the synthesis of the complexes, the efficiency of electron transfer between the dyes, the life times of the generated electron–hole pairs, *etc.* are discussed, and possible improvements by means of modifications to the molecules are suggested. The present work has established a new concept of molecular tandem-based devices that could have important implications in photovoltaic applications. Work towards a proof of concept based on the results of this work is being conducted.

Acknowledgements

KBØ and KST would like to thank the Danish Council for Independent Research's DFF-Sapere Aude program (grant no. 11-1051390) for financial support. JMGL acknowledges support from the Spanish Ministry of Economy and Competitiveness under Projects FIS2010-21282-C02-01 and FIS2012-30996 and through Ramon y Cajal grant RYC-2011-07782. FJH acknowledges funding by the Department of Energy, Basic Energy Sciences, Contract no. DE-SC0006931. AR acknowledges financial support from the European Research Council Advanced Grant DYNamo (ERC-2010-AdG-267374), Spanish Grant (FIS2013-46159-C3-1-P), Grupos Consolidados UPV/EHU del Gobierno Vasco (IT578-13) and European Community FP7 project CRONOS (Grant number 280879-2).

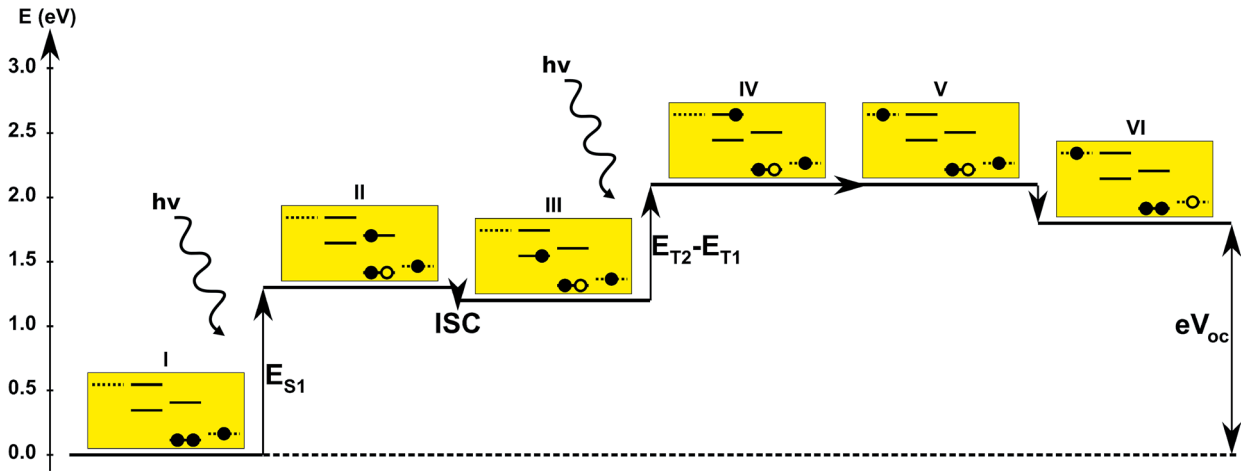

Fig. 6 One-particle state-based sketch of the steps involved in the single-dye intermediate triplet state scheme. For each state the energetics are indicated by the *y*-axis while the one-particle mechanism associated with the step is shown in the corresponding yellow box. Here the filled circles represents electrons and the empty circles represents holes. From right to left in each box the dotted state is the redox mediator, the first set of solid lines represents the singlet ground state and the first singlet excited state of the dye, the second set of solid lines represents the first and second triplet excited state of the dye and the last dotted line represents the conduction band of the semi-conductor. The step involving inter-system-crossing is marked by ISC.

References

1 A. Hagfeldt, G. Boschloo, L. Sun, L. Kloo and H. Pettersson, *Chem. Rev.*, 2010, **110**, 6595–6663.
2 B. O'Regan and M. Grätzel, *Nature*, 1991, **353**, 737–740.
3 H. S. Jung and J.-K. Lee, *J. Phys. Chem. Lett.*, 2013, **4**, 1682–1693.
4 L. Li, Y. Hao, X. Yang, J. Zhao, H. Tian, C. Teng, A. Hagfeldt and L. Sun, *ChemSusChem*, 2011, **4**, 609–612.
5 A. Yella, H.-W. Lee, H. N. Tsao, C. Yi, A. K. Chandiran, M. K. Nazeeruddin, E. W.-G. Diau, C.-Y. Yeh, S. M. Zakeeruddin and M. Grätzel, *Science*, 2011, **334**, 629–634.
6 J. Luo, M. Xu, R. Li, K.-W. Huang, C. Jiang, Q. Qi, W. Zeng, J. Zhang, C. Chi, P. Wang and J. Wu, *J. Am. Chem. Soc.*, 2013, **136**, 265–272.
7 D. Feldman, G. Barbose, R. Margolis, T. James, S. Weaver, N. Darghouth, R. Fu, C. Davidson, S. Booth and R. Wiser, *Photovoltaic System Pricing Trends, National Renewable Energy Laboratory Technical Report NREL/PR-6A20-62558*, 2014.
8 A. Nattestad, A. J. Mozer, M. K. R. Fischer, Y.-B. Cheng, A. Mishra, P. Bauerle and U. Bach, *Nat. Mater.*, 2010, **9**, 31–35.
9 S. K. Balasingam, M. Lee, M. G. Kang and Y. Jun, *Chem. Commun.*, 2013, **49**, 1471–1487.
10 J. Y. Kim, K. Lee, N. E. Coates, D. Moses, T.-Q. Nguyen, M. Dante and A. J. Heeger, *Science*, 2007, **317**, 222–225.
11 J. You, L. Dou, K. Yoshimura, T. Kato, K. Ohya, T. Moriarty, K. Emery, C.-C. Chen, J. Gao, G. Li and Y. Yang, *Nat. Commun.*, 2013, **4**, 1446.
12 F. C. Krebs, *Sol. Energy Mater. Sol. Cells*, 2009, **93**, 394–412.
13 W. Cao and J. Xue, *Energy Environ. Sci.*, 2014, **7**, 2123–2144.
14 W. Zou, C. Visser, J. A. Maduro, M. S. Pshenichnikov and J. C. Hummelen, *Nat. Photonics*, 2012, **6**, 560–564.
15 M. R. Ribas, R. P. Steer and R. Rüther, *Chem. Phys. Lett.*, 2014, **605**, 126–130.
16 V. Gray, D. Dzebo, M. Abrahamsson, B. Albinsson and K. Moth-Poulsen, *Phys. Chem. Chem. Phys.*, 2014, **16**, 10345–10352.
17 L. M. Peter, *J. Phys. Chem. Lett.*, 2011, **2**, 1861–1867.
18 S. Meng, E. Kaxiras, M. K. Nazeeruddin and M. Grätzel, *J. Phys. Chem. C*, 2011, **115**, 9276–9282.
19 F. De Angelis, S. Fantacci, A. Selloni, M. K. Nazeeruddin and M. Grätzel, *J. Phys. Chem. C*, 2010, **114**, 6054–6061.
20 M. Pastore, E. Mosconi, F. De Angelis and M. Grätzel, *J. Phys. Chem. C*, 2010, **114**, 7205–7212.
21 N. Martsinovich and A. Troisi, *Energy Environ. Sci.*, 2011, **4**, 4473–4495.
22 K. B. Ørnsø, J. M. Garcia-Lastra and K. S. Thygesen, *Phys. Chem. Chem. Phys.*, 2013, **15**, 19478–19486.
23 K. B. Ørnsø, C. S. Pedersen, J. M. Garcia-Lastra and K. S. Thygesen, *Phys. Chem. Chem. Phys.*, 2014, **16**, 16246–16254.
24 L.-L. Li and E. W.-G. Diau, *Chem. Soc. Rev.*, 2013, **42**, 291–304.
25 S. Mathew, A. Yella, P. Gao, R. Humphry-Baker, B. F. E. Curchod, N. Ashari-Astani, I. Tavernelli, U. Rothlisberger, M. K. Nazeeruddin and M. Grätzel, *Nat. Chem.*, 2014, **6**, 242–247.
26 J. He, H. Lindström, A. Hagfeldt and S.-E. Lindquist, *Sol. Energy Mater. Sol. Cells*, 2000, **62**, 265–273.
27 A. Luque and A. Marti, *Phys. Rev. Lett.*, 1997, **78**, 5014–5017.
28 A. Luque, A. Marti and C. Stanley, *Nat. Photonics*, 2012, **6**, 146–152.
29 N. J. Ekins-Daukes and T. W. Schmidt, *Appl. Phys. Lett.*, 2008, **93**, 063507.
30 W. Kohn and L. J. Sham, *Phys. Rev.*, 1965, **140**, A1133–A1138.
31 J. P. Perdew, K. Burke and M. Ernzerhof, *Phys. Rev. Lett.*, 1996, **77**, 3865–3868.
32 J. Enkovaara, C. Rostgaard, J. J. Mortensen, J. Chen, M. Dulak, L. Ferrighi, J. Gavnholt, C. Glinsvad, V. Haikola, H. A. Hansen, H. H. Kristoffersen, M. Kuisma, A. H. Larsen, L. Lehtovaara, M. Ljungberg, O. Lopez-Acevedo, P. G. Moses, J. Ojanen, T. Olsen, V. Petzold, N. A. Romero, J. Stausholm-Møller, M. Strange, G. A. Tritsaris, M. Vanin, M. Walter, B. Hammer, H. Häkkinen, G. K. H. Madsen, R. M. Nieminen, J. K. Nørskov, M. Puska, T. T. Rantala, J. Schiøtz, K. S. Thygesen and K. W. Jacobsen, *J. Phys.: Condens. Matter*, 2010, **22**, 253202.
33 A. H. Larsen, M. Vanin, J. J. Mortensen, K. S. Thygesen and K. W. Jacobsen, *Phys. Rev. B: Condens. Matter Mater. Phys.*, 2009, **80**, 195112.
34 B. Liu, W. Zhu, Y. Wang, W. Wu, X. Li, B. Chen, Y.-T. Long and Y. Xie, *J. Mater. Chem.*, 2012, **22**, 7434–7444.
35 G. te Velde, F. M. Bickelhaupt, E. J. Baerends, C. Fonseca Guerra, S. J. A. van Gisbergen, J. G. Snijders and T. Ziegler, *J. Comput. Chem.*, 2001, **22**, 931–967.
36 F. Neese, *Orca, Program Version 3.0.1*.
37 T. Yanai, D. P. Tew and N. C. Handy, *Chem. Phys. Lett.*, 2004, **393**, 51–57.
38 J. He, H. Lindström, A. Hagfeldt and S.-E. Lindquist, *J. Phys. Chem. B*, 1999, **103**, 8940–8943.
39 N. K. Subbaiyan, C. A. Wijesinghe and F. D'Souza, *J. Am. Chem. Soc.*, 2009, **131**, 14646–14647.
40 J. Warnan, Y. Pellegrin, E. Blart and F. Odobel, *Chem. Commun.*, 2012, **48**, 675–677.
41 M. Planells, L. Pelleja, P. Ballester and E. Palomares, *Energy Environ. Sci.*, 2011, **4**, 528–534.
42 A. D. Vos, *J. Phys. D: Appl. Phys.*, 1980, **13**, 839–846.
43 W. Shockley and H. J. Queisser, *J. Appl. Phys.*, 1961, **32**, 510–519.
44 S. Sista, Z. Hong, L.-M. Chen and Y. Yang, *Energy Environ. Sci.*, 2011, **4**, 1606–1620.
45 T. Ameri, N. Li and C. J. Brabec, *Energy Environ. Sci.*, 2013, **6**, 2390–2413.
46 Y. Tao, C. Yang and J. Qin, *Chem. Soc. Rev.*, 2011, **40**, 2943–2970.
47 H. Song, M. A. Reed and T. Lee, *Adv. Mater.*, 2011, **23**, 1583–1608.
48 R. J. Nichols, W. Haiss, S. J. Higgins, E. Leary, S. Martin and D. Bethell, *Phys. Chem. Chem. Phys.*, 2010, **12**, 2801–2815.

49 S. V. Aradhya and L. Venkataraman, *Nat. Nanotechnol.*, 2013, **8**, 399–410.
50 G. Sedghi, V. M. Garcia-Suarez, L. J. Esdaile, H. L. Anderson, C. J. Lambert, S. Martin, D. Bethell, S. J. Higgins, M. Elliott, N. Bennett, J. E. Macdonald and R. J. Nichols, *Nat. Nanotechnol.*, 2011, **6**, 517–523.
51 J. S. Meisner, S. Ahn, S. V. Aradhya, M. Krikorian, R. Parameswaran, M. Steigerwald, L. Venkataraman and C. Nuckolls, *J. Am. Chem. Soc.*, 2012, **134**, 20440–20445.
52 A. Osuka, G. Noya, S. Taniguchi, T. Okada, Y. Nishimura, I. Yamazaki and N. Mataga, *Chem.–Eur. J.*, 2000, **6**, 33–46.
53 J. M. DeGraziano, P. A. Liddell, L. Leggett, A. L. Moore, T. A. Moore and D. Gust, *J. Phys. Chem.*, 1994, **98**, 1758–1761.
54 J.-H. Yum, E. Baranoff, F. Kessler, T. Moehl, S. Ahmad, T. Bessho, A. Marchioro, E. Ghadiri, J.-E. Moser, C. Yi, M. K. Nazeeruddin and M. Grätzel, *Nat. Commun.*, 2012, **3**, 631.
55 S. M. Feldt, G. Wang, G. Boschloo and A. Hagfeldt, *J. Phys. Chem. C*, 2011, **115**, 21500–21507.
56 K. Pettersson, K. Kilså, J. Mårtensson and B. Albinsson, *J. Am. Chem. Soc.*, 2004, **126**, 6710–6719.
57 W. M. Campbell, A. K. Burrell, D. L. Officer and K. W. Jolley, *Coord. Chem. Rev.*, 2004, **248**, 1363–1379.
58 M.-S. Liao and S. Scheiner, *J. Comput. Chem.*, 2002, **23**, 1391–1403.
59 M.-S. Liao and S. Scheiner, *J. Chem. Phys.*, 2002, **117**, 205–219.
60 A. Wiehe, H. Stollberg, S. Runge, A. Paul, M. O. Senge and B. Röder, *J. Porphyrins Phthalocyanines*, 2001, **5**, 853–860.
61 M. B. Smith and J. Michl, *Chem. Rev.*, 2010, **110**, 6891–6936.

Appendix F

Paper V

Electrochemical control of single-molecule conductance by Fermi-level tuning and conjugation switching
M. Baghernejad, X. Zhao, K. B. Ørnsø, M. Füeg, P. Moreno-Garcia, A. V. Rudnev, V. Kaliginedi, S. Vesztergom, C. Huang, W. Hong, P. Broekmann, T. Wandlowski, K. S. Thygesen and M. R. Bryce
J. Am. Chem. Soc., **2014**, *136*, 17922-17925

JACS
JOURNAL OF THE AMERICAN CHEMICAL SOCIETY

Communication

pubs.acs.org/JACS

Electrochemical Control of Single-Molecule Conductance by Fermi-Level Tuning and Conjugation Switching

Masoud Baghernejad,[†,#] Xiaotao Zhao,[‡,#] Kristian Baruël Ørnsø,[§,#] Michael Füeg,[†] Pavel Moreno-García,[†] Alexander V. Rudnev,[†] Veerabhadrarao Kaliginedi,[†] Soma Vesztergom,[†] Cancan Huang,[†] Wenjing Hong,*[,†] Peter Broekmann,[†] Thomas Wandlowski,[†] Kristian S. Thygesen,*[,§] and Martin R. Bryce*[,‡]

[†]Department of Chemistry and Biochemistry, University of Bern, Freiestrasse 3, CH-3012, Bern, Switzerland

[‡]Department of Chemistry, Durham University, Durham DH1 3LE, United Kingdom

[§]Center for Atomic-scale Materials Design, Department of Physics, Technical University of Denmark, 2800 Kgs. Lyngby, Denmark

Supporting Information

ABSTRACT: Controlling charge transport through a single molecule connected to metallic electrodes remains one of the most fundamental challenges of nano-electronics. Here we use electrochemical gating to reversibly tune the conductance of two different organic molecules, both containing anthraquinone (AQ) centers, over >1 order of magnitude. For electrode potentials outside the redox-active region, the effect of the gate is simply to shift the molecular energy levels relative to the metal Fermi level. At the redox potential, the conductance changes abruptly as the AQ unit is oxidized/reduced with an accompanying change in the conjugation pattern between linear and cross conjugation. The most significant change in conductance is observed when the electron pathway connecting the two electrodes is via the AQ unit. This is consistent with the expected occurrence of destructive quantum interference in that case. The experimental results are supported by an excellent agreement with ab initio transport calculations.

Controlled switching between different charge-transport states of single-molecule components is one of the most essential and challenging aspects of molecular electronics. Conductance switching in molecular junctions has been demonstrated previously using various means, including light,[1] bias pulses,[2] electrostatic gating,[3] and electrochemical gating.[4] The concept of "electrochemical gating", which provides the opportunity to overcome the technical challenges of incorporating a gate electrode in a solid-state molecular device, has been employed in electrochemically active molecular systems, including viologens,[5] oligoaniline,[6] ferrocene,[7] transition metal complexes,[4b,8] perylenebisimides,[9] redox-active proteins,[10] quinones,[11] and tetrathiafulvalene,[12] as well as redox-inactive molecules.[13] In the case of redox-inactive molecules, or more generally when the electrode potential does not overlap with the molecule's redox potential, the effect of the gate is simply to shift the molecular levels up or down in energy relative to the Fermi level. In a simple picture where tunneling through the molecule is described by "Lorentzian" transmission peaks centered at the discrete energy levels of the molecule, a large on/off conductance ratio can be achieved by moving the frontier molecular level in and out of resonance with the Fermi level E_F.

Recently, the concept of quantum interference (QI) in molecular transport junctions has been introduced theoretically and verified experimentally.[14] Destructive QI leads to very low conductance—much lower than anticipated from a simple "Lorentzian" model treating each molecular level as an independent transport channel. It occurs as a result of a (nearly) complete cancellation of transmission probability due to interference between different electron pathways, and it is predicted to take place in organic molecules whenever the path connecting the left and right electrodes via the molecule is cross conjugated.[14a,15] For example, independent measurements show that the conductance of a cross-conjugated anthraquinone (AQ) is ~100 times lower than that of a linearly conjugated anthracene,[14f,15,16] even though the molecular length, electronic energy levels, and optical properties of the two molecules are very similar.

In this work, two π-conjugated molecules, isomeric AQ-1,5 and AQ-1,4, with an anthraquinone core unit (Figure 1a), were synthesized, and their electronic conductance was measured under electrochemical gating using the scanning tunneling microscopy break-junction (STM-BJ) technique. We demonstrate gate potential control of the molecular energy levels over almost 1 eV with conductance variations of >1 order of magnitude. The origin of the conductance variation is a combined effect of continuous Fermi level tuning (for potentials outside the redox-active region) and abrupt changes to the conjugation pattern of the molecule as a consequence of oxidation/reduction of the molecule when the electrode potential crosses the redox potential. These experimental observations are complemented by density functional theory (DFT)-based transport calculations. Plotting the calculated transmission function of the reduced and oxidized molecule on the electrode potential scale, we find excellent agreement with experiments for the conductance versus gate potential in a 1 V range around the AQ redox potential.

Received: October 8, 2014
Published: December 15, 2014

   dx.doi.org/10.1021/ja510335z | J. Am. Chem. Soc. 2014, 136, 17922−17925

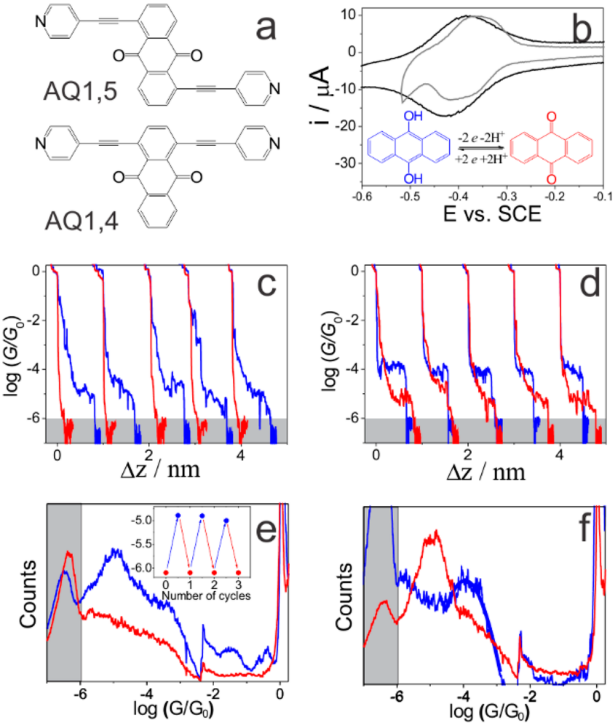

Figure 1. (a) The molecules studied in this work. (b) CV of AQ-1,5 (black) and AQ-1,4 (gray) assembly measured in the STM cell with sweep rate of 100 mV s^{-1} in 0.1 M $KClO_4$ aqueous electrolyte. Typical conductance vs distance traces of rAQ-1,5 (c, blue, −530 mV), AQ-1,5 (c, red, −280 mV), rAQ-1,4 (d, blue, −520 mV), AQ-1,4 (d, red, 280 mV) relative to SCE. (e,f) 1D conductance histograms generated from 1100 individual curves without any data selection for rAQ-1,5 (e, blue), AQ-1,5 (e, red), rAQ-1,4 (f, blue), and AQ-1,4 (f, red). (e, inset) Three sequential *in situ* highly reversible switching cycles between rAQ-1,5 and AQ-1,5 triggered by the electrode potential. The data points are the most probable conductances of rAQ-1,5 (blue) and AQ-1,5 (red). The noise level is indicated by the gray area in panels c–f. The spike at $\log(G/G_0) \approx -2.2$ is the switching of the amplifier.

Conductance measurements of both AQ-1,4 and AQ-1,5 were performed in an STM-BJ setup in 0.1 M $KClO_4$ (pH ~5.8) using a cell with a four-electrode configuration, with Au as tip and substrate, and Pt wires as counter-electrode and quasi-reference electrode in an oxygen-free atmosphere (see SI).[17] Figure 1b shows the cyclic voltammogram (CV) of AQ-1,5 recorded in the STM cell. Two redox peaks are located around −0.42 V for AQ-1,5 and −0.37 V for AQ-1,4 (Figure 1b).

Figure 1c shows typical conductance–distance traces of AQ-1,5 in the reduced and oxidized states obtained from the STM-BJ experiment.[18] For both redox states, the conductance curves exhibit a short plateau at $1G_0$ due to atomic gold point contacts existing just before rupture. In addition to the $1G_0$ plateau, the blue curves show a more extended plateau, with conductances ranging from $10^{-4.6}G_0$ to $10^{-5.4}G_0$, which can be assigned to the conductance of the reduced AQ-1,5 single-molecule junctions. In contrast, no low-conductance plateaus were observed for AQ-1,5 in the oxidized state (red curve). From this, we conclude that the conductance of the oxidized form is below the detection limit of our STM-BJ setup equipped with a linear $I-V$ convertor ($10^{-6}G_0$). Figure 1e shows the one-dimensional histograms of AQ-1,5 in its reduced (blue) and oxidized (red) states, constructed from 1100 conductance traces without any data selection. A pronounced conductance peak centered at $10^{-5.0}G_0$ is observed for the reduced state (rAQ-1,5), while no clear peaks above the detection limit are found for the oxidized form. The inset of Figure 1e shows the change in conductance of AQ-1,5 over three consecutive cycles of the potential across the redox potential. No significant decrease of the on/off ratio is observed, which suggests that the manipulation of molecular redox states is a highly reversible process.

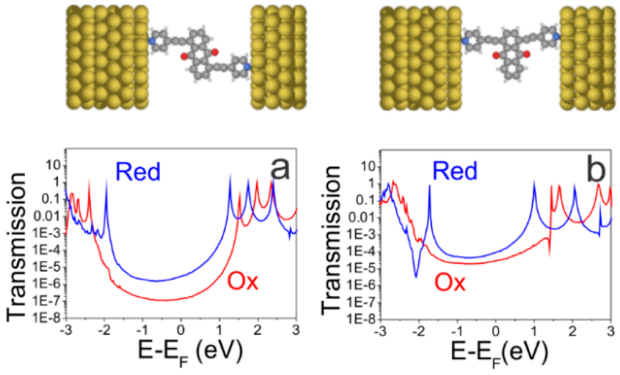

Figure 2. Calculated transmission function for the two charge states of AQ-1,5 (a) and AQ-1,4 (b). The supercells used for the transport calculations are also shown. The energy scale is relative to the Au Fermi level.

Figure 1d,f shows individual conductance–distance traces and histograms of AQ-1,4 in the reduced (blue) and oxidized (red) states, respectively. For this molecule, clear conductance plateaus are observed around $10^{-4.0}G_0$ and $10^{-5.0}G_0$ for the reduced and oxidized species, respectively, leading to peaks in the conductance histogram at these values. We attribute these peaks to the formation of rAQ-1,4 and AQ-1,4 single-molecule junctions.

The smaller difference in the conductance of the two redox states of AQ-1,4, compared to AQ-1,5, can be explained by the different electron pathways between the pyridyl units in the cross-conjugated AQ-1,5 and linearly conjugated AQ-1,4 molecules. For AQ-1,4 the change in conductance results primarily from a change in effective electron density of the functional group attached as a "gating" unit to the OPE-type backbone. In contrast, the electron pathway for AQ-1,5 goes directly via the AQ unit, and thus the change from linear- (reduced state) to cross-conjugation (oxidized state) directly lowers the transmission probability.

In Figure 2, we show the transmission functions of AQ-1,5 (a) and AQ-1,4 (b) in reduced and oxidized forms calculated from DFT. All the calculations were performed using the GPAW electronic structure[19] code using a double zeta plus polarization (DZP) basis set. To overcome the well-known problem of DFT to describe molecular energy levels we have used the DFT+ Sigma scheme to correct the DFT eigenvalues as described in previous studies.[20,21] More details on the computations are given in the SI. Our transport calculations predict that the oxidized states generally have lower conductance than the reduced states. This holds not only for energies at the gold Fermi level but over the entire range of energies within the HOMO–LUMO gap. Moreover, AQ-1,4 is predicted to have higher conductance than AQ-1,5 in both charge states. Finally, the change in conductance upon changing the redox state is predicted to be larger for AQ-1,5

dx.doi.org/10.1021/ja510335z | J. Am. Chem. Soc. 2014, 136, 17922–17925

than for AQ-1,4. These findings are all consistent with the experimental observations. The first two findings can be explained by the variations in the HOMO−LUMO gap: for both charge states the HOMO−LUMO gap is larger for AQ-1,5 than for AQ-1,4, and for both molecules the HOMO−LUMO gap is larger in the oxidized state than in the reduced state. However, the third finding, namely that the conductance change upon oxidation is larger for AQ-1,5 than for AQ-1,4, cannot be explained simply from the size of the HOMO−LUMO gap. Indeed, the increase in HOMO−LUMO gap upon oxidation is very similar for the two molecules. Instead, the larger suppression of the conductance in oxidized AQ-1,5 is a result of destructive QI occurring because the electron pathway connecting the left and right electrodes goes via the cross-conjugated AQ unit. We note that the QI effect is not very pronounced in oxidized AQ-1,5; in particular, the characteristic transmission anti-resonance often observed in QI molecules is not observed. Outside the redox-active region, the effect of the gate potential should simply shift the molecular levels up or down relative to the metal Fermi energy. Since the conductance is proportional to the transmission function at the Fermi energy, Figure 2 suggests that a significant gating effect should be observable when the Fermi level is close to either the HOMO or LUMO, and previous studies have shown that AQ-1,4 and AQ-1,5, in the absence of gating potentials, conduct through the LUMO.[22]

To investigate the conductance versus gate potential, we constructed conductance histograms for the two molecules at different (fixed) electrode potentials. The histograms are shown in Figure 3 for AQ-1,5 and AQ-1,4, and the conductance peaks versus gate potential are plotted in Figure 4a,b. For potentials higher than the redox potential, the molecules are in their oxidized state. In this potential region, the peaks in the conductance histograms shift to higher conductance as the potential is moved toward more negative values (the Fermi level is moved upward). This indicates that transport is indeed mediated by the LUMO for the oxidized molecules. At a potential around −0.4 V vs SCE, the conductance increases sharply by approximately 1 order of magnitude due to the redox process. For AQ-1,5 the conductance continues to rise as the potential is decreased further, indicating that transport is also LUMO-mediated in the reduced state. A significant conductance change from $10^{-6.1}G_0$ (−330 mV vs SCE) to $10^{-6.5}G_0$ (−30 mV vs SCE) for AQ-1,5 in the oxidized state was observed by carrying out the experiment in a complementary STM-BJ with a developing logarithm $I-V$ convertor with better current sensitivity, which is in good agreement with the results presented in Figure 1, showing that the oxidized state conductance of AQ-1,5 is $<10^{-6}G_0$. For AQ-1,4, it is found that the conductance increases with positive potential in the reduced state. At the potential close to redox potential (−420 mV vs SCE), we can still observe a less-pronounced conductance peak around $10^{-4.5}G_0$, which suggests the existence of small amounts of molecules in the oxidized state at the transition potential. We note that although the conductance change induced by adjusting the electrode potential is relatively small in the redox-inactive potential region, as compared to the change taking place as the potential crosses the redox peak potential, it is still comparable to those of several other previously studied molecular switches.[4a,23]

To enable a more precise comparison between the experiments (Figure 4a,b) and the calculations, we plotted the calculated transmission using the electrochemical energy

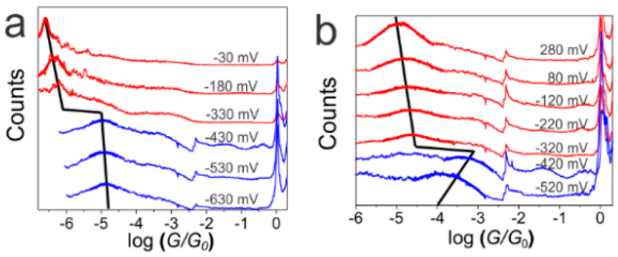

Figure 3. Conductance histograms obtained at different potentials vs SCE for (a) AQ-1,5 and (b) AQ-1,4. Black lines indicate the conductance changes with electrode potential.

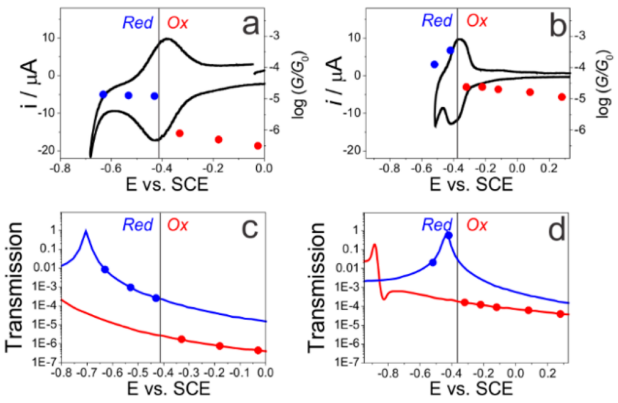

Figure 4. Experimental (a,b) and calculated (c,d) molecular conductance as a function of the applied gating potential vs SCE for AQ-1,5 (a,c) and AQ-1,4 (b,d). The vertical gray line indicates the measured redox potential for the two molecules. The transmission curves shown in the lower panels are the same as in Figure 2, but are plotted here on the electrochemical energy scale relative to SCE.

scale relative to SCE in Figure 4c,d. Conversion of the electrochemical energy scales is achieved based on the Fermi level in the transport calculations corresponding to the (negative) work function of Au(111), which is taken to be 5.3 eV, while the SCE is 4.68 eV relative to vacuum.[24] The gray line indicates the measured redox potentials. For potentials to the left of the gray line, the molecule is in the reduced state and the transmission is given by the blue curve. For potentials to the right of the dashed line, the molecule is in the oxidized state and the transmission is given by the red curve. The dots indicate the predicted conductance at the potentials used to produce the experimental conductance curve in Figure 4a,b. The striking agreement between the calculations and experiments strongly supports the interpretations of the conduction mechanisms put forward in this paper and suggests that (semi)quantitative modeling of single-molecule transport under electrochemical control is possible using relatively simple computational models. Finally, we note that although the qualitative agreement between theory and experiments is excellent, there are significant differences at the quantitative level, in particular for the reduced states. We ascribe this to an incorrect level alignment in the DFT+Sigma calculation for reduced AQ-1,4 and a breakdown of the phase-coherent transport mechanism close to the resonance in the case of reduced AQ-1,5 (see SI for a more detailed discussion).

In summary, we have studied charge transport through single-molecule junctions formed by two isomeric AQ-based derivatives, AQ-1,5 and AQ-1,4, by employing an STM-BJ

dx.doi.org/10.1021/ja510335z | J. Am. Chem. Soc. 2014, 136, 17922−17925

technique under electrochemical control. For both AQ-1,5 and AQ-1,4, the conductance has been controlled over 1 order of magnitude by varying the electrode potential over a range of ∼1 V. In the redox-inactive potential region, the effect of the gating is to shift the Fermi level relative to the molecular resonances, leading to a modest change in conductance. At the redox potential, large and reversible jumps of the conductance were observed due to the change in redox state, which is accompanied by changes in the conjugation pattern from linear (in the reduced state) to cross-conjugated (in the oxidized state). All these observations were supported by our DFT-based transport calculations. In particular, we found an excellent agreement between experiments and calculations for the conductance versus gate potential both outside and inside the redox-active regimes.

■ ASSOCIATED CONTENT

Supporting Information

Synthetic procedures, computational, and single-molecule measurement details. This material is available free of charge via the Internet at http://pubs.acs.org.

■ AUTHOR INFORMATION

Corresponding Authors

hong@dcb.unibe.ch
thygesen@fysik.dtu.dk
m.r.bryce@durham.ac.uk

Author Contributions

#M.B., X.Z., and K.B.Ø contributed equally to this work.

Notes

The authors declare no competing financial interest.

■ ACKNOWLEDGMENTS

We acknowledge discussions with Prof. Hans Siegenthaler and Prof. Silvio Decurtins. This work was generously supported by the Swiss National Science Foundation (200020-144471; NFP 62), the EC FP7 ITN "MOLESCO" project no. 606728, the Scientific Exchange Programme NMSch (SciEx 13.060), FP7 project ACMOL (618082), and the University of Bern. K.B.Ø. and K.S.T. thank the Danish Council for Independent Research's DFF Sapere Aude program (grant no. 11-1051390) for financial support.

■ REFERENCES

(1) van der Molen, S. J.; Liao, J.; Kudernac, T.; Agustsson, J. S.; Bernard, L.; Calame, M.; van Wees, B. J.; Feringa, B. L.; Schoenenberger, C. *Nano Lett.* **2009**, *9*, 76.

(2) Lortscher, E.; Ciszek, J. W.; Tour, J.; Riel, H. *Small* **2006**, *2*, 973.

(3) Song, H.; Kim, Y.; Jang, Y. H.; Jeong, H.; Reed, M. A.; Lee, T. *Nature* **2009**, *462*, 1039.

(4) (a) Kay, N. J.; Higgins, S. J.; Jeppesen, J. O.; Leary, E.; Lycoops, J.; Ulstrup, J.; Nichols, R. J. *J. Am. Chem. Soc.* **2012**, *134*, 16817. (b) Ricci, A. M.; Calvo, E. J.; Martin, S.; Nichols, R. J. *J. Am. Chem. Soc.* **2010**, *132*, 2494.

(5) (a) Haiss, W.; van Zalinge, H.; Higgins, S. J.; Bethell, D.; Hobenreich, H.; Schiffrin, D. J.; Nichols, R. J. *J. Am. Chem. Soc.* **2003**, *125*, 15294. (b) Pobelov, I. V.; Li, Z.; Wandlowski, T. *J. Am. Chem. Soc.* **2008**, *130*, 16045.

(6) Chen, F.; He, J.; Nuckolls, C.; Roberts, T.; Klare, J. E.; Lindsay, S. *Nano Lett.* **2005**, *5*, 503.

(7) (a) Xiao, X.; Brune, D.; He, J.; Lindsay, S.; Gorman, C. B.; Tao, N. *Chem. Phys.* **2006**, *326*, 138. (b) Zhou, X.-S.; Liu, L.; Fortgang, P.; Lefevre, A.-S.; Serra-Muns, A.; Raouafi, N.; Amatore, C.; Mao, B.-W.; Maisonhaute, E.; Schoellhorn, B. *J. Am. Chem. Soc.* **2011**, *133*, 7509.

(8) Albrecht, T.; Guckian, A.; Kuznetsov, A. M.; Vos, J. G.; Ulstrup, J. *J. Am. Chem. Soc.* **2006**, *128*, 17132.

(9) Li, C.; Mishchenko, A.; Li, Z.; Pobelov, I.; Wandlowski, T.; Li, X. Q.; Würthner, F.; Bagrets, A.; Evers, F. *J. Phys.: Condens. Matter* **2008**, *20*, No. 374122.

(10) Della Pia, E. A.; Chi, Q.; Jones, D. D.; Macdonald, J. E.; Ulstrup, J.; Elliott, M. *Nano Lett.* **2011**, *11*, 176.

(11) Tsoi, S.; Griva, I.; Trammell, S. A.; Blum, A. S.; Schnur, J. M.; Lebedev, N. *ACS Nano* **2008**, *2*, 1289.

(12) Leary, E.; Higgins, S. J.; van Zalinge, H.; Haiss, W.; Nichols, R. J.; Nygaard, S.; Jeppesen, J. O.; Ulstrup, J. *J. Am. Chem. Soc.* **2008**, *130*, 12204.

(13) Capozzi, B.; Chen, Q.; Darancet, P.; Kotiuga, M.; Buzzeo, M.; Neaton, J. B.; Nuckolls, C.; Venkataraman, L. *Nano Lett.* **2014**, *14*, 1400.

(14) (a) Markussen, T.; Stadler, R.; Thygesen, K. S. *Nano Lett.* **2010**, *10*, 4260. (b) Garcia-Suarez, V. M.; Lambert, C. J.; Manrique, D. Z.; Wandlowski, T. *Nanotechnology* **2014**, *25*, No. 205402. (c) Xia, J.; Capozzi, B.; Wei, S.; Strange, M.; Batra, A.; Moreno, J. R.; Amir, R. J.; Amir, E.; Solomon, G. C.; Venkataraman, L.; Campos, L. M. *Nano Lett.* **2014**, *14*, 2941. (d) Arroyo, C. R.; Tarkuc, S.; Frisenda, R.; Seldenthuis, J. S.; Woerde, C. H. M.; Eelkema, R.; Grozema, F. C.; van der Zant, H. S. J. *Angew. Chem., Int. Ed.* **2013**, *52*, 3152. (e) Darwish, N.; Diez-Perez, I.; Da Silva, P.; Tao, N.; Gooding, J. J.; Paddon-Row, M. N. *Angew. Chem., Int. Ed.* **2012**, *51*, 3203. (f) Guedon, C. M.; Valkenier, H.; Markussen, T.; Thygesen, K. S.; Hummelen, J. C.; van der Molen, S. J. *Nat. Nanotechnol.* **2012**, *7*, 304.

(15) Valkenier, H.; Guedon, C. M.; Markussen, T.; Thygesen, K. S.; van der Molen, S. J.; Hummelen, J. C. *Phys. Chem. Chem. Phys.* **2014**, *16*, 653.

(16) Hong, W.; Valkenier, H.; Meszaros, G.; Manrique, D. Z.; Mishchenko, A.; Putz, A.; Garcia, P. M.; Lambert, C. J.; Hummelen, J. C.; Wandlowski, T. *Beilstein J. Nanotechnol.* **2011**, *2*, 699.

(17) (a) Li, Z.; Pobelov, I.; Han, B.; Wandlowski, T.; Blaszczyk, A.; Mayor, M. *Nanotechnology* **2007**, *18*, No. 044018. (b) Weibel, N.; Grunder, S.; Mayor, M. *Org. Biomol. Chem.* **2007**, *5*, 2343. (c) Li, C.; Mishchenko, A.; Li, Z.; Pobelov, I.; Wandlowski, T.; Li, X. Q.; Wuerthner, F.; Bagrets, A.; Evers, F. *J. Phys.: Condens. Matter* **2008**, *20*, No. 374122.

(18) (a) Hong, W.; Manrique, D. Z.; Moreno-Garcia, P.; Gulcur, M.; Mishchenko, A.; Lambert, C. J.; Bryce, M. R.; Wandlowski, T. *J. Am. Chem. Soc.* **2012**, *134*, 2292. (b) Li, C.; Pobelov, I.; Wandlowski, T.; Bagrets, A.; Arnold, A.; Evers, F. *J. Am. Chem. Soc.* **2008**, *130*, 318.

(19) Enkovaara, J.; Rostgaard, C.; Mortensen, J. J.; Chen, J.; Dulak, M.; Ferrighi, L.; Gavnholt, J.; Glinsvad, C.; Haikola, V.; Hansen, H. A.; Kristoffersen, H. H.; Kuisma, M.; Larsen, A. H.; Lehtovaara, L.; Ljungberg, M.; Lopez-Acevedo, O.; Moses, P. G.; Ojanen, J.; Olsen, T.; Petzold, V.; Romero, N. A.; Stausholm-Moller, J.; Strange, M.; Tritsaris, G. A.; Vanin, M.; Walter, M.; Hammer, B.; Hakkinen, H.; Madsen, G. K. H.; Nieminen, R. M.; Norskov, J. K.; Puska, M.; Rantala, T. T.; Schiotz, J.; Thygesen, K. S.; Jacobsen, K. W. *J. Phys.: Condens. Matter* **2010**, *22*, 253202.

(20) Mowbray, D. J.; Jones, G.; Thygesen, K. S. *J. Chem. Phys.* **2008**, *128*, 111103.

(21) Quek, S. Y.; Venkataraman, L.; Choi, H. J.; Louie, S. G.; Hybertsen, M. S.; Neaton, J. B. *Nano Lett.* **2007**, *7*, 3477.

(22) (a) Hoft, R. C.; Ford, M. J.; Garcia-Suarez, V. M.; Lambert, C. J. *J. Phys.: Condens. Matter* **2008**, *20*, No. 025207. (b) Schelhaas, M.; Glomsda, S.; Hansler, M.; Jakubke, H. D.; Waldmann, H. *Angew. Chem., Int. Ed.* **1996**, *35*, 106.

(23) Li, Z.; Li, H.; Chen, S.; Froehlich, T.; Yi, C.; Schönenberger, C.; Calame, M.; Decurtins, S.; Liu, S.-X.; Borguet, E. *J. Am. Chem. Soc.* **2014**, *136*, 8867.

(24) Trasatti, S. *Pure Appl. Chem.* **1986**, *58*, 955.

Appendix G

Paper VI

Controlling electrical conductance through a π-conjugated cruciform molecule via selective anchoring to gold electrodes
C. Huang, S. Chen, K. B. Ørnsø, D. Reber, M. Baghernejad, Y. Fu, T. Wandlowski, S. Decurtins, W. Hong, K. S. Thygesen and S.-X. Liu
2015, *submitted*

Controlling Electrical Conductance through a π-Conjugated Cruciform Molecule via Selective Anchoring to Gold Electrodes**

Cancan Huang, Songjie Chen, Kristian Baruël Ørnsø, David Reber, Masoud Baghernejad, Yongchun Fu, Thomas Wandlowski, Silvio Decurtins, Wenjing Hong,*, Kristian Sommer Thygesen,*, and Shi-Xia Liu*,

Abstract: Tuning charge transport at the single-molecule level plays a crucial role in the construction of molecular electronics devices. Here we introduce a promising and operationally simple approach to tune two distinct charge transport pathways through a cruciform molecule. Upon in-situ cleavage of the triisopropylsilyl group, complete conversion from the **M1**-N junctions to the **M1**-C junctions is achieved with a conductance increase by more than one order of magnitude, which is consistent with predictions from ab-initio transport calculations. Our results provide a new approach to tune the conductance of single-molecule junctions via chemically controllable anchoring sites.

The idea to integrate individual molecules into electronic circuits was theoretically proposed by Aviram and Ratner in 1974.[1] Despite of various experimental approaches employed for the formation of molecular junctions between two metal electrodes,[2] it is highly desirable to incorporate a third (gate) electrode, *e.g.* a solid-state back gate electrode[3] or electrochemical electrode, to adjust molecular energy levels relative to the Fermi level or trigger redox reactions on the molecule.[4] In conjunction with this idea, it is of great interest to integrate molecules with multiple terminals into an electrical circuit to allow differentiating and switching between different charge transport (CT) pathways. However, it still remains a challenge to control the metal-molecule contact to a degree that allows for injection/extraction of charges at different points of the same molecule and thereby explore multiple electron pathways. A possible way to overcome this challenge is to exploit the sizeable variation in binding energies of different anchor groups on a gold surface.

Here, we report the design and synthesis of a cruciform conjugated molecule (**M1**) consisting of two orthogonally disposed π-systems. Within this molecule the two linear arms are terminated with pyridyl and TIPS-protected (TIPS = triisopropylsilyl) acetylene groups, respectively (Figure 1). Cruciform molecules have received significant attention due to their special structural topology and opportunities for their modulation[5] and therefore they are considered to be promising "hub" units for integration of different functional units in single-molecule circuits. Within the context of the single-molecule conductance, only two papers on cruciform molecules have appeared in the literature.[6,7] Differentiating charge transport pathways, however, has been unexplored so far. To elaborate on our concept for achieving high selectivity of anchoring sites on Au leads, we apply the desilylation chemistry[8] which allows us to trap molecules between two Au electrodes through *in-situ* generated C-Au bonds. Single-molecule junctions formed via the C-Au σ-bonds should be energetically favored over junctions via pyridyl anchoring groups, due to the larger binding strength of the covalent bond compared to the coordination bonding between the gold and lone pair atoms.[9] Therefore, one can set the course for a controllable conductance pathway in a molecule, for example, with well-studied pyridyl and trimethylsilyl-protected acetylene termini.[4a, 9]

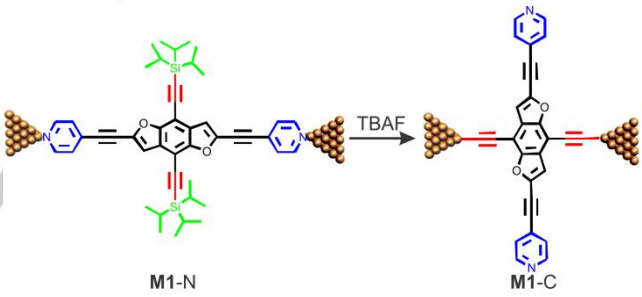

Figure 1. Setting a course for molecular conductance along different pathways based on the **M1**-N and **M1**-C configurations.

To realize this goal, we specifically synthesized a cruciform molecule **M1** (Figure 1) based on the benzo[1,2-*b*:4,5-*b'*]difuran (BDF) core[10] to explore the possibility of chemical tuning of anchoring sites in single-molecule devices. Charge transport properties of the single-molecule junctions before and after the desilylation were investigated using the mechanically controllable break junction technique (MCBJ).[11] Upon desilylation, the conductance value is more than one order of magnitude higher, which is comparable with other conductance tuning approaches through energy level tuning or redox processes. In the present study, the origin of the conductance difference lies in a complete conversion of two charge transport pathways in a well-controlled way, as confirmed by density functional theory (DFT)-based transport calculations.

[*] C. Huang, Dr. S. Chen, D. Reber, M. Baghernejad, Dr. Y. Fu, Prof. T. Wandlowski, Prof. S. Decurtins, Dr. W. Hong, Dr. S.-X. Liu
Department of Chemistry and Biochemistry
University of Bern
Freiestrasse 3, CH-3012 Bern, Switzerland
E-mail: hong@dcb.unibe.ch; liu@dcb.unibe.ch

K. Baruël Ørnsø, Prof. K. S. Thygesen
Center for Atomic-scale Materials Design (CAMD), Department of Physics
Technical University of Denmark
Fysikvej, 2800 Kgs. Lyngby, Denmark
E-mail: thygesen@fysik.dtu.dk
C. H. and S. C. contributed equally to the paper

[**] This work was generously supported by the Swiss National Science Foundation (grant No. 200020-144471and 200021-147143; NFP 62), the EC FP7 ITN "MOLESCO" project number 606728, and the University of Bern. KBØ and KST thank the Danish Council for Independent Research's DFF Sapere Aude program (grant No. 11-1051390) for financial support.

Supporting information for this article is given via a link at the end of the document.((Please delete this text if not appropriate))

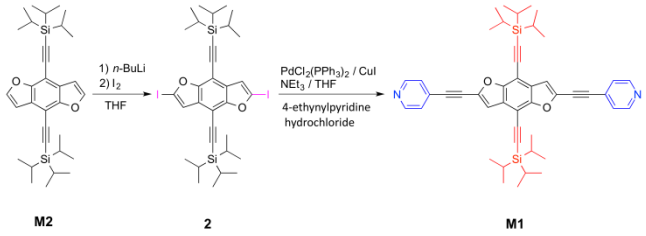

Scheme 1. The synthetic route to the target molecule **M1**.

As illustrated in Scheme 1, the target molecule **M1** was readily prepared from **2** in 69% yield *via* a Sonogashira reaction with 4-ethynylpyridine hydrochloride. The synthesis of precursor **2** was accomplished in 54% yield by iodination of **M2**[12] *via* double deprotonation in the presence of *n*-BuLi followed by treatment with iodine. The details are given in the SI.

The initial single-molecule conductance measurement was carried out in a THF : mesitylene solution (1 : 4, *v* : *v*) containing 0.1 mM molecule **M1**, and then tetrabutylammonium fluoride (TBAF) was added for *in-situ* cleavage of TIPS to form the Au-C bonds. Figure 2A displays typical conductance (*G*) *versus* distance (Δ*z*) stretching traces, as plotted in a semi-logarithmic scale. In these traces, after the rapture of gold-gold atomic contacts (plateau at $G_0 = 2e^2/h$, quantum conductance), the formation of molecular junctions is identified by the presence of additional plateaus in the range $10^{-0.3}\ G_0 \geq G \geq 10^{-7.0}\ G_0$. Some typical traces are shown for pyridyl-terminated junctions **M1**-N (blue) in the initial state and the acetylide-terminated junctions **M1**-C (red), upon the cleavage of TIPS. The plateau length of **M1**-N is significantly longer than that of **M1**-C, while the plateau of **M1**-C is in the higher conductance regime.

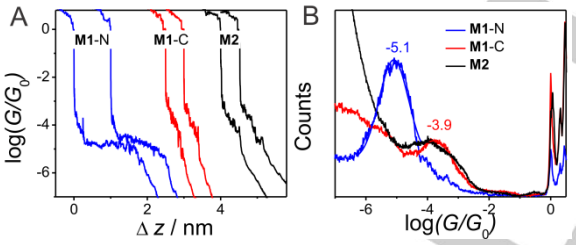

Figure 2. (A) Typical conductance - relative distance traces for **M1**-N and **M1**-C configurations. (B) One-dimensional (1D) conductance histograms of **M1**-N, **M1**-C and **M2**.

Thousands of these individual traces are used to construct one-dimensional (1D) conductance histograms without data selection[11a] (Figure 2B). In the initial state (blue curve), the conductance peak centered at $G = 10^{-5.1\pm0.1}\ G_0$ by Gaussian fitting is assigned as the statistically most probable conductance of the **M1**-N molecular junctions. Upon the addition of 2 equivalents of TBAF, a distinct conductance was detected at $G = 10^{-3.9\pm0.1}\ G_0$. The observed increase in molecular conductance is attributed to the **M1**-C charge transport pathway. It is also found that the conductance of the **M1**-C configuration is in perfect agreement with the molecular junction of the reference molecule **M2** ($G = 10^{-4.0\pm0.1}\ G_0$) featured only with one charge transport pathway through the 4, 8-axis of the BDF core. Remarkably, the conductance difference for the two junction configurations is comparable with the reported single-molecule conductance change via Fermi level tuning[13] and redox processes.[14]

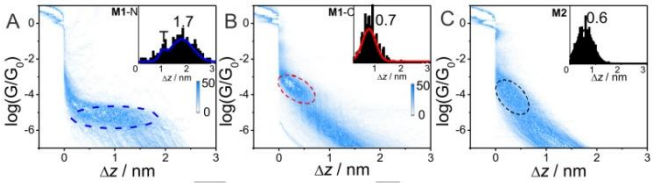

Figure 3. Two-dimensional (2D) conductance histograms and stretching distance Δ*z** distributions (inset). (A) **M1**-N, (B) **M1**-C, (C) **M2**.

For the **M1** molecule, the **M1**-N and **M1**-C configurations lead to a significant change of the molecular lengths of the single-molecule junctions. To further explore the evolution of conductance as a function of the molecular length, the 2D histograms are displayed in Figure 3. Two clear intensity clouds are observed for **M1**-N (Figure 3A) and **M1**-C configurations (Figure 3B). Notably, the plateau length for **M1**-N is longer than for **M1**-C. The most probable stretched distance Δ*z** was determined from the plateau distribution histograms (inset histograms of Figures 3A and 3B) to be 1.7 nm and 0.7 nm, respectively. After adding the snap-back distance correction, the most probable absolute distance *z** (*z** = Δ*z** + 0.5 nm)[11b] between two gold tips is 2.2 nm for **M1**-N, and 1.2 nm for **M1**-C, which agrees well with the length of the corresponding orientations (2.4 nm for **M1**-N and 1.2 nm for **M1**-C cells based on DFT calculation). The good agreement between the experimentally and theoretically determined junction lengths verifies the proposed junction configurations. All these results provide direct evidence for the chemically stimulated change of the charge transport pathway from **M1**-N to **M1**-C.

It can be noted that the peak located at 1.7 nm, corresponding to the **M1**-N junction (inset Figure 3A), disappeared completely for the **M1**-C junction (inset Figure 3B), indicating that the conversion from the **M1**-N to **M1**-C charge transport pathway can reach up to ~100% (9 in 1000 traces which show stretching distances longer than 1.5 nm). Such a high selectivity is attributed to the fact that the covalent C-Au bonds are much stronger than the Au-N bond, as confirmed by DFT calculations. The binding energies for the pyridyl and acetylide groups on the Au electrodes are calculated to be 0.6 eV and 3.2 eV, respectively. The DFT total energy calculations were performed with the GPAW code[14a] using a real space grid with grid spacing 0.18 Å and the PBE exchange-correlation functional. The atomic structure of the metal-molecule interface was modeled as described in SI.

Figure 4 shows the transmission functions of **M1**-N and **M1**-C calculated from DFT. The charge transport calculation was performed using the GPAW electric structure[15] code using a double zeta plus polarization (DZP) basis set and the PBE exchange-correlation functional. To overcome the well-known problem of DFT to describe molecular energy levels we have

used the DFT+Sigma scheme to correct the DFT eigenvalues as described in previous studies.[16] As illustrated in Figure 4, the charge transport is predominantly *via* the LUMO for the **M1**-N configuration and the HOMO for the **M1**-C configuration, respectively. The switching of the dominant molecular orbital is in good agreement with previous theoretical studies.[11b, 17]

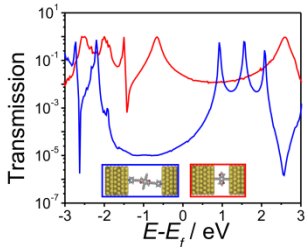

Figure 4. Calculated transmission function for the two states of the molecular junctions (blue for **M1**-N and red for **M1**-C).

In summary, two distinct charge transport pathways of a cruciform molecule are verified by single-molecule conductance measurements using the MCBJ technique with the conductance difference of more than one order of magnitude. Unlike the acetyl-protected thiol-terminated molecules that can be trapped between two Au electrodes in the absence of deprotection agents, the TIPS-protected molecules are very stable as, the deprotection only occurs in the presence of bases such as TBAF, which allows us to tune the charge transport pathways of **M1** in the more controllable way. Upon *in-situ* cleavage of the TIPS group, the complete conversion from the **M1**-N junctions to the **M1**-C junctions could be achieved. More importantly, the conductance tuning *via* the high selectivity of different anchoring groups provides a unique flexibility in the modulation design. The interpretation of the experiments was supported by *ab-initio* total energy and transport calculations. This present work demonstrates that the conductance of single-molecule junctions can be tuned *via* the chemically controllable preferred anchoring sites. To realize the reversible tuning of charge transport pathways in single-molecule junctions is a major focus in our ongoing work.

Keywords: *ab initio* calculations • desilylation • single-molecule studies • benzodifuran • anchoring effect

[1] A. Aviram, M. A. Ratner, *Chem. Phys. Lett.* **1974**, *29*, 277–283.

[2] a) R. C. Chiechi, E. A. Weiss, M. D. Dickey, G. M. Whitesides, *Angew. Chem. Int. Ed.* **2008**, *47*, 142-144; *Angew. Chem.* **2008**, *120*, 148-150; b) W. Haiss, H. van Zalinge, S. J. Higgins, D. Bethell, H. Höbenreich, D. J. Schiffrin, R. J. Nichols, *J. Am. Chem. Soc.* **2003**, *125*, 15294-15295; c) M. A. Reed, C. Zhou, C. J. Muller, T. P. Burgin, J. M. Tour, *Science* **1997**, *278*, 252-254; d) B. Xu, N. J. Tao, *Science* **2003**, *301*, 1221-1223.

[3] H. Song, Y. Kim, Y. H. Jang, H. Jeong, M. A. Reed, T. Lee, *Nature* **2009**, *462*, 1039-1043.

[4] a) C. Huang, A. V. Rudnev, W. Hong, T. Wandlowski, *Chem. Soc. Rev.* **2015,** 44, 889-901; b) X. Xiao, D. Brune, J. He, S. Lindsay, C. B. Gorman, N. Tao, *Chem. Phys.* **2006**, *326*, 138-143.

[5] a) J. E. Klare, G. S. Tulevski, K. Sugo, A. de Picciotto, K. A. White, C. Nuckolls, *J. Am. Chem. Soc.* **2003**, *125*, 6030-6031; b) J. N. Wilson, U. H. F. Bunz, *J. Am. Chem. Soc.* **2005**, *127*, 4124-4125; c) A. J. Zucchero, P. L. McGrier, U. H. F. Bunz, *Acc. Chem. Res.* **2009**, *43*, 397-408; d) M. A. Saeed, H. T. M. Le, O. Š. Miljanić, *Acc. Chem. Res.* **2014**, *47*, 2074-2083.

[6] S. Grunder, R. Huber, S. Wu, C. Schönenberger, M. Calame, M. Mayor, *Eur. J. Org. Chem.* **2010**, *2010*, 833-845.

[7] a) C. R. Parker, Z. Wei, C. R. Arroyo, K. Jennum, T. Li, M. Santella, N. Bovet, G. Zhao, W. Hu, H. S. J. van der Zant, M. Vanin, G. C. Solomon, B. W. Laursen, K. Nørgaard, M. B. Nielsen, *Adv. Mater.* **2013**, *25*, 405-409; b) C. R. Parker, E. Leary, R. Frisenda, Z. Wei, K. S. Jennum, E. Glibstrup, P. B. Abrahamsen, M. Santella, M. A. Christensen, E. A. Della Pia, T. Li, M. T. Gonzalez, X. Jiang, T. J. Morsing, G. Rubio-Bollinger, B. W. Laursen, K. Nørgaard, H. van der Zant, N. Agrait, M. B. Nielsen, *J. Am. Chem. Soc.* **2014**, *136*, 16497-16507.

[8] a) Y. Fu, S. Chen, A. Kuzume, A. Rudnev, C. Huang, V. Kaliginedi, M. Baghernejad, W. Hong, T. Wandlowski, S. Decurtins, S.-X. Liu, *Nat. Commun.* **2015**, *6*; 6403 b) W. Hong, H. Li, S.-X. Liu, Y. Fu, J. Li, V. Kaliginedi, S. Decurtins, T. Wandlowski, *J. Am. Chem. Soc.* **2012**, *134*, 19425-19431.

[9] E. Leary, A. La Rosa, M. T. Gonzalez, G. Rubio-Bollinger, N. Agrait, N. Martin, *Chem. Soc. Rev.* **2015**, *44*, 920-942.

[10] a) C. Yi, C. Blum, M. Lehmann, S. Keller, S.-X. Liu, G. Frei, A. Neels, J. Hauser, S. Schürch, S. Decurtins, *J. Org. Chem.* **2010**, *75*, 3350-3357; b) H. Li, P. Jiang, C. Yi, C. Li, S.-X. Liu, S. Tan, B. Zhao, J. Braun, W. Meier, T. Wandlowski, S. Decurtins, *Macromolecules* **2010**, *43*, 8058-8062.

[11] a) W. Hong, H. Valkenier, G. Meszaros, D. Z. Manrique, A. Mishchenko, A. Putz, P. M. Garcia, C. J. Lambert, J. C. Hummelen, T. Wandlowski, *Beilstein J. Nanotechnol.* **2011**, *2*, 699-713; b) W. Hong, D. Z. Manrique, P. Moreno-Garcia, M. Gulcur, A. Mishchenko, C. J. Lambert, M. R. Bryce, T. Wandlowski, *J. Am. Chem. Soc.* **2012**, *134*, 2292-2304.

[12] Y. Aeschi, H. Li, Z. Cao, S. Chen, A. Amacher, N. Bieri, B. Özen, J. Hauser, S. Decurtins, S. Tan, S.-X. Liu, *Org. Lett.* **2013**, *15*, 5586-5589.

[13] a) M. Baghernejad, D. Z. Manrique, C. Li, T. Pope, U. Zhumaev, I. Pobelov, P. Moreno-Garcia, V. Kaliginedi, C. Huang, W. Hong, C. Lambert, T. Wandlowski, *Chem. Commun.* **2014**, *50*, 15975-15978; b) R. J. Brooke, C. Jin, D. S. Szumski, R. J. Nichols, B.-W. Mao, K. S. Thygesen, W. Schwarzacher, *Nano Lett.* **2015**, *15*, 275-280; c) B. Capozzi, Q. Chen, P. Darancet, M. Kotiuga, M. Buzzeo, J. B. Neaton, C. Nuckolls, L. Venkataraman, *Nano Lett.* **2014**, *14*, 1400-1404.

[14] a) M. Baghernejad, X. Zhao, K. Baruël Ørnsø, M. Füeg, P. Moreno-García, A. V. Rudnev, V. Kaliginedi, S. Vesztergom, C. Huang, W. Hong, P. Broekmann, T. Wandlowski, K. S. Thygesen, M. R. Bryce, *J. Am. Chem. Soc.* **2014**, *136*, 17922-17925; b) N. Darwish, I. Díez-Pérez, P. Da Silva, N. Tao, J. J. Gooding, M. N. Paddon-Row, *Angew. Chem. Int. Ed.* **2012**, *51*, 3203-3206; *Angew. Chem.* **2012**, *124*, 3257-3260; c) Z. Li, H. Li, S. Chen, T. Froehlich, C. Yi, C. Schönenberger, M. Calame, S. Decurtins, S.-X. Liu, E. Borguet, *J. Am. Chem. Soc.* **2014**, *136*, 8867-8870; d) X.-S. Zhou, L. Liu, P. Fortgang, A.-S. Lefevre, A. Serra-Muns, N. Raouafi, C. Amatore, B.-W. Mao, E. Maisonhaute, B. Schöllhorn, *J. Am. Chem. Soc.* **2011**, *133*, 7509-7516.

[15] J. Enkovaara, C. Rostgaard, J. J. Mortensen, J. Chen, M. Dułak, L. Ferrighi, J. Gavnholt, C. Glinsvad, V. Haikola, H. A. Hansen, H. H. Kristoffersen, M. Kuisma, A. H. Larsen, L. Lehtovaara, M. Ljungberg, O. Lopez-Acevedo, P. G. Moses, J. Ojanen, T. Olsen, V. Petzold, N. A. Romero, J. Stausholm-Møller, M. Strange, G. A. Tritsaris, M. Vanin, M. Walter, B. Hammer, H. Häkkinen, G. K. H. Madsen, R. M. Nieminen, J. K. Nørskov, M. Puska, T. T. Rantala, J. Schiøtz, K. S. Thygesen, K. W. Jacobsen, *J. Phys.: Condens. Matter* **2010**, *22*, 253202.

[16] D. J. Mowbray, G. Jones, K. S. Thygesen, *J. Phys. Chem.* **2008**, *128*, 111103.

[17] R. C. Hoft, M. J. Ford, V. M. García-Suárez, C. J. Lambert, M. B. Cortie, *J. Phys.: Condens. Matter* **2008**, *20*, 025207.

WILEY-VCH

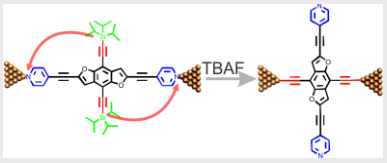

Cancan Huang, Songjie Chen, Kristian Baruël Ørnsø, David Reber, Masoud Baghernejad, Yongchun Fu, Thomas Wandlowski, Silvio Decurtins, Wenjing Hong, Kristian Sommer Thygesen,* and Shi-Xia Liu**

Controlling Electrical Conductance through a π-Conjugated Cruciform Molecule via Selective Anchoring to Gold Electrodes

For the first time, it has been demonstrated that two distinct charge transport pathways through a cruciform molecule at the single-molecule level can be tuned via chemically controllable anchoring sites. Upon in-situ cleavage of the triisopropylsilyl group, complete conversion from the M1-N junctions to the M1-C junctions is achieved with a conductance increase by more than one order of magnitude.